Journal of Chemistry

Applications and Green Synthesis of Metal Oxide Composites

Lead Guest Editor: Rabia Rehman
Guest Editors: Madeeha Batool and Mehdi Vosoughi

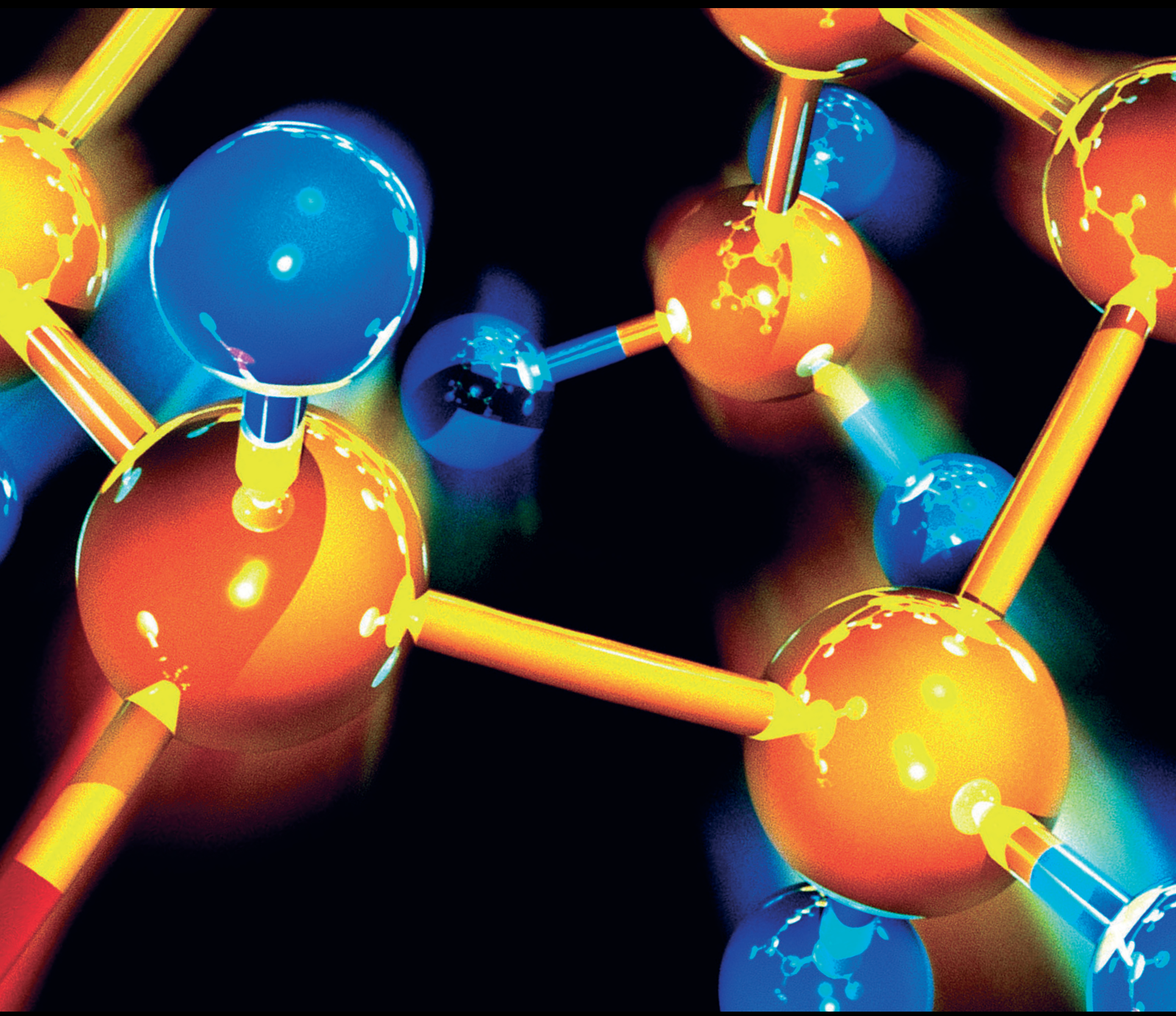

Applications and Green Synthesis of Metal Oxide Composites

Journal of Chemistry

Applications and Green Synthesis of Metal Oxide Composites

Lead Guest Editor: Rabia Rehman
Guest Editors: Madeeha Batool and Mehdi Vosoughi

Contents

Retracted: Effectiveness of Oil Filling in Tight Sandstone Reservoirs of Yancheng Formation in Ordos Basin
Journal of Chemistry
Retraction (1 page), Article ID 9834670, Volume 2023 (2023)

Retracted: Exploration of Erdaohe Silver Polymetallic Deposit in Inner Mongolia based on Induced Polarization Method
Journal of Chemistry
Retraction (1 page), Article ID 9761347, Volume 2023 (2023)

[Retracted] Prediction of Chemical Corrosion Rate and Remaining Life of Buried Oil and Gas Pipelines in Changqing Gas Field
Xianbing Li, Rui Liu, Dong Ma, Yang Bai, Yukai Shi, and Badm Anhouck
Research Article (8 pages), Article ID 7296454, Volume 2023 (2023)

[Retracted] Sedimentary Facies Evaluation of Tight Oil Reservoirs of Yanchang Formation in the Ordos Basin
Yu Peng, Huaijie Zhang, Xiaoli Zheng, Yi Wang, Jiye Li, Yinhui Zhu, and Quine Doolen
Research Article (11 pages), Article ID 9605436, Volume 2023 (2023)

[Retracted] Damage of Green Synthetic Cement Slurry to Clastic Rock Reservoir
Meng Xu, Xin Tan, Libo Yang, Hanlie Cheng, and David Cofell
Research Article (7 pages), Article ID 8937828, Volume 2023 (2023)

[Retracted] Effectiveness of Oil Filling in Tight Sandstone Reservoirs of Yancheng Formation in Ordos Basin
Yu Han, Peiru Wanyan, Haoli Wang, Mengfei Qu, Hanlie Cheng, and Fahim Theon
Research Article (8 pages), Article ID 9907772, Volume 2022 (2022)

[Retracted] Geochemical Characteristics of Crude Oil in Member 7 of Yanchang Formation in Yanchang Oilfield
Wenming Li, Zhendong Gao, Yongdong Wang, Jingyang Pu, Hanlie Cheng, and Fahim Theon
Research Article (7 pages), Article ID 2797655, Volume 2022 (2022)

[Retracted] Exploration of Erdaohe Silver Polymetallic Deposit in Inner Mongolia based on Induced Polarization Method
Baoyou Li, Zhiqing Shi, Zhiguang Yang, Lan Xu, Hanlie Cheng, and David Sturdivant
Research Article (9 pages), Article ID 7053491, Volume 2022 (2022)

[Retracted] Integrated Design Technology of Geological Engineering for Pressure Flooding and Water Injection in Low Permeability Reservoirs: Take the Reservoir of Keshang Formation in Wu2 East Area as an Example
Ming Qin, Chao Chen, Qingsen Yu, Zhenping Liu, Zhibo Liu, Hanlie Cheng, and Fahim Theon
Research Article (8 pages), Article ID 1392831, Volume 2022 (2022)

Contents

Hindawi
Journal of Chemistry
Volume 2023, Article ID 9891764, 1 page
https://doi.org/10.1155/2023/9891764

Retraction

Retracted: Characteristics of Sedimentary Microfacies of Late Triassic Yanchang Formation in North-Central Ordos Basin

Journal of Chemistry

Received 28 November 2023; Accepted 28 November 2023; Published 29 November 2023

This article has been retracted by Hindawi, as publisher, following an investigation undertaken by the publisher [1]. This investigation has uncovered evidence of systematic manipulation of the publication and peer-review process. We cannot, therefore, vouch for the reliability or integrity of this article.

Please note that this notice is intended solely to alert readers that the peer-review process of this article has been compromised.

Wiley and Hindawi regret that the usual quality checks did not identify these issues before publication and have since put additional measures in place to safeguard research integrity.

We wish to credit our Research Integrity and Research Publishing teams and anonymous and named external researchers and research integrity experts for contributing to this investigation.

The corresponding author, as the representative of all authors, has been given the opportunity to register their agreement or disagreement to this retraction. We have kept a record of any response received.

References

[1] J. Wei, F. Li, S. Zhang, H. Cheng, Q. Qin, and D. Cadasse, "Characteristics of Sedimentary Microfacies of Late Triassic Yanchang Formation in North-Central Ordos Basin," *Journal of Chemistry*, vol. 2022, Article ID 1513503, 10 pages, 2022.

Hindawi
Journal of Chemistry
Volume 2023, Article ID 9864546, 1 page
https://doi.org/10.1155/2023/9864546

Retraction

Retracted: Damage of Green Synthetic Cement Slurry to Clastic Rock Reservoir

Journal of Chemistry

Received 28 November 2023; Accepted 28 November 2023; Published 29 November 2023

This article has been retracted by Hindawi, as publisher, following an investigation undertaken by the publisher [1]. This investigation has uncovered evidence of systematic manipulation of the publication and peer-review process. We cannot, therefore, vouch for the reliability or integrity of this article.

Please note that this notice is intended solely to alert readers that the peer-review process of this article has been compromised.

Wiley and Hindawi regret that the usual quality checks did not identify these issues before publication and have since put additional measures in place to safeguard research integrity.

We wish to credit our Research Integrity and Research Publishing teams and anonymous and named external researchers and research integrity experts for contributing to this investigation.

The corresponding author, as the representative of all authors, has been given the opportunity to register their agreement or disagreement to this retraction. We have kept a record of any response received.

References

[1] M. Xu, X. Tan, L. Yang, H. Cheng, and D. Cofell, "Damage of Green Synthetic Cement Slurry to Clastic Rock Reservoir," *Journal of Chemistry*, vol. 2023, Article ID 8937828, 7 pages, 2023.

Hindawi
Journal of Chemistry
Volume 2023, Article ID 9837090, 1 page
https://doi.org/10.1155/2023/9837090

Retraction

Retracted: Prediction of Chemical Corrosion Rate and Remaining Life of Buried Oil and Gas Pipelines in Changqing Gas Field

Journal of Chemistry

Received 28 November 2023; Accepted 28 November 2023; Published 29 November 2023

This article has been retracted by Hindawi, as publisher, following an investigation undertaken by the publisher [1]. This investigation has uncovered evidence of systematic manipulation of the publication and peer-review process. We cannot, therefore, vouch for the reliability or integrity of this article.

Please note that this notice is intended solely to alert readers that the peer-review process of this article has been compromised.

Wiley and Hindawi regret that the usual quality checks did not identify these issues before publication and have since put additional measures in place to safeguard research integrity.

We wish to credit our Research Integrity and Research Publishing teams and anonymous and named external researchers and research integrity experts for contributing to this investigation.

The corresponding author, as the representative of all authors, has been given the opportunity to register their agreement or disagreement to this retraction. We have kept a record of any response received.

References

[1] X. Li, R. Liu, D. Ma, Y. Bai, Y. Shi, and B. Anhouck, "Prediction of Chemical Corrosion Rate and Remaining Life of Buried Oil and Gas Pipelines in Changqing Gas Field," *Journal of Chemistry*, vol. 2023, Article ID 7296454, 8 pages, 2023.

Hindawi
Journal of Chemistry
Volume 2023, Article ID 9831807, 1 page
https://doi.org/10.1155/2023/9831807

Retraction

Retracted: Bioactivation of Polyaniline for Biomedical Applications and Metal Oxide Composites

Journal of Chemistry

Received 28 November 2023; Accepted 28 November 2023; Published 29 November 2023

This article has been retracted by Hindawi, as publisher, following an investigation undertaken by the publisher [1]. This investigation has uncovered evidence of systematic manipulation of the publication and peer-review process. We cannot, therefore, vouch for the reliability or integrity of this article.

Please note that this notice is intended solely to alert readers that the peer-review process of this article has been compromised.

Wiley and Hindawi regret that the usual quality checks did not identify these issues before publication and have since put additional measures in place to safeguard research integrity.

We wish to credit our Research Integrity and Research Publishing teams and anonymous and named external researchers and research integrity experts for contributing to this investigation.

The corresponding author, as the representative of all authors, has been given the opportunity to register their agreement or disagreement to this retraction. We have kept a record of any response received.

References

[1] K. A. Omran, "Bioactivation of Polyaniline for Biomedical Applications and Metal Oxide Composites," *Journal of Chemistry*, vol. 2022, Article ID 9328512, 9 pages, 2022.

Hindawi
Journal of Chemistry
Volume 2023, Article ID 9819656, 1 page
https://doi.org/10.1155/2023/9819656

Retraction

Retracted: Integrated Design Technology of Geological Engineering for Pressure Flooding and Water Injection in Low Permeability Reservoirs: Take the Reservoir of Keshang Formation in Wu2 East Area as an Example

Journal of Chemistry

Received 28 November 2023; Accepted 28 November 2023; Published 29 November 2023

This article has been retracted by Hindawi, as publisher, following an investigation undertaken by the publisher [1]. This investigation has uncovered evidence of systematic manipulation of the publication and peer-review process. We cannot, therefore, vouch for the reliability or integrity of this article.

Please note that this notice is intended solely to alert readers that the peer-review process of this article has been compromised.

Wiley and Hindawi regret that the usual quality checks did not identify these issues before publication and have since put additional measures in place to safeguard research integrity.

We wish to credit our Research Integrity and Research Publishing teams and anonymous and named external researchers and research integrity experts for contributing to this investigation.

The corresponding author, as the representative of all authors, has been given the opportunity to register their agreement or disagreement to this retraction. We have kept a record of any response received.

References

[1] M. Qin, C. Chen, Q. Yu et al., "Integrated Design Technology of Geological Engineering for Pressure Flooding and Water Injection in Low Permeability Reservoirs: Take the Reservoir of Keshang Formation in Wu2 East Area as an Example," *Journal of Chemistry*, vol. 2022, Article ID 1392831, 8 pages, 2022.

Hindawi
Journal of Chemistry
Volume 2023, Article ID 9807940, 1 page
https://doi.org/10.1155/2023/9807940

Retraction

Retracted: Design of Noise-Reducing Two-Stage Cage Control Valve and Its Fluid Characteristics and Cavitation Study

Journal of Chemistry

Received 28 November 2023; Accepted 28 November 2023; Published 29 November 2023

This article has been retracted by Hindawi, as publisher, following an investigation undertaken by the publisher [1]. This investigation has uncovered evidence of systematic manipulation of the publication and peer-review process. We cannot, therefore, vouch for the reliability or integrity of this article.

Please note that this notice is intended solely to alert readers that the peer-review process of this article has been compromised.

Wiley and Hindawi regret that the usual quality checks did not identify these issues before publication and have since put additional measures in place to safeguard research integrity.

We wish to credit our Research Integrity and Research Publishing teams and anonymous and named external researchers and research integrity experts for contributing to this investigation.

The corresponding author, as the representative of all authors, has been given the opportunity to register their agreement or disagreement to this retraction. We have kept a record of any response received.

References

[1] R. Yu and X. Lu, "Design of Noise-Reducing Two-Stage Cage Control Valve and Its Fluid Characteristics and Cavitation Study," *Journal of Chemistry*, vol. 2022, Article ID 7322655, 23 pages, 2022.

Hindawi
Journal of Chemistry
Volume 2023, Article ID 9785450, 1 page
https://doi.org/10.1155/2023/9785450

Retraction

Retracted: Sedimentary Facies Evaluation of Tight Oil Reservoirs of Yanchang Formation in the Ordos Basin

Journal of Chemistry

Received 28 November 2023; Accepted 28 November 2023; Published 29 November 2023

This article has been retracted by Hindawi, as publisher, following an investigation undertaken by the publisher [1]. This investigation has uncovered evidence of systematic manipulation of the publication and peer-review process. We cannot, therefore, vouch for the reliability or integrity of this article.

Please note that this notice is intended solely to alert readers that the peer-review process of this article has been compromised.

Wiley and Hindawi regret that the usual quality checks did not identify these issues before publication and have since put additional measures in place to safeguard research integrity.

We wish to credit our Research Integrity and Research Publishing teams and anonymous and named external researchers and research integrity experts for contributing to this investigation.

The corresponding author, as the representative of all authors, has been given the opportunity to register their agreement or disagreement to this retraction. We have kept a record of any response received.

References

[1] Y. Peng, H. Zhang, X. Zheng et al., "Sedimentary Facies Evaluation of Tight Oil Reservoirs of Yanchang Formation in the Ordos Basin," *Journal of Chemistry*, vol. 2023, Article ID 9605436, 11 pages, 2023.

Hindawi
Journal of Chemistry
Volume 2023, Article ID 9764037, 1 page
https://doi.org/10.1155/2023/9764037

Retraction

Retracted: Differential Scanning Calorimetry Material Studies: Benzil Melting Point Method for Eliminating the Thermal History of DSC

Journal of Chemistry

Received 28 November 2023; Accepted 28 November 2023; Published 29 November 2023

This article has been retracted by Hindawi, as publisher, following an investigation undertaken by the publisher [1]. This investigation has uncovered evidence of systematic manipulation of the publication and peer-review process. We cannot, therefore, vouch for the reliability or integrity of this article.

Please note that this notice is intended solely to alert readers that the peer-review process of this article has been compromised.

Wiley and Hindawi regret that the usual quality checks did not identify these issues before publication and have since put additional measures in place to safeguard research integrity.

We wish to credit our Research Integrity and Research Publishing teams and anonymous and named external researchers and research integrity experts for contributing to this investigation.

The corresponding author, as the representative of all authors, has been given the opportunity to register their agreement or disagreement to this retraction. We have kept a record of any response received.

References

[1] Z. Zhu, W. Li, Y. Yin, R. Cao, and Z. Li, "Differential Scanning Calorimetry Material Studies: Benzil Melting Point Method for Eliminating the Thermal History of DSC," *Journal of Chemistry*, vol. 2022, Article ID 3423429, 9 pages, 2022.

Hindawi
Journal of Chemistry
Volume 2023, Article ID 9864308, 1 page
https://doi.org/10.1155/2023/9864308

Retraction

Retracted: Geochemical Characteristics of Crude Oil in Member 7 of Yanchang Formation in Yanchang Oilfield

Journal of Chemistry

Received 15 August 2023; Accepted 15 August 2023; Published 16 August 2023

This article has been retracted by Hindawi following an investigation undertaken by the publisher [1]. This investigation has uncovered evidence of one or more of the following indicators of systematic manipulation of the publication process:

(1) Discrepancies in scope

(2) Discrepancies in the description of the research reported

(3) Discrepancies between the availability of data and the research described

(4) Inappropriate citations

(5) Incoherent, meaningless and/or irrelevant content included in the article

(6) Peer-review manipulation

The presence of these indicators undermines our confidence in the integrity of the article's content and we cannot, therefore, vouch for its reliability. Please note that this notice is intended solely to alert readers that the content of this article is unreliable. We have not investigated whether authors were aware of or involved in the systematic manipulation of the publication process.

Wiley and Hindawi regrets that the usual quality checks did not identify these issues before publication and have since put additional measures in place to safeguard research integrity.

We wish to credit our own Research Integrity and Research Publishing teams and anonymous and named external researchers and research integrity experts for contributing to this investigation.

The corresponding author, as the representative of all authors, has been given the opportunity to register their agreement or disagreement to this retraction. We have kept a record of any response received.

References

[1] W. Li, Z. Gao, Y. Wang, J. Pu, H. Cheng, and F. Theon, "Geochemical Characteristics of Crude Oil in Member 7 of Yanchang Formation in Yanchang Oilfield," *Journal of Chemistry*, vol. 2022, Article ID 2797655, 7 pages, 2022.

Hindawi
Journal of Chemistry
Volume 2023, Article ID 9834670, 1 page
https://doi.org/10.1155/2023/9834670

Retraction

Retracted: Effectiveness of Oil Filling in Tight Sandstone Reservoirs of Yancheng Formation in Ordos Basin

Journal of Chemistry

Received 15 August 2023; Accepted 15 August 2023; Published 16 August 2023

This article has been retracted by Hindawi following an investigation undertaken by the publisher [1]. This investigation has uncovered evidence of one or more of the following indicators of systematic manipulation of the publication process:

(1) Discrepancies in scope

(2) Discrepancies in the description of the research reported

(3) Discrepancies between the availability of data and the research described

(4) Inappropriate citations

(5) Incoherent, meaningless and/or irrelevant content included in the article

(6) Peer-review manipulation

The presence of these indicators undermines our confidence in the integrity of the article's content and we cannot, therefore, vouch for its reliability. Please note that this notice is intended solely to alert readers that the content of this article is unreliable. We have not investigated whether authors were aware of or involved in the systematic manipulation of the publication process.

Wiley and Hindawi regrets that the usual quality checks did not identify these issues before publication and have since put additional measures in place to safeguard research integrity.

We wish to credit our own Research Integrity and Research Publishing teams and anonymous and named external researchers and research integrity experts for contributing to this investigation.

The corresponding author, as the representative of all authors, has been given the opportunity to register their agreement or disagreement to this retraction. We have kept a record of any response received.

References

[1] Y. Han, P. Wanyan, H. Wang, M. Qu, H. Cheng, and F. Theon, "Effectiveness of Oil Filling in Tight Sandstone Reservoirs of Yancheng Formation in Ordos Basin," *Journal of Chemistry*, vol. 2022, Article ID 9907772, 8 pages, 2022.

Hindawi
Journal of Chemistry
Volume 2023, Article ID 9761347, 1 page
https://doi.org/10.1155/2023/9761347

Retraction

Retracted: Exploration of Erdaohe Silver Polymetallic Deposit in Inner Mongolia based on Induced Polarization Method

Journal of Chemistry

Received 15 August 2023; Accepted 15 August 2023; Published 16 August 2023

This article has been retracted by Hindawi following an investigation undertaken by the publisher [1]. This investigation has uncovered evidence of one or more of the following indicators of systematic manipulation of the publication process:

(1) Discrepancies in scope
(2) Discrepancies in the description of the research reported
(3) Discrepancies between the availability of data and the research described
(4) Inappropriate citations
(5) Incoherent, meaningless and/or irrelevant content included in the article
(6) Peer-review manipulation

The presence of these indicators undermines our confidence in the integrity of the article's content and we cannot, therefore, vouch for its reliability. Please note that this notice is intended solely to alert readers that the content of this article is unreliable. We have not investigated whether authors were aware of or involved in the systematic manipulation of the publication process.

Wiley and Hindawi regrets that the usual quality checks did not identify these issues before publication and have since put additional measures in place to safeguard research integrity.

We wish to credit our own Research Integrity and Research Publishing teams and anonymous and named external researchers and research integrity experts for contributing to this investigation.

The corresponding author, as the representative of all authors, has been given the opportunity to register their agreement or disagreement to this retraction. We have kept a record of any response received.

References

[1] B. Li, Z. Shi, Z. Yang, L. Xu, H. Cheng, and D. Sturdivant, "Exploration of Erdaohe Silver Polymetallic Deposit in Inner Mongolia based on Induced Polarization Method," *Journal of Chemistry*, vol. 2022, Article ID 7053491, 9 pages, 2022.

Hindawi
Journal of Chemistry
Volume 2023, Article ID 9837090, 1 page
https://doi.org/10.1155/2023/9837090

Retraction

Retracted: Prediction of Chemical Corrosion Rate and Remaining Life of Buried Oil and Gas Pipelines in Changqing Gas Field

Journal of Chemistry

Received 28 November 2023; Accepted 28 November 2023; Published 29 November 2023

This article has been retracted by Hindawi, as publisher, following an investigation undertaken by the publisher [1]. This investigation has uncovered evidence of systematic manipulation of the publication and peer-review process. We cannot, therefore, vouch for the reliability or integrity of this article.

Please note that this notice is intended solely to alert readers that the peer-review process of this article has been compromised.

Wiley and Hindawi regret that the usual quality checks did not identify these issues before publication and have since put additional measures in place to safeguard research integrity.

We wish to credit our Research Integrity and Research Publishing teams and anonymous and named external researchers and research integrity experts for contributing to this investigation.

The corresponding author, as the representative of all authors, has been given the opportunity to register their agreement or disagreement to this retraction. We have kept a record of any response received.

References

[1] X. Li, R. Liu, D. Ma, Y. Bai, Y. Shi, and B. Anhouck, "Prediction of Chemical Corrosion Rate and Remaining Life of Buried Oil and Gas Pipelines in Changqing Gas Field," *Journal of Chemistry*, vol. 2023, Article ID 7296454, 8 pages, 2023.

Hindawi
Journal of Chemistry
Volume 2023, Article ID 7296454, 8 pages
https://doi.org/10.1155/2023/7296454

Research Article

Prediction of Chemical Corrosion Rate and Remaining Life of Buried Oil and Gas Pipelines in Changqing Gas Field

Xianbing Li,[1] Rui Liu,[1] Dong Ma,[1] Yang Bai,[1] Yukai Shi,[2] and Badm Anhouck[3]

[1]*The No. 5 Gas Production Plant of Changqing Oilfield Company, PetroChina, Xi'an, Shaanxi 710018, China*
[2]*The No. 3 Gas Production Plant of Changqing Oilfield Company, PetroChina, Xi'an, Shaanxi 710018, China*
[3]*The King's School, Bujumbura BP1560, Burundi*

Correspondence should be addressed to Badm Anhouck; badmanhouck@ksu.edu.bi

Received 10 October 2022; Revised 26 October 2022; Accepted 24 March 2023; Published 25 April 2023

Academic Editor: Rabia Rehman

Green synthesis and metal oxide composites have attracted much attention from researchers of industry and academia. As a typical application of green synthesis and metal oxide composites, the continuous change of industrial technology and the continuous improvement of the social and economic level, the demand for oil and gas are also increasing. However, the spatial gap between the place of origin and the place of demand for oil and gas resources is large, so the long-distance oil and gas pipeline came into being. However, under the action of time, coupled with the corrosion effect of the soil due to deep burial, some pipelines have serious aging and corrosion phenomena. Therefore, in order to give corresponding guarantees for economic development, we need to conduct in-depth research and analysis of the corrosion of oil and gas long-distance pipelines and give effective solutions. In this paper, the corrosion rate prediction of buried oil and gas pipelines is studied in Changqing gas field. By improving the inertial weights and learning factors of the traditional particle swarm algorithm, the parameters of the generalized regression neural network are optimized and selected, and the corrosion rate prediction model of buried pipelines is finally constructed. Comparative analysis with other swarm intelligence algorithms shows that the improved particle swarm algorithm has stronger convergence ability and higher prediction accuracy than the BP model and SVM model. In addition, based on the detection data collected at the site of the gathering and transportation pipeline in Changqing gas field, this paper uses the extreme value distribution theory and the local corrosion progress formula to establish a prediction model for the residual life of corrosion of buried pipelines. The model established in this paper can effectively determine the risk pipe segment of buried pipeline and provide a decision-making basis for pipeline management departments. The work provides an important application guidance to green synthesis and metal oxide composites.

1. Introduction

It is important to investigate green synthesis and metal oxide composites. As a typical application of green synthesis and metal oxide composite materials, mechanical damage such as scratches, scratches, pits, and mussel eyes of the pipeline itself are internal factors that affect its service life, while soil corrosion, bacterial corrosion, and stray current corrosion in primary batteries are external factors that affect its service life. In order to inhibit the corrosion of the outer wall of the pipeline by the surrounding environment, the long-distance pipeline generally adopts the dual protection measures of anticorrosion layer and cathodic protection [1–3]. However, due to the limited construction conditions on site, in the construction process of the pipeline, the quality of the pipeline anticorrosion coating cannot be guaranteed [4–7]. At the same time, with the increase of the service life, the anticorrosion coating is aging, cracking, and even peeling, and the soil corrosive medium is immersed, thus providing conditions for the occurrence and development of corrosion, and the possibility of corrosion of the pipeline is greatly increased, increasing the unsafe operation of the pipeline. In addition, due to the poor management of pipeline operation, the pipe body bears too much load, so that the pipeline is "tired into a disease" for a long time, which increases the danger of pipeline operation [8–11]. Therefore, with the

increase in the service life of buried long-distance pipelines, the possibility of accidents such as perforation, leakage, and cracking has also increased, causing huge economic losses to the production and operation management departments and bringing very serious impacts on social life and the ecological environment. Therefore, it is necessary to predict the remaining corrosion life of the pipeline, that is, to determine the remaining corrosion life of the pipeline in advance, so as to formulate a reasonable inspection and maintenance cycle in advance, to prevent accidents and avoid unnecessary waste caused by premature replacement of the pipeline, and to reduce the probability of pipeline corrosion perforation leakage accidents and the resulting economic and resource losses.

The remaining life of the pipeline can be divided into three aspects, namely, corrosion life, subcritical crack propagation life, and damage life. Among them, in addition to the subcritical crack propagation life (especially fatigue crack propagation life) is easier to predict, the study of corrosion life and damage life is far from mature, and foreign countries have not formed standards in this regard [12–15]. The research idea is to obtain the statistical results of corrosion rate through the statistical analysis of the on-site corrosion number of a large number of pipelines, or to obtain the calculation of corrosion rate through a large number of corrosion data inside and outside the pipe, and to generalize to general pipelines. There is no literature on the remaining life prediction study considering the efficiency of antiseptic layers, cathodic protection, and corrosion inhibitor protection [16–19]. The former Soviet Union has the longest pipeline system and the largest pipe diameter in the world, and their pipeline design life requirement is about 35 years. According to statistics, the main cause of the accident is corrosion, accounting for 33%–68% of the total number of accidents, so the study of corrosion life is very important. However, the main load of the pipeline is the internal pressure. In the pumping station, the internal pressure of the pipeline fluctuates only in a small range and will not alternate, so fatigue is not the main problem [20–23].

According to the analysis of more than 1500 abstracts of domestic oil and gas industry corrosion research literature retrieved on China Petroleum Abstracts, it shows that between 1985 and 1992, there were less than 20 research literatures on corrosion life prediction, and most of them studied the corrosion fatigue life and the protective life of corrosion inhibitors and coatings, etc. Only two articles have been reported on the basic corrosion rate of corrosion residual life prediction research [24–27]. Although these data do not fully and accurately reflect the status of domestic corrosion residual life research, it can be seen that domestic research in this area is indeed lacking. In recent years, with the advent of the international research climax of operational adaptability (FFS) including residual strength, residual life, and defect detection, the study of residual life of corrosion has begun to be involved, but in general, it is only in the initial stage of exploration. At present, the corrosion life prediction methods are all based on historical inspection data and reasonable mathematical models. This prediction has good reliability in a short time. With the extension of prediction time, the reliability of prediction is not high.

The external corrosion detection technologies of pipelines at home and abroad are mainly divided into two categories: ① the detection of the protection effect of the external coating of pipelines, including the current attenuation method (PCM), current gradient detection method (ACVG), and DC potential gradient method (DCVG) in multi frequency tubes; ② the detection of the cathodic protection effect is mainly CIPS.

Most of the oil and gas pipelines in service in Changqing oil field were constructed in the 1970s, and their service life is close to or more than the initial design life. There are many factors affecting the corrosion of oil and gas pipelines, and the factors also affect each other, which objectively increases the difficulty of predicting the remaining life of oil and gas pipelines due to corrosion. The corrosion rate plays a decisive role in predicting the remaining corrosion life of oil and gas pipelines. However, if the traditional probability statistics calculation method is used, the prediction accuracy error will be large due to the insufficient number of data samples. In this paper, by introducing the particle swarm algorithm and generalized regression neural network concept and algorithm flow, this paper improves the particle swarm algorithm, constructs the PSO optimized GRNN buried pipeline corrosion rate prediction model, combines the buried pipeline corrosion data, takes the rough set as the feature engineering before the model input, and then trains and learns the prediction model, completes the corrosion rate prediction of buried pipeline, and compares and analyzes the model performance. In addition, the corrosion depth of a corrosion defect area of the collection and transportation pipeline is analyzed and processed by probabilistic statistical method, and the maximum corrosion depth of the pipeline is obtained by the extreme value distribution method, and the remaining service life of the pipeline is calculated by combining the empirical formula of local corrosion progress.

2. Methods and Theories

2.1. Establishment of Corrosion Rate Prediction Model Based on Green Synthesis. Inspired by RBF network, Specht proposed a new algorithm–general regression neural network–(GRNN) in 1991. GRNN is a prefeedback neural network based on nonlinear regression theory, which is an important branch of RBF. GRNN has many advantages, such as fast training speed, good global convergence, and few adjusting parameters. In order to simplify the pipeline sample data and reduce the corrosion characteristic dimension, the attribute reduction in RS theory is first used to select the corrosion factor, and then, the reduced sample data are used as the input of GRNN, and the improved PSO is used to optimize the selection of network parameters to construct the corrosion rate prediction model of buried pipelines. Considering the problem of parameters to be optimized in GRNN, particle swarm optimization (PSO) is introduced to automatically optimize the smoothing factor of GRNN. As a classical intelligent optimization algorithm,

PSO was proposed by James Kennedy and Russell Eberhart in 1995. The basic PSO is inspired by birds' foraging behavior. If there is a D dimension search space, there are n particles to form a population.

2.1.1. Modeling Steps. The basic steps of the buried pipeline corrosion prediction model based on RS-PSO-GRNN are as follows:

Step 1: Construct an index system, collect, and sort out the original data set of buried pipelines according to the actual engineering background, sort out and summarize the corrosion factors of pipelines, and determine the original sample set

Step 2: Discrete the data and establish a decision table, including the conditional attribute set and the decision attribute set, the conditional attribute set is the selected feature index, and the decision attribute set is the obtained pipeline corrosion rate

Step 3: Under the condition of maintaining the unidentifiable relationship between conditional attributes and decision attributes, use attribute reduction to delete redundant (conflict) attributes in the decision table to obtain the core indicator attribute set

Step 4: In view of the inconsistency of the dimensions of each indicator, normalize the core indicator data set, and take turns to divide the training sample set and the test sample set

Step 5: Take the training sample set as the input to the model, select the appropriate fitness function, use the modified PSO to find the best smoothing factor b, and determine the optimal RS-PSO-GRNN model

Step 6: Input the test samples into the learned RS-PSO-GRNN model, obtain the network output prediction results, compare the analysis results, and verify the model performance

2.1.2. Data Standardization. Data standardization refers to the scaling of the attribute value of the sample to a specific interval, and the reasons for data standardization are as follows: first, the difference of orders of magnitude will lead to a huge advantage in the attributes of the magnitude; second, the difference of orders of magnitude will seriously reduce the iterative convergence speed of the algorithm; third, algorithms involving sample distances are particularly sensitive to the magnitude of the data. There are two common ways to standardize data: min-max normalization and z-score normalization. This paper uses root mean square error (RMSE) as the fitness function of PSO. RMSE can be used as a standard to measure the true error between the predicted value and the true value and is sensitive to predictions with large errors, and if the predicted value is far away from the true value, the value of the RMSE will increase sharply.

Prediction of pipeline corrosion is based on the actual corrosion of past and present pipelines to speculate on future pipeline corrosion trends, and part of the sample set during the sample period is used to build a predictive model to reproduce the situation of the sample period by simulating historical data, which is called historical simulation. The use of prediction models for extrapolated predictions is generally divided into two categories: preprediction and postevent prediction. Postevent projections are only based on predictions made for certain periods that have occurred during the sample period. Advance prediction refers to the prediction of future situations that have not yet occurred. In general, the performance of model predictions should be measured by the results of prior predictions, but the future situation is unknown and cannot be evaluated. In fact, the corrosion mechanism of pipeline is relatively complex, but the development and expansion of pipeline corrosion defect size are a monotonous increasing process, and in a relatively short time, the corrosion development rate is relatively stable, and the corrosion development changes slowly. Therefore, it is assumed that the development trend of pipeline corrosion will increase exponentially over a period of time.

Therefore, in the actual forecasting work, the two methods of fit test and extrapolation test are generally used for evaluation. (1) Fitting test refers to the ability to estimate the prior prediction error of the fit of historical data through the model and mainly to reproduce the ability of the model to fit historical data. The fit test generally uses the following two indicators: mean squared error and relative mean error. The extrapolation test is a test that compares the post-prediction result with the actual value and generally uses the following error indicators to reflect it, generally including extrapolation test, Hill unequal coefficient, and mean absolute percentage error (MAPE). MAPE can be used to measure the predictive power of different models. Table 1 is an evaluation explanation of the prediction accuracy of MAPE.

2.2. Buried Corrosion Pipeline Remaining Life Prediction Method: Extreme Value Statistical Method Based on Green Synthesis. The remaining life of buried pipelines has strong randomness and uncertainty, and for the elderly buried pipelines with low working pressure, corrosion perforation is the most important cause of pipeline failure. Therefore, the maximum corrosion pit depth of the buried pipeline determines the service time of the pipeline, and as the corrosion pit depth deepens, when the depth exceeds the minimum wall thickness allowed for the safe operation of the pipeline, the pipeline will be in danger of corrosion perforation. The maximum allowable corrosion depth of the pipeline is determined according to the manufacturing process and corrosion parameters of the pipeline and can be determined according to ASME B31G standard. When the operating pressure value of corroded pipeline reaches the failure pressure value, the corrosion defect depth is the maximum allowable corrosion depth. Erosion has a probabilistic characteristic, and the maximum value of these local pore erosion depths follows the Gumble extreme value distribution. Extreme value type I, also known as the Gubi distribution, includes two types: "minimum extreme value

Table 1: Predictive evaluation of MAPE with green synthesis and metal oxide composites.

MAPE value	MAPE < 10%	10% < MAPE < 20%	20% < MAPE < 50%	MAPE > 50%
Prediction results	High	Good	Reasonable	Not suitable

type I asymptotic distribution" and "maximum extreme value I type asymptotic distribution," which are used to study the phenomenon of the maximum or minimum value of a variable. It is widely used in the analysis and evaluation of many engineering practical problems.

Maximum corrosion depth prediction of the Gubi distribution:

$$F(x) = \exp\left[-\exp\left(-\frac{x-\lambda}{\alpha}\right)\right], \tag{1}$$

where $F(x)$ is the probability that the depth is less than x; X is random variable for maximum corrosion depth, mm; λ is pitting hole depth with the highest probability density, mm; α is average value of the corrosion hole depth, mm.

Because the pipeline is buried in the ground, when collecting the depth data of the pipeline corrosion pit, it is impossible to excavate the pipeline as a whole and collect the information of the corrosion pit, so the amount of engineering is huge and it is not necessary. Usually, engineering excavation of areas with severe corrosion of pipelines is carried out for sampling and data collection. The deepest corrosion depth thus obtained is highly random, and the deepest corrosion depth of multiple locations cannot be simply averaged, and the deepest corrosion depth cannot be used as a standard for life prediction. The most reasonable method is to statistically process the detected data, obtain statistical parameters λ and α, and then calculate the probability that the deepest corrosion depth does not exceed a certain value according to formula (1).

The N maximum corrosion pit depth data measured under the same conditions are arranged in sequence from smallest to largest, marked with sequence number i and the corresponding corrosion pit depth value x_i, and then, the cumulative distribution function is calculated using the averaging method:

$$F(x) = \frac{i}{N+1}. \tag{2}$$

We take both ends of formula (1) 2 times the logarithm at the same time to get

$$\begin{aligned} y &= -\ln\ln\left(\frac{1}{F(x)}\right) \\ &= \alpha(x-\lambda). \end{aligned} \tag{3}$$

We obtain the statistical parameters λ and α, substitute them into the equation, and then get the probability of $F(X < x)$ that the maximum corrosion depth does not exceed a certain value. If x is used as the abscissa and $-\ln(\ln(1/F))$ as the ordinate, each $(x_i, -\ln(\ln(1/F))$ is drawn in a rectangular coordinate system. If these points show a linear relationship, these decaying data follow the Gubi extreme value distribution. Then, we perform the least squares linear fitting to obtain the slope α and intercept of the fitted straight line $-\alpha\lambda$.

The relationship between the regression period $T(x)$ and the cumulative probability $F(x)$ is

$$T(x) = \frac{1}{(1-F(x))}. \tag{4}$$

The regression period is the expected value of a measurement value x as the observation sequence number. That is, N samples are taken from a certain Gubi distribution, and the maximum value means the pit depth of the entire local section from the maximum pit depth of a small number of small segments of the sample.

$$T(x) = \frac{L}{l}. \tag{5}$$

According to formula (5), the approximate maximum corrosion pit depth for the entire section of long pipe can be obtained. We can substitute the $F(x)$ value obtained by formulas (4) into (3) to obtain a y value. Finally, the y-value is substituted into the fitted straight line equation to find the maximum local corrosion pit depth.

The modeling idea for predicting the corrosion remaining life of buried pipelines is as follows: first, select several pipe sections, excavate and inspect these pipe sections, determine the corrosion defect parameters of weak pipe sections, and calculate the maximum allowable corrosion depth. Then, the corrosion depth detection data are obtained through the embedded film test, and the PSO-GRNN corrosion depth prediction model at different time points is built in combination with the corrosion development trend prediction method, giving the maximum corrosion depth development law of buried pipelines. Finally, the remaining service life of buried pipeline is predicted according to this rule and the maximum allowable corrosion depth.

3. Results and Discussion

3.1. Corrosion Rate Calculation Based on Green Synthesis. Due to the complexity and variety of soil properties, the corrosion status of pipelines varies with different regions. In order to fully understand the operation condition of the pipeline, the detection work of this study mainly determines the sampling area through the early data collection and the macroscopic detection of the field survey and arranges the sampling points, so as to carry out soil detection, stray current detection, and embedded film experiment at the sampling points to calculate the corrosion rate and excavate the relationship between the corrosion factors and the corrosion rate.

Table 2: Folding cross-validation of specific divisions with green synthesis and metal oxide composites.

Number of crossovers	The training set	The verification set	The test set
1st time	5, 6, 7, 8, 9, 10, 11, 12, 13, 14, 15, 16	1, 2, 3, 4	17, 18, 19, 20
2nd time	1, 2, 3, 4, 9, 10, 11, 12, 13, 14, 15, 16	5, 6, 7, 8	
3rd time	1, 2, 3, 4, 5, 6, 7, 8, 13, 14, 15, 16	9, 10, 11, 12	
4th time	1, 2, 3, 4, 5, 6, 7, 8, 9, 10, 11, 12	13, 14, 15, 16	

Table 3: Comparison of each cross-validation with green synthesis and metal oxide composites.

Number of cross-validations	Convergence status		RMSE		Smoothing factor	
	Standard PSO	Improved PSO	Standard PSO	Improved PSO	Standard PSO	Improved PSO
1	65	54	0.0353	0.0303	0.933	1.251
2	90	68	0.0349	0.0332	0.853	1.284
3	121	78	0.0335	0.0309	0.763	1.182
4	97	62	0.0315	0.0306	0.821	1.243
Mean	93.25	65.5	0.0338	0.03125	0.8425	1.24

In order to verify the performance of the model, we selected 20 sets of buried pipeline inspection data from Changqing gas field for simulation experiments. The main factors causing corrosion of buried pipes are soil resistivity, redox potential, PH value, stray current, and sulfate ion content. We use the 4-fold cross-verification method to divide the core index data set after the reduction of rough set properties into 3 parts: training set, verification set, and test set, of which the training set contains 12 samples, the verification set is 4 samples, and the test set is also 4 samples, which are divided into the following as shown in Table 2.

To verify the improved algorithmic performance of the PSO, we compare the standard PSO with a learning factor set to $c_1 = c_2 = 1$. We use the same value for the rest parameters: the number of populations, the maximum number of iterations, and the particle dimension are set to 100, 200, and 1, respectively. The convergence state and minimum RMSE of each cross-verification are shown in Table 3.

Table 3 shows that although the minimum RMSE of the two methods is relatively close, in the process of iterative optimization, the results of four cross-validations show that the convergence speed of the improved PSO is significantly faster than that of the standard PSO, and the analysis results can be obtained. The average values of the convergence states of the standard PSO and the improved PSO are 93.25 and 65.5, respectively, and the average values of the smoothing factor are 0.8425 and 1.24, respectively. The convergence rate of the improved PSO is faster, the optimization ability is stronger, and the stability is better.

Four sets of test samples are brought into a trained PSO-GRNN model for prediction, and the output is denormalized. In order to analyze the performance of the model, the error backpropagation (BP) neural network model and the rough set fusion support vector machine (RS-SVM) model are compared, and the prediction value and the actual value comparison result are shown in Figure 1, and for a more objective evaluation of the performance of the prediction model, the relative error RE is used as the evaluation criterion, as shown in Figure 2.

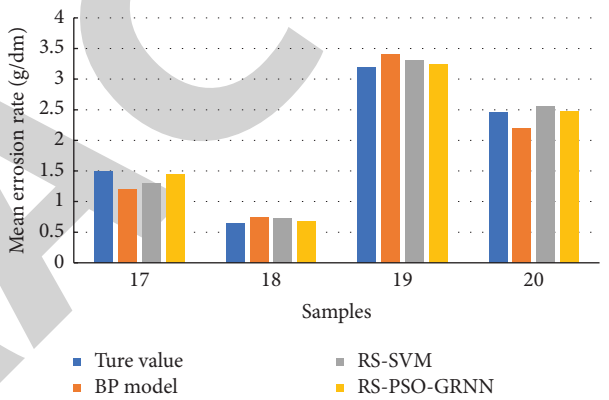

Figure 1: Comparison of predicted and actual values with green synthesis and metal oxide composites.

Although the three models can correctly predict the corrosion defect level of buried pipes, from the overall point of view, whether it is relative error, mean squared error, average absolute percentage error or residual comparison, RS-PSO-GRNN prediction accuracy is the highest, and from the MAPE prediction index evaluation, BP model and RS-SVM model have good results, while RS-PSO-GRNN achieves higher accuracy; therefore, RS-PSO-GRNN model prediction effect is better. The accuracy of the model design scheme is verified, and the evaluation results are more reliable. In summary, it can be seen that the model built in this paper has stronger robustness and better prediction performance, which provides reference significance and decision-making basis for relevant maintenance personnel to learn and grasp the corrosion development status of pipelines (Figures 3 and 4).

3.2. Prediction of the Remaining Life of Buried Corrosion Pipelines Based on Green Synthesis. Detect the soil environment in the area where the pipe section is easy to corrode, and obtain the test data of external corrosion factors. Through experimental analysis, the main corrosion factors

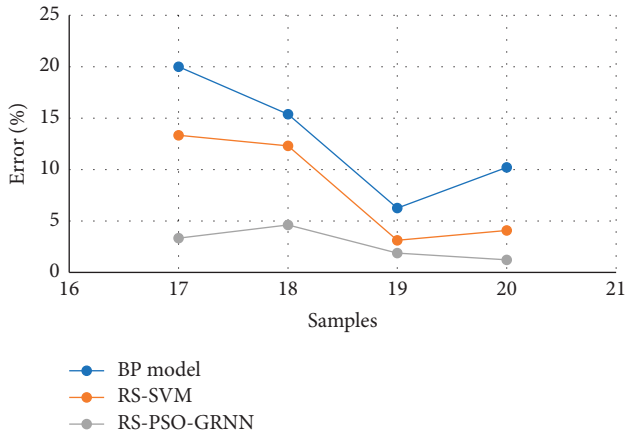

Figure 2: Comparison of relative errors of models with green synthesis and metal oxide composites.

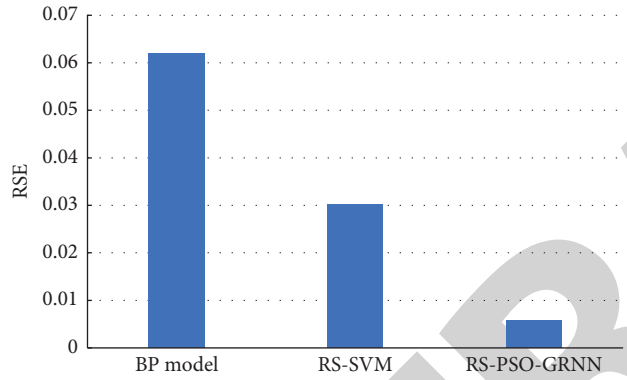

Figure 3: Comparison of RSE between different models with green synthesis and metal oxide composites.

have been determined, the external corrosion index system has been established, and the buried sheet test has been carried out for the soil areas along the pipeline section prone to corrosion. According to the embedding time, samples are taken in three batches of 0.5, 1, and 1.5 years in order to test the maximum corrosion depth of embedded films at each test point at different times.

As of 2010, Changqing oil field has built nearly 1700 km of oil transmission trunk lines and 10728 km of internal gathering and transmission pipelines. Most of its oil and gas pipelines are composed of metal pipelines and equipment and are buried underground. The oil and gas pipelines are corroded due to the contact between the pipeline and various surrounding media. The soil along the line is mostly saline soil, the soil resistivity is low, generally in 20–40 ohms/m, and the soil corrosivity is medium. In this paper, after the excavation of a serious corrosion area is detected by the external anticorrosion layer, the remaining life prediction calculation is performed. The local corrosion pit data measured after excavation are recorded as shown in Figure 5.

$T(x) = 200$ is obtained from formula (5), and then, $F(x)$ is obtained as 0.995. Bringing the value of $F(x)$ into equation (3) of the fitting equation yields a maximum local corrosion pit depth of 5.69 mm. Combined with the

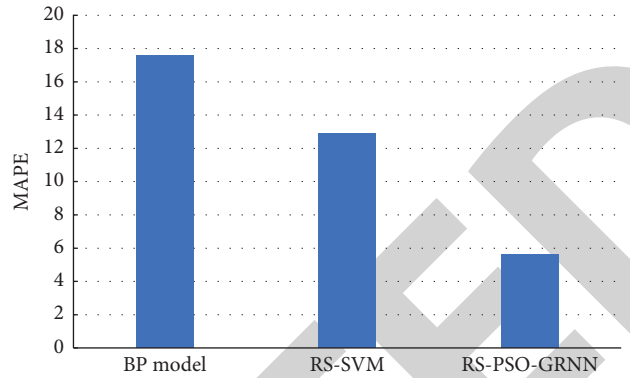

Figure 4: Comparison of different models of MAPE with green synthesis and metal oxide composites.

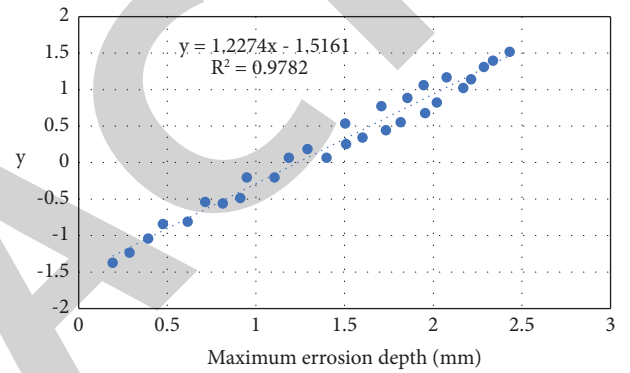

Figure 5: The straight-line fitting results with green synthesis and metal oxide composites.

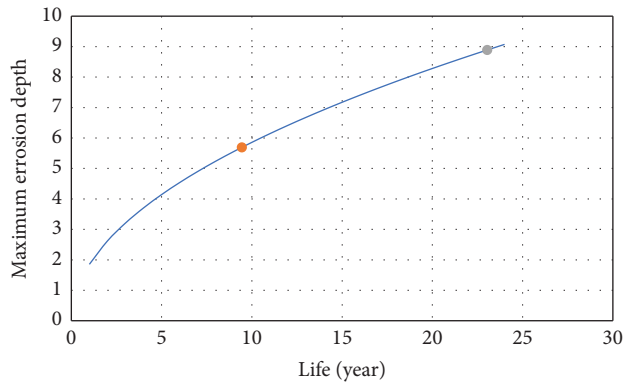

Figure 6: Remaining life of the pipe with green synthesis and metal oxide composites.

formula recommended by APIRP579, the critical corrosion depth of the corrosion pipeline is calculated to be 8.89 mm, and then, the local corrosion progression formula in the form of curtain index is used to calculate the local uniform corrosion of the pipeline to obtain a power law coefficient of 1.852. By taking the critical corrosion depth of 5.69 mm into the power law calculation formula, it can be found that the remaining life of the corrosion of the pipeline is $t = 23.04 - 9.44 = 13.6$ years (Figure 6).

Due to the constant and changing corrosion of pipelines, on the one hand, repair and maintenance plans should be developed for these pipelines. On the other hand, it is also necessary to determine the future detection time of the defective pipeline based on the prediction results, so as to continuously use new information to optimize the model performance and correct the previous prediction conclusions. Therefore, the corrosion development status of the pipeline can be grasped timely and accurately, and the deficiency that the model is only suitable for medium and short-term corrosion prediction can be avoided.

4. Conclusion

Aiming at the corrosion problem of long-distance oil and gas pipelines, this paper studies the prediction of corrosion rate of buried oil and gas pipelines in Changqing gas field. By improving the inertia weight and learning factor of the traditional particle swarm optimization algorithm, the parameters of the generalized regression neural network are optimized, and the corrosion rate prediction model of buried pipelines is finally constructed. The specific results are as follows:

(1) This paper proposes an improved PSO optimization GRNN buried pipeline corrosion rate prediction method. This study establishes the network mapping model between the key influencing factors of buried pipeline corrosion and corrosion rate, combines the buried piece test data and pipeline detection data, and evaluates the prediction performance of the model. The results show that the model can accurately predict and evaluate the corrosion status of buried pipelines with good results, compared with other prediction models. It has relative superiority and also lays a scientific and reliable foundation for the study of the remaining life of pipeline corrosion in the fifth chapter.

(2) The extreme value distribution prediction method mainly analyzes the maximum corrosion depth in the local corrosion area through the extreme value distribution and uses the local progress empirical formula to determine the remaining life of the pipeline, which is suitable for the uniform corrosion of the pipeline for life prediction and can be applied in the Changqing gas field.

The method selected in this paper has opened up a new way for corrosion residual life prediction of buried pipelines, and has certain reference value, but some aspects still need to be further improved and perfected. For example, the positive impact of the anticorrosion coating and cathodic protection on the pipeline anticorrosion shall be considered during the embedded film test. In addition, although oil and gas will be treated by desulfurization, dehydration, and corrosion inhibitor before transmission, weak internal corrosion will still occur, which is also the future research direction.

Data Availability

The data supporting the current study are available from the corresponding author upon request.

Conflicts of Interest

The authors declare that they have no conflicts of interest.

Acknowledgments

The authors would like to show sincere thanks to those techniques who have contributed to this research.

References

[1] A. A. Soomro, A. A. Mokhtar, J. C. Kurnia, N. Lashari, H. Lu, and C. Sambo, "Integrity assessment of corroded oil and gas pipelines using machine learning: a systematic review," *Engineering Failure Analysis*, vol. 131, Article ID 105810, 2022.

[2] H. U. Khalid, M. C. Ismail, and N. Nosbi, "Permeation damage of polymer liner in oil and gas pipelines: a review," *Polymers*, vol. 12, no. 10, p. 2307, 2020.

[3] X. Zheng, J. Shi, G. Cao et al., "Progress and prospects of oil and gas production engineering technology in China," *Petroleum Exploration and Development*, vol. 49, no. 3, pp. 644–659, 2022.

[4] Q. Wang and L. Zhan, "Assessing the sustainability of the shale gas industry by combining DPSIRM model and Raga-PP techniques: an empirical analysis of Sichuan and Chongqing, China," *Energy*, vol. 176, pp. 353–364, 2019.

[5] F. Xu, H. Wu, X. Hu, and Z. C. Wang, "Experimental study on the corrosion of buried pipeline in coastal area under the interference of stray current," *Transactions on Electrical and Electronic Materials*, vol. 20, no. 5, pp. 431–436, 2019.

[6] F. Mao, "Underground coal gasification (UCG): a new trend of supply-side economics of fossil fuels," *Natural Gas Industry B*, vol. 3, no. 4, pp. 312–322, 2016.

[7] J. He, S. Fang, F. Hou et al., "Vertical zonation of weathered crust ancient karst and reservoir evaluation and prediction—a case study of M55–M51 sub-members of Majiagou Formation in gas fields, central Ordos Basin, NW China," *Petroleum Exploration and Development*, vol. 40, no. 5, pp. 572–581, 2013.

[8] F. Li, W. Wang, J. Xu, J. Yi, and Q. Wang, "Comparative study on vulnerability assessment for urban buried gas pipeline network based on SVM and ANN methods," *Process Safety and Environmental Protection*, vol. 122, pp. 23–32, 2019.

[9] E. O. Obanijesu, V. Pareek, R. Gubner, and M. O. Tade, "Corrosion education as a tool for the survival of natural gas industry," *Nafta*, vol. 61, no. 12, pp. 555–563, 2010.

[10] Y. Li, W. Zeng, X. Li, F. Ren, and H. Hu, "Rank predictions of internal corrosion of gathering pipelines in a natural Gas field with a multi-kernel SVM method," in *Proceedings of the Pressure Vessels and Piping Conference*, vol. 83884, American Society of Mechanical Engineers, Atlanta, GA, USA, August 2020.

Hindawi
Journal of Chemistry
Volume 2023, Article ID 9785450, 1 page
https://doi.org/10.1155/2023/9785450

Retraction

Retracted: Sedimentary Facies Evaluation of Tight Oil Reservoirs of Yanchang Formation in the Ordos Basin

Journal of Chemistry

Received 28 November 2023; Accepted 28 November 2023; Published 29 November 2023

This article has been retracted by Hindawi, as publisher, following an investigation undertaken by the publisher [1]. This investigation has uncovered evidence of systematic manipulation of the publication and peer-review process. We cannot, therefore, vouch for the reliability or integrity of this article.

Please note that this notice is intended solely to alert readers that the peer-review process of this article has been compromised.

Wiley and Hindawi regret that the usual quality checks did not identify these issues before publication and have since put additional measures in place to safeguard research integrity.

We wish to credit our Research Integrity and Research Publishing teams and anonymous and named external researchers and research integrity experts for contributing to this investigation.

The corresponding author, as the representative of all authors, has been given the opportunity to register their agreement or disagreement to this retraction. We have kept a record of any response received.

References

[1] Y. Peng, H. Zhang, X. Zheng et al., "Sedimentary Facies Evaluation of Tight Oil Reservoirs of Yanchang Formation in the Ordos Basin," *Journal of Chemistry*, vol. 2023, Article ID 9605436, 11 pages, 2023.

Hindawi
Journal of Chemistry
Volume 2023, Article ID 9605436, 11 pages
https://doi.org/10.1155/2023/9605436

Research Article

Sedimentary Facies Evaluation of Tight Oil Reservoirs of Yanchang Formation in the Ordos Basin

Yu Peng,[1] Huaijie Zhang,[2] Xiaoli Zheng,[3] Yi Wang,[4] Jiye Li,[5] Yinhui Zhu,[6] and Quine Doolen[7]

[1]*Department of Geology, Northwest University, Xi'an, Shaanxi 710127, China*
[2]*No. 5 Oil Production Plant of PetroChina Changqing Oilfield Company, Dingbian, Shaanxi 718600, China*
[3]*No. 2 Oil Production Plant of PetroChina Changqing Oilfield Company, Qingyang, Gansu 745000, China*
[4]*No. 6 Oil Production Plant of PetroChina Changqing Oilfield Company, Yulin, Shaanxi 719000, China*
[5]*No. 4 Production Plant PetroChina Huabei Oilfield Company, Langfang, Hebei 065000, China*
[6]*No. 5 Oil Production Plant of PetroChina Qinghai Oilfield Company, Haixi, Qinghai 816400, China*
[7]*Light University of Bujumbur, The King's School, BP 1560, Bujumbura, Burundi*

Correspondence should be addressed to Quine Doolen; quinedoolen@ksu.edu.bi

Received 14 September 2022; Accepted 26 September 2022; Published 27 March 2023

Academic Editor: Rabia Rehman

Tight sandstone gas has become one of the important unconventional resources. It is of great significance to study the pore throat structure of tight sandstone for the development of tight sandstone gas reservoirs. On the basis of previous research results, this paper studies the tight reservoir characteristics of Yanchang Formation by combining geological data with geophysical logging. The reservoir characteristics are described and studied in detail by ordinary thin section, casting thin section, graphic granularity, and scanning electron microscope experiment. The experimental results show that the reservoir sandstone types of long 6 segments are mainly lithic feldspathic sandstone and feldspathic lithic sandstone, with high component maturity and structural maturity. The components of cement mainly include authigenic clay minerals illite, chlorite, and carbonate minerals. The reservoir space is mainly composed of feldspar-dissolved pores and residual intergranular pores. Compaction and cementation are the decisive factors of pore reduction. At present, the average porosity of the reservoir is 8.33% and the average permeability is $0.12 \times 10^{-3}\ \mu m^2$, which belong to an ultralow porosity and ultralow permeability reservoir. On the basis of studying the origin, superimposition, and distribution of sand bodies and taking into account the sedimentary characteristics, origin, and trigger mechanism of gravity flow, a multisource sedimentary model is established in the study area, which is dominated by sandy debris flow, accompanied by turbidity current and local development of sandy slump. The thick massive sandstone with the most exploration significance in the study area is formed by the superimposition of multistage sandy clastic flow sediments along the gully in the direction of delta to lake. Summarizing the characteristics of reservoir development and evaluating and predicting it can provide geological basis for the next exploration and development of deep-water tight reservoirs in the study area.

1. Introduction

As one of the main types of unconventional tight oil and gas resources, tight sandstone reservoirs play an increasingly significant role in the strategic structure of energy development. China is rich in tight sandstone oil and gas resources, and their development has attracted a great deal of attention. Especially since the "12th Five-Year Plan," large-scale development and utilization of resources have been realized, and various studies and predictions show that their development prospects are good.

Domestic exploration practice has proved that tight sandstone has great exploration potential and development value. In foreign countries, the Elkins method is generally used to define the physical conditions of tight sandstone reservoirs: porosity is less than 10% and

permeability is less than 0.1 mD. However, in China, scholars in different research areas have different opinions. Usually, tight sandstone reservoirs are defined as reservoirs with overburden permeability less than 0.1 MD [1–5]. In the process of diagenesis, the physical properties of the tight sandstone reservoir become worse, and heterogeneity is very strong after strong mechanical compaction and cementation. Therefore, the pore structure is an important factor to determine the physical properties and oil and gas productivity of the reservoir. The pore structure in the sandstone reservoir has a certain impact on the oil-bearing property. In the actual exploration and understanding process, it is necessary to clarify the characteristics of the pore structure, master its type, and analyze the oil-bearing property of the reservoir according to the actual situation. Through the analysis of the control effect of pore structures on the oil-bearing property of sandstone reservoirs, it can provide the corresponding reference for exploitation so that the exploitation can be carried out smoothly.

Zahid et al. [6, 7] put forward "reservoir description," which is also called reservoir characteristic description. Its research contents mainly include reservoir sedimentary characteristics, reservoir petrology characteristics, reservoir diagenetic evolution characteristics, reservoir physical properties characteristics, pore throat structure characteristics, and heterogeneity characteristics. The description of oil and gas reservoirs is the basis of oil and gas reservoir evaluation and prediction, oilfield development and adjustment, etc. Around the 1980s, Yang et al. [8–11] improved the theory, method, and testing means of reservoir research, which played an important role in the exploration and development of oil and gas fields all over the world. The research on the characteristics of oil and gas reservoirs in China started late, but with the rapid development of oil and gas exploration and development and the continuous introduction of new technologies, the research on the characteristics of oil and gas reservoirs is becoming more and more perfect.

Scholars at home and abroad have systematically studied the main controlling factors of tight sandstone reservoirs. The results show that sedimentary environment, diagenesis, and tectonism jointly control the formation of tight sandstone reservoirs [12–16]. The research by Wu et al. [17, 18] shows that sedimentary environment is the most basic factor affecting the development of tight sandstone reservoirs. For example, the favorable reservoir of the Quan4 member in the Songliao Basin is developed in the delta front-delta plain underwater distributary channel microfacies, in which sandstone has been transported and washed by water for a long time, with good sorting and rounding of clastic particles and low shale content, thus becoming a favorable oil and gas reservoir facies belt. The research results of Walker et al. [19, 20] pointed out that the tight sandstone reservoirs in the Alberta Basin and the Williston Basin of North American tight sandstone gas-bearing basins developed in deep lake environment and deep-sea environment, respectively, with low maturity of grain composition and texture and strong plasticity. The characteristics of this kind of sediment will lead to obvious mechanical compaction effects and destroy primary intergranular pores to a greater extent. Therefore, the sedimentary environment has a direct impact on early diagenesis. When studying the main controlling factors of tight sandstone reservoirs, we should first analyze the sedimentary environment. The effect of tectonic stress on physical properties has both advantages and disadvantages. On the one hand, the formation is squeezed by tectonic movements, which can produce cracks, which effectively improve the physical properties of the reservoir. Cheng et al. [21] proposed in 2018 that the whole pore throat of the tight sandstone reservoir in the Linxing block, the eastern margin of the Ordos Basin, is characterized by extremely fine-fine pore throat, poor sorting, and poor seepage capacity, and the development of desert areas is obviously controlled by fractures. On the other hand, tectonic compression also produces strong mechanical compaction, which makes the primary pores of the reservoir smaller and the physical properties worse. For example, Wang and Gao [22, 23] found that the Bogda Mountains in the Taibei depression of the Turpan–Hami Basin were squeezed from north to south, which made the reservoir physical properties in the piedmont zone the worst in the whole area. The key of reservoir description lies in reservoir space, pore structure, physical properties, and heterogeneity.

The tight sandstone reservoir is different from the traditional clastic reservoir in exploration and development because of its compactness. Therefore, when analyzing the main controlling factors of tight sandstone reservoirs, we should focus on the reservoir space, pore structure, physical properties, and compactness. The reservoir of long 6 segments of Yanchang Formation in the Ordos Basin is located in the center of hydrocarbon generation, which is favorable for oil and gas accumulation. As an important pay zone in tight oil, predecessors have carried out a great deal of research on the sedimentary system, provenance characteristics, and reservoir distribution law of the Chang 6 reservoir. On the basis of the above achievements, this paper studies the reservoir characteristics of the sixth member of Yanchang Formation, analyzes the main controlling factors of the reservoir, deepens the geological understanding, and looks for the "sweet spot" reservoir development area, which provides a certain basis for the exploration and deployment of the Yanchang Formation area.

2. Research Materials and Methods

2.1. Research Materials. The rock samples used in this paper were obtained from Well N54, Well Z46, Well Z26, Well Z55, Well N24, and Well N71 of Yanchang Formation in Ordos. Among them, 30 typical samples were selected, among which the rocks used for the casting thin section experiment were taken from Well Z46 at 690.55 m and Well N71 at 1321.25 m, and the rocks used for the scanning electron microscope experiment were taken from Well Z55 at 1240.83 m and Well Z46 at 664.77 m. The cores used in the X-ray diffraction experiment were taken from Well N54 at 1375.47 m, Well Z26 at 1633.96 m, and Well N24 at 1309.34 m.

2.2. Research Methods. In this paper, the scanning electron microscope, X-ray diffraction, and core casting thin section experiments are comprehensively used to analyze tight sandstone cores:

(1) Experimental analysis of the scanning electron microscope: the micromorphology of the core sample to be tested is mainly obtained by electronic signal imaging. Further collection, classification, amplification, and processing of the processed signal carrying information of the electron beam spot can obtain the micromorphology of the core surface for further analysis.

(2) Analysis of the X-ray diffraction experiment: the diffraction pattern of crystals in rock samples is measured by using an X-ray diffractometer, and the intensity of characteristic peaks in the pattern is positively correlated with the content of the mineral in the sample. Based on the experiment, the positive correlation between the content of a mineral in rock samples and the intensity of its characteristic diffraction peaks can be determined, and then, the content of the mineral can be obtained by measuring the intensity of the characteristic peaks of the mineral in unknown samples.

(3) Thin section analysis of rock casting: the microscopic morphology of the rock sample to be measured is mainly obtained by electronic signal imaging. The micromorphology and chemical composition of the sample surface can be obtained by further collecting, classifying, amplifying, and processing the processed signal carrying information of the electron beam spot for further analysis. Thus, the rock types of the Yanchang Formation reservoir in Ordos can be defined, and the characteristics of tight oil reservoirs can be compared and analyzed.

3. Results and Discussion

3.1. Regional Geological Background. The Ordos Basin is a typical superimposed basin, which is located at the junction of central and western China. The basin has experienced many tectonic movements in geological history, but the overall regional environment is stable for a long time. Tectonically, it belongs to the secondary tectonic unit of the North China Craton and is a large multicycle craton basin with overall stable subsidence, depression migration, and obvious twisting.

This paper mainly studies Longdong District of the Ordos Basin, which is located in the southwest of the Ordos Basin and the southwest of the Yi-Shan slope. It is high in the east and low in the west, with a stable structure in the east and an unstable structure in the west. The base of the study area belongs to the metamorphic crystallization of early Proterozoic and Archaean and forms a set of marine carbonate deposits of the late Proterozoic and early Paleozoic Era at the earliest [24, 25]. The geological conditions of the study area are shown in Figure 1. The Triassic Yanchang Formation sediments in this area are mainly controlled by the southwest provenance, and some areas are also affected by the northeast provenance. By comparing the progradational structures in two directions, it is found that the progradational structures in the western part of the study area are characterized by a high dip angle of progradational layers, so the extension distance is short; the dip angle of the eastern forest is slightly small, but its extension distance is relatively long. This difference indicates that near source deep-water facies sediments are developed in the west of the study area, while far source delta facies sediments are developed in the east of the study area.

Yanchang Formation in the study area has the characteristics of large reservoir thickness, high oil and gas content, wide distribution, low permeability and porosity, etc. The stratum sandstone contains a large amount of feldspar and cuttings. During the burial process, due to strong compaction and strong cementation, a large number of original pores are lost, pore positions are occupied, and throats are narrowed or blocked, which leads to the decrease in rock porosity and permeability. Based on the above situation, we will focus on the study of lithology and physical properties of Yanchang Formation in the Ordos Basin and provide technical support for oil and gas development in this area.

3.2. Evaluation of Basic Characteristics of Tight Reservoirs

3.2.1. Petrological Characteristics of Reservoirs. Reservoir petrological characteristics include the composition and structural characteristics of sediments. Through the analysis and statistics of 230 rock slices, 80 graphic grain sizes, and 80 scanning electron microscope samples, the petrological characteristics of the Chang 6 reservoir in the study area are studied in detail. It is considered that the relative content of fine sandstone and siltstone is over 80%, and the experimental results are shown in Figure 2, which is the main reservoir sandstone in the study area.

3.2.2. Composition Characteristics of Reservoir Rock Debris

(1) Shi Ying. The content of Shi Ying particles in the sandstone of the Chang 6 reservoir varies greatly, ranging from 15% to 72%, with an average of 35.3%. The secondary enlargement of the periphery of particles is common. The rigidity of Shi Ying makes it unlikely to deform when it is pressed strongly. Therefore, the contact types are mainly the point and line, and the concave-convex shape is extremely rare.

(2) Feldspar. The content of feldspar in sandstone of long 6 segments in the study area is high, ranging from 4.8% to 59%, with an average of 27.7%. Its main materials include plates, columns and particles. Its cleavage and twinning are very developed and easy to be broken. In terms of chemical properties, feldspar is easy to dissolve. The sediment in the study area has a fine grain size and little wear during transportation, which makes feldspar mostly subangular and angular, with neat grain edges, as shown in Figure 3.

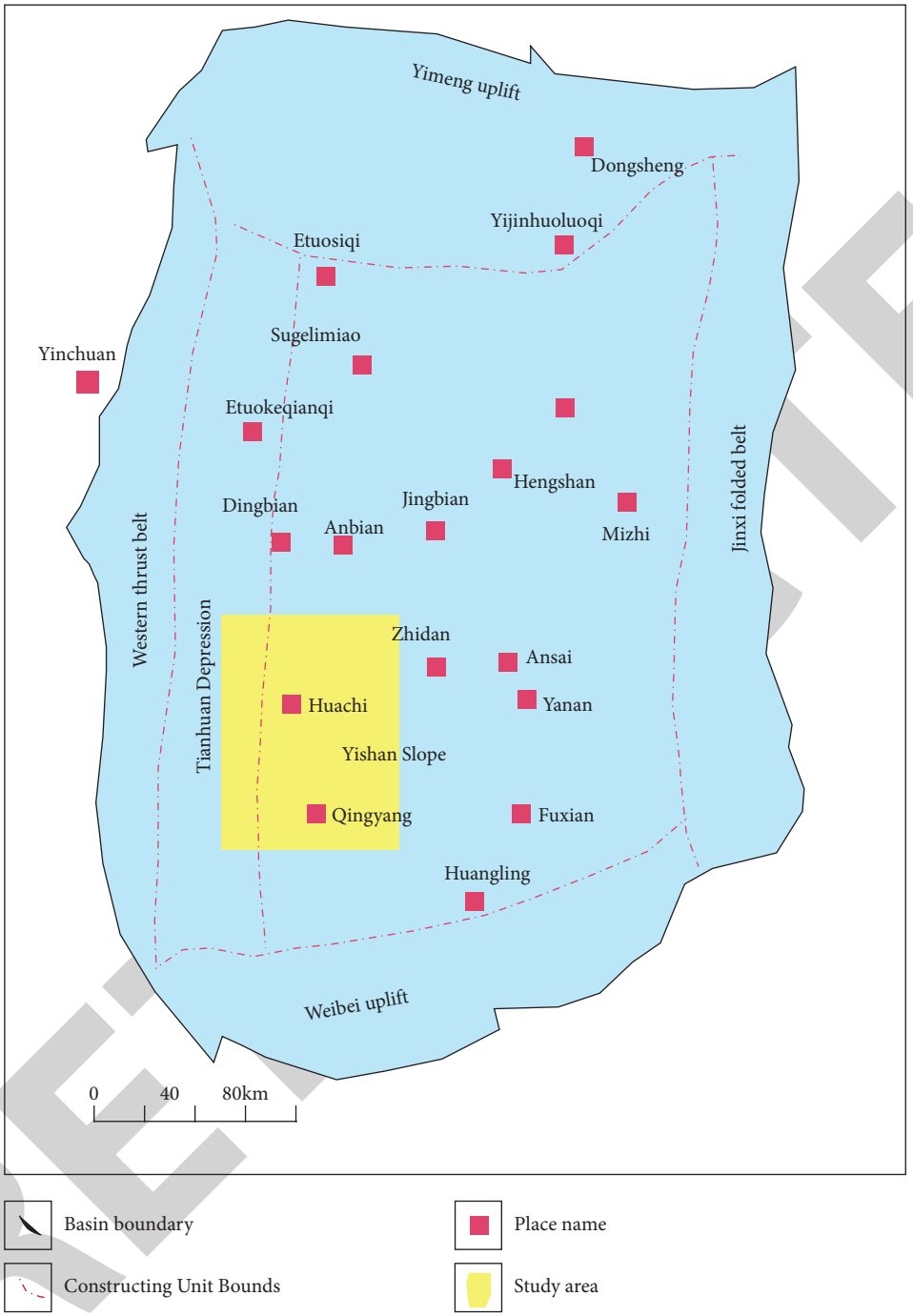

Figure 1: Location of the study area.

(3) Rock debris. The content of cuttings in the sandstone of long 6 segments is between 6% and 45%, with an average of 15.12%. Its composition is complex, mainly metamorphic rock cuttings, followed by sedimentary rock cuttings, and the content of magmatic rock cuttings is the least. It is worth noting that plastic particles such as mica, dolomite, and phyllite account for a large proportion of cuttings. The experimental results are shown in Figure 4. These plastic minerals are easy to deform and fill pores under compaction, resulting in poor physical properties.

3.2.3. Characteristics of Reservoir Rock Fillers. Through thin section microscopic observation and statistics, the average content of miscellaneous groups in long 6 segments of the study area is 6.7%, and the main components are clay minerals such as illite, chlorite, and kaolinite. Compared with the average value of 2.2% in other exploration areas in the south of the Ordos Basin, the impurity content in the study area is higher. This is related to the deep-water sedimentary environment in the study area. The cement content of sandstone in long 6 segments of the study area varies

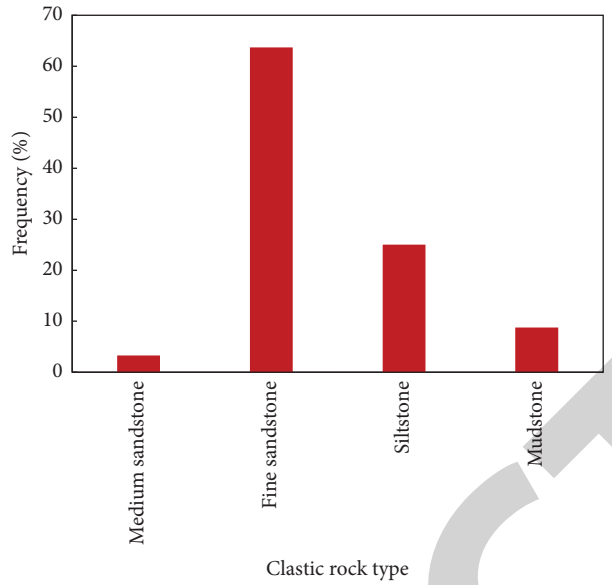

Figure 2: Main clastic rock types of long 6 segments of Yanchang Formation.

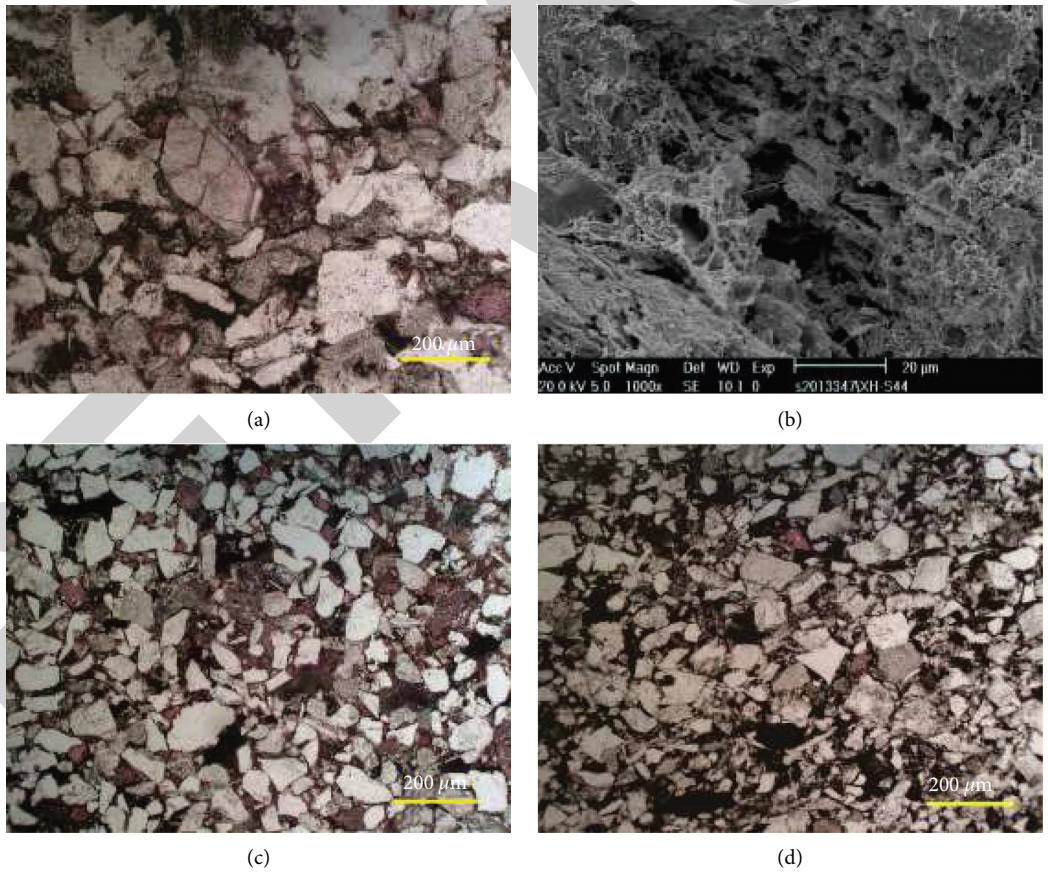

Figure 3: Microscopic characteristics of Chang 6 long stone sandstones in Yanchang Formation. (a) Fine sandstone, feldspar fracture, and (b) dissolved pores in feldspar grains. (c) Mostly angular-subangular fine-grained feldspathic sandstone. (d) Subangular fine-grained lithic feldspathic sandstone.

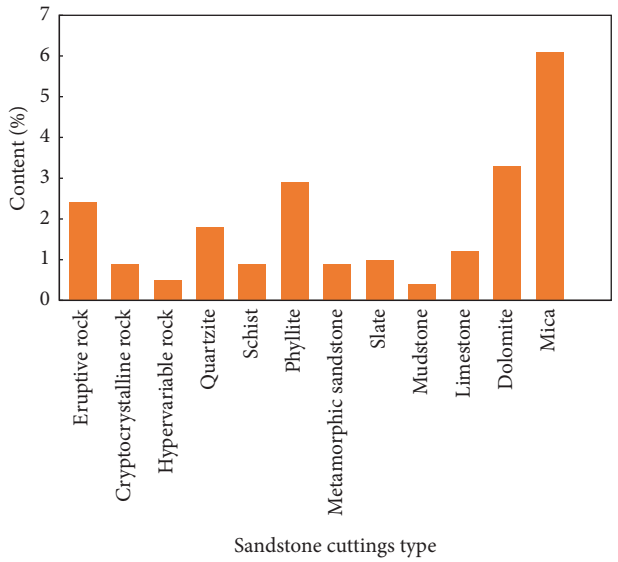

Figure 4: Histogram of cuttings types and contents of sandstone in long 6 segments of Yanchang Formation.

greatly, with the highest being 35%, the lowest being 3.4%, and the average being 14.16%. These include authigenic clay cements, carbonate cements, siliceous cements and feldspar cements. The results are shown in Figure 5.

3.2.4. Structural Characteristics of Reservoir Rock Debris. According to the statistics of sorting and roundness of debris particles in the study area, the results are shown in Figure 6. The sum of medium, medium-poor, and poor sorting accounts for 72.7% of all samples, and good sorting accounts for 22.6%. Subangular particles account for 93.5% of statistical rocks. It can be seen that the detritus in the study area has poor sorting and roundness, and its structural maturity is medium and low. Generally, with the increase in transportation distance, sorting and roundness of debris will become better. However, under the special sedimentary environment, more complicated situations may occur. Deep-water sediments in the study area are formed by the detritus of delta front sliding down to the deep-water area, and in this process, they are mixed with a clay matrix in the deep-water environment, resulting in the decrease of structural maturity of sandstone.

The microangle of reservoir quality is affected by the rock structure, and the main structural parameters are particle size, sorting, and roundness. Porosity gradually becomes better with the increase in particles. Although porosity varies widely in different particle size ranges, the larger the particles, the better the porosity, indicating that the particle size has an impact on tight reservoirs. Porosity also shows an increasing trend with the improvement of the sorting degree, but the overall difference is small, indicating that sorting has a certain impact on reservoir quality, but the correlation is getting worse. The reservoir quality is also affected by roundness to some extent. From subangular to subcircular, reservoir porosity gradually increases, but the increase is not obvious, indicating that roundness has an impact on the reservoir quality, but the impact is poor. In general, the rock structure has a weak impact on the reservoir quality, indicating that the control of the original sedimentary conditions on the reservoir quality is weakening, and the quality of the reservoir is also affected by other factors.

3.2.5. Overall Characteristics of Reservoir Porosity and Permeability. According to the statistical analysis of measured porosity and permeability, the porosity distribution range of the sandstone reservoir in long 6 segments of the study area is 3~19.91%, with an average of 8.33%. The permeability distribution ranges from 0.01 to $17.44 \times 10^{-3}\,\mu m^2$, with an average value of $0.12 \times 10^{-3}\,\mu m^2$. The overall physical property of the reservoir is poor, and it belongs to low porosity and ultralow permeability reservoirs.

As shown in Figure 7, the distribution histogram of porosity and permeability of the submember of Chang 6 shows that the average porosity and permeability of the submember of Chang 6 in the study area are basically the same, and the porosity and permeability of Chang 61 are slightly higher than those of Chang 62. The porosity distribution of each sublayer in long 6 segments is "single peak," and the main peak is between 7% and 9%. The permeability distribution is "approximately step-shaped," mainly distributed in three intervals $(0.03\sim0.1) \times 10^{-3}\,\mu m^2$, less than $0.03 \times 10^{-3}\,\mu m^2$, and $(0.1\sim0.3) \times 10^{-3}\,\mu m^2$.

Generally, the size and plane distribution of porosity and permeability are controlled by the distribution of sand bodies, which are mainly controlled by the development of sedimentary facies. Sedimentary facies are the basis of reservoir development, and to a large extent, they control the physical properties and space-time distribution of the reservoir. The sedimentary type of Chang 6 oil-bearing formation is mainly gravity flow sedimentation with semideep lake sedimentation as the background, and sand bodies are mainly distributed in sandy clastic flow, turbidity current, and semideep lake mud sedimentary microfacies.

3.3. Sedimentary Characteristics of the Study Area. The characteristics of sediments formed in different sedimentary environments are different. On the basis of previous research results, this paper confirms the sedimentary environment by observing and describing 36 coring wells, 432.16 m cores, and grain size analysis in the study area. Combined with the logging data of 106 wells, according to the lithology, sedimentary structure, and logging curve shape of long 6 segments, the genetic types of various sand bodies in the study area are identified.

3.3.1. Analysis of Sedimentary Environments. Tuff is the most important stratigraphic correlation sign of the Triassic in the Ordos Basin because of its stability and extensiveness. Its existence represents volcanic eruption. Previous studies have confirmed that volcanic activity not only forms widely distributed tuff but also causes violent tectonic movements [26]. During the Chang-6 sedimentary period, the study area was in the active stage of tectonic activity in the Qinling

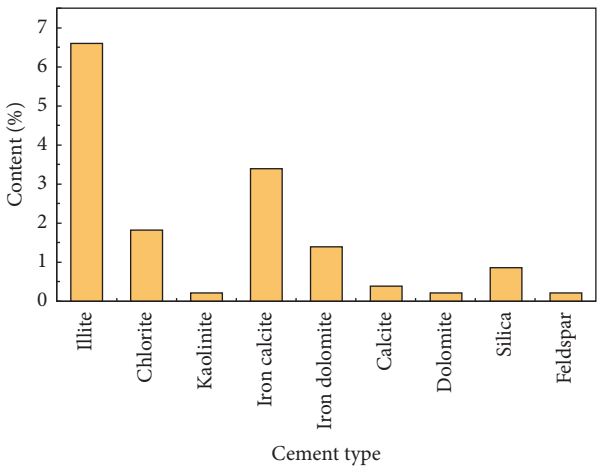

Figure 5: Types and contents of main cements of sandstone in long 6 segments.

orogenic belt, and the intestinal liquefied sandstone vein and other structural features reflecting paleoearthquakes were identified in the core of the study area. Some scholars have also confirmed that there is a slope break belt with a certain slope angle near the southwest of the study area [27–29].

The existence of above volcanoes, earthquakes, and slope break zones indicates that the study area has good external conditions for the development of gravity flow deposits. In addition to the above analysis, this paper attempts to determine the sedimentary environment of the study area by using lithology and grain size data. Core observation shows that black mudstone is widely distributed in the study area, and coal line and horizontal bedding are occasionally seen. The top of the interface is abrupt contact [30–32]. Thick black mudstone and shale reflect extremely weak hydrodynamic conditions and represent the deep-water sedimentary environment. According to the analysis of the grain size characteristics of sandstone in the Chang 6 member, in the C-M diagram, the sample points form a long outline roughly parallel to the C = M baseline, and the grain size composition of the samples is concentrated, narrow, and close to the C = M baseline, reflecting the characteristics of gravity flow deposition.

Based on the above tuff, sedimentary structural characteristics and previous research results, verified by the C-M diagram of lithology and grain size, and combined with the paleogeographic knowledge of the semideep water-deep water environment of Chang 6 lake in the previous study area, it is considered that Chang 6 lake in the study area is a deep lake gravity flow deposit. Geologically, it belongs to the category of deep-water sedimentation. Further considering the characteristics of lithology and sedimentary structure, the main sand bodies in the study area are divided into three causes: sandy debris flow, turbid flow, and sandy slump.

Sandy debris flow is a rheological laminar sedimentary flow. Sediments are usually deposited by means of overall freezing. The contact between the top and bottom of sediment and mudstone is important evidence for the freezing deposition of the sediment. Turbidity sedimentation is another form of gravity flow sedimentation in the study area. It is located at the bottom of gravity flow sediments, and its flow state is turbulent. Slumping sand body is a sand body located in the delta front. Under the external force, the excess pore water pressure generated by fluid is not enough to support the gravity of sediments. The sand body is liquefied and transported as a whole, rotating shear movement occurs along the concave sliding surface, and sliding stays at the foot of the front slope and accumulates to form rocks. In the process of collapse, the sand body is often curled and deformed, forming deformation bedding, microfolds, rotating flame structure, and ball pillow structure. At the interface of sand and mud, there are friction mirrors formed by collapse, and these friction mirrors become an important feature to identify collapsed sand bodies.

3.3.2. Depositional Model. Gravity flow sediment refers to a kind of density flow sediment containing a large amount of dispersion, which is pushed by gravity on land, at the bottom of water or in water body. Sediment maintains obvious boundary and flows as a whole during gravity flow, so it is also called "block flow sedimentation." According to the supporting mechanism of suspended particles in gravity flow, underwater gravity flow sedimentation can be divided into four types: debris flow sedimentation, particle flow sedimentation, liquefaction sedimentation, and turbidity flow sedimentation. The theoretical and experimental study of gravity flow is a hotspot in sedimentology nowadays, and gravity flow-induced reservoirs in deep sea and lake basin deep-water areas are the key and difficult points in oil and gas exploration nowadays. With the deepening of deep-water sedimentation research, people gradually realize that deep-water sedimentation is far more complex than we imagined, and the multiplicity of deep-water sedimentation models is becoming increasingly prominent, especially in continental lake basins with relatively limited lake basin area, variable material supply, and frequent lake level fluctuation. The complexity of deep-water gravity flow development laws is particularly prominent, which seriously restricts the progress of oil and gas exploration in continental lake basins.

Based on the above research on rock types and facies sequence combination types, the sand body distribution law in the Panke-Shuanglong area, and the genesis, triggering mechanism, and sedimentary characteristics of gravity flow deposition, a gravity flow deposition model in the study area is established. The deposition schematic diagram is shown in Figure 8. The delta front sand bodies controlled by northeast provenance, south provenance, and southwest provenance are triggered by volcanoes, earthquakes, and other factors and become unstable and fall into the semideep water-deep water environment. Under various transportation modes, different types of gravity flow deposits are formed. The types of gravity flow sedimentary sand bodies in the study area are mainly sandy clastic flow sand bodies and turbid flow sand bodies, and sandy slump sand bodies are found locally.

Delta front sediments are carried by water flow, fall into gullies, and accumulate nearby to become sandy slump sand

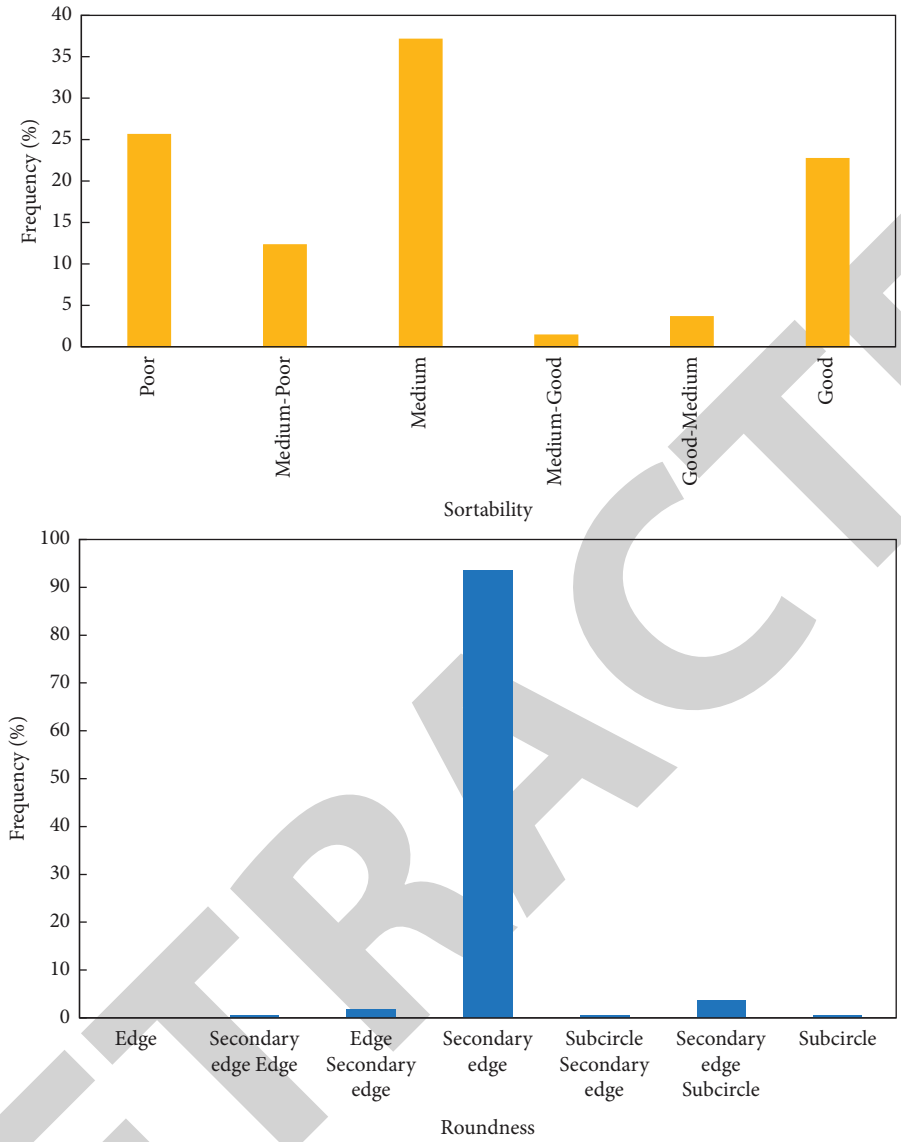

Figure 6: Histogram of clastic particle sorting and roundness distribution of sandstone in long 6 segments.

bodies. With the frequent occurrence of tectonic activities caused by external forces, sediments continue to fall into semideep lakes and continue to migrate under the action of gravity and current. At the semideep lake-deep lake concave sliding surface, the flow pattern of water gradually changes into laminar flow, forming sediments dominated by sandy debris flow. In the area close to the slope break zone, the sandy debris flow sand body is located in the upper part of the sandy slump sand body. With the increasing number of detrital materials provided by the provenance, the sandy detrital flowing sand body develops more and more, showing that tongue-shaped bodies are piled forward along the gully direction in multiple stages, and finally, the most important thick-bedded massive sandstone in the study area is formed. Sediments continue to move towards deep lake. With the increasing volume content of water, the viscosity of sandy debris flow gradually decreases and then turns into turbid flow. Because its flow mode is turbulent flow with high velocity, it can carry fine sediments to a long distance, up to the deep lake plain. Seen from the plane, the turbidite sand bodies in the study area are distributed in the front or top of clastic flow sand bodies. However, due to its fine grain size and thin thickness formed in a single period, sediment products in different periods are often separated by (semi) deep lake mud, which makes it difficult to form effective sand bodies. To sum up, the most valuable sandy debris flow thick massive sand bodies are distributed along the gully in the direction of deep lake in the delta front channel. Controlled by the provenances in the southwest, south, and northeast, the sand bodies in the mixed source areas in the west and middle of the study area are the best. Through the comprehensive study on the lithofacies types, facies sequence combination, and sedimentary model of the study area, it is found that the main sandy clastic flow thick massive sand body in the study area is developed along the gully in the direction of delta front waterway. The sand body

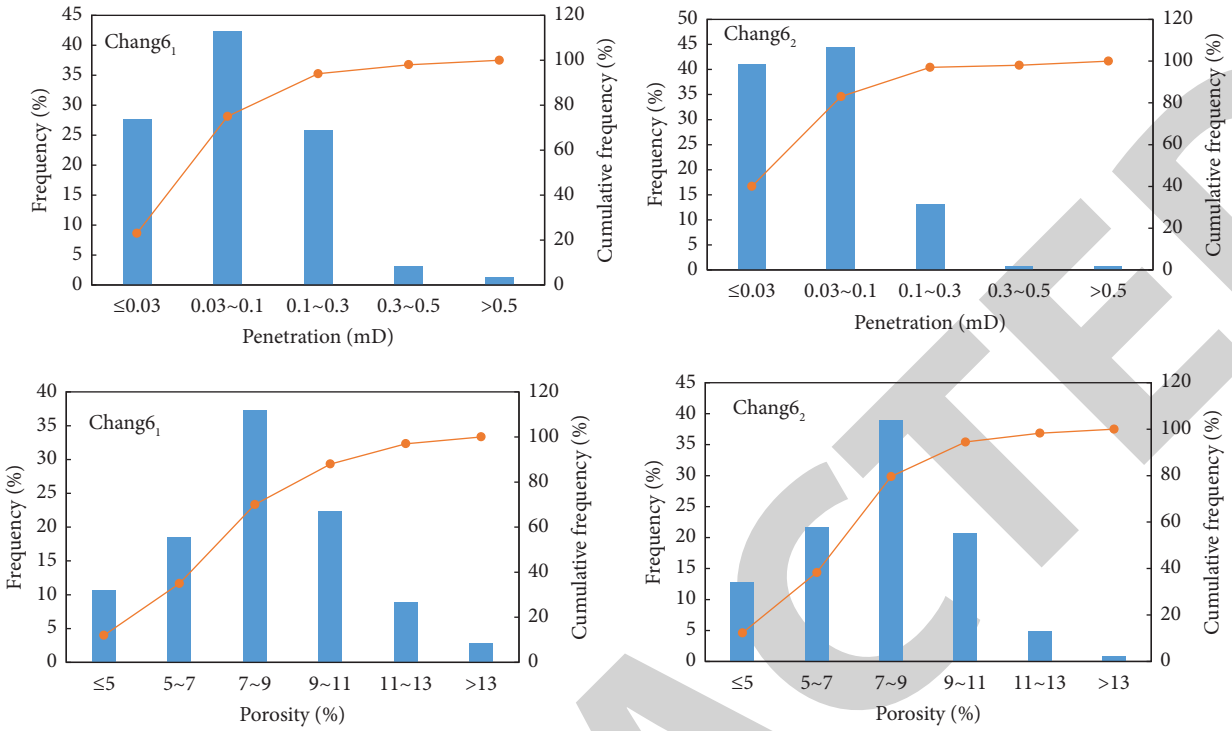

Figure 7: Porosity and permeability distribution histogram of the Chang 6 submember of Yanchang Formation.

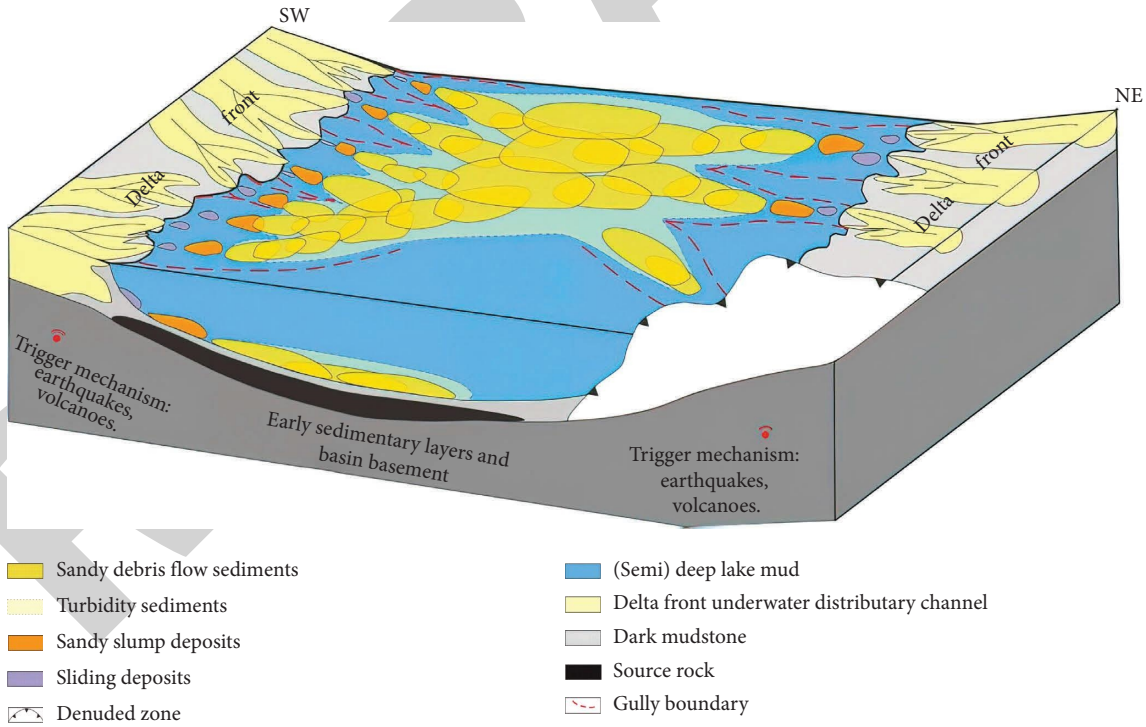

Figure 8: Schematic diagram of the gravity flow deposition model of Chang 6 in Yanchang Formation.

has the characteristics of not extending far in the longitudinal direction and overlapping in the transverse direction. On the plane, it shows an irregular overlapping shape of lingual bodies. Therefore, large-scale sand bodies superimposed by sandy clastic flows should be found in the gullies along the channel direction of the delta front of the upper concave slip surface in exploration.

The Chang 6 oil-bearing formation of the Upper Triassic Yanchang Formation in the south of the Ordos Basin is a typical lithologic reservoir, with many types of reservoirs

forming assemblages, such as lower generation and upper reservoir, self-generation and self-storage, and good reservoir forming conditions. The continuous distribution of sandy clastic flow deposits in the Chang 6 Member is the main oil and gas reservoir sand body, which not only directly controls the scale and distribution of oil and gas reservoirs but also determines the productivity difference of oil wells, and is the key factor to determining the formation and enrichment of tight oil. The sandy clastic flow sedimentary body of Chang 6 oil-bearing formation goes deep into the hinterland of the lake basin and directly contacts Chang 7 hydrocarbon source rock in the lake basin to form a continuously distributed finger-shaped sand body. On the one hand, it fully absorbs oil and gas formed by the hydrocarbon source rock, and on the other hand, the hydrocarbon source rock acts as a good cover to form a stratigraphic lithologic reservoir with good reservoir forming conditions.

4. Conclusion

Tight sandstone gas has become one of the important unconventional resources. It is important to study the pore throat structure of tight sandstone for the development of tight sandstone gas reservoirs. On the basis of previous research results, combined with geological data and geophysical logging, through ordinary thin section, casting thin section, graphical grain size, and scanning electron microscope experiments, this paper describes and studies the characteristics of tight reservoirs in the 6th member of Yanchang Formation in the Longdong area of the Ordos Basin in detail. The conclusions are as follows:

(1) The reservoir lithology of Chang 6 is mainly fine sandstone and siltstone, and the sandstone types are mainly lithic feldspathic sandstone and feldspathic lithic sandstone. Among them, the feldspar content is high, and cuttings are mainly deformable plastic particles. The components of cement mainly include authigenic clay minerals illite, chlorite, and carbonate minerals. The sorting property of particles is moderately poor, roundness is mainly subangular, and structural maturity is moderately low. Reservoir space is dominated by feldspar-dissolved pores and residual intergranular pores. Compaction and cementation are the decisive factors to reduce the porosity of reservoirs in the study area, resulting in the original porosity loss rate as high as 85.46%. Dissolution and fracture improve the permeability of the reservoir and increase porosity by 7.65%. At present, the average porosity is 8.33% and the average permeability is $0.12 \times 10^{-3}\ \mu m^2$, which belong to the ultralow porosity and ultralow permeability reservoir.

(2) We compare the sedimentary characteristics, petrological characteristics, reservoir space characteristics, diagenesis characteristics, median radius characteristics, physical properties, and reservoir heterogeneity characteristics of different genetic sand bodies. It is considered that the sandy clastic flow sand body develops a large section of thick massive fine sandstone with high composition maturity and structural maturity. After weak destructive diagenesis and strong constructive diagenesis, the absolute content of intergranular pores and feldspar-dissolved pores is high, the median radius is large, porosity and permeability are good, and heterogeneity is the weakest, making it the best reservoir sand body in the study area.

(3) We establish a sedimentary model in which sandy debris flow is dominant, turbidity current is associated, and sandy slump develops locally. Turbulent flow sand bodies are distributed in the front or top of clastic flow sand bodies in the study area. However, due to its fine grain size and thin thickness formed in a single period, sediment products in different periods are often separated by (semi) deep lake mud, which makes it difficult to form effective sand bodies. Therefore, the most valuable sandy debris flow thick massive sand bodies are distributed along the delta front channel to the gully in the direction of deep lake. Controlled by the provenances in the southwest, south, and northeast, the sand bodies in the mixed source areas in the west and middle of the study area are the best.

Data Availability

The figures used to support the findings of this study are included in the article.

Conflicts of Interest

The authors declare that they have no conflicts of interest.

Acknowledgments

The authors would like to show sincere thanks to those techniques that have contributed to this research. This work was supported by the Geological Evaluation of Deep-Water Fine-Grained Reservoirs, Project number: 2017ZX05009-02-04.

References

[1] C. E. Wang, L. J. Chen, J. Cao, and Z. Q. Liu, "Sequence stratigraphic characteristics of the triassic Yanchang formation in fuxian-Huangling area, Ordos Basin," *Petroleum Geology and Engineering*, vol. 32, no. 4, p. 6, 2018.

[2] C. Zou, R. Zhu, K. Liu, L. Su, B. Bai, and X. W. J. Zhang, "Tight gas sandstone reservoirs in China: characteristics and recognition criteria," *Journal of Petroleum Science and Engineering*, vol. 88, pp. 82–91, 2012.

[3] H. Gao, J. Cao, C. Wang et al., "Comprehensive characterization of pore and throat system for tight sandstone reservoirs and associated permeability determination method using SEM, rate-controlled mercury and high-pressure mercury," *Journal of Petroleum Science and Engineering*, vol. 174, pp. 514–524, 2019.

[4] S. Yin, D. Lv, and W. Ding, "New method for assessing microfracture stress sensitivity in tight sandstone reservoirs

Hindawi
Journal of Chemistry
Volume 2023, Article ID 9864546, 1 page
https://doi.org/10.1155/2023/9864546

Retraction

Retracted: Damage of Green Synthetic Cement Slurry to Clastic Rock Reservoir

Journal of Chemistry

Received 28 November 2023; Accepted 28 November 2023; Published 29 November 2023

This article has been retracted by Hindawi, as publisher, following an investigation undertaken by the publisher [1]. This investigation has uncovered evidence of systematic manipulation of the publication and peer-review process. We cannot, therefore, vouch for the reliability or integrity of this article.

Please note that this notice is intended solely to alert readers that the peer-review process of this article has been compromised.

Wiley and Hindawi regret that the usual quality checks did not identify these issues before publication and have since put additional measures in place to safeguard research integrity.

We wish to credit our Research Integrity and Research Publishing teams and anonymous and named external researchers and research integrity experts for contributing to this investigation.

The corresponding author, as the representative of all authors, has been given the opportunity to register their agreement or disagreement to this retraction. We have kept a record of any response received.

References

[1] M. Xu, X. Tan, L. Yang, H. Cheng, and D. Cofell, "Damage of Green Synthetic Cement Slurry to Clastic Rock Reservoir," *Journal of Chemistry*, vol. 2023, Article ID 8937828, 7 pages, 2023.

Hindawi
Journal of Chemistry
Volume 2023, Article ID 8937828, 7 pages
https://doi.org/10.1155/2023/8937828

Research Article

Damage of Green Synthetic Cement Slurry to Clastic Rock Reservoir

Meng Xu,[1] Xin Tan,[1] Libo Yang,[1] Hanlie Cheng,[2] and David Cofell[3,4]

[1]*No. 1 Cementing Company, BHDC, Renqiu, Hebei 062552, China*
[2]*Cosl-Expro Testing Services (Tianjin) Co. Ltd., Tianjin 300457, China*
[3]*Light University of Bujumbura, BP 1368, Bujumbura, Burundi*
[4]*The King's School, BP 1560, Bujumbura, Burundi*

Correspondence should be addressed to David Cofell; davidcofell@ksu.edu.bi

Received 9 October 2022; Revised 21 October 2022; Accepted 24 November 2022; Published 4 February 2023

Academic Editor: Rabia Rehman

Green synthesis and metal oxide composites have attracted much attention from researchers of industry and academia. As a typical application of green synthesis and metal oxide composites, the protection of oil and gas reservoirs is related to various links such as exploration, drilling, completion, and development. It is a complex and systematic project, which directly affects whether the oil and gas fields can be discovered, evaluated, and efficiently developed in time, and it is also related to the development of oil and gas fields recovery rate. As the most critical part of oil and gas well construction, the cementing process mainly pays attention to the safe pumping of the cement slurry and the long-term effective interlayer isolation capability of the cement sheath. Less attention is paid to the reservoir protection during the cementing process. The high-pressure difference between the annulus and the formation, the high fluid loss, and the high solids content of the cementing slurry during the cementing process have also become major challenges. In order to solve this problem, this study takes a typical clastic rock block in an oilfield in western China as the research object and carries out a geological survey of fracture development, pressure deficit, and cement slurry permeability leakage in the reservoir. The reservoir physical properties, clay mineral characteristics, and formation water quality of rock reservoirs are analyzed. The influence of cement slurry filtrate and solid phase particles on reservoir clay expansion rate and permeability was tested by core porosity and permeability tester. XRD and SEM techniques were used to analyze the damage mechanism of cement slurry filtrate and solid phase particles to the reservoir. The research results show that the average porosity of the clastic rock reservoir in the study area is 15%, the permeability is high, the average pore size of the reservoir is between 37 and 56 μm, the microfractures are developed in the reservoir section, and the porosity and permeability conditions are good; high-valent cations and inorganic ions in the filtrate generate inorganic scales such as $CaCO_3$ and $Mg(OH)_2$ and cross-link with dissolved polymers to form flocculation substances, which cause the filtrate to damage the reservoir, and at the same time, the cement particles in the pore throats in the near wellbore zone are lost along with the leakage. Furthermore, hydration, tightly bonding the inert admixture and the clastic rock formation, forms a tight sealing layer, which reduces the permeability of the reservoir sharply; the expansive clay particles in the reservoir absorb the moisture of the cement slurry filtrate and expand. The volume of the particles increases, and the porous formation containing expansive clay minerals absorbs moisture and causes internal expansion, and the volume expansion rate can reach 9%, which eventually causes the porosity and permeability of the reservoir to decrease, resulting in reservoir damage and solid phase in the cement slurry. The damage of particles to the reservoir is mainly due to the blockage of the reservoir pore throats and the hydration and consolidation of cement particles inside the reservoir caused by the external admixtures in the cement slurry that do not participate in the hydration reaction. The solid phase particles form a filter cake on the surface of the reservoir core and cannot enter the reservoir, but under the condition of porous formation leakage, the solid phase particles with a particle size of 1–10 μm in the cement slurry will directly penetrate into the reservoir rock resulting in shallow plugging in the reservoir near the wellbore. The research results provide theoretical data support for the research on low-damage cementing slurry technology in clastic rock reservoirs. The work provides an important application guidance to green synthesis and metal oxide composites.

1. Introduction

It is important to investigate green synthesis and metal oxide composites. As a typical application of green synthesis and metal oxide composites, reservoir damage directly affects the loss of oil and gas resources, increases production costs, and is more likely to cause complex and serious problems in the production process of oil and gas wells [1–3]. Before the exploitation of oil and gas reservoirs, the rock, mineral components, and fluids contained in the oil and gas reservoirs are in a state of equilibrium. However, this equilibrium state is likely to be broken during the construction of oil and gas wells and subsequent production, resulting in the formation of reservoirs, and damage occurs. Reservoir damage is mainly manifested as a linear drop in the absolute or relative permeability of the reservoir [4–7]. The protection of oil and gas reservoirs is related to various links such as exploration, drilling, completion, and development. It is a complex and systematic project, which directly affects whether the oil and gas fields can be discovered, evaluated, and efficiently developed in time, and it is also related to the development of oil and gas fields recovery rate [8–11]. As the most critical part of oil and gas well construction, the cementing process mainly pays attention to the safe pumping of the cement slurry and the long-term effective interlayer isolation capability of the cement sheath. Less attention is paid to the reservoir protection during the cementing process. The high-pressure difference between the annulus and the formation, the high fluid loss, and high solids content of the cementing slurry during the cementing process have also become major challenges [12–15].

Scholars at home and abroad have carried out research on the damage mechanism of oil and gas reservoirs in the cementing process and have achieved certain research results. Some researchers have carried out the internal relationship between the quality of the mud cake of the drilling fluid and the degree of damage to the reservoir by the cement slurry [10, 16–18]. The formation of better quality internal and external mud cakes can effectively prevent the damage of drilling fluid and cement slurry to oil and gas reservoirs, so as to achieve the purpose of protecting reservoirs. Some researchers took the low-porosity and low-permeability reservoirs in the Songnan area as the research object, studied the damage degree of the cement slurry to the reservoir, established a damage model, and checked that the intrusion depth of cement slurry filtrate in this area is generally within 5 cm [12, 19–21]. The damage to the reservoir is small, and this damage can be canceled by perforating. Some researchers have carried out research on the damage degree of cement slurry filtrate to the reservoir, showing that the cement slurry filtrate will cause serious reservoir damage [22–25]. The combination of fine cement particles blocks the pore throats of the reservoir, resulting in a decrease in the permeability of the reservoir. Therefore, reducing the fluid loss of the cement slurry can effectively reduce the damage to the reservoir during the cementing process. Some researchers have studied the effect of different cement admixtures on the ionic composition of cement slurry filtrate. When the types of admixtures are different, the ionic content in the filtrate will cause different damage to the reservoir, mainly because long-chain admixtures can cause harmful effects. The increase of the ion concentration is not conducive to the protection of the reservoir, and the retarder can effectively reduce the harmful ion concentration of the filtrate to achieve the purpose of protecting the reservoir. Some researchers have studied the compatibility of cement slurry filtrate and formation water, the influence of crystals and sediments on reservoir conductivity through experiments, and explored the damage mechanism of the cement slurry to the reservoir and the impermeability and low water loss cement. Research on reservoir protection by slurry: Some researchers have evaluated the damage caused by the cement slurry filtrate and its precipitates to the reservoir through experiments because the reaction of the cement slurry filtrate and the solid phase particles in the filtrate with the reservoir begins immediately after the cement slurry is in contact with the reservoir, although the cement slurry is in contact with the reservoir. The slurry filtrate has a wide range of filtration loss, but the insoluble matter or precipitation reaction reacts rapidly in the area where the filtrate penetrates, resulting in the precipitation of high-capacity and low-molecular-weight hydration products near the wellbore. Changes in the volume of the solid phase depend on the mass balance (material balance). Some researchers took clastic rock reservoirs as the research object and carried out research on the damage of cementing cement slurry to clastic rock reservoirs in a medium-porous and medium-permeable sandstone reservoir in an oilfield. The lithological characteristics, physical characteristics, pore throat characteristics, and temperature and pressure characteristics of the clastic rock reservoir are analyzed, and the factors that may cause potential damage to the reservoir are analyzed from the aspects of clay mineral content, formation fluid properties, and cementing slurry characteristics, and the study area is obtained. Potential damage factors for blocks include sensitivity damage, inorganic scale precipitation damage, and cement slurry solid phase particle blockage damage.

The most critical part of the development and construction of oil and gas wells: During the cementing process, the high-pressure difference between the annulus and the formation, the high fluid loss, and the high solids content of the cementing slurry cause serious damage to the reservoir. Damage has also become a major problem. In this paper, taking a typical clastic rock reservoir in an oilfield in western China as the research object, the geological investigation of fracture development, pressure deficit, and cement slurry permeability loss during the cementing process was carried out in the reservoir, and the reservoir of clastic rock reservoir was studied. Analysis of physical properties, clay mineral characteristics, and formation water quality. The influence of cement slurry filtrate and solid phase particles on the expansion rate and permeability of reservoir clay was tested by using a core porosity and permeability tester. The damage mechanism of

solid phase particles to the reservoir is of great significance to the development of low-damage cementing slurry technology for clastic rock reservoirs.

2. Geological Features

2.1. Geological Overview Based Green Synthesis. In this paper, the typical clastic rock block *D* of an oilfield in western my country is selected as the research background, and the reservoir characteristics and cementing overview of the block are carried out. The oil and gas-bearing scrotal rock reservoirs in the study area are mainly distributed in the Paleogene Kumugelimu Group, the Cretaceous Bashkirqike Formation, and the Brazil Reorganization, among which the Paleogene Kumugelimu Group lithology mainly includes fine sandstone, argillaceous siltstone, glutenite, and silty mudstone; Cretaceous Bashkirqike Formation lithology mainly includes fine sandstone, argillaceous siltstone, siltstone, silty mudstone, and mudstone; the reorganized lithology in Brazil is mainly mudstone, silty mudstone, fine sandstone, and argillaceous siltstone. On the whole, the stratum is characterized by "mud above and below sand." Table 1 shows the temperature of the reservoir section in the study area. It can be seen from Table 1 that the temperature gradient of the reservoir is 1.98~2.11°C/100 m, the burial depth is in the range of 4000~5000 m, and the temperature is between 100 and 200°C.

Table 2 gives the pressure measurement coefficients of the reservoir sections in the study area. It can be seen from Table 2 that after years of oil and gas exploitation, the clastic rock reservoir section has appeared obvious pressure deficit, and the pressure coefficient has generally dropped below 1. At the same time, due to the pressure deficit, the pressure difference during cementing is relatively low, high, or even as high as 15~25 MPa.

Through geological survey and core observation, the clastic rock reservoir in the study area is loose due to the low pressure of the overlying stratum, and the rock cementation in the upper part of the reservoir is loose, mainly in the pore-type stratum, and the lower reservoir is due to the pressure of the overlying stratum. Larger, the rock cementation is tight, but under the action of geological tectonic deformation and tectonic stress, rupture has occurred, forming shrinkage fractures or structural fractures, and the permeability of the reservoir is good. Through the study of drilling cores in this block, it is found that 8 of the 45 cores in the reservoir section of the study area have structural fractures or shrinkage fractures, and the fractures account for as high as 18%, of which the largest fracture width is 0.4 mm.The width is large, and under the action of high-pressure difference in cementing, the cement slurry can completely enter the reservoir through the fracture; at the same time, the average porosity of the core reaches 15%, the average permeability is 118.6 mD, and the pore size distribution is 37–56 μm. The pore types are mainly intergranular dissolved pores and intragranular dissolved pores. The average clay mineral content in this area is between 2% and 11%, and the clay mineral type is mainly illite, accounting for about 50% of the clay content. %~80%, the ratio is 25%~35%, the ratio of which is 25%~35%. The salinity of formation water is as high as 1.84×10^5 mgL, and the concentration of Ca^{2+} in the formation water is higher, and it also contains a higher concentration of Mg^{2+} and SO_4^{2-}.

2.2. Overview of Cementing Based Green Synthesis. The cementing in this block mainly adopts the 5-layer casing structure of 20" × 133/8" × 7" × 5", the liner cementing process, and the one-time cementing scheme. A survey was carried out, and the LD cement slurry system was mainly used, and the formula of each well was not much different. In this paper, the liner cementing slurry of a certain well is randomly selected to carry out experimental research. Table 3 gives the cement slurry formulation. For fractured shoulder rock reservoir, polysulfonate antisloughing drilling fluid system (%), temporary plugging agent (24%), caustic soda (0.4%), and weighting agent are mainly used. In cementing, a microstrength isolation fluid system is used, and the main ingredients are weighting agent (50%), retarder (3%), dispersant (3%), suspending agent (1%), defoamer (0.5%), water.

In the cementing process, the cementing conditions, reservoir characteristics, and the damage of cement slurry to the reservoir are highly correlated. When the reservoir does not leak, it is necessary to consider the damage to the reservoir caused by the cement slurry of the mud cake inside and outside the drilling fluid. When leakage occurs in the reservoir, the type of leakage is related to the characteristics of the reservoir. In the upper part of the scribbled rock reservoir, the reservoir type is mainly pore-type strata, and the conditions of porosity and permeability are good. The bottom of the clastic rock reservoir is mainly a pore-fracture type formation, and fracture leakage often occurs.

The development of fractures in the reservoir provides space for oil and gas accumulation, provides channels for natural oil and gas migration, and plays an extremely important role in the seepage of oil and gas in the reservoir. For pore-fractured formations, permeability leakage may occur during cementing under the action of high-pressure difference, cement slurry easily flows into the fractures, and hydration occurs and finally solidifies and blocks microfractures in the reservoir, which will cause damage to oil and gas production in the later stage more serious impact.

2.3. Test Conditions Based Green Synthesis. The test material in this paper is the core of typical clastic rock block *D* in an oilfield in the west. The ingredients used for cementing cement are simulated formation water, *G*-grade cement, mutual force silica fume, coagulant, fluid loss reducer, dispersant, retarder, and defoamer. The test mainly used a constant speed stirrer, high temperature, and high-pressure water loss instrument: DKS-2 core porosity and permeability tester, DX-2000 X-ray diffractometer, TM-1000 electron scanning microscope, and CPD-II high-temperature and high-pressure dilatometer.

In order to truly simulate the damage of the cement slurry to the clastic rock reservoir under this working condition, artificial fractures were made on the reservoir

Table 1: Reservoir section temperature in the study area with green synthesis and metal oxide composites.

Block	Geothermal gradient	Clastic reservoir temperature
D	1.98~2.11°C/100 m	100~200°C

Table 2: Pressure measurement coefficients of reservoir sections in the study area.

Hashtag	Horizon	Mid-depth of gas layer (m)	Formation pressure (MPa)	Pressure coefficient
D-02	*E*	5140	56.5	1.13
D-08	*E*	5032	50.1	1.01
D-15	*E* + *K*	4942	48.6	0.92
D-24	*E* + *K*	4831	45.2	0.89
D-32	*E*	5261	41.6	0.81

Table 3: Cement slurry formula with green synthesis and metal oxide composites.

Type	G class	Cement	Silicon powder	Water retarder	Dispersant	åwater loss reducer	Defoamer
Addition (%)	100	36	34	2.5	1.3	5.2	0.

cores, and the dynamic experiments of the cement slurry were carried out using the fractured cores. Figure 1 shows the dynamic experimental flow of the cement slurry. In the test, the cores contaminated with cement slurry were placed in a high-temperature and high-pressure curing kettle for curing. The temperature during curing was set to 120°C, the curing pressure was 75 MPa, and the curing time was taken out after 24 hours. The acid solution with a concentration of 15% was used to simulate acid dissolution. Its permeability recovery value is plugged and calculated. For pore-fractured formations, when the cement slurry leaks out, it causes serious damage to the reservoir, the fractures in the core are filled with cement, and the permeability damage rate exceeds 80%. Due to the consolidation ability of cement slurry, the acid solubility of cement stone after curing with conventional cement slurry is low, and the permeability recovery value after plugging by acid dissolution is less than 50%. The reservoir damage caused by cement slurry consolidation still cannot be effectively relieved.

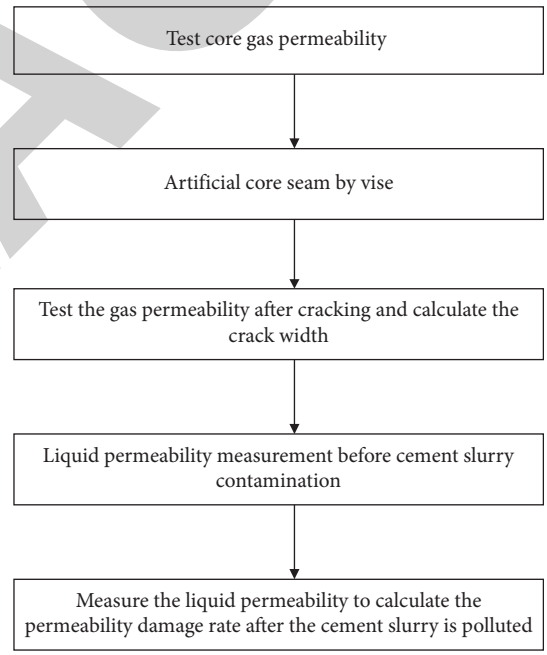

Figure 1: Dynamic experiment flow of cement slurry with green synthesis and metal oxide composites.

3. Damage of Cement Slurry to Clastic Rock Reservoir

3.1. Damage to Reservoir by Cement Slurry Filtrate Based Green Synthesis. In this paper, the cement slurry filtrate and formation water are mixed and placed in a wide-mouth bottle according to different volume ratios and then cured in a water bath. The curing temperature is 90°C and the curing time is 24 hours. After that, the scaling phenomenon occurs, and the scaling form is granular. Crystallized and flocculated precipitates. The flocculated substances generated were analyzed by infrared spectroscopy, and it was obvious that the flocculent scale was obviously organic, indicating that the cement slurry admixture contained high-molecular polymers. Under the action of high-valent cations in the formation of water, the polymer molecules were a cross-linked phenomenon, resulting in flocculationlike scaling. These flocculated scales are more likely to block the critical parts of the reservoir pore throat isosmotic flow. Table 4 and Figure 2 show the scaling amount of different ratios of cement slurry filtrate and formation water. It can be seen from Table 4 and Figure 2 that with the increase of the ratio of cement slurry filtrate and formation water, the scaling amount first increases and then decreases. When the volume ratio of the filtrate to formation water is 3 : 2, the amount of scaling is the largest.

CPD-II type high temperature and high-pressure dilatometer was used to test the volume expansion rate of clastic rock reservoir cores under the action of cement slurry

Table 4: Compatibility test results of cement slurry filtrate and formation water.

Serial number	Cement slurry filtrate volume (ml)	Formation water volume (ml)	Scaling amount (g)
1	20	80	0.07
2	40	60	0.31
3	60	40	0.68
4	80	20	0.21

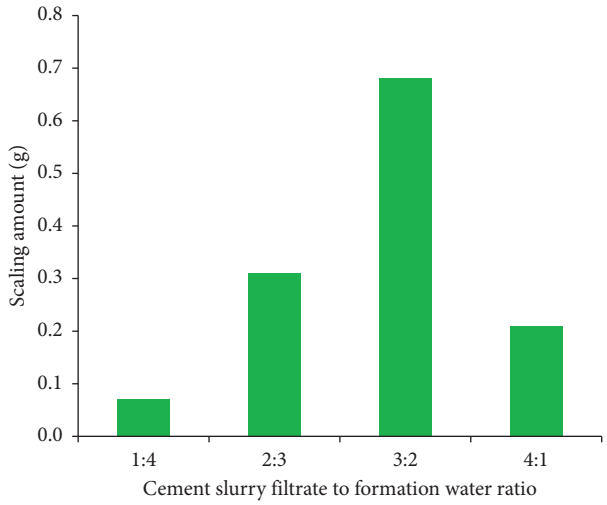

Figure 2: Scaling amount of different ratios of cement slurry filtrate and formation water with green synthesis and metal oxide composites.

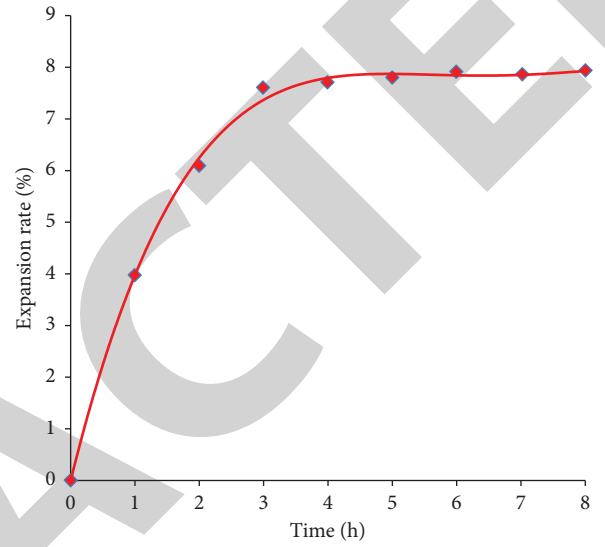

Figure 3: Reservoir rock expansion rate test with green synthesis and metal oxide composites.

filtrate. Figure 3 shows the test results of the reservoir rock expansion rate. It can be seen from Figure 3 that with the extension of time, under the action of the cement slurry filtrate, the reservoir core will undergo obvious hydration expansion, and the expansion rate of the filtrate and the reservoir rock will increase rapidly in the first 2 hours after contact; the final volume expand Rate will reach 8%.

The core-flooding device was used to carry out the damage experiment of the cement slurry filtrate on the core. Table 5 shows the influence of the cement slurry filtrate on the core permeability. It can be seen from Table 5 that the cement slurry filtrate has a great influence on the core permeability up to 92%. In the test, the porosity and permeability of reservoir core before filtrate damage are good, and a large amount of flocculent scaling appeared at the pore throat after the damage, which caused the blockage of the pore throat.

Through the core damage test of cement slurry filtrate, the main reason is that during the hydration process and the crystallization of inorganic substances damages the cement slurry and produces many inorganic ions. In a higher *pH* environment, the inorganic ions generated by hydration will exist in the cement in a saturated state. During cementing construction, after the filtrate enters the reservoir, the original ion balance is destroyed, resulting in the precipitation of $CaCO_3$, $Mg(OH)_2$, and the like. The crystals were separated and obtained by suction filtration, and analyzed by X-ray diffractometer, which proved that $Mg(OH)_2$ and

Table 5: Experiment on the effect of cement slurry filtrate on core permeability.

Rock sample number	Permeability (mD)			D (%)
	Ka	K_o	K_d	
1	41	0.25	0.07	81
2	75	4.03	0.59	86
3	108	4.27	0.41	89
4	135	5.84	0.56	92

$CaCO_3$ existed in the crystals. The cement slurry filtrate is strongly alkaline. Once the filtrate enters the reservoir, it will affect the chargeability of the clay mineral lattice surface of the reservoir. The amount of OH^- adsorption on the clay surface will increase, and the electrostatic repulsion between the clay mineral crystal layers will increase. For the reservoir, clay minerals are more likely to swell and disperse.

3.2. Analysis of the Damage Mechanism of Cement Slurry Solid Phase Particles to the Reservoir Based Green Synthesis. In cementing construction, with the filtration of cement slurry, cement particles and external admixtures will enter the reservoir together with the filtrate, undergo a hydration reaction, and finally consolidate inside the reservoir, while the external admixture directly blocks the reservoir. Layer pore throats cause damage. For cores that have not been

Table 6: Barkman and Abrams blocking criteria.

Particle size range	Damage result
The rock pore size is less than 3 times the solid phase particle size	Surface bridging to form a filter cake
3 times the particle size of the solid phase < rock pore diameter < 10 times the particle size of the solid phase	Shallow plugging near wellbore
If the rock pore size is greater than 10 times the solid phase particle size	Deep blockage

damaged by cement slurry, pore throats are more developed. When the cement slurry damages the reservoir, the amorphous cementitious components contained in the pore throats fill the rock pores and fractures and contain spherical particles, indicating that the cement slurry does not participate in the hydration reaction of external admixtures.

Through the analysis of the particle size distribution and cumulative particle size distribution of the cement slurry solid phase particles, the particle size of the solid phase particles in the cement slurry is between 1 and 1000 μm, and the overall particle size is relatively large. The volume of phase particles accounts for the largest proportion, while the smaller particles with a particle size of 1–10 μm account for about 15% of the total volume of the solid phase.

According to the plugging criteria of Barkman and Abrams (Table 6), it can be seen that when the pore size of the reservoir rock is less than 3 times the particle size of the solid phase, the solid phase particles will bridge the surface of the permeable layer to form a filter cake; When the rock pore size is less than 10 times the solid particle size, the solid particles enter the reservoir near the wellbore to form shallow plugging; if the rock pore size is greater than 10 times the solid particle size, the solid particles enter the deep part of the permeable layer, increasing the depth of plugging.

According to the pore size test results of clastic rock reservoirs under different working conditions, the particle size distribution, and cumulative particle size distribution of cement slurry solid phase, it can be concluded that under the condition of no leakage, the original pore size of the reservoir is 0.1~100 μm. Among them, the pore size in the range of 1–10 μm accounts for the largest proportion, and the pore size is similar to the smaller particle size in the cement slurry. Therefore, under this working condition, the solid phase particles of the cement slurry cannot enter the reservoir. As a result, a filter cake will be formed on the surface of the reservoir core; under the leakage condition, due to the loss of the protection of the mud cake in the drilling fluid, the solid phase particles of the cement slurry will directly contact the reservoir rock. The proportion between ~50 μm is the largest, and the part of the solid particles in the cement slurry with a solid particle size of 1 to 10 μm will enter the reservoir and form shallow plugging in the reservoir near the wellbore.

4. Conclusion

The protection of oil and gas reservoirs is related to various links such as exploration, drilling, completion, and development. It is a complex and systematic project, which directly affects whether the oil and gas fields can be discovered, evaluated, and efficiently developed in time, and it is also related to the development of oil and gas fields recovery rate. The damage to the reservoir is caused by the high-pressure difference between the annulus and the formation, the high fluid loss, and the high solids content of the cementing slurry during the cementing process. In this paper, taking a typical clastic rock block in an oilfield in western China as the research object, the geological investigation of fracture development, pressure deficit, and cement slurry permeability loss in the cementing process was carried out in the reservoir, and the reservoir of clastic rock reservoir was studied. The physical properties, clay mineral characteristics, and formation water quality are analyzed. The influence of cement slurry filtrate and solid phase particles on the expansion rate and permeability of reservoir clay was tested by using a core porosity and permeability tester. XRD and SEM were used to analyze the cement slurry filtrate and solid phase. The damage mechanism of facies particles to the reservoir provides theoretical data support for the research on low-damage cementing slurry technology in clastic rock reservoirs. The main research results are as follows:

(1) The average porosity of the clastic rock reservoir in the study area is 15%, the permeability is high, the average pore size of the reservoir is between 37 and 56 μm, the microfractures are developed in the reservoir section, and the porosity and permeability conditions are good, the high price of formation water. The cations and inorganic ions in the filtrate generate inorganic scales such as $CaCO_3$ and $Mg(OH)_2$, which cross-link with the dissolved macromolecular polymers to form flocculation substances, which cause the filtrate to damage the reservoir. Hydration, tightly bonding the inert external admixture and the clastic rock formation, forms a tight sealing layer, which drastically reduces the reservoir permeability.

(2) The expansive clay particles in the reservoir absorb the moisture of the cement slurry filtrate and expand, increasing the volume of the particles. The porous formation containing expansive clay minerals absorbs moisture and causes internal expansion, and the volume expansion rate can reach 9%, which will eventually cause the reservoir to expand. The decrease of the porosity and permeability of the layer will cause damage to the reservoir; the damage to the reservoir caused by the solid particles in the cement slurry is mainly due to the blockage of the reservoir pore throats and the cement particles caused by the external admixtures in the cement slurry that do not participate in the hydration reaction. In the

Hindawi
Journal of Chemistry
Volume 2023, Article ID 9834670, 1 page
https://doi.org/10.1155/2023/9834670

Retraction

Retracted: Effectiveness of Oil Filling in Tight Sandstone Reservoirs of Yancheng Formation in Ordos Basin

Journal of Chemistry

Received 15 August 2023; Accepted 15 August 2023; Published 16 August 2023

This article has been retracted by Hindawi following an investigation undertaken by the publisher [1]. This investigation has uncovered evidence of one or more of the following indicators of systematic manipulation of the publication process:

(1) Discrepancies in scope

(2) Discrepancies in the description of the research reported

(3) Discrepancies between the availability of data and the research described

(4) Inappropriate citations

(5) Incoherent, meaningless and/or irrelevant content included in the article

(6) Peer-review manipulation

The presence of these indicators undermines our confidence in the integrity of the article's content and we cannot, therefore, vouch for its reliability. Please note that this notice is intended solely to alert readers that the content of this article is unreliable. We have not investigated whether authors were aware of or involved in the systematic manipulation of the publication process.

Wiley and Hindawi regrets that the usual quality checks did not identify these issues before publication and have since put additional measures in place to safeguard research integrity.

We wish to credit our own Research Integrity and Research Publishing teams and anonymous and named external researchers and research integrity experts for contributing to this investigation.

The corresponding author, as the representative of all authors, has been given the opportunity to register their agreement or disagreement to this retraction. We have kept a record of any response received.

References

[1] Y. Han, P. Wanyan, H. Wang, M. Qu, H. Cheng, and F. Theon, "Effectiveness of Oil Filling in Tight Sandstone Reservoirs of Yancheng Formation in Ordos Basin," *Journal of Chemistry*, vol. 2022, Article ID 9907772, 8 pages, 2022.

Hindawi
Journal of Chemistry
Volume 2022, Article ID 9907772, 8 pages
https://doi.org/10.1155/2022/9907772

Research Article

Effectiveness of Oil Filling in Tight Sandstone Reservoirs of Yancheng Formation in Ordos Basin

Yu Han,[1] Peiru Wanyan,[1] Haoli Wang,[1] Mengfei Qu,[1] Hanlie Cheng,[2] and Fahim Theon[3]

[1]*No. 8 Oil Production Plant of Changqing Oilfield Company, PetroChina, Yinchuan, Ningxia 750000, China*
[2]*School of Energy Resource, China University of Geosciences (Beijing), Beijing 434000, China*
[3]*The King's School, BP1560, Bujumbura, Burundi*

Correspondence should be addressed to Fahim Theon; fahimtheon@ksu.edu.bi

Received 30 August 2022; Revised 20 September 2022; Accepted 23 September 2022; Published 4 October 2022

Academic Editor: Rabia Rehman

The Ordos basin is one of the important oil-bearing basins in China, with abundant tight sandstone oil resources, wide distribution, and large thickness. It is the most realistic field of unconventional oil and gas exploration in China, and it is also an important oil and gas replacement resource at present. Oil accumulation in tight reservoirs is obviously different from conventional oil and gas accumulation, and the key lies in studying the effectiveness of oil filling in tight reservoirs. In order to solve this problem, this paper takes the tight sandstone reservoir of Member 7 of the Yancheng Formation in Ordos Basin as the research object, introduces the geological characteristics of this area after sorting out the previous research results, carries out the physical simulation experiment of oil filling, studies the relationship between the filling pressure and the lower limit of the filling throat, analyzes the effective accumulation space of the tight sandstone reservoir, defines the oil filling mechanism of the tight sandstone reservoir, and discusses the effectiveness and reservoir-forming effect of oil filling in different types of reservoirs. The results show that the rock types of tight sandstone reservoirs in the 7th member of the Yancheng Formation are mainly lithic feldspathic sandstone and feldspathic lithic sandstone, and the reservoirs have experienced strong compaction and carbonate cementation. The late iron-bearing carbonate cementation has further strengthened the degree of reservoir densification, and the reservoirs have been densified at the time of large-scale oil and gas filling. Through the simulation experiment of oil filling with natural cores with different physical properties, the relationship model between filling pressure and effective accumulation space of different types of tight sandstone reservoirs in Member 7 of the Yancheng Formation is established. With the change in filling pressure, the change trend and range of effective accumulation space of different types of tight sandstone reservoirs are obviously different. According to the relationship model between the filling pressure and the lower limit of the effective filling pore throat, the oil filling effectiveness of different types of tight sandstone reservoirs in the 7th member of the Yancheng Formation is determined. Class I and class II1 reservoirs are effective reservoirs for oil filling of tight sandstone reservoirs, which constitute the main oil-bearing section of tight sandstone reservoirs in member 7 of the Yancheng formation, while class II2 reservoirs are poor tight reservoirs, and class III reservoirs are basically oil-free, which are noneffective reservoirs for oil filling of tight sandstone reservoirs. The results provide theoretical data support for the next step of oil exploration and exploitation in tight sandstone reservoirs.

1. Introduction

With the continuous growth of global oil and gas demand, conventional oil and gas production is declining, and the exploration and development of unconventional oil and gas resources are gradually being paid attention to and have become the main way to increase global oil and gas production. In China, tight sandstone reservoirs are widely distributed in the Ordos Basin, Junggar Basin, Sichuan Basin, Songliao Basin, and other major basins, which are rich in oil resources and have good exploration prospects [1–4]. The tight sandstone reservoir in the Ordos Basin is rich in oil

resources, with a resource reserve of 30×108 t. The demonstration area of tight reservoir oil horizontal wells and Xin'anbian oilfield of 100 million tons have been built, which has achieved a major breakthrough in tight reservoir oil exploration in China [5–8]. The lacustrine tight sandstone reservoir in the 7th member of the Yanchang Formation has poor physical properties, a complex pore structure, and a widely developed micronano pore throat system, which has differences in the effectiveness of oil occurrence, resulting in strong heterogeneity of oil distribution in a tight sandstone reservoir. Therefore, it is of great significance for oil exploration and exploitation to study the oil occurrence state and oil filling effectiveness in tight sandstone reservoirs [9–12].

The tight sandstone of the Yanchang Formation in the Ordos Basin is a typical tight reservoir in China's continental basins, which have considerable reserves and great exploration and development value. Scholars have conducted in-depth research on the oil filling characteristics and reservoir-forming mechanisms of tight sandstone reservoirs and achieved fruitful results [13–16]. Some researchers have mainly studied the dynamic conditions of oil migration and accumulation in tight sandstone reservoirs; the characteristics of oil seepage in tight sandstone reservoirs; and the lower limit of oil filling pore throat in tight sandstone reservoirs. Some researchers have suggested that the influence of pore structure on oil accumulation in tight reservoirs is mainly manifested in the effectiveness of oil filling and accumulation in micronano pore throat systems; that is, the lower limit of oil filling pore throat, which is the smallest throat diameter that oil can reach from source rock to reservoir under geological conditions [17–20]. Some researchers have studied clastic reservoirs with different grain sizes and determined the throat diameter distribution range of conventional and tight sandstone reservoirs and the diameter range of different organic molecules from asphaltene to methane, which provided a theoretical basis for the comparison of the pore throat distribution characteristics of different reservoirs, the critical pore throat conditions of oil filling, and the potential of fine-grained rocks as reservoirs. Some researchers put forward nano-scale oil and gas reservoir pores and theoretically calculated that the lower limit of critical pore throat for methane desorption (mobility) in tight sandstone gas reservoirs is 40 nm and the lower limit of tight sandstone oil occurrence pores is 54 nm [17, 21–23]. At the same time, the lower limit of oil-bearing pores in unconventional tight sandstone reservoirs is determined by scanning electron microscopy (SEM), which is 44~58 nm. Based on the theory of fluid mechanics and the balance principle of reservoir-forming power and resistance, some researchers have calculated the lower limit of oil-filled pore throat at the source-reservoir interface and inside the reservoir of tight reservoirs in many basins and proved that the lower limit of oil-filled pore throat at the source-reservoir interface is generally smaller than that inside the reservoir [24–27]. Some researchers use the chloroform asphalt "a" obtained by the extraction method to establish a relationship with the average pore size of nitrogen adsorption, calculate the boundary between oil-bearing and nonoil-bearing pores on the intersection map, and calculate that the average lower limit of oil-bearing pores of the dense sandstone in member 7 of the Yancheng formation is 30 nm. Some researchers use various methods to study the lower limit of oil filling in tight sandstone reservoirs, which is mainly between 20 and 60 NM. At the same time, the lower limit of static pore throat where oil may exist does not consider the change of the lower limit of pore throat under different geological conditions; that is, there are certain differences between different filling pressures and the matching lower limit of filling pore throat.

The Ordos basin is one of the important oil-bearing basins in China, with abundant tight sandstone oil resources, wide distribution, and large thickness. Oil accumulation in tight sandstone reservoirs is obviously different from conventional oil and gas accumulation, and the key lies in studying the effectiveness of oil filling in tight reservoirs [28–31]. In this paper, taking the tight sandstone reservoir of Member 7 of the Yancheng Formation in the Ordos Basin as the research object, after sorting out the previous research results, the geological characteristics of this area are introduced, and the physical simulation experiment of oil filling is carried out. The relationship between filling pressure and the lower limit of filling pore throat is studied, the effective accumulation space of a tight sandstone reservoir is analyzed, the oil filling mechanism of a tight sandstone reservoir is defined, and the effectiveness and reservoir-forming efficiency of oil filling in tight sandstone reservoirs are discussed, which provides theoretical data support for oil exploration and exploitation in tight sandstone reservoirs [32].

2. Geological Characteristics of the Reservoir

2.1. General Situation of Reservoir Geology. The Ordos Basin is a large Meso-Cenozoic continental basin in Central China. It is a stable cratonic sedimentary basin with a total area of about 250,000 km^2. The research area is located in the southwest of the Ordos Basin, starting from Huanxian County in the west, Taibai in the east, Zhengning in the south, and Dingbian in the north; structurally, it belongs to the southwest of the Yishan slope in the Ordos Basin and is connected with the Tianhuan depression. It is a west-dipping monocline with a dip angle of only half a degree and a nearly north-south direction. The nose-shaped uplift is developed locally, with an area of about 50000 km^2, accounting for about 25% of the area of the Ordos Basin.

The Yancheng Formation studied in this paper is the first source-reservoir system developed after the formation of a large inland depression lake basin in the Ordos Basin. It is a sedimentary system of braided river delta, meandering river delta, and turbidite fan, which is mainly composed of medium-fine sandstone and mudstone. Oil shale is locally developed, including coal seam interlayer. There are 10 oil reservoirs in the Yancheng Formation from bottom to top, all of which are found. Among them, the 7th member of the Yancheng Formation (Table 1) is the peak period of lake basin development, and the average permeability of sandstone in oil reservoirs is less than 0.3×10^{-3} μm^2, which is the typical reservoir in tight oil. The middle-lower Chang 73 submember

Table 1: Description of 7 segments of the Yancheng Formation.

Characteristic	Lithology description	Thickness (m)
Yancheng group 71	Thick fine sandstone and siltstone mixed with argillaceous siltstone and mudstone	35~45 m
Yancheng group 72	Thick fine sandstone, thin siltstone interbedded with mudstone, and thick mudstone and muddy siltstone.	25~35 m
Yancheng group 73	Black oil shale and occasionally thin tuff deposits.	35~45 m

is mainly a deep lacustrine facies, and its lithology is mainly mudstone and silty mudstone. Middle-upper Chang 71 and Chang 72 are mainly semideep lacustrine facies, and their lithology is mainly fine sandstone and siltstone.

2.2. Petrological Characteristics of the Reservoir. The tight oil reservoir (Table 2) of the 7th member of the Yancheng Formation in Ordos has a fine grain size, mainly composed of fine sandstone, extremely fine sand, siltstone, and mudstone, which are well sorted as a whole, and most of the grains are subangular. The rock types are mainly lithic feldspathic sandstone and feldspathic lithic sandstone, followed by feldspathic sandstone. The reservoir detrital composition (Table 3) is mainly Shi Ying, feldspar and cuttings, among which the content of Shi Ying is the highest, and the content of cuttings in metamorphic rocks is the highest, reaching 40% of the rocks.

2.3. Hydrocarbon Accumulation Process. The Ordos basin has experienced four different degrees of tectonic uplift and stratum denudation since the deposition of the Yancheng Formation in the Late Triassic. Figure 1 shows the hydrocarbon accumulation process in the Ordos Basin. From the late Jurassic to the early Cretaceous, the buried depth of the source rocks in the 7th member of the Yancheng Formation was mostly distributed at 1000~1500 m and they entered the hydrocarbon generation threshold to generate a small amount of oil, which was discharged from the source rocks and migrated to the adjacent favorable reservoirs, forming the early small-scale oil filling. At the end of the early Cretaceous (110~100 ma), the buried depth of strata was the highest, and it began to enter the peak of hydrocarbon generation, generating a large number of liquid hydrocarbons, which were injected into tight sandstone reservoirs on a large scale, forming oil accumulation in tight sandstone reservoirs of Member 7 of the Yancheng Formation. The temperature measurement of core fluid inclusions shows that the average temperature of salt water inclusions corresponding to small-scale reservoir formation in early tight sandstone reservoirs is 70~90°C, and the average degree of saltwater inclusions corresponding to the main filling period of petroleum in late tight sandstone reservoirs is 90~115°C.

2.4. Physical Simulation Experiment of Oil Filling. In this paper, the NMR fluid displacement equipment of the Institute of Geology and Geophysics, Chinese Academy of Sciences, is adopted, which consists of a fluid injection system, fluid displacement system, NMR imaging system, and a computer data processing system. The fluid injection system is composed of a constant pressure and constant speed displacement pump, a ring pressure pump, and a temperature and pressure sensor, which provide axial pressure (filling pressure) and apply ring pressure to the whole system. The fluid displacement system consists of a high-pressure core holder and an intermediate container. The ring pressure of the core holder is controlled by a ring pressure pump, and the maximum axial pressure can reach 30 MPa during the experiment. A nuclear magnetic resonance imaging system is composed of nuclear magnetic resonance instruments, mainly including fluid detection units and data imaging units, which can detect the fluid in the rock core online. The main resonance frequency of the NMR instrument is 10 MHz, the waiting time is 3000 ms, the echo time is 0.2 ms, the number of scans is 64, the number of echoes is 4200, and the magnet temperature is 25°C. The whole displacement equipment is controlled by the computer data processing system. In the experiment, the lateral relaxation time spectrum of the fluid is measured once every 3 minutes to monitor the oil filling process (oil displacement water) in real time.

In the experiment, natural tight sandstone core samples are used to carry out filling simulation experiments. The basic physical parameters of the samples are shown in Table 4. The experimental displacement device adopts an axial pressure of 1, 4, 8, 12, 16, and 20 MPa, and a certain confining pressure (up to 30 MPa) is set. Simulated formation oil (3# white oil) or Chang 7 crude oil is used to displace the core plunger saturated with simulated formation water, simulating the filling process of petroleum in tight reservoirs, and identifying the fluid by means of nuclear magnetic resonance T2 spectrum. The core samples selected in the experiment are mainly distributed in the distribution area of tight sandstone oil core and have a certain physical property gradient.

Figure 2 Shows the physical simulation experiment process of petroleum filling. In the experiment, the core was evacuated at 105°C for 24 hours, at −0.098 MPa for 24 hours, and pressurized at 30 MPa for 48 hours, and the simulated saturated manganese ions were more than 20000 ppm. During the experiment, the NMR signal (T2 spectrum of the oil phase) was measured online every 3 minutes. When the T2 spectrum remained stable for a long time (i.e., oil saturation remained unchanged), the axial pressure was increased and the filling experiment was continued until it was stable under the maximum pressure.

3. Filling Effectiveness of Tight Sandstone Reservoir

3.1. Test Results. Through the physical simulation experiment of oil filling, the relationship between filling pressure and oil saturation is obtained. The oil saturation of simulated

Table 2: Lithologic composition of tight oil reservoir in member 7 of Yancheng formation in Ordos.

Rock character	Fine sandstone	Very fine sand	Siltstone	Mudstone	Other
Proportion (%)	60.3	10.1	7.2	9.3	13.1

Table 3: Composition and diagenetic types of reservoir debris.

Composition classification	Composition			Diagenetic type		
	Quartz	Feldspar	Debris	Metamorphic rock debris	Magmatic rock cuttings	Sedimentary cuttings
Proportion (%)	45.7	32.9	21.4	45	35	20

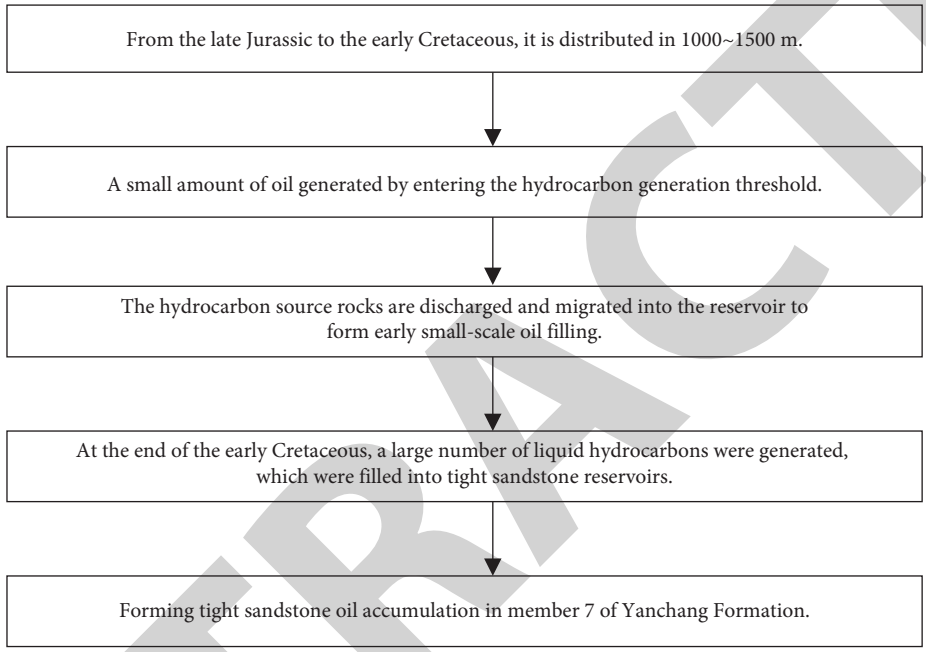

Figure 1: Hydrocarbon accumulation process in the Ordos basin.

Table 4: Basic physical parameters of natural tight sandstone core samples.

Sample number	Depth	Average diameter/mm	Average length/mm	Permeability/mD	Porosity/%	Simulated oil	Reservoir type	Horizon
YC-1	1741	25.31	49.98	0.0218	9.56	3# white oil	II2	Long 7
YC-2	2015	25.62	50.15	0.0398	10.41	3# white oil	II2	Long 7
YC-3	1720	25.72	50.27	0.0653	11.04	3# white oil	II1	Long 7
YC-4	2020	24.89	50.42	0.0757	10.18	3# white oil	II1	Long 7
YC-5	1929	25.05	50.08	0.1485	9.51	3# white oil	I	Long 7
YC-6	2082	25.02	50.19	0.4259	12.26	3# white oil	I	Long 7
YC-7	2015	25.41	49.87	0.0163	7.37	Crude oil	III	Long 7
YC-8	1728	25.11	50.45	0.1270	10.19	Crude oil	II1	Long 7

oil gradually increases with the increase of filling pressure, but there are some differences in the changing trends of different oil saturations with filling pressure, which is mainly due to the differences in physical properties and pore structures of rock samples, as well as the properties of white oil and crude oil. Under the condition of white oil filling, the increasing trend of oil saturation can be roughly divided into three types: gradually increasing type (Figure 3), gradually increasing-stabilizing type (Figure 4) and rapidly increasing-slowly increasing type (Figure 5).

Gradually increasing type means that the growth rate of oil saturation basically keeps constant with the increase of filling pressure, mainly for samples YC-1 and YC-2. The physical properties and pore structure of the two samples are not significantly different, but the oil saturation growth rate and final oil saturation of sample YC-2 are higher than those of sample YC-1, and the oil saturation is at least 10% higher. When the filling pressure is increased from 16 MPa to 20 MPa, the oil saturation of sample YC-1 increases more than that of sample YC-2, which is mainly related to the local wettability change of the sample.

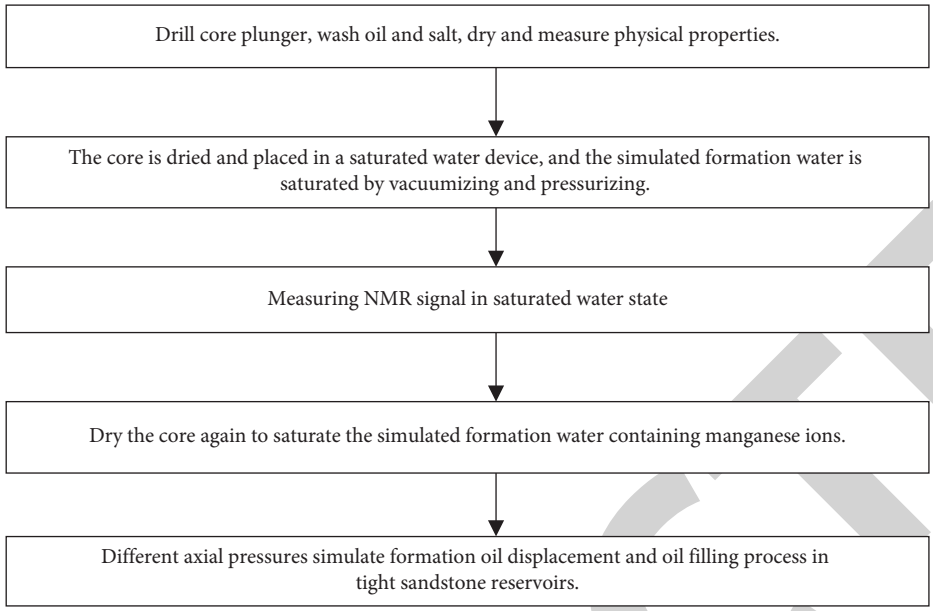

Figure 2: Experimental process of petroleum filling physical simulation experiment.

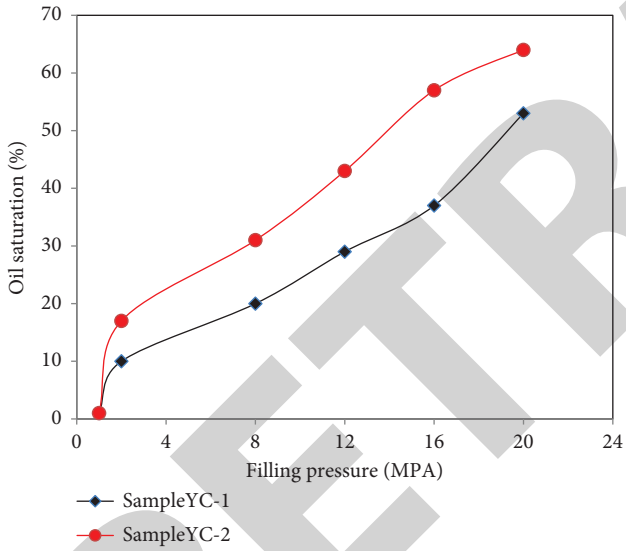

Figure 3: The relationship between filling pressure and oil saturation is gradually increasing.

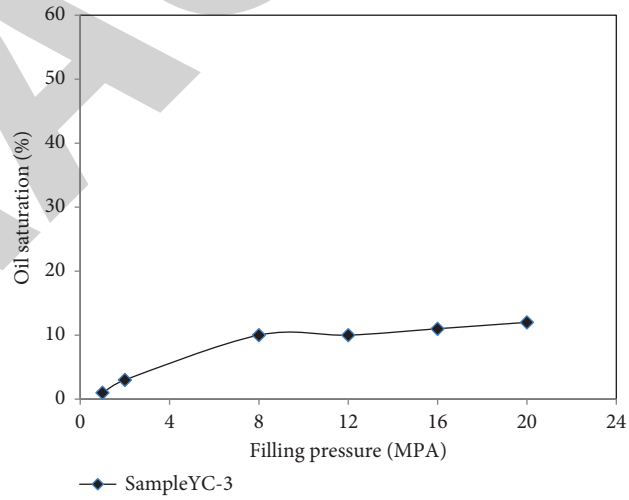

Figure 4: The relationship between filling pressure and oil saturation is gradually increasing-tending to be stable.

Gradually increasing-stabilizing type means that the growth rate of oil saturation generally decreases gradually and finally tends to zero, and sample YC-3 is typical. When the filling pressure is lower than 8 MPa, the oil saturation gradually increases with the increase of the filling pressure; when the filling pressure is greater than 8 MPa, with the increase of the filling pressure, the growth rate of oil saturation gradually decreases, and finally the oil saturation tends to be stable.

The rapid growth-slow growth type means that the oil saturation growth rate at low filling pressure is obviously higher than that at high filling pressure, mainly including samples YC-4, YC-5, and YC-6. When the filling pressure is less than 4 MPa, the oil saturation increases rapidly with the increase of the filling pressure, up to 40%. When the filling pressure is greater than 4 MPa, the increase in oil saturation is obviously slowed down with the increase of the filling pressure. Within the filling pressure span of 4 MPa to 20 MPa, the oil saturation increases by about 25%.

3.2. Filling Effectiveness of Tight Sandstone Reservoir. In the process of oil accumulation in tight sandstone reservoirs, the filling pressure required to reach a certain oil saturation is complementary to the pore throat size, that is, the sample with a small pore throat radius needs a higher filling pressure, while the sample with a large pore throat radius needs a lower filling pressure. Therefore, to reach the lower limit of oil saturation, physical properties (especially permeability) and filling pressure are complementary. When

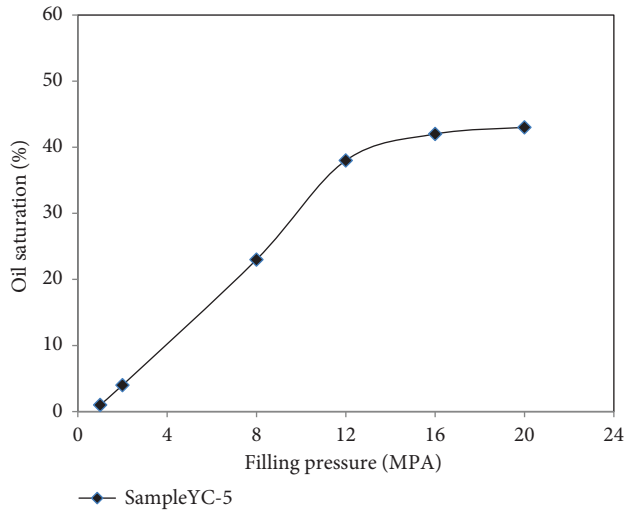

Figure 5: The relationship between filling pressure and oil saturation is a rapid growth-slow growth type.

the oil saturation of a tight sandstone reservoir reaches 30%~40%, oil accumulation is formed. The simulation experiment shows that the filling pressure can increase the oil saturation of the reservoir to a certain extent. Tight sandstone reservoirs with different compactness require different filling pressures to reach the lower limit of oil saturation. The denser the reservoir, the higher the filling pressure. Through the comparison of experimental samples, the II2 reservoirs represented by samples YC-1 and YC-2 can reach the lower limit of reservoir formation when the filling pressure is 12~16 MPa; The lower limit of reservoir-forming power of II1 reservoirs represented by samples YC-3 and YC-4 is about 4~8 MPa; The lower limit of reservoir-forming power for II1 reservoirs represented by YC-5 and YC-6 samples with lower densification degree is only about 1~4 MPa. When the degree of reservoir densification is too high, the capillary force resistance is too large. Under certain geological conditions, the filling pressure is no longer the sufficient condition for reservoir formation. For example, the oil saturation of sample yc-7 is only 11% under the filling pressure of 20 MPa, and the type III tight sandstone reservoir represented by it is impossible to form reservoirs. Therefore, it can be considered that the filling pressure and pore throat capillary resistance jointly determine the oil saturation growth process of tight sandstone oil and gas. In the process of oil filling and accumulation in the actual tight reservoir, the coupling of reservoir-forming power (overpressure of source rock) and reservoir-forming resistance (capillary force) controls the oil filling and retention in the tight reservoir.

According to the analysis of reservoir formation and filling effectiveness of four different types of tight sandstone reservoirs in the 7th member of the Yancheng Formation, it can be seen that the effective reservoir space of Class I is 69%~85%, with an average of 76%. The effective accumulation space is obviously higher than the lower limit of oil saturation, an oil enrichment degree. When the filling pressure is not less than 10 MPa, this kind of reservoir is rich in oil and is a high-quality tight reservoir. The pore throat radius that this kind of reservoir needs to break through in order to reach the oil enrichment degree ranges from 0.18 to 0.67 μm, with an average of 0.37 μm, which is obviously higher than the lower limit of pore throat radius (0.094 μm), so the oil saturation of this kind of reservoir is often higher than 60%. In actual exploration, Class I reservoir is the best part of the "sweet spot" of a tight sandstone reservoir.

Class II reservoir is an effective tight reservoir, and its effective accumulation space is distributed in 50%~84%, with an average of 59%. The effective accumulation space is obviously higher than the lower limit of oil saturation, in which the effective reservoir space of some rocks is over 60%, and this kind of reservoir is widely distributed, so this kind of reservoir is the main tight sandstone oil reservoir in the 7th member of the Yancheng Formation. To reach the oil saturation value of the reservoir, the pore throat radius of oil breakthrough is 0.11~0.26 μm, with an average of 0.16 μm, which is obviously higher than the lower limit of pore throat radius (0.094 μm), so its oil saturation is obviously higher than 40%. The pore throat radius that this kind of reservoir needs to break through in order to enrich oil is distributed in the range of 0.04~0.17 μm, with an average of 0.09 μm, which is close to the lower limit of pore throat radius for reservoir formation, so the oil content of some reservoirs may reach 60%, that is, the reservoir is enriched with oil.

Class II reservoirs are poor-tight reservoirs. The effective accumulation space of a reservoir ranges from 33% to 62%, with an average of 41.8%. The effective reservoir space basically swings up and down at the oil saturation value of the reservoir formation, in which some rocks can form reservoirs, but the oil saturation is generally low, so the oil content of these kinds of reservoirs can hardly reach the enrichment degree. In order to reach the oil saturation value of the reservoir, the pore throat radius of oil breakthrough ranges from 0.075 to 0.153 μm, with an average of 0.11 μm, which is slightly higher than the lower limit value of the pore throat radius of the reservoir formation. The pore throat radius that this kind of reservoir needs to break through in order to enrich oil ranges from 0.026 to 0.101 μm, with an average of 0.056 μm, which is obviously small.

Class III reservoir is a noneffective tight reservoir. The effective accumulation space of the reservoir ranges from 2% to 34%, with an average of 10.1%. When the reservoir reaches the lower limit of oil saturation, the pore throat radius of oil breakthrough ranges from 0.008 to 0.079 μm, with an average of 0.031 μm, far less than the lower limit of pore throat radius of the reservoir formation. Under geological conditions, the possible oil saturation of this kind of reservoir is basically less than 20%, which is far less than the lower limit of reservoir-forming saturation. Therefore, Class III reservoirs are ineffective reservoirs for oil accumulation.

To sum up, Class I and II1 reservoirs are effective reservoirs for oil filling and accumulation in tight sandstone reservoirs, which constitute the most important oil-bearing interval of tight sandstone oil in member 7 of the Yancheng Formation, and are the most realistic part for oil exploration and development in tight sandstone reservoirs. However, a

Class III reservoir is basically oil-free, while a Class II2 reservoir is a poor tight reservoir, which is a noneffective oil accumulation reservoir of tight sandstone reservoir.

4. Conclusion

The Ordos Basin is one of the important oil-bearing basins in China, with abundant tight sandstone oil resources, wide distribution, and large thickness. It is the most realistic field of unconventional oil and gas exploration in China, and it is also an important oil and gas replacement resource at present. In this paper, taking the tight sandstone reservoir of Member 7 of the Yancheng Formation in Ordos Basin as the research object, after sorting out the previous research results, the geological characteristics of this area are introduced, the physical simulation experiment of oil filling is carried out, the relationship between filling pressure and the lower limit of filling pore throat is studied, the effective accumulation space of the tight sandstone reservoir is analyzed, the oil filling mechanism of the tight sandstone reservoir is defined, and the effectiveness and reservoir-forming effect of oil filling in different types of reservoirs are discussed, which provides theoretical data support for the next exploration and exploitation of tight sandstone reservoir. The main research results are:

(1) The rock types of tight sandstone reservoirs in the 7th member of the Yancheng Formation are mainly lithic feldspathic sandstone and feldspathic lithic sandstone. The reservoirs have experienced strong compaction and carbonate cementation, and the late iron-bearing carbonate cementation has further strengthened the degree of reservoir densification. At the time of large-scale oil and gas filling, the reservoirs have been densified. Through the simulation experiment of oil filling with natural cores with different physical properties, the relationship model between filling pressure and effective accumulation space of different types of tight sandstone reservoirs in member 7 of Yancheng Formation is established. With the change in filling pressure, the change trend and range of effective accumulation space of different types of tight sandstone reservoirs are obviously different.

(2) According to the relationship model between filling pressure and the lower limit of effective filling pore throat, combined with the evolution results of source and reservoir pressure in the study area, it is determined that the lower limit of effective filling pore throat radius of a tight sandstone reservoir in Member 7 of the Yancheng Formation in the study area is about 0.1 μm·m. On this basis, the effectiveness of oil filling in different types of tight sandstone reservoirs in the 7th member of the Yancheng Formation is clarified: Class I and II1 reservoirs are effective reservoirs for oil filling in tight sandstone reservoirs, which constitute the most important oil-bearing section of tight sandstone reservoirs in the 7th member of the Yancheng Formation and are the most realistic part of oil exploration and development in tight sandstone reservoirs. However, the II2 reservoir is a poor tight reservoir, and the III reservoir is basically oil-free, both of which are noneffective reservoirs filled with oil in tight sandstone reservoirs.

Data Availability

The figures and tables used to support the findings of this study are included in the article.

Conflicts of Interest

The authors declare that they have no conflicts of interest.

Acknowledgments

The authors would like to show sincere thanks to those techniques who have contributed to this research.

References

[1] B. Bin, Z. Rukai, W. Songtao et al., "Multi-scale method of Nano (Micro)-CT study on microscopic pore structure of tight sandstone of Yancheng Formation, Ordos Basin," *Petroleum Exploration and Development*, vol. 40, no. 3, pp. 354–358, 2013.

[2] R. D. Thomas and D. C. Ward, "Effect of overburden pressure and water saturation on gas permeability of tight sandstone cores," *Journal of Petroleum Technology*, vol. 24, no. 02, pp. 120–124, 1972.

[3] Z. X. Jiang, Z. Li, F. Li et al., "Tight sandstone gas accumulation mechanism and development models," *Petroleum Science*, vol. 12, no. 4, pp. 587–605, 2015.

[4] H. Yin, J. Zhao, G. Tang, L. Zhao, X. Ma, and S. Wang, "Pressure and fluid effect on frequency-dependent elastic moduli in fully saturated tight sandstone," *Journal of Geophysical Research: Solid Earth*, vol. 122, no. 11, pp. 8925–8942, 2017.

[5] B. Shi, X. Chang, W. Yin, Y. Li, and L. Mao, "Quantitative evaluation model for tight sandstone reservoirs based on statistical methods-A case study of the Triassic Chang 8 tight sandstones, Zhenjing area, Ordos Basin, China," *Journal of Petroleum Science and Engineering*, vol. 173, pp. 601–616, 2019.

[6] T. Guo, S. Tang, S. Liu et al., "Physical simulation of hydraulic fracturing of large-sized tight sandstone outcrops," *SPE Journal*, vol. 26, no. 01, pp. 372–393, 2021.

[7] A. Reinicke, E. Rybacki, S. Stanchits, E. Huenges, and G. Dresen, "Hydraulic fracturing stimulation techniques and formation damage mechanisms—implications from laboratory testing of tight sandstone–proppant systems," *Geochemistry*, vol. 70, pp. 107–117, 2010.

[8] C. Guo, J. Xu, M. Wei, and R. Jiang, "Experimental study and numerical simulation of hydraulic fracturing tight sandstone reservoirs," *Fuel*, vol. 159, pp. 334–344, 2015.

[9] J. Cai, C. Li, K. Song et al., "The influence of salinity and mineral components on spontaneous imbibition in tight sandstone," *Fuel*, vol. 269, Article ID 117087, 2020.

[10] S. Yin and Z. Wu, "Geomechanical simulation of low-order fracture of tight sandstone," *Marine and Petroleum Geology*, vol. 117, Article ID 104359, 2020.

Hindawi
Journal of Chemistry
Volume 2023, Article ID 9864308, 1 page
https://doi.org/10.1155/2023/9864308

Retraction

Retracted: Geochemical Characteristics of Crude Oil in Member 7 of Yanchang Formation in Yanchang Oilfield

Journal of Chemistry

Received 15 August 2023; Accepted 15 August 2023; Published 16 August 2023

This article has been retracted by Hindawi following an investigation undertaken by the publisher [1]. This investigation has uncovered evidence of one or more of the following indicators of systematic manipulation of the publication process:

(1) Discrepancies in scope

(2) Discrepancies in the description of the research reported

(3) Discrepancies between the availability of data and the research described

(4) Inappropriate citations

(5) Incoherent, meaningless and/or irrelevant content included in the article

(6) Peer-review manipulation

The presence of these indicators undermines our confidence in the integrity of the article's content and we cannot, therefore, vouch for its reliability. Please note that this notice is intended solely to alert readers that the content of this article is unreliable. We have not investigated whether authors were aware of or involved in the systematic manipulation of the publication process.

Wiley and Hindawi regrets that the usual quality checks did not identify these issues before publication and have since put additional measures in place to safeguard research integrity.

We wish to credit our own Research Integrity and Research Publishing teams and anonymous and named external researchers and research integrity experts for contributing to this investigation.

The corresponding author, as the representative of all authors, has been given the opportunity to register their agreement or disagreement to this retraction. We have kept a record of any response received.

References

[1] W. Li, Z. Gao, Y. Wang, J. Pu, H. Cheng, and F. Theon, "Geochemical Characteristics of Crude Oil in Member 7 of Yanchang Formation in Yanchang Oilfield," *Journal of Chemistry*, vol. 2022, Article ID 2797655, 7 pages, 2022.

Hindawi
Journal of Chemistry
Volume 2022, Article ID 2797655, 7 pages
https://doi.org/10.1155/2022/2797655

Research Article

Geochemical Characteristics of Crude Oil in Member 7 of Yanchang Formation in Yanchang Oilfield

Wenming Li,[1] Zhendong Gao,[1] Yongdong Wang,[1] Jingyang Pu,[2] Hanlie Cheng,[3] and Fahim Theon [4]

[1]*Yanchang Oilfield Co., Ltd., Yan'an 716000, Shaanxi, China*
[2]*School of Petroleum Engineering, China University of Petroleum (East China), Qingdao 266580, Shandong, China*
[3]*School of Energy Resource, China University of Geosciences (Beijing), Beijing 434000, China*
[4]*The King's School, BP 1560, Bujumbura, Burundi*

Correspondence should be addressed to Fahim Theon; fahimtheon@ksu.edu.bi

Received 19 August 2022; Accepted 23 September 2022; Published 4 October 2022

Academic Editor: Rabia Rehman

Oil is an important primary energy for national production and life and national defense, and China is the key to rapid development. It is of great strategic significance to ensure the safe and efficient production of the oil industry. Yanchang Oilfield is located in the main position of oil and gas accumulation in Ordos Basin, China, and the seventh member of the Yanchang Formation is the area with the richest crude oil output at present. Studying the geochemical characteristics of its crude oil exploitation is of great engineering significance for the exploration of oil and gas content in similar terrain and the continuous improvement of oil extraction and refining technology. On the other hand, it also provides first-hand data and important technical references for the exploration and exploitation of oil and gas resources in other areas of the Ordos Basin. Firstly, this paper points out the important strategic significance of the petroleum industry for China's development, and briefly describes the basic situation of Yanchang Oilfield and the basic characteristics of crude oil. The power and diversion system of the Yanchang Formation in Yanchang Oilfield are studied, and the main factors of formation and flow of deep reservoirs in the Yanchang Formation are explored, as well as the regional geological survey of the Yanchang Formation No. 7 in Yanchang Oilfield. The characteristics of crude oil and its maturity evaluation system are emphatically discussed, and the changes in crude oil characteristics under the action of microorganisms are comparatively studied. In this paper, Yanchang Oilfield, the main reservoir area of the Ordos Basin, is taken as the research object, and the formation mechanism of the oil reservoir and the geochemical characteristics of crude oil in the 7th member of the Yanchang Formation are deeply explored, so as to provide a preliminary theoretical study for the research of crude oil exploitation in reservoirs and other oilfields in the Ordos Basin.

1. Preface

Oil, known as "industrial blood" and "black gold," is one of the most critical primary energy sources in the world. Although the concept of environmental protection is deeply rooted in people's hearts, with the increasing demand for energy from human development, the oil output will remain stable and rise in the future [1–3]. According to the information disclosure of British Petroleum, BP, the annual growth rate of global oil and gas in the recent ten years is about 8.17%. Oil has important strategic significance in the world, so the development of the oil industry is not only influenced by resources, market, technical level, and other factors but also interfered with by international political situation [4, 5].

After more than one hundred years of development, the petroleum system has formed a perfect industrial system and solutions to various engineering and technical problems and has spawned a series of supporting chemical and electric power industries and specialized talent training schools

[6, 7]. With the continuous progress of technology, unconventional oil and gas exploitation such as offshore oil and shale gas has also entered a new historical stage. China is rich in oil and gas resources, with a vast territory and abundant resources. There are more than 500 sedimentary basins including Bohai Bay Basin, Sichuan Basin, and Ordos Basin, which have formed a unique oil and gas distribution area [8–10]. Since the founding of the People's Republic of China, the revolutionary ancestors have worked hard for more than half a century. China has built a complete and independent oil industry system, fundamentally removed the hat of a poor oil country, and ensured national oil security [11, 12].

Yanchang Oilfield is located in Ordos Basin (Qilicun Township, Yanchang County, Shaanxi Province)-the eastern slope of northern Shaanxi. It has been the first well in China since 1907. The basement of the Ordos Basin is composed of Archean and Proterozoic metamorphic rocks, while the sedimentary cover is composed of middle-upper Proterozoic and lower Paleozoic marine carbonates [13–15]. In Cenozoic, Ordos Basin began to subside again (thickness about 50~100 m). Tight oil content in Ordos Basin ranks first in China, and it is predicted that its total amount is about $35\sim40\times10^8$ tons, while Yanchang Oilfield is located in the central and southern part of the basin, and its tight oil is mainly distributed in the western and southern exploration areas. Chang 6, Chang 7, Chang 8, and Chang 9 are the main development strata in tight oil, with an estimated total amount of about 3.7×10^8 tons [16–18]. Among them, the Chang-8 member lake basin is small and mostly swamped, and the lake generally presents a shallow water environment, with relatively flat terrain and a dry climate [19]. The sedimentary type of the lake is still mainly shallow lake delta, and the semideep area and deeper area are limited. The sixth member is mainly distributed in 50~70 m, and it is mainly the delta front deposit [20, 21]. The 7th member is mainly distributed in the range of 10~40 m, mainly oil shale and turbidite, and its auxiliary reservoir is a gravity flow turbidite fan, with a sand thickness of 5~25 m [22].

Oil is a viscous, colored, and odorous combustible in the liquid phase, but it is mainly composed of two elements carbon (C, content of about 83%~87%) and hydrogen (H, content of about 10%~14%), and some trace elements such as oxygen, nitrogen, and sulfur exist in the form of mixtures [23–25]. Its density varies greatly with temperature, and it is stipulated in China that its density is the standard density at 20°C [26]. When the temperature changes at 5°C, its variation curve can be linear locally, which can be described as $\rho 20 = \rho t + \gamma(t - 20^\circ\text{C})$, where $\rho 20$ is the density at 20°C (g/ml) and γ is the average temperature coefficient (g/ml) and the petrochemical structure is different, and its density also changes greatly [27]. For example, the density of aromatic hydrocarbon is much higher than that of alkane under the same number of carbon atoms, and the density is also affected by different producing areas (raw materials) [28–30]. The petroleum density of major producing areas in China is shown in Table 1.

The geochemical characteristics of crude oil are the direct reflection of reservoir address information. By studying the characteristics of crude oil in the 7th member of the Yanchang Formation in Yanchang Oilfield, the accuracy of underground rock structure research can be effectively proved [31–33]. At the same time, combined with reservoir description, the target oil production area can be accurately screened, providing reliable research data for the exploration and exploitation of tight oil and other oil and gas resources in the Ordos Basin, promoting the development of geological exploration and oil exploitation technology in China and helping the iterative updating of national oil and gas technology.

Table 1: Oil density of different producing areas in China.

Serial number	Place of production	Density (g/ml)	Type
One	Xinjiang Wuerhe	0.96	Heavy quality
2	Gaosheng of Liaohe River	0.96	Heavy quality
Three	Dagang Yangsanmu	0.94	Heavy quality
Four	Shengli Gudao	0.94	Heavy quality
Five	Liao	0.88	Mesoplasm
Six	Win	0.88	Mesoplasm
Seven	Grand Celebration	0.86	Light
Eight	Changqing	0.84	Light

2. Materials and Methods

2.1. Power and Diversion System of Extension Group. The hydrocarbon-generating capacity of source rocks is not only the material basis for the formation of oil and gas but also an important index reflecting the formation of organic matter content. Oil shale and mudstone are the main source rocks in the Ordos basin, and the current evolution degree is the peak stage of oil production. Influenced by many factors, such as crustal movement and groundwater dynamics, the stratum is in different states of deposition and compaction, and the deposition is unidirectional, so the pressure distribution of underground rock structure is unknown and complicated. According to the knowledge, the excess pressure in the Ordos Basin is in a "NW-SE" trend as a whole, with a pattern of "uplift-depression interaction" in the plane distribution. The main components of the western and southern rock formations are mudstone and oil shale, so the overall process pressure is also high. The parts of the Yanchang Formation with high excess pressure are all located on the slope where the source rocks are well developed. This geographical structure provides a prerequisite for the formation and multidirectional migration of oil and gas in the reservoir. The oil and gas in the reservoir are gradually transferred and accumulated into oil and gas reservoirs in favorable areas driven by the process pressure. Among them, the thick mudstone distribution in the central and western Ordos Basin is the main factor leading to the sudden change of pressure structure. In the vertical distribution, there is only an abnormal high-pressure distribution between Chang 7 and Chang 9 members. Chang 7~Chang 8 also have some abnormal high pressure in the north-south direction, so it is also a favorable area for oil and gas formation. The residual pressure of rock formation is the active power source for the accumulation and movement of oil and gas in the reservoir, and it is of great significance to explore its dynamic characteristics for the exploration of oil and gas resources.

According to the residual power of the underground reservoir, the oil and gas accumulation area is not the location of oil and gas generation but is formed by oil and gas generation and multiple movements to favorable positions. Therefore, to study the characteristics of oil and gas itself, it is necessary to consider the path of its reservoir underground diversion system, which is not only related to the formation pores of the reservoir underground sedimentary environment but also directly related to physical and chemical reactions such as dissolution and cementation. In the early stage of Ordos Basin formation, on the basis of the recovery of the permeability characteristics of the Yanchang Formation, the late superimposed action affected the formation of the present sand body distribution. Especially after the oil and gas movement, the existing reservoir gap will be enlarged, and residual substances will be left. With the accumulation and increase of substances, a solid structure with larger particles will be formed, and then the reservoir diversion system will be affected.

2.2. Main Factors of Deep Reservoir in Yanchang Formation. The formation of oil and gas reservoirs is influenced by many factors, among which the excess pressure of rock strata and strata movement are the most significant. The main function of the excess pressure of rock stratum is to form density space between reservoir-cap medium and surrounding rock wall, so as to seal oil and gas and change it into the present oil and gas reservoir through long-term underground pressure. However, the excess pressure of the rock stratum is one of the main factors for the formation of oil and gas reservoirs. According to the statistical law, we can compare and analyze the geological environment of oil and gas-rich areas, find their common characteristics and analyze their key factors, and finally get the distribution of oil and gas reservoirs in geological relations. On the one hand, by analyzing the proven areas rich in oil and gas, it is clear that the areas with higher excess pressure are richer in oil and gas reservoirs; On the other hand, oil and gas enrichment will be formed at the corresponding low-pressure funnel of two adjacent oil and gas-rich reservoir areas in areas with high excess pressure. It can be seen from the above analysis that the residual pressure has a certain influence on the formation and content of oil and gas reservoirs.

Paleotectonic factors are also one of the key factors for the formation and enrichment of oil and gas, and its structural high point value is the key representation that directly affects the degree of oil and gas enrichment. Wuchangpu block of Yanchang Oilfield is a typical case of a paleotectonic-controlled reservoir, and its high-productivity well (Well Wu 45#) belongs to the paleotectonic high point value in the Early Cretaceous. At the same time, well Wu 9#, a high-yield well located in the same location as well Wu 45#, is found to have normal excess pressure, so it can be concluded that the excess pressure is not the only factor for the formation of oil and gas reservoirs, nor is it the main control factor here. Paleostructure plays a key role in oil and gas migration from the aspect of geographical profile and can ensure oil and gas communication horizontally.

The above-mentioned two major factors of reservoir formation have been explained, and there is a third type of reservoir-"excess pressure-paleostructure" double-acting type in the proven reservoirs, which is jointly acted by the two factors. Its characteristics are as follows: (1) excess pressure, as the power source of oil and gas movement, drives oil and gas to flow in the reservoir; (2) the flow direction is the structural high point of paleostructure rather than the pressure low point of "excess pressure reservoir"; (3) oil and gas flow to the closed circle with the highest structural value of paleotectonic point to form oil and gas reservoirs. Songshan oil area and Danba 446 well area in Yanchang oilfield belong to this kind of oil reservoir, but due to the double factors, there is some oil-water mixing in this oil area, which brings difficulties to crude oil exploitation.

2.3. Geological Survey of Yanchang Group 7 Area in Yanchang Oilfield. Ordos Basin, where Yanchang Oilfield is located, belongs to the central part of northern China, and its status is described as E106 20′~E110 30′, N34 00′~N41 30′, with a large administrative span (Shaanxi, Gansu, Ningxia, and Jinmeng). Structurally, it belongs to a large depression area in North China, and the present Ordos Basin is a residual basin after multistage reconstruction. Based on rock density and magnetism, it can be divided into six structural units, which are as follows: (1) Northern Shaanxi Slope; (2) Tianhuan depression; (3) West Shanxi fold belt; (4) thrust belt in the western margin; (5) Yimeng uplift; (6) Weibei Uplift, Yanchang Oilfield studied in this paper is located in the northern Shaanxi slope structural belt, which belongs to the main body of oil and gas accumulation in the basin. Figure 1 shows the distribution of the Ordos Basin and its neighboring Mesozoic and Cenozoic basins. The development of the Yanchang Formation has gone through five stages, among which the first stage is the oil layer (thickness 250~350 m) corresponding to Chang 10 at the bottom. As the initial stage of the lake basin, it is mainly composed of coarse-grained rocks such as feldspathic sandstone, which is flesh-red in color and mixed with mudstone layers. The second stage corresponds to the oil layers of Chang 9 (80~110 m) and Chang 8 (75~90 m), with large-scale delta deposition; The third stage is the main stage of development, including 7 segments, 6 segments, 4 segments, and 5 segments, the thickness of which is about 110~130 m at the sixth segment, and about 80~90 m after entering the fourth segment and 5 segments. The fourth stage consists of the Chang 2 oil layer (90~110) and the Chang 3 oil layer (120~1500). The lido of the Chang 3 oil layer is relatively small, while the Chang 2 oil layer is coarser. The fifth stage is corresponding to the oil layer (0~240 m) of Chang-1 member, which is affected by extensive weathering, and the lakes gradually disappear to form swamps, and carbonaceous mudstone gradually develops.

3. Results

3.1. Composition and Maturity Evaluation of Crude Oil. Figure 2 shows the composition of crude oil. Crude oil is a mixture of organic matter, including the corresponding normal alkanes, which were acyclic sort defensibly diene

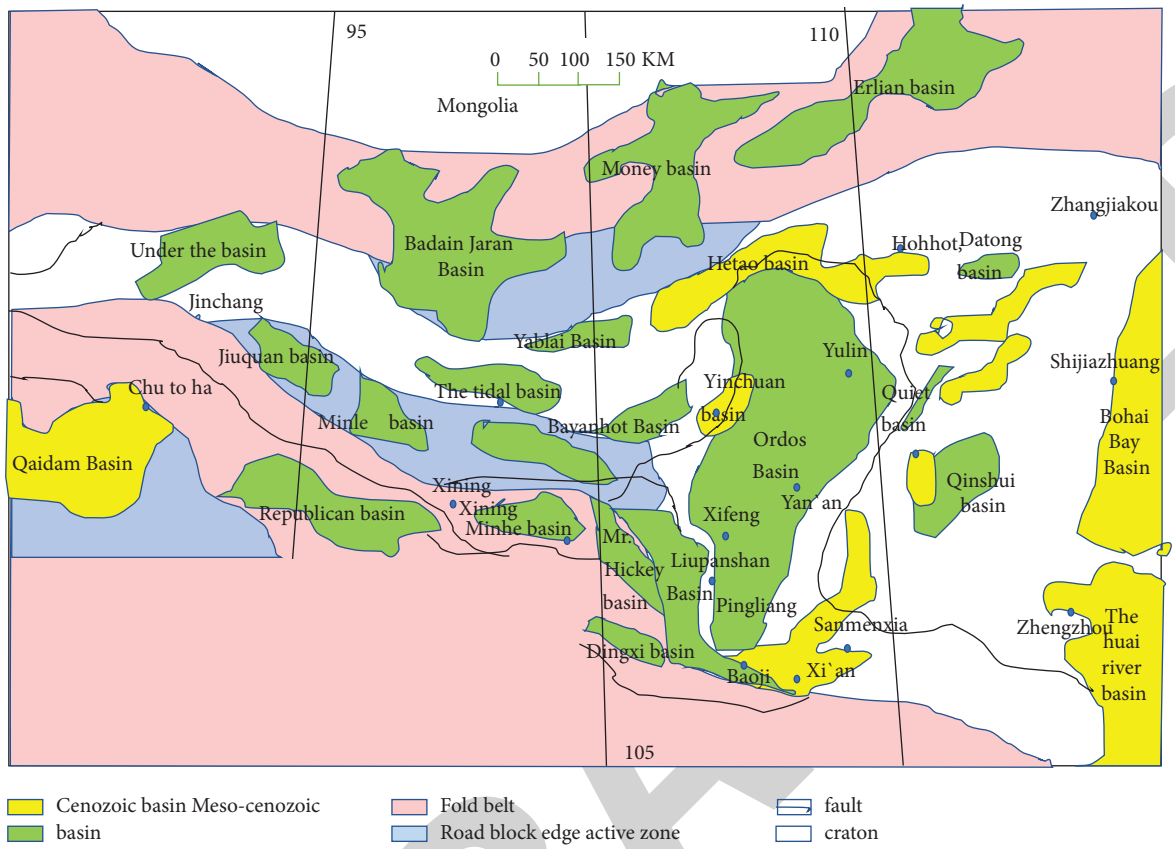

Figure 1: Distribution map of Ordos basin and its neighboring Mesozoic-Cenozoic basins.

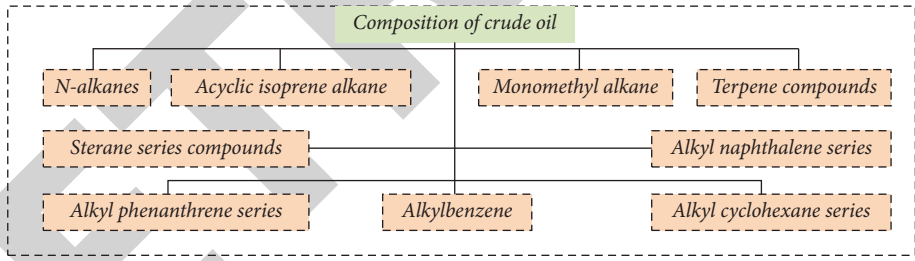

Figure 2: Composition of crude oil.

alkanes, single methyl alkanes, sterane, and terpene series compounds, alkyl benzene, alkyl naphthalene series, alkyl phenanthrene series and so on the many kinds of organic matter, according to the different proportion of different organic matter composition, crude oil also presents various characteristics. The hydrocarbons with the highest content in crude oil are n-alkanes, which are converted from lipid compounds of animals and plants. Lower organisms such as algae and phytoplankton constitute low-carbon n-alkanes, while higher organisms constitute high-carbon n-alkanes. Acyclic isoprenoid alkanes are the core indicators to distinguish different crude oils. Pristane and phytane, which are derived from chlorophyll (where photosynthesis occurs), are used to distinguish the salinity of oxidation and Pr/Ph REDOX environments in sedimentary environments. Monomethylalkanes are the main discriminant basis for the origin of crude oil. Tricyclic terpenes (mainly C19–C30) are widely distributed in crude oil, which are probably derived from microorganisms and algae. Terpenes are mainly used to determine the formation age of crude oil. Steranes (long see C27~C29) are three-carbon steranes, which generally exist in crude oil and hydrocarbon source rocks. It is generally believed that C27 comes from lower aquatic organisms and C29 from higher plants. The crude oil with a different composition also shows different characteristics in the actual inspection. According to these characteristics, the crude oil composition can be better distinguished, so as to provide data basis for crude oil refining.

The maturity of crude oil is a geochemical characteristic parameter reflecting the evolution of the organic chemical composition of crude oil and source rocks. As the maturity of crude oil is difficult to be measured directly by instruments, the maturity of samples to be measured is often characterized by the content of organic components.

Table 2: C29 mature marks of sterane crude oil.

Alkanes C29 class	Immature crude oil	Mature crude oil
C29$\alpha\alpha\alpha$	<0.3	>0.3
C29$\alpha\alpha\beta$	<0.32	>0.32

Table 3: Terpene crude oil maturity mark.

Specific value	Oil generation stage	Balance point	Overripe-over-ripe
Epihopane C31-$\alpha\beta$22S/(C31-$\alpha\beta$22S + C31-$\alpha\beta$22R)	0.5~0.54	0.6	0.57~0.63
β hopane/β α monane	1.0	4.0~7.0	>7.0

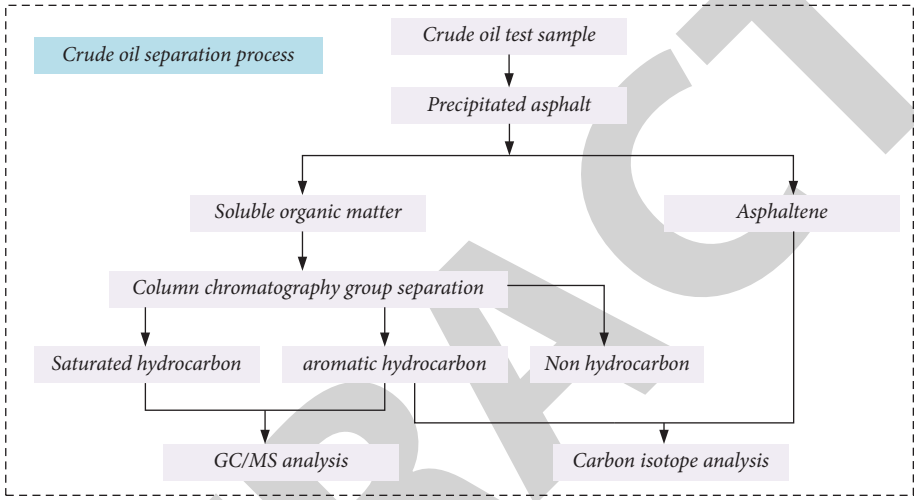

Figure 3: Crude oil separation process.

Generally speaking, with the increase of the maturity of crude oil, the contents of steranes and terpenes will decrease. Firstly, the steranes are C29$\alpha\alpha\alpha$ α and C29$\alpha\alpha\beta$. In immature crude oil, C29$\alpha\alpha\alpha$-20R mainly exists in the form of C29α α-20R. With the increase of crude oil maturity, C29α α-20R will change to C29α α-20s. It is generally believed that the ratio of C29α α to C29$\alpha\alpha\beta$ can be used as an index of crude oil maturity. According to China's "Ninth Five-Year Plan" research results, the definition of crude oil maturity mark can be shown in Table 2.

The content of rearranged steranes is positively correlated with the maturity of crude oil, so the ratio of rearranged steranes/regular steranes can also be used as an index of crude oil maturity. Academics think that the ratio of rearranged steranes to regular steranes is 0.25 as a watershed. If it is greater than 0.25, it is considered mature, otherwise, it is immature. However, its ratio will be affected by the characteristics of rock strata, so it can only be used as an auxiliary judgment condition rather than an independent judgment condition.

Terpene TS and Terpene TM are isomers, and TS has better thermal stability in chemical properties. It is generally believed that TM will gradually transform into TS with the increase of maturity, and the ratio of the two will change correspondingly in this process, so TS/TM is also the core index of crude oil maturity. Generally speaking, TS/TM > 1 is considered as mature crude oil, and vice versa is defined as immature crude oil. Moreover, TS and TM have a great catalytic reaction on clay and are affected by microbial action, so the measurement of carbonate crude oil is not accurate enough. Epihopane C31-$\alpha\beta$22R has the same characteristics as sterane, and will gradually change to C31-$\alpha\beta$22S with the increase of maturity. Its parameters as an indicator of crude oil maturity are shown in Table 3. Similarly, α β hopane β α moane has similar characteristics. β β hopane inherited from organisms is extremely unstable, and it will gradually transform into α β hopane β α moane in the process of maturity, and its ratio indicates maturity, which is also listed in Table 3.

In particular, norhopane C31-$\alpha\beta$22R is different from C29 sterane, and its ratio is not affected by microbial explanation, so it has a quite stable effect.

3.2. Characteristic Changes under the Action of Microorganisms. There are a lot of organic mixtures in crude oil, and aerobic microorganisms are the main reason for degrading crude oil, while anaerobic microorganisms can be neglected because of their slow action. Microbial degradation mainly consumes n-alkanes, and the structures of alkylbenzene and dialkylbenzene are easily destroyed by bacteria, while C19~C45 tricyclic terpenes have a strong

antidegradation ability and are not easily decomposed. Some components used for maturity evaluation are also distinguished according to antimicrobial explanation, such as terpene TS has better degradation resistance than terpene TM, and C29$\alpha\alpha\alpha$-20S has a more stable performance than C29α α-20r. Microbial degradation of crude oil is an extremely complex multistage process, and the order of degraded compounds is also affected by the types and quantities of microorganisms. Although both industrial and academic circles have carried out relevant research on it, there is still no systematic and comprehensive description.

Figure 3 shows the separation process of crude oil group changes before and after the microbial reaction. First, the crude oil test sample needs to be deposited in Petroleum Ether (PE) and filtered, and the asphalt adhered to the filter paper is cleaned with trichloromethane ($CHCL_3$), and its weight is measured. The filtrate was separated by Al_2O_3/silica gel column chromatography and then cleaned by PE, benzene (C_6H_6), and ether ($C_2H_5OC_2H_5$) to obtain saturated hydrocarbons, aromatic hydrocarbons, and nonhydrocarbons. The weight of different organic compounds was tested. Finally, the stable carbon isotope analysis and GC/MS analysis were completed. Finally, the change characteristics of crude oil before and after microbial action were determined.

4. Conclusion

In this paper, taking Yanchang Oilfield, the core area of Ordos Basin, as an example, taking Yanchang Chang 7 crude oil as the research object, the geochemical characteristics of crude oil are studied. In the beginning, it points out the importance of the petroleum industry to a national economy and national security, introduces the basic situation and characteristics of Yanchang Oilfield, focuses on the power and diversion system of Yanchang Oilfield, explores the main factors for the formation of oil and gas reservoirs in Yanchang Formation and the geological survey of Yanchang Formation, especially discusses the characteristics and maturity evaluation indexes of crude oil, and considers the changes of crude oil properties under the action of microorganisms.

With the shortage of primary energy in the world, it is the key point to improve oil recovery technology and oil and gas recovery quality. In this paper, taking the oil from the 7th member of the Yanchang Formation in Yanchang Oilfield as an example, by studying its formation mechanism and geochemical characteristics, the formation principle of oil and gas reservoirs and chemical properties of crude oil are explored, so as to provide basic theoretical research and first-hand engineering data for high-quality oil and gas exploitation and unconventional oil and gas resource exploration. In the next step, practical engineering research will be carried out in combination with other characteristics of crude oil, so as to accumulate experience for upgrading oil and gas exploration and development technology in China.

Data Availability

The figures and tables used to support the findings of this study are included in the article.

Conflicts of Interest

The authors declare that they have no conflicts of interest.

Acknowledgments

The authors would like to show sincere thanks to those techniques who have contributed to this research.

References

[1] H. D. Beggs and J. R. Robinson, "Estimating the viscosity of crude oil systems," *Journal of Petroleum Technology*, vol. 27, no. 9, pp. 1140-1141, 1975.

[2] M. Gisser and T. H. Goodwin, "Crude oil and the macroeconomy: tests of some popular notions: note," *Journal of Money, Credit, and Banking*, vol. 18, no. 1, pp. 95–103, 1986.

[3] R. Alquist and L. Kilian, "What do we learn from the price of crude oil futures?" *Journal of Applied Econometrics*, vol. 25, no. 4, pp. 539–573, 2010.

[4] A. Jobson, F. D. Cook, and D. W. S. Westlake, "Microbial utilization of crude oil," *Applied Microbiology*, vol. 23, no. 6, pp. 1082–1089, 1972.

[5] H. Cheng, D. Yang, C. Lu, Q. Qin, and D. Cadasse, "Intelligent oil production stratified water injection technology," *Wireless Communications and Mobile Computing*, vol. 2022 Article ID 39544467 pages, 2022.

[6] D. Langevin, S. Poteau, I. Hénaut, and J. F. Argillier, "Crude oil emulsion properties and their application to heavy oil transportation," *Oil and Gas Science and Technology*, vol. 59, no. 5, pp. 511–521, 2004.

[7] K. A. Kvenvolden and C. K. Cooper, "Natural seepage of crude oil into the marine environment," *Geo-Marine Letters*, vol. 23, no. 3-4, pp. 140–146, 2003.

[8] I. A. Wiehe and R. J. Kennedy, "The oil compatibility model and crude oil incompatibility," *Energy and Fuels*, vol. 14, no. 1, pp. 56–59, 2000.

[9] Z. K. Hou, H. L. Cheng, S. W. Sun, J. Chen, D. Q. Qi, and Z. B. Liu, "Crack propagation and hydraulic fracturing in different lithologies," *Applied Geophysics*, vol. 16, no. 2, pp. 243–251, 2019.

[10] S. H. Kang, S. M. Kang, and S. M. Yoon, "Forecasting volatility of crude oil markets," *Energy Economics*, vol. 31, no. 1, pp. 119–125, 2009.

[11] K. Sugiura, M. Ishihara, T. Shimauchi, and S. Harayama, "Physicochemical properties and biodegradability of crude oil," *Environmental Science & Technology*, vol. 31, no. 1, pp. 45–51, 1996.

[12] H. I. Essaid, B. A. Bekins, W. N. Herkelrath, and G. N. Delin, "Crude oil at the bemidji site: 25 years of monitoring, modeling, and understanding," *Ground Water*, vol. 49, no. 5, pp. 706–726, 2011.

[13] J. Han, H. Cheng, Y. Shi, L. Wang, Y. Song, and W. Zhnag, "Connectivity analysis and application of fracture cave carbonate reservoir in Tazhong," *Science Technology and Engineering*, vol. 16, no. 5, pp. 147–152, 2016.

[14] P. J. Grantham, "The occurrence of unusual C27 and C29 sterane predominances in two types of oman crude oil," *Organic Geochemistry*, vol. 9, no. 1, pp. 1–10, 1986.

[15] S. Ashoori, M. Sharifi, M. Masoumi, and M. Mohammad Salehi, "The relationship between SARA fractions and crude oil stability," *Egyptian Journal of Petroleum*, vol. 26, no. 1, pp. 209–213, 2017.

Hindawi
Journal of Chemistry
Volume 2023, Article ID 9761347, 1 page
https://doi.org/10.1155/2023/9761347

Retraction

Retracted: Exploration of Erdaohe Silver Polymetallic Deposit in Inner Mongolia based on Induced Polarization Method

Journal of Chemistry

Received 15 August 2023; Accepted 15 August 2023; Published 16 August 2023

This article has been retracted by Hindawi following an investigation undertaken by the publisher [1]. This investigation has uncovered evidence of one or more of the following indicators of systematic manipulation of the publication process:

(1) Discrepancies in scope
(2) Discrepancies in the description of the research reported
(3) Discrepancies between the availability of data and the research described
(4) Inappropriate citations
(5) Incoherent, meaningless and/or irrelevant content included in the article
(6) Peer-review manipulation

The presence of these indicators undermines our confidence in the integrity of the article's content and we cannot, therefore, vouch for its reliability. Please note that this notice is intended solely to alert readers that the content of this article is unreliable. We have not investigated whether authors were aware of or involved in the systematic manipulation of the publication process.

Wiley and Hindawi regrets that the usual quality checks did not identify these issues before publication and have since put additional measures in place to safeguard research integrity.

We wish to credit our own Research Integrity and Research Publishing teams and anonymous and named external researchers and research integrity experts for contributing to this investigation.

The corresponding author, as the representative of all authors, has been given the opportunity to register their agreement or disagreement to this retraction. We have kept a record of any response received.

References

[1] B. Li, Z. Shi, Z. Yang, L. Xu, H. Cheng, and D. Sturdivant, "Exploration of Erdaohe Silver Polymetallic Deposit in Inner Mongolia based on Induced Polarization Method," *Journal of Chemistry*, vol. 2022, Article ID 7053491, 9 pages, 2022.

Hindawi
Journal of Chemistry
Volume 2022, Article ID 7053491, 9 pages
https://doi.org/10.1155/2022/7053491

Research Article

Exploration of Erdaohe Silver Polymetallic Deposit in Inner Mongolia based on Induced Polarization Method

Baoyou Li,[1] Zhiqing Shi,[1] Zhiguang Yang,[2] Lan Xu,[3] Hanlie Cheng,[4] and David Sturdivant[5]

[1]*No. 3 Institute of Geology and Mineral Resources Exploration of Inner Mongolia, Inner Mongolia, Hohhot 010011, China*
[2]*Inner Mongolia Geological Exploration Co. Ltd, Inner Mongolia, Hohhot 010010, China*
[3]*No. 115 Institute of Geology Exploration of Inner Mongolia, Inner Mongolia, Ulan Hot 137400, China*
[4]*School of Energy Resource, China University of Geosciences (Beijing), Beijing 434000, China*
[5]*The King's School, BP 1560, Bujumbura, Burundi*

Correspondence should be addressed to David Sturdivant; davidsturdivant@ksu.edu.bi

Received 22 August 2022; Accepted 19 September 2022; Published 3 October 2022

Academic Editor: Rabia Rehman

The exploration of Erdaohe Cu-Ag-Pb-Zn deposit in Zhalantun City, Inner Mongolia has entered the stage of blind exploration. It is a difficult problem at this stage whether common geophysical methods can find anomalies caused by 300~1000 m or deeper Pb-Zn deposits in this area. Whether the problem is solved or not has a strong practical significance for the current and future prospecting work in this area. According to the theory of induced polarization sounding in time domain, it is considered in this paper that when the parameters such as high power, suitable device, and time delay are well coupled with the deep blind ore, it is possible to find anomalies caused by deep lead-zinc ore larger than 300 m. In order to prove the feasibility of the deep application of this method, the high-power induced polarization sounding experiment with different devices and different power supply cycles was carried out in Erdaohe copper-silver lead-zinc mine. The test results show that by adopting the measurement method of the encrypted equipotential device and selecting the appropriate polar distance, when the power supply period is 32 s, the time delay is 200 s and the sampling width is 200 s, a good deep lead-zinc mine anomaly can be found. The equipotential symmetrical quadrupole sounding MN/AB = 1/10 and the depth correction coefficient is 0.41 for inversion can accurately determine the anomaly location, which is worthy of popularization and application in this area. The ore bodies in this area are controlled by structures and distributed in lenticular layers along the fault footwall interlayer fracture zone. The ore bodies may change with the occurrence of the fracture surface. The characteristics of low resistivity, low slow, and high polarization of IP and single peak anomaly of IP sounding are important signs of lead-zinc prospecting in this area.

1. Introduction

With the increasing difficulty of prospecting and the progress of science and technology, geophysical instruments have been widely used in the exploration and evaluation of ore bodies. For the mining areas in the stage of presurvey and general survey, geophysical methods play a more prominent role. Induced polarization method (IP) has been applied in China for more than 50 years. It is a traditional and effective geophysical method. Based on different devices, this method can meet a variety of geological conditions and work purposes.

Erdaohe copper-silver-lead-zinc mine is located in the forest swamp area of Daxing' anling, with serious forest vegetation coverage, few outcrops of surface bedrock, and great difficulty in prospecting [1–5]. As an effective combination of exploration methods, induced polarization ladder device and symmetrical four-level sounding have been applied in this area, and good exploration results have been achieved [6–8]. Induced polarization method is an

electrical exploration method based on the difference of induced polarization effect of rock and ore, which aims at finding underground minerals or solving geological problems by observing and studying the distribution law of induced polarization effect of underground media. In recent years, the induced polarization method has played an important role in the exploration of metal ore and graphite ore, especially in the search for hidden ore and deep ore. The deeper buried lead-zinc ore body can be found by increasing power, changing equipment, and measuring parameters. Previous studies have held that improving signal-to-noise ratio, selecting the array with large detection depth, and under the condition that proper sampling parameters are well coupled with deep ore, high-power IP measurement can obtain better deep lead-zinc ore anomalies, which is the key of IP method to search for deep concealed ore [9–12]. On the basis of previous studies, this paper carried out high-power induced polarization experiments on the known ore bodies in Erdaohe copper-silver-lead-zinc mine, Inner Mongolia, with different devices, different power supply cycles, different time delays and different sampling widths, and summarized the application effect of this method, so as to provide reference for future deep prospecting research and metallogenic prognosis.

IP survey provides an important geophysical basis for the discovery of Erdaohe silver lead-zinc deposit. According to the time domain-induced polarization sounding theory, when the parameters such as high power, appropriate instruments, and time delay are well coupled with the deep blind ore, it is possible to find the anomalies caused by the deep lead-zinc ore body more than 300 m. In order to prove the feasibility of the deep application of this method, high-power induced polarization sounding experiments with different devices and power supply periods were carried out in Erdaohe copper-silver-lead-zinc mine, Inner Mongolia. The test results show that the measurement method of densified equipotential device can accurately determine the abnormal position, which is worthy of popularization and application in this area.

2. Geological Background and Geological Characteristics of Mining Area

The working area of this paper is located in the southwest of Zhalantun City, Inner Mongolia, the middle section of Daxinganling metallogenic belt and the south section of Delbe dry metallogenic belt, which is the intersection of the ancient Asian tectonic domain vein and the Pacific Rim tectonic domain. The northern Daxing' anling-Late Paleozoic accretionary orogenic belt is located between Hegenshan, Urn-Oroqen fault, and Delbe main fault. The southern accretion part of the continental margin of the Siberian ancient plate (Northeast Asia and craton) is the first-order tectonic unit, the Daxinganling-Zhonghua and the western part of the Yougeosyncline fold belt, and it is located in the third-order tectonic unit-Aershan, the southeast wing of anticlinorium, Wulanhaote and the west side of the syncline north [13, 14]. Aeromagnetic characteristics of Erdaohe mining area are mainly stable positive magnetic field, which is distributed in the magnetic field area, showing irregular northeast strip distribution, reflecting the magnetic characteristics of Indosinian fine-grained granite, Jurassic volcanic rocks, Ordovician sandstone, and slate distributed in the mining area.

The exposed stratum in the area is the Permian Linxi formation. The main lithology is argillaceous, silty, and siliceous slate. The argillaceous and silty slate are relatively broken and the siliceous slate is relatively complete. Affected by the later structure, the slate at the known mineralization outcrop is strongly broken, forming an obvious broken alteration zone. The broken alteration zone is generally ferritized, and there are alteration marks reflecting hydrothermal activities such as silicification and calcitization. Limonite and lead alum are developed on the surface of silicified vein, and a small amount of galena is occasionally seen in the fresh section.

42 copper, lead-zinc, and silver ore bodies have been discovered, including 28 exposed on the surface and 14 blind ore bodies. According to the content of lead, zinc, silver, and copper components, there are 8 lead ore bodies, 8 zinc ore bodies, 4 silver ore bodies, 1 copper ore body, 7 lead-zinc ore bodies, 2 lead-zinc silver copper ore bodies, 8 lead-zinc silver ore bodies, 1 zinc silver ore body, 2 silver copper ore bodies, and 1 lead silver ore body. The ore body is lenticular, veined, or layered.

3. Geophysical Characteristics of Mining Area

3.1. Magnetism. Geophysical exploration methods are based on the study of certain physical properties of rocks, which are often expressed as physical characteristic parameters such as gravity, magnetic parameters, electrical parameters, and seismic wave parameters. Based on the study of the physical properties of rock mass, many geophysical exploration methods have been derived, mainly including the following four types of exploration methods, namely, gravity exploration, magnetic exploration, electrical exploration, and seismic exploration.

The lead-zinc ore and skarn containing magnetite in this area have strong magnetism, while tuff, andesite, metamorphic sandstone, and granite porphyry have medium magnetism, while granite and lead-zinc ore have weak magnetism. See Table 1 for statistical results.

3.2. Electrical Properties. The instrument used in this electrical test is SCIP sample core IP tester, and the tests are all completed in the field. The cores and samples are cut into regular columns by cutting machine, and after 24 hours of soaking, the dimensions are measured by multifunctional vernier caliper, and the process is carried out in strict accordance with Technical Specification for Physical Property Investigation of Rock and Ore (DD 2006-03) 8.2.5.3 [15–17]. The core electrical test is carried out by the core taken from the ore-finding borehole ZK4701 in Erdaohe copper-silver-lead-zinc mine. See Table 2 for the test statistics of the electrical parameters of rock and ore [18–21].

Table 1: Measurement results of magnetic parameters of surface rock ore.

Rock character	Quantity (pieces)	Magnetic susceptibility κ ($4\pi\times10^{-6}$ SI)			The remanent magnetization Jr (10^{-3} A/m)		
		Average/mean value	Maximum	Minimum value	Average/mean value	Maximum	Minimum value
Tuff	32	200	670	10	Four hundred	830	230
Andesite	36	320	750	60	310	640	110
Skarn	32	800	2500	200	600	1500	400
Metamorphic sandstone	33	90	340	40	80	320	60
Granite porphyry	30	90	450	0	170	640	0
Granite	32	60	770	0	120	510	0
Lead-zinc ore	40	50	210	0	70	220	0
Pyritized lead-zinc ore	37	560	820	330	380	750	190

Table 2: Measurement results of electrical parameters of super rock ore.

Rock character	Quantity (pieces)	Polarizability η (%)			Resistivity ρ (ω m)		
		Minimum value	Maximum	Average/mean value	Minimum value	Maximum	Average/mean value
Tuff	36	1.5	3.1	1.8	976	2816	2775
Andesite	35	1.5	4.4	1.7	1322	8552	3622
Skarn	31	2.4	9.3	3.9	900	6718	2865
Metamorphic sandstone	30	1.7	4.8	1.8	491	4075	2263
Slate	33	1.5	4.2	2.6	552	4718	1665
Granite porphyry	32	0.9	3.2	1.1	535	4971	2475
Granite	40	0.8	3.9	1.8	1495	9182	3063
Lead-zinc ore	33	8.9	29.5	12.5	99	848	590
Pyrite tuff	34	4.2	24.1	10.2	736	2930	1036
Pyrite fine-grained diorite	34	10.5	34.1	15.2	748	2970	1074

According to the data in Table 2, the polarizability η values of granite, tuff, andesite, sandstone, and slate in the area are low, with an average value of 1.7%–2.6%, forming a normal field in the area, with a resistivity ρ value of 1,500 Ω m–3,600 Ω·m, which is characterized by relatively high resistivity. However, the polarizability η of lead-zinc ore and sulfide ore increases obviously, with the highest value of 34.1% and the highest average value of 15.2%. Corresponding to the characteristics of low resistance, lead-zinc, sulfide ores form obvious high polarization and low resistance anomalies, which is one of the important prospecting indicators in this area, while its surrounding rocks, such as granite and tuff, are characterized by low polarization and relatively high resistance, and the electrical differences between the ore and surrounding rocks are obvious [22]. Combined with the strong magnetic characteristics of lead-zinc ores and skarns containing magnetite in this area, it has obvious geophysical premise to search for sulfide deposits containing magnetite by high-precision magnetic method and IP area measurement in this area. However, pyritization rocks can form high polarization interference [23].

From 2009 to 2010, Inner Mongolia, No. 3 geological exploration Co., Ltd. carried out 1 : 10000 magnetic method and IP medium ladder short traverse survey, respectively, in Erdaohe copper polymetallic survey area, and circled a number of irregular sheets and band shaped electrical and magnetic anomalies [24–26]. When carrying out the integrated exploration project in 2014, we mainly carried out IP middle ladder profile survey, high-precision magnetic profile survey, IP sounding and audio frequency large IP sounding in No. 2 mining area. The electrical and magnetic anomalies are consistent with the stratigraphic trend, with regular shape and good coincidence. Most of the magnetic anomalies are related to the contact zones and structures, which basically reflect the overall lithology and structural pattern of the northeast and northwest directions in this area, mainly in the northeast direction, and show obvious regularity.

IP anomalies are distributed in the strata of the bare River formation of the Ordovician system and the OBO formation of the Manketou formation of the Jurassic system, and are distributed in a belt shape along the northeast direction, consistent with the direction of the main structural line [27]. The main part of the apparent charge rate anomaly is located in the low resistivity zone, showing the characteristics of low resistivity and high polarization. The main IP anomaly distributed in the Jurassic volcanic rocks is consistent with the geochemical anomaly, which is verified as a lead-zinc silver ore body by engineering [28].

4. Working Methods of Geophysical Prospecting in Mining Area

4.1. Methods and Equipment. The measurement results of rock and ore electrical parameters show that this area has the premise of induced polarization measurement. However, according to past experience, if induced polarization method wants to reach deeper exploration depth, it must have higher power, appropriate polar distance, and the best measurement parameters. In order to solve these problems and get better results in the measurement, this time, the experimental-induced polarization measurement was carried out centering on the borehole ZK4701 (see the ore depth $H = 468$). The instrument adopts WDFZ-10T high-power IP transmission system produced by Chongqing Pentium Instrument Factory, and the receiving system adopts WDJS-3 multichannel digital DC IP receiver.

4.2. Selection of Electrode Arrangement Direction. The working section is centered on the drilling hole ZK4701, which is basically vertical in structure, stratigraphic strike, and ore body strike. In order to further study the layout of polarizer, the direction of electrode arrangement is perpendicular to the direction of polarizer along the section, and the direction of electrode arrangement is as consistent as possible with the topographic contour. Therefore, the electrode arrangement direction is set to 26.

4.3. IP Ladder Measurement. According to the characteristics of ore bodies in the mining area, the width of ore bodies in this area is 30~350 m. In order to obtain a better step anomaly of induced IP with the increase of exploration depth, lMN polar distance, which is equivalent to the maximum width of deep ore body, is considered in this experiment. According to the symmetrical four-stage exploration with equal ratio, lAB/2 is at 1150 m and lMN is at 115 m, which can obtain good deep ore-induced anomalies. Comprehensive measurement of various factors shows that the measurement parameters of IP middle ladder section are lMN/2 = 100 m, lAB/2 = 1500 m, measuring point distance 20 m, power supply period 32 s, time delay 200 ms, and sampling width 200.

The ore body has obvious IP anomaly, which reflects the characteristics of high charging rate and low resistivity. The apparent charge rate is 100 ms~130 ms and the apparent resistivity is 600 m~1800 gm. IP anomaly is the main ore prospecting sign. The inversion section of audio magneto telluric sounding is in good agreement with the ore body and geological content (ore bearing structural fracture zone). The corresponding Kania resistivity on the ore body is of low resistance, with a value of 200 Ω·m~600 Ω·m. Audio magneto telluric sounding can be used to search for ore bearing structures as an indirect ore prospecting sign.

5. Data Processing and Results Analysis

5.1. Analysis of Polarizability and Resistivity of Different MN/2 Polar Distances. At borehole ZK4701, the field data of symmetrical four-level sounding were collected by induced polarization method, and the measured data were Vp (mV), I (mA), and η (%). By calculating the device coefficients k and ρ, lglAB/2 is used as the abscissa of unequal devices, the arithmetic average of the measured values of small lMN and large lMN is used as the mapping data of the polar distance change part, lAB/2 is used as the abscissa of equipotential devices, and the polarizability and resistivity are used as the ordinate of each device. The experimental results are shown in Figures 1 and 2.

It can be seen from Figure 1 that the induced polarization sounding anomalies obtained by different lMN/lAB have similar polarizability curves in the shallow part, while each polarizability curve in the deep part shows different morphological characteristics, although it has an attenuation trend. LAB/2 starts from 250, the peak characteristic of lMN/lAB ≈ 0.18 is more obvious than that of lMN/lAB ≈ 0.3, but both of them show the characteristics of sharp data jump and weak continuity. LMN/lAB = 0.10 not only has obvious peak anomaly and anomaly width, but also has good anomaly continuity, rich data information, and large amount of information. It can be seen from Figure 2 that lMN/lAB = 0.10 also has better high resistance abnormal reflection than the other two groups, with obvious abnormal peak and width, and smooth and continuous curve shape. The above situation shows that lMN/lAB = 0.10 has good polarizability and resistivity anomalies, and the obtained deep information is more reliable, which is more conducive to inferring deep geological bodies.

5.2. Analysis of Polarizability and Resistivity in Different Power Supply Cycles. It can be seen from the curve of lMN/lAB with a power cycle of 16 s as a constant ratio device that the depth attenuation is very obvious. During the measurement process, by increasing the power supply voltage and current, and decreasing or increasing lMN, the normal measurement values could not be continued or obtained, which indicates that the measurement depth may be limited when the power supply period is 16 s. Therefore, in this paper, two groups of data with longer power supply period of 32 s and 64 s are added by encrypting the equipotential device.

Figures 3 and 4 show that Lab/2 is less than 1000 m, and the curve shape characteristics of polarizability and resistivity are similar in different power supply cycles of the encrypted equal ratio device. The overall characteristics of the curve are single peak, high polarizability, high resistivity, obvious peak value, abnormal continuity, and wide multipoint width. The polarizability of the two groups with short power supply period has large and strong abnormal amplitude. When the power supply period is 16 s, the lAB/2 starts to exceed 950 m, and the polarization curve decays rapidly, and the measured value is less than 0.02%. There is no measured value after lAB/2 greater than 1100 m. The resistivity curve shows that the high resistivity peak in the shallow part is obviously abnormal, and the low resistivity anomaly in the deep part is not reflected. When the power supply period is 32 s, lAB/2 starts to exceed 950 m, and the

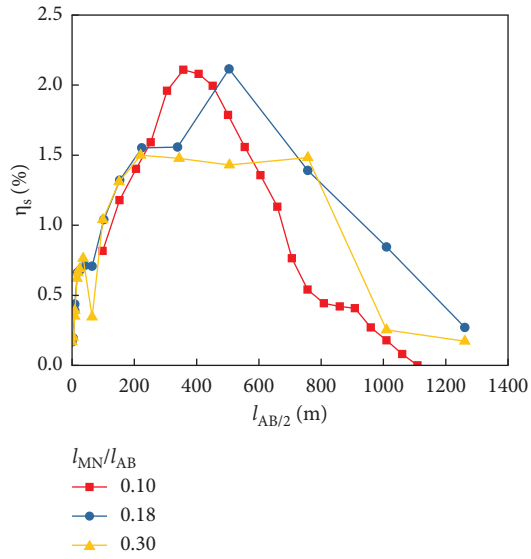

Figure 1: Polarization curves of different MN/2 polar distances.

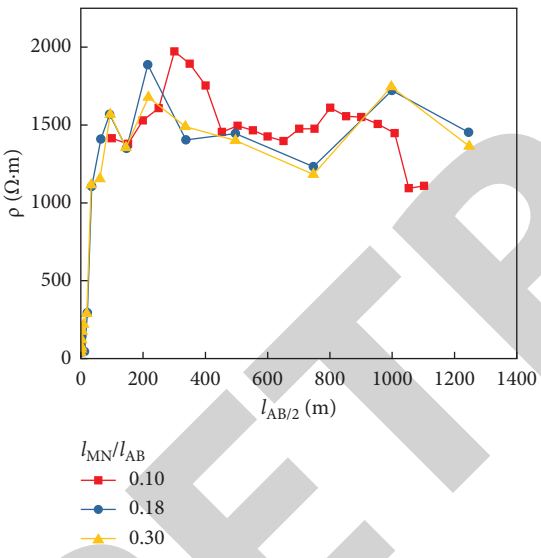

Figure 2: Resistivity curves of different MN/2 polar distances.

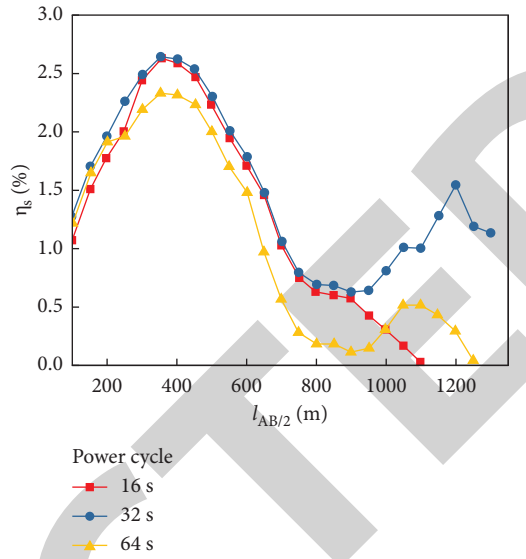

Figure 3: Polarization curves of different power supply cycles.

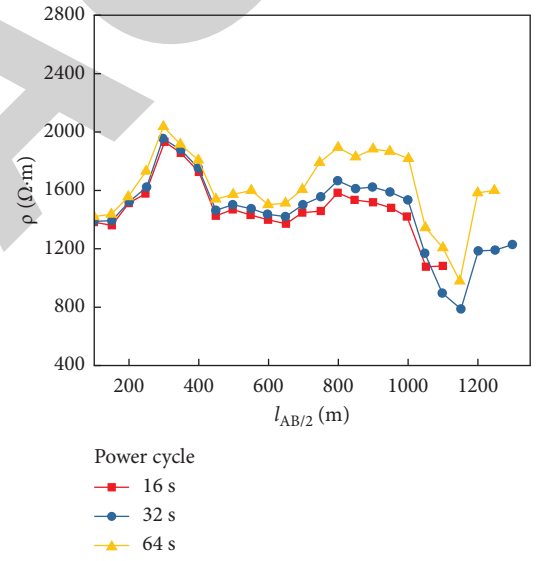

Figure 4: Resistivity curves of different power supply cycles.

polarizability gradually increases, forming a deep single peak anomaly, reaching the highest value of 1.55% at lAB/2 = 1200 m, then gradually becoming stable, and the high polarizability anomaly is obvious. The resistivity at Lab/2 = 250~450 m is basically the same as that in a short power supply period, and the high resistivity is extremely obvious, and the curve shape is continuous and smooth. In the deep section of lAB/2 = 1000–1200 m, there is a *V*-shaped low resistivity anomaly, which is obvious and the resistivity is as low as 400 Ω·m. When the power supply period is 64 s and lAB/2 is greater than 950 m, the polarizability value gradually increases, and there is a high polarizability anomaly, but the anomaly amplitude is not large, the intensity is not high, and the anomaly width is large and gentle. The resistivity is basically the same as that of the smaller power supply period, and the high resistance is unusually obvious. When lAB/2 > 450 m, the amplitude increases, which is higher than the sounding values of two groups with short power supply period. At the deep section of lAB/2 = 1000–1200 m, the profile shows "*V*"-shaped low resistance anomaly, and the resistivity is as low as 520 ω·m.

To sum up, when the power-off time is 16 s, 32 s, and 64 s, it can well reflect the shallow lAB/2 < 1000 m with shallow polarizability anomaly; When the deep lAB/2 > 1000 m, the smaller power supply period is affected by the measurement time, and the measurement depth is limited. The power supply period of 16 s fails to reflect the deep low resistance and high-grade anomaly. The power supply periods of 32 s and 64 s can well reflect the deep low resistance and high-grade anomaly, and there is no big difference in resistivity characteristics. However, the peak value of polarization

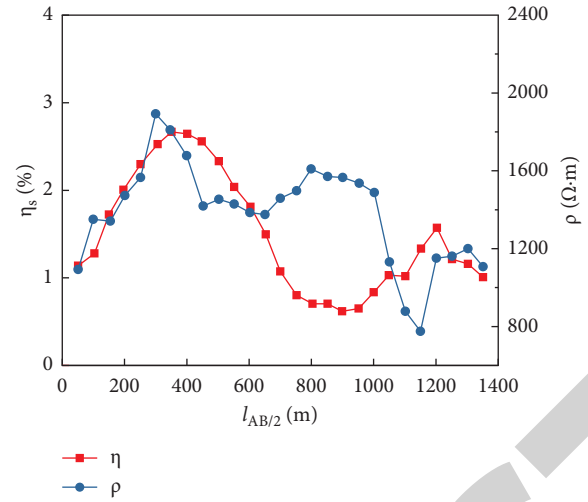

Figure 5: $T = 32$ s polarizability resistivity curve of sounding.

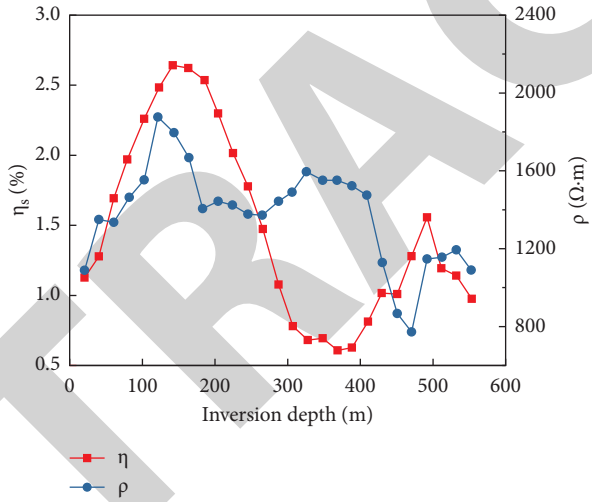

Figure 6: $T = 32$ s polarizability resistivity inversion curve of sounding.

anomaly obtained by the power supply period of 32 s is more obvious, and the abnormal amplitude is larger, which indicates that the power supply period of 32 s has low resistance and high polarization in this area.

5.3. Application Effect of Induced Polarization Method in Geological Geophysical Prospecting. Through the comparative analysis of several groups of sounding data and borehole ZK7401, it is found that there is a big difference between each abnormal depth and the actual mineralized alteration zone and ore-finding location, which needs to be corrected empirically by combining physical property test and known ore-finding location in the working process.

And the test results of the power supply period of the device show that when $T = 32$ s, it can better reflect the deep geological body anomalies. According to its polarizability and resistivity anomalies (Figure 5), compared with the test results of electrical parameters, we find that the high resistivity and high polarizability anomalies in the shallow part are consistent with the mineralization alteration characteristics. lAB/2 = 350 m, the maximum polarizability of 2.63% is taken as the buried depth of the mineralized zone, and the depth correction coefficient is 0.41. After correcting the sounding curve of $T = 32$ s (Figure 6), the abnormal depth of high resistivity and high polarization in the shallow part is 143~164 m, and the abnormal depth of low resistivity and high polarization in the deep part is 471~492 m, which is basically consistent with the ore-finding depth of 468 m.

Through the sounding test, it is considered that the deep IP sounding anomaly can be obtained under the conditions of proper power supply period, large power supply polar distance, and measuring polar distance. However, induced polarization method is difficult and inefficient in field data acquisition. If the ladder device can find the abnormal position on the plane by induced polarization method, and

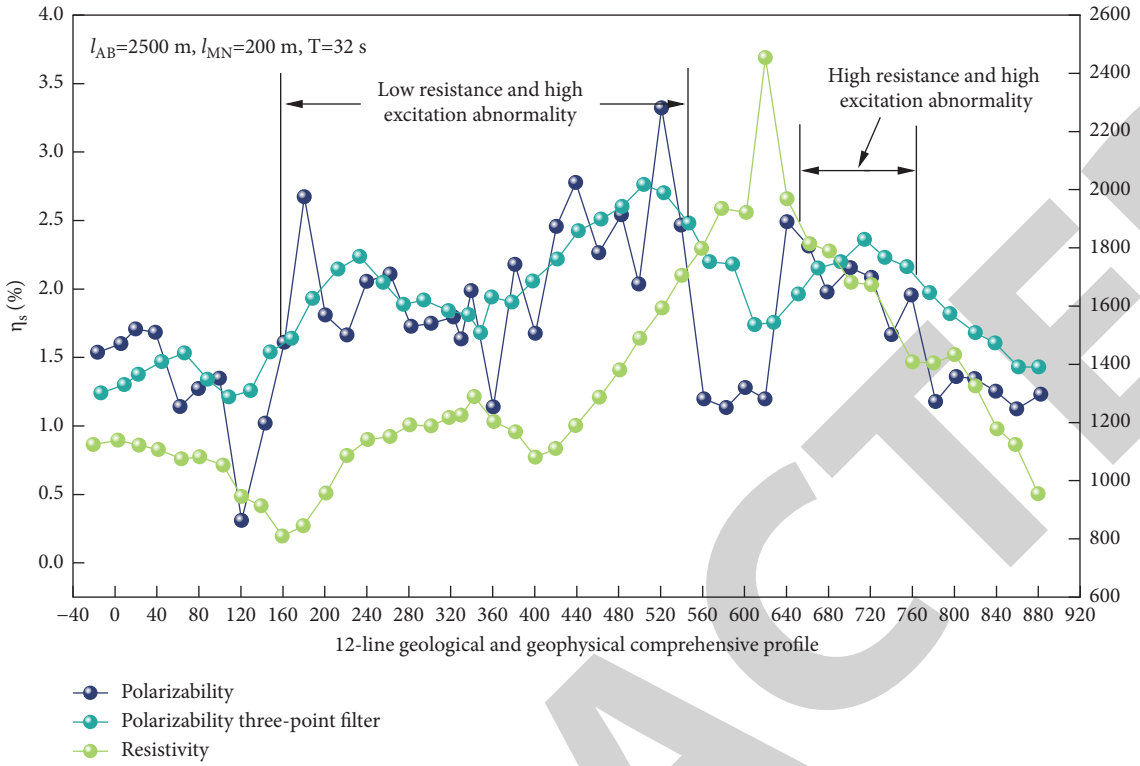

Figure 7: Comprehensive profile of geological and geophysical exploration of Line 12.

then carry out sounding verification, it can get twice the result with half the effort. According to the test results, the power supply pole distance lAB = 2500 m, the measuring pole distance lMN = 200 m, and $T = 32$ s are selected, and the middle ladder measurement is made online 12. From the measurement results, the section 160/12–560/12 has obvious low resistance and high polarization, and the section 640/12–760/12 has obvious high resistance and high polarization. However, the curve of polarizability jumps. Through three-point filtering of polarizability data, the jump points are removed, and the anomaly becomes obvious (Figure 7). According to the physical property test results, the low resistivity and high polarizability anomalies in section 160/12–560/12 are in line with the characteristics of ore-induced anomalies. It is inferred that this anomaly is caused by the deep lenticular ore body caused by ore, which corresponds to the ore body ZK4701. The anomaly of high resistance and high-grade rate in section 60/12–760/12 may be caused by the anomaly of deep low-grade ore bodies, which has deep prospecting significance.

Induced polarization method is an important method to explore various metallic minerals. This method has achieved good ore prospecting results in this area, and has brought into play the specialty of IP in finding concealed metal ore bodies. With the continuous progress of electronic technology and the research of exploration technology, the pseudo-random multifrequency-induced polarization method can be used to identify "carbonaceous" interference anomalies. The development and production of induced polarization instruments at home and abroad have also made great progress, and the exploration depth has reached more than 2000 meters. It can be expected that the application of induced polarization method in other fields will be more and more extensive.

6. Conclusion

According to the time domain induced polarization sounding theory, when the parameters such as high power, appropriate instruments, and time delay are well coupled with the deep blind ore, it is possible to find the anomalies caused by the deep lead-zinc ore body more than 300 m. In order to prove the feasibility of the deep application of this method, high-power induced polarization sounding experiments with different devices and power supply periods were carried out in Erdaohe copper-silver-lead-zinc mine, Inner Mongolia. The results are as follows:

(1) Based on the significant difference of electrical characteristics between ore and surrounding rock, combined with the geophysical data mining of ore-finding borehole, the correction coefficient of data processing inversion depth is 0.41, which can improve the accuracy of inference of mine-induced anomalies, and the adjacent areas can be used for reference.

(2) According to the test results of high-power induced polarization method with different polar distances and different parameters, the IP-induced anomalies with a depth of more than 300 m can be obtained by encrypting the 1AB and 1M middle ladder scanning surfaces with large polar distances, and selecting an

appropriate power supply period T (the best period in this test is 32 s).

(3) The ore bodies in this area are controlled by the structure, and distributed along the lenticular layered features of the interlayer fracture zone in the footwall of the fault, and the ore bodies may change with the occurrence of the fracture plane. The characteristics of low resistance, low slow, and high polarization in IP and single peak anomaly in IP sounding are the important signs of prospecting for lead and zinc in this area.

Data Availability

The figures and tables used to support the findings of this study are included in the article.

Conflicts of Interest

The authors declare that they have no conflicts of interest.

References

[1] B. Jing, "Research on geochemical prospecting method in forest swamp covered area of Daxinganling," *World Nonferrous Metals*, no. 21, p. 57+59, 2019.

[2] P. Zhao, *Study on Geological and Geochemical Characteristics and Prospecting Methods of Shangkengguo Lead-Zinc Deposit in the Northern Part of Daxing' anling*, China University of Geosciences, Beijing, China, 2013.

[3] Y. Zhang, B. Zhang, and Q. Ma, "Study on geochemical prospecting method in forest swamp area of southern Daxing' anling—a case study of 1 : 50, 000 mineral survey in Zhonggongtun area of Hulunbeier, Inner Mongolia," *Northwest Geology*, vol. 50, no. 2, pp. 115–121, 2017.

[4] J. M. Shan, X. Lu, D. Zeng et al., "Geological characteristics and ore-forming material sources of Erdaohe Pb-Zn-Ag polymetallic deposit in the middle part of Daxinganling," *Journal für Mineralstoffwechsel*, vol. 41, no. 2, pp. 150–162, 2021.

[5] C. Shen, F. Yang, J. Wang, X. Wu, T. Zhang, and H. Dong, "New progress in prospecting silver, lead and zinc polymetallic deposits in Daxinganling area, Inner Mongolia and analysis of exploration prospect," *Geology and Exploration*, vol. 55, no. 4, pp. 899–912, 2019.

[6] Z. Jiao, A. Hu, Y. Li, and L. Wang, "Comprehensive application of induced polarization method and controlled source audio magnetotelluric method in lead-zinc mine exploration in northwest Guizhou," *Minerals and Geology*, vol. 34, no. 5, pp. 962–968, 2020.

[7] Z. Jiao, L. Wang, L. Yi, A. Hu, Q. Huang, and J. Wang, "Application of induced polarization method in lead-zinc exploration in Wuliping area of northwest Guizhou," *Modern Mining*, vol. 32, no. 12, pp. 85–88, 2016.

[8] J.-jiao Wang, "Application of induced polarization method in the exploration of a lead-zinc mine in northwest Guizhou," *Journal of Sichuan Geology*, vol. 34, no. 1, pp. 130-131+135, 2014.

[9] B. Li, Z. Yang, Z. Shi, L. Li, Y. Yan, and Q. Yu, "Application of induced polarization method in exploration of Erdaohe silver polymetallic deposit in Inner Mongolia," *Petrochemical Technology*, vol. 29, no. 6, pp. 108–110, 2022.

[10] F. Lu, Y. Zou, and Z. Li, "Application of IP measurement method in searching for concealed lead-zinc ore bodies in the periphery of Xiashui lead-zinc mine area," *Resource Information and Engineering*, vol. 31, no. 6, pp. 12–14+16, 2016.

[11] J. Zhang, Q. Zhao, Y. Han, and S. Hu, "High power induced polarization method and its application in copper mine," *Value Engineering*, vol. 34, no. 1, pp. 294-295, 2015.

[12] B. Yang, R. Zhou, B. Li, J. Huang, and S. Zhang, "Application of high-power IP three-pole sounding in mahuanggou lead-zinc mine exploration," *Gansu Metallurgy*, vol. 42, no. 05, pp. 86–89, 2020.

[13] C. Liang, D. Zhang, D. Yongjun et al., "Preliminary study on regional metallogenic regularity in the middle-south section of Daxinganling," *Geological Prospecting Essays*, vol. 24, no. 4, pp. 267–271+281, 2009.

[14] C. Zheng, J. Zhou, W. Jin et al., "Tectonic chronology of the northern part of delbe dry fault zone in Daxinganling area," *Journal of Petrology*, vol. 25, no. 8, pp. 1989–2000, 2009.

[15] W. Tang, "Research and application of rock and ore physical properties in Sandaowanziyan gold deposit, Heilongjiang," *World Nonferrous Metals*, no. 5, pp. 270-271, 2020.

[16] M. Xu, M. Chai, and J. Gao, "Study on physical properties and seismic wave group characteristics of rocks and ores in Zhusujihua mining area, Inner Mongolia," *Geology and Exploration*, vol. 51, no. 6, pp. 1168–1174, 2015.

[17] G. Li and J. Duan, "Analysis of the determination method of rock and ore electrical properties," *Earth*, vol. 0, no. 10, p. 147, 2016.

[18] H. Cheng, P. Ma, G. Dong, S. Zhang, J. Wei, and Q. Qin, "Characteristics of carboniferous volcanic reservoirs in Beisantai oilfield, Junggar basin," *Mathematical Problems in Engineering*, vol. 2022, Article ID 7800630, 10 pages, 2022.

[19] H. Cheng, J. Wei, and Z. Cheng, "Study on sedimentary facies and reservoir characteristics of paleogene sandstone in Yingmaili block, Tarim basin," *Geofluids*, vol. 2022, Article ID 1445395, 14 pages, 2022.

[20] H. Cheng, D. Yang, C. Lu, Q. Qin, and D. Cadasse, "Intelligent oil production stratified water injection technology," *Wireless Communications and Mobile Computing*, vol. 2022, Article ID 3954446, 7 pages, 2022.

[21] W. Zhang, Z. Cheng, H. Cheng, Q. Qin, and M. Wang, "Research of tight gas reservoir simulation technology IOP conference series: earth and environmental science," *IOP Conference Series: Earth and Environmental Science*, vol. 804, no. 2, Article ID 022046, 2021.

[22] G. Z. Zhang, L. G. Zhou, and Y. H. Wang, "Application of integrated electrical mathods to silver lead-zinc mine zone of Chaaobao in Inner Mongolia," *Progress in Geophysics*, vol. 30, no. 2, pp. 867–871, 2015.

[23] Y. Li, D. Zhang, L. Dai, G. Wan, and B. Hou, "Characteristics of structurally superimposed geochemical haloes at the polymetallic Xiasai silver-lead-zinc ore deposit in Sichuan province, SW China," *Journal of Geochemical Exploration*, vol. 169, pp. 100–122, 2016.

[24] Y. Fan, Y. Wan, H. Wang et al., "Application of an airborne hyper-spectral survey system CASI/SASI in the gold-silver-lead-zinc ore district of Huaniushan, Gansu, China," *Geologia Croatica*, vol. 74, no. 1, pp. 73–83, 2021.

Hindawi
Journal of Chemistry
Volume 2023, Article ID 9819656, 1 page
https://doi.org/10.1155/2023/9819656

Retraction

Retracted: Integrated Design Technology of Geological Engineering for Pressure Flooding and Water Injection in Low Permeability Reservoirs: Take the Reservoir of Keshang Formation in Wu2 East Area as an Example

Journal of Chemistry

Received 28 November 2023; Accepted 28 November 2023; Published 29 November 2023

This article has been retracted by Hindawi, as publisher, following an investigation undertaken by the publisher [1]. This investigation has uncovered evidence of systematic manipulation of the publication and peer-review process. We cannot, therefore, vouch for the reliability or integrity of this article.

Please note that this notice is intended solely to alert readers that the peer-review process of this article has been compromised.

Wiley and Hindawi regret that the usual quality checks did not identify these issues before publication and have since put additional measures in place to safeguard research integrity.

We wish to credit our Research Integrity and Research Publishing teams and anonymous and named external researchers and research integrity experts for contributing to this investigation.

The corresponding author, as the representative of all authors, has been given the opportunity to register their agreement or disagreement to this retraction. We have kept a record of any response received.

References

[1] M. Qin, C. Chen, Q. Yu et al., "Integrated Design Technology of Geological Engineering for Pressure Flooding and Water Injection in Low Permeability Reservoirs: Take the Reservoir of Keshang Formation in Wu2 East Area as an Example," *Journal of Chemistry*, vol. 2022, Article ID 1392831, 8 pages, 2022.

Hindawi
Journal of Chemistry
Volume 2022, Article ID 1392831, 8 pages
https://doi.org/10.1155/2022/1392831

Research Article

Integrated Design Technology of Geological Engineering for Pressure Flooding and Water Injection in Low Permeability Reservoirs: Take the Reservoir of Keshang Formation in Wu2 East Area as an Example

Ming Qin,[1] Chao Chen,[1] Qingsen Yu,[1] Zhenping Liu,[1] Zhibo Liu,[2] Hanlie Cheng,[3] and Fahim Theon[4]

[1]*Exploration and Development Research Institute, Xinjiang Oilfield, CNPC, Karamay, Xinjiang 834000, China*
[2]*Jerry Energy Services Ltd, Yantai, Shandong 264000, China*
[3]*School of Energy Resource, China University of Geosciences (Beijing), Beijing 434000, China*
[4]*The King's School, BP1560, Bujumbura, Burundi*

Correspondence should be addressed to Fahim Theon; fahimtheon@ksu.edu.bi

Received 1 September 2022; Accepted 15 September 2022; Published 3 October 2022

Academic Editor: Rabia Rehman

The objective factors of low permeability reservoir determine that there is obvious starting pressure gradient in waterflooding development, and the injection pressure is high. Conventional waterflooding has the technical bottleneck of "no injection and no flooding." It highlights the development contradictions such as serious under-injection, rapid production decline and difficult production of reserves. Pressurized water injection is a new technology of unconventional water injection to enhance oil recovery, which can improve the production degree of low permeability reservoir reserves and solve the problem of water injection difficulty. In order to ensure the reliability of scheme design and the success rate of field implementation, the key technologies of unconventional oil and gas reservoir geological engineering integration are applied for the first time, including 3D geological modeling technology, geomechanics modeling technology, complex fracture network simulation technology of geological engineering integration and numerical simulation technology, and a fine 3D dynamic and static model covering all elements of geology and engineering is objectively established. Through numerical simulation research, the optimal water injection parameters of pressure flooding are determined, and the implementation effect of the optimal scheme is predicted, which provides a scientific basis for field implementation.

1. Introduction

The technology of "pressure flooding and water injection" draws lessons from the idea of stimulation of unconventional reservoir fracturing, combines fracturing technology with water injection development, and through high-precision injection rate control, high-pressure and high-speed injection under near-fracture or super-fracture pressure conditions, quickly pressurizes the formation to form artificial fractures and micro-fracture networks, changes the fluid displacement mode, improves the micro-pore roar sweep capacity, improves the reservoir seepage capacity, and expands the limit sweep radius, thus increasing the recovery factor of water flooding development. Karamay oil field is the first large oil field discovered in 1955 after the liberation of our country. "Karamay" is the transliteration of Uyghur "black oil," named after the discovery of Karamay oil field. It is now a natural asphalt Hill—black oil mountain in the east corner of Karamay City. In January, 2018, it was selected into the first batch of China's industrial heritage protection list. At present, the conventional water injection pressure of Keshang Formation reservoir in No. 52 East Area of Karamay Oilfield is high, and the problem of under-injection is serious [1]. There are some problems in water injection

enhancement measures such as surface pump, acidizing or water well fracturing, such as little water injection, short validity period, or ineffectiveness. Therefore, the integrated scheme design of pressure flooding and water injection geological engineering can not only provide guidance for the on-site implementation of pressure flooding, solve the problems of conventional water injection development, improve the utilization degree of reserves, but also provide reference for the design of pressure flooding and water injection in similar reservoirs.

2. Geological Reservoir Characteristics

The reservoir of Keshang formation in Wudong district is located in the footwall of Karamay fault, bounded by Baijiantan fault in the southeast and Qixi District, and adjacent to Wu2 West and Wu3 Middle district in the southwest, which is a glutenite reservoir. So far, 25 oil and gas fields have been discovered in Karamay, with proved geological oil reserves of 1.829 billion tons and proved geological natural gas reserves of 76.66 billion cubic meters; In 2004, 11.11 million tons of crude oil and 2.55 billion cubic meters of natural gas were produced, an increase of 30 times and 751 times, respectively, over 1958. The average ground elevation of the reservoir is −280 m, the middle depth of the reservoir is 1720 m, the oil-bearing area is 7.67 km^2, the geological reserve is 824.3×104 t, the average effective thickness of the reservoir is 9.2 m, the porosity is 5.4~22.3%, the main distribution range is 10~20%, the average porosity is 15.3%, and the permeability is $0.04\sim2850 \times 10-30$. The reservoir is divided into *S*5, *S*4, *S*3, *S*2, and *S*15 sand groups from bottom to top. *S*5 and *S*1 sand groups are the main oil layers, and their geological reserves account for 36.2% and 21.9% of the total reserves, respectively. The reservoir is mainly composed of sandy conglomerate, gravelly sandstone, and mudstone interbedded with unequal thickness, with strong heterogeneity between layers and within layers, and complex distribution of sand bodies in different provenance directions [2]. Along the direction of provenance, the main sand group has a large thickness and relatively good connectivity, while the sand body vertical to provenance has complex distribution and poor connectivity. The reservoir was put into development in 1989 with 350 m reverse seven-point injection-production pattern. At present, the comprehensive water cut is 90.2%, the recovery degree of geological reserves is 7.3%, and the oil recovery rate is 0.2%. It is in the stage of high water cut and low speed exploitation. In general, the geological characteristics of the reservoir are different in each region. These characteristics mainly include many parameters such as the depth, location, and permeability of the reservoir, which are also affected by many factors. Geology and climate are two of the most influential.

3. Establishment and Fitting of the Model

3.1. Geomechanical Model. In the geological work area, the vertical well group model is set up by typical wells in the under-injection area in the north-central part of the reservoir. There are 7 oil production wells and 7 water injection wells in the work area, with an area of 0.83 km^2. The grid model direction design is consistent with the material source direction, and the plane grid accuracy is $15\text{ m} \times 15\text{ m}$. The horizon model includes *S*1~*S*5 sand groups, with a vertical grid step of 0.5 m and a grid setting of $85 \times 85 \times 360$, with a total grid number of 2,601,000. The geological characteristics of some oil reservoirs also have certain uniqueness. The quality of oil reservoirs is directly related to physical properties, permeability, and saturation. When some individual oil reservoirs are exploited in the initial stage, because the buried position is relatively shallow and the compactness is relatively small, it is easy to cause sand production during the initial exploitation. Therefore, we need to pay more attention.

On the basis of geological model, constrained by the calculation results of one-dimensional mechanical parameters of 14 single wells in the well group, the geomechanical model of the well group is established by three-dimensional finite element simulation technology [3]. The geological grid is expanded and generated based on the geological model grid. The grid accuracy of the reservoir area remains unchanged. The top surface of the middle and upper covering areas in the surrounding rock area extends to the ground surface, the bottom surface of the lower covering area extends to 4000 m, and the side border area extends to three times the size of the geological model work area. The surrounding rock area is discretely treated according to the logarithmic space grid, and the grid is set at $117 \times 117 \times 401$, with a total number of 5,489,289 grids. The reservoir geological model is the final result of comprehensive research on reservoir description. It is a high generalization of reservoir type, sand body geometry, size, reservoir parameters, spatial distribution of fluid properties, diagenesis, and pore structure. Therefore, it is an idealized model. Generally speaking, reservoir geological model is the synthesis of data volume and two-dimensional graphic display reflecting reservoir characteristics. The reservoir rock attribute model inherits the geological model, and the attribute of the middle border region of the surrounding rock area is obtained by extrapolation of the attribute of the reservoir area. The rock mechanics data of the overlying and underlying areas are based on the selected values of the reservoir area. In order to further eliminate the influence of stress concentration, a rigid plate with a thickness of 50 m is added at the boundary. The location of each area of the geomechanical grid is shown in Figure 1, and the rock mechanics parameters of the surrounding rock area are shown in Table 1.

On the basis of geomechanical grid and rock property modeling, taking the single well geostress calculation results as constraint conditions, setting the initial values of strain boundary conditions, carrying out three-dimensional finite element numerical simulation, iteratively solving, fitting the single well geostress calculation results, and finally establishing the three-dimensional geostress model of well groups. Statistics show that the average horizontal maximum stress of the well group is 42.1 MPa, the minimum horizontal stress is 29.6 MPa, the horizontal stress difference is 12.5 MPa, and the maximum horizontal stress direction is 135. See Table 2 for the in-situ stress data of each sand group.

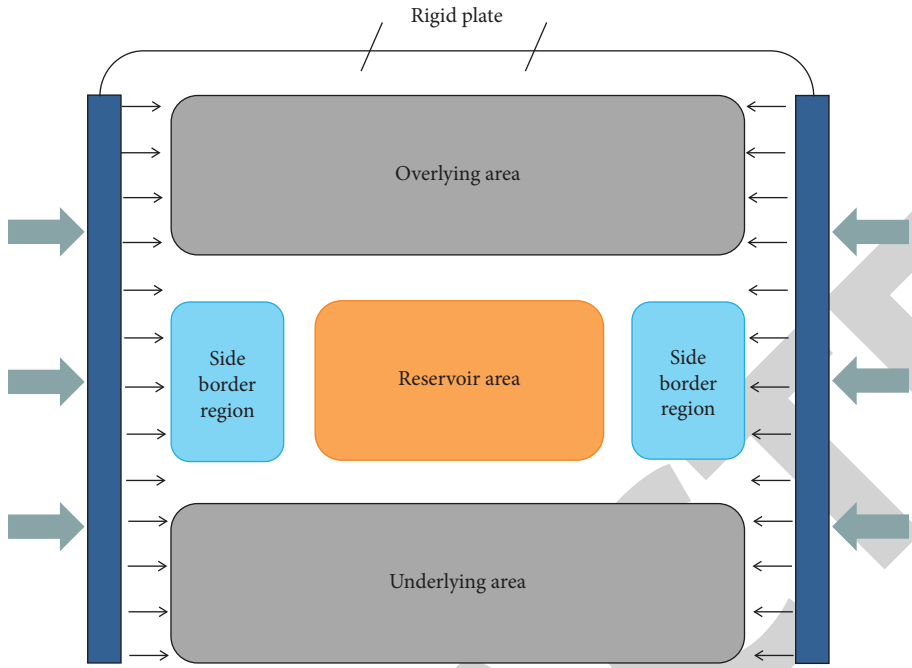

Figure 1: Location diagram of geomechanical grid area.

Table 1: Table of mechanical parameters of rock mechanics model surrounding rock area.

Location	Young's modulus (GPa)	Poisson's ratio	Rock density (g/cm^3)	Compressive strength (bar)	Internal friction angle (deg)
Underlying area	17.1	0.32	2.50	650	29.8
Overlying area	18.5	0.31	2.38	782	24.6
Rigid plate	50.0	0.35	2.90	/	/

Table 2: Statistical table of in-situ stress data of sand group *S*1~*S*5.

Sand formation	Minimum horizontal principal stress (MPa)	Maximum horizontal principal stress (MPa)	Horizontal stress difference (MPa)
*S*1	28.2	41.1	12.9
*S*2	29.2	41.1	11.9
*S*3	29.6	42.3	12.7
*S*4	30.0	42.5	12.5
*S*5	30.9	43.4	12.5

The establishment of the geological model lays the foundation for integrated simulation evaluation and design of pressure drive geological engineering.

3.2. Reservoir Dynamic Model. At present, the methods of constraint modeling mainly include fault controlled quantitative modeling method of fault block structure modeling, phase controlled quantitative modeling under phase zone constraint, seismic modeling under logging constraint, and analogy constraint modeling of known models. Based on the geomechanical model of the well group, the complex fracture network simulation of geological engineering integration is carried out, and the hydraulic fracturing simulation is carried out according to the pumping program data of oil-water well fracturing construction, and the fracture network models of seven oil wells and two peripheral water injection wells inj2 and inj6 are established (Figure 2). On the basis of this model, the unstructured grid subdivision technology is adopted to finely characterize the simulated fracturing in the form of unstructured grid, and a three-dimensional unstructured grid numerical model (Figure 3) is established, so that the dynamic and static information of fracturing simulation, production history fitting, and prediction can be seamlessly connected [4].

3.3. Historical Fitting. By repeatedly adjusting the parameters of dynamic and static models, and taking the pressure monitoring data and production-suction profile test results as quality control data [5], the production history fitting of well groups is completed (Table 3). The data comparison shows that the fitting error of each index is less than 5%, and the fitting result is good. At the same time of well group

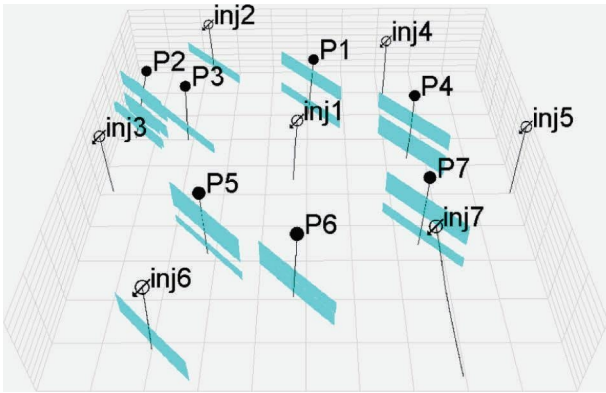

Figure 2: Three-dimensional display of fracturing model in oil and water wells.

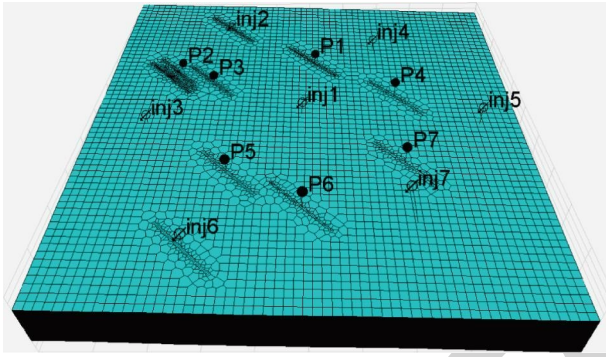

Figure 3: Three-dimensional numerical model of unstructured grid.

fitting, the single well was fitted cooperatively. The structural model mainly describes the structural location, geometric shape, strike, dip angle, fault displacement, etc. of faults, fractures, and folds. For low permeability sandstone reservoirs, the direction of in-situ stress and the distribution of fractures are of great significance for the development of low permeability reservoirs, and special attention should be paid to the description. Except for well *P*3 in the well control range of *P*2, which was in a low-yield state for a long time, the fitting error of water production was large, and the other six wells were all fitted perfectly, with a fitting rate of 85.7% [6, 7]. By fitting the dynamic and static model of quality control, its perfection degree is high, and it can objectively reproduce the reservoir development process, which lays a foundation for the subsequent design of pressure flooding water injection parameters and effect prediction [8–13].

4. Optimization of Pressure Drive Parameters

4.1. Periodic Water Injection Rate. The field experience of flooding shows that the injection rate is usually 0.8~2.0 m^3/min. When optimizing the cyclic water injection rate, the lower *S*3~*S*5 sand groups should be designed first. The optimized cyclic water injection rate scheme includes $1.0 \times 104\ m^3$, 2.0×104 m3, $3.0 \times 104\ m^3$, $4.0 \times 104\ m^3$, and $5.0 \times 104\ m^3$, which is predicted for 5 years [14–18]. In order to characterize the fracturing mechanism of pressure drive, firstly, the development morphology of pressure drive fractures under different water injection rates is simulated, and the spatial allocation relationship between the dynamic fracture network of pressure drive fractures in oil wells and water injection wells is obtained, and the influence law of the fracture end spacing along the direction of maximum horizontal principal stress between pressure drive fractures and pressure drive fractures on productivity is known. The water injection rate of $3.0 \times 104\ m^3$ was taken as an example. See Figure 4 for the distance between the fracture ends of pressure fractures and pressure drive fractures. See Table 4 for the prediction data of the relationship between the oil increase at different stages and the interval between seam ends under different water injection rates.

From the data analysis in Table 4, it can be seen that with the increase of water injection, the distance between the fracture and the fracture end of the pressure drive decreases, and the oil increase in the first year shows a slow downward trend, while the cumulative oil increase at the end of the fifth year shows a trend of first increasing and then decreasing. When the water injection rate is $1.0 \times 104\ m^3$, the half-length of the pressure drive fracture is 31 m, and the interval between the fracture ends is 124 m, so the water drive spread range is limited and the stimulation effect is poor. When the water injection rate increases to $3.0 \times 104\ m^3$, the half-length of the pressure drive fractures is 109 m, and the spacing between the fracture ends is reduced to 76 m. This configuration of the fracture network not only improves the swept radius of water drive, but also avoids the influence of too small spacing between the fracture ends on the productivity of oil wells as much as possible [19, 20]. When the water injection rate exceeds $3.0 \times 104\ m^3$, with the increase of water injection rate, the interval between fracture ends decreases, and the faster the injected water spreads to the oil well end, the lower the oil increasing effect. To sum up, combined with the existing underground water storage and channeling risk of well group at present, it is determined that the reasonable periodic water injection rate of *S*3~*S*5 sand group is $1.0 \times 104\ m^3$, which will be adjusted according to the pressure response at the oil well end in the implementation process.

4.2. Injection Cycle. On the basis of determining the water injection rate of *S*3~*S*5 sand groups, the injection conversion period was further optimized, and the injection conversion period was designed to be 6 months, 12 months, 18 months, 24 months, and 36 months, with a forecast of 5 years. See Table 5 for the prediction results of cumulative water injection and oil increase in different injection cycles. According to the data analysis, the difference of oil increase in the first year is small under different injection conversion cycles, and the injection conversion cycle increases. At the end of the fifth year, the cumulative oil increases first and then decreases. The shorter the injection cycle, the more injection rounds, the larger the cumulative water injection amount, the faster the injected water will spread to the oil well end, the earlier the water flooding, the faster the oil well productivity decline, and the worse the stimulation effect.

Table 3: Statistical table of development data fitting.

Contrast index	Accumulated oil production (104 t)	Produced water (104 m^3)	Moisture content (%)	Geological reserves of (104 t)
Real data	1.62	5.39	80.8	42.8
Calculation result	1.60	5.33	84.3	41.3
Relative error (%)	1.23	1.11	4.33	3.50

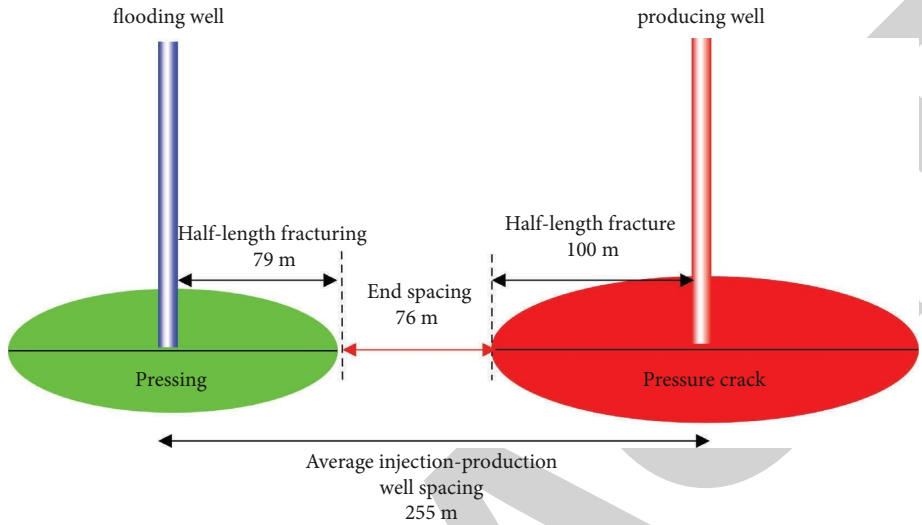

Figure 4: Schematic diagram of the gap between the pressure fracture and the pressure drive fracture.

Table 4: Comparative data table of pressure drive effect under water injection rate in different periods.

Periodic water injection (104 m^3)	Annual oil increase (t)	Accumulated oil quantity (t)	Half-length of fracturing (m)	End spacing (m)
1.0	1735	1931	31	124
2.0	1671	3053	55	100
3.0	1413	5417	79	76
4.0	1225	5056	109	46
5.0	1014	4541	130	25

Table 5: Comparative data table of pressure flooding effect in different injection cycles.

Injection cycle	Annual oil increase (t)	Accumulated oil quantity (t)	Accumulated water injection (104 m^3)
6 months	936	2530	30
12 months	1413	6457	15
18 months	1413	8055	12
24 months	1413	7830	9
36 months	1413	6302	6

Over-injection cycle, the formation energy cannot be replenished in time in the production cycle, and the oil well production declines obviously, which affects the final production increase effect. Based on the above analysis, it is determined that the reasonable injection conversion period is 18 months, and the field implementation is optimized and adjusted according to the degree of formation pressure maintenance in the production period.

5. Design of Pressure Drive Scheme

Combined with the characteristics of reservoir geological stratification and the current development problems of well groups, layered pressure drive is adopted for fine water injection. The total water injection rate in a single cycle is $5 \times 104\ m^3$, of which the *S*3, *S*4, and *S*5 sand groups are a co-injection horizon, and the periodic water injection rate is $1.0 \times 104\ m^3$; *S*1 and *S*2 sand groups are a co-injection horizon, and the same idea of water injection optimization as *S*3, *S*4, and *S*5 sand groups is adopted to determine the periodic water injection rate of $4.0 \times 104\ m^3$. The construction displacement is based on the concept of micro-pressure flooding, pressure control, and channeling prevention, and the design range of pump injection program is 0.8~1.5 m^3/min, so as to achieve the goal of large-scale mesh joint, avoid the formation of large main joint, and ensure the

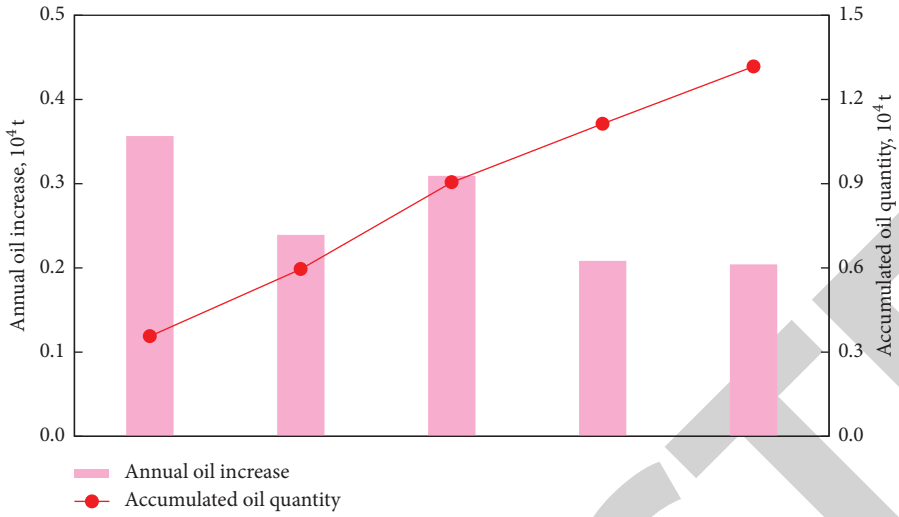

Figure 5: Prediction results of pressure flooding and water injection stimulation effect.

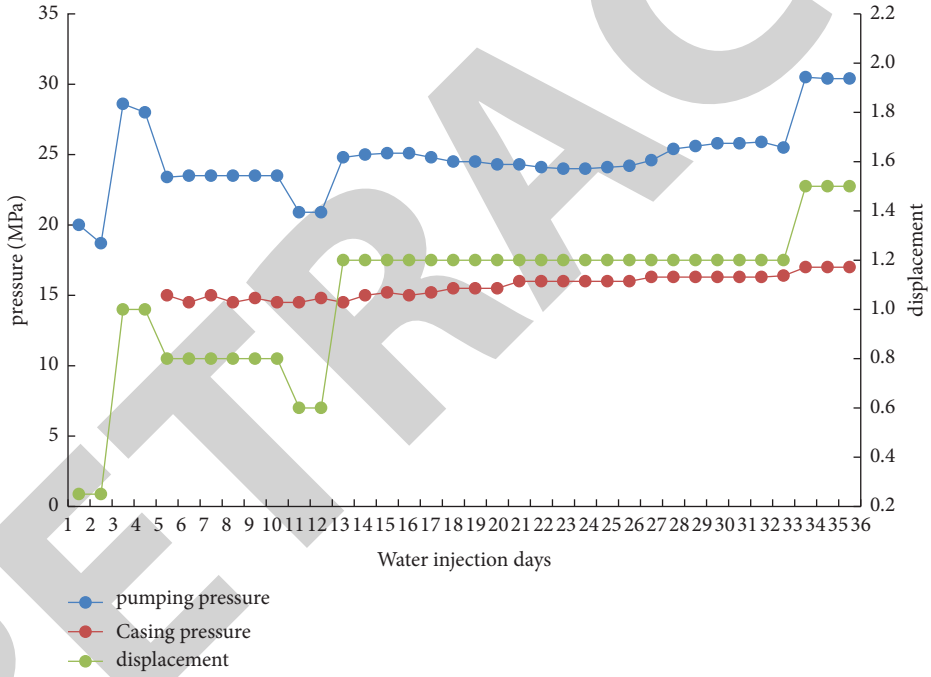

Figure 6: Pumping curve of pressure drive construction.

effect of pressure flooding. The Junggar basin, the main working object of Karamay Oilfield, has a huge thickness of oil generating strata, containing 8.6 billion tons of oil resources and 2.1 trillion cubic meters of natural gas resources. At present, the exploration rate is only about 20% and 3.4%, respectively, and the exploration and development potential is huge.

6. Implementation Effect Prediction

After comprehensive development, the crude oil output in 1985 reached 4.945 million tons. In 1998, Xinjiang Petroleum Administration Bureau, with it as the core, produced 8.71 million tons of crude oil and 471 million cubic meters of natural gas, becoming an important oil industry base in China. The flooding effect is predicted for 5 years, totaling 4 rounds of water injection, with a cumulative water injection of $20 \times 104\,m^3$, of which the cumulative water injection of *S*3, *S*4, and *S*5 sand groups is $4 \times 104\,m^3$, and that of *S*1 and *S*2 sand groups is $16 \times 104\,m^3$. It is predicted that the oil production of the well group will increase by 0.36×104 t in the first year, and by 1.32×104 t at the end of the fifth year, increasing the oil recovery by 3.2% (Figure 5). Among them, *S*3, *S*4 ,and *S*5 sand groups increased oil by 0.1735×104 t in the first year, and accumulated oil by 0.3984×104 t; *S*1 and *S*2 sand groups increased oil by 0.1892×104 t in the first year, and accumulated oil by 0.9190×104 t.

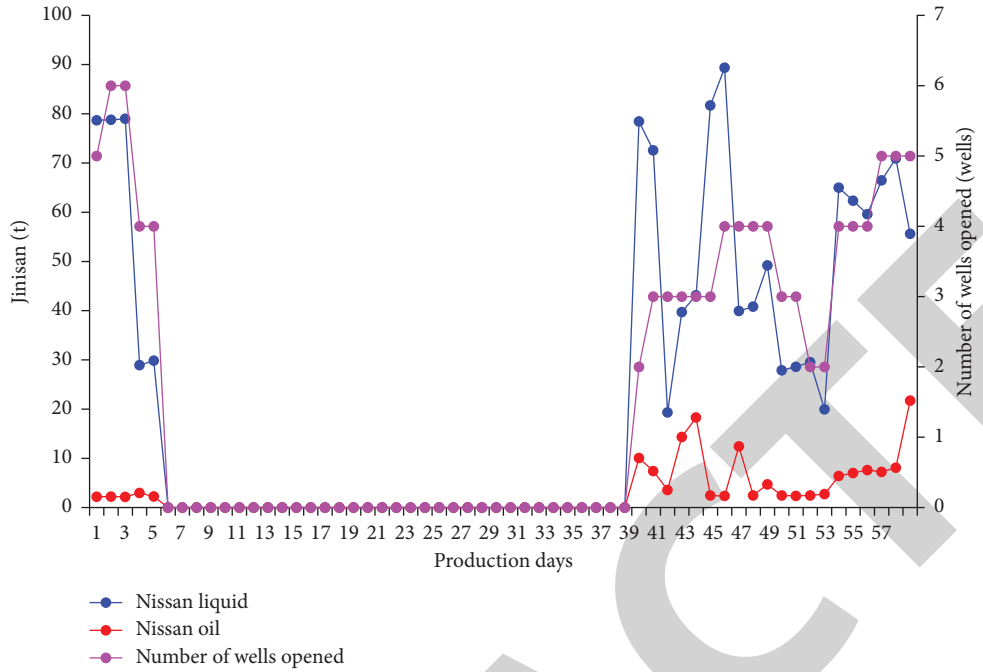

Figure 7: Daily production curve of pressure drive well group.

7. Field Test

In 2007, Karamay Oilfield added 69.6 million tons of proved geological oil reserves, and produced 12.1706 million tons of crude oil and 2.905 billion cubic meters of natural gas throughout the year. Oil and gas exploration has gradually embarked on a path of benign development. Crude oil production has maintained steady growth for 27 consecutive years. Guided by the design results of the scheme, the field construction trial injection displacement is 0.25~0.6 m^3/min, the displacement of pressure flooding water injection is 0.8~1.5 m^3/min, and the peak pump pressure is 30.5 MPa (Figure 6). The total injection days are 36 days, and the accumulated water injection is 50755 m^3, including 10528 m^3 in *S*3, *S*4, and *S*5 sand groups and 40227 m^3 in *S*1 and *S*2 sand groups. After the completion of the construction, the well was soaked for 2 days, and the oil wells were opened for production according to the optimized opening sequence. Before the pressure drive, the daily fluid production of the well group was 59 t/d, the daily oil production was 2.4 t/d, and the water cut was 95.9%. After the pressure drive, the initial daily fluid production was 78.45 t/d, the daily oil production was increased to 10.5 t/d, and the water cut was 87.2%. The peak daily oil production was 21.7 t/d, which was accumulated in 20 days (Figure 7) [19, 20].

8. Conclusion

(1) Based on the three-dimensional geomechanical model, the spatial allocation relationship between oil well fracturing and water injection well fracturing dynamic fracture network is finely depicted, which is more in line with the technical requirements of water injection evaluation, and effectively supports the scheme optimization and parameter design.

(2) By comprehensively applying the key technologies of geological engineering integration of unconventional oil and gas reservoirs, the coordinated simulation of geology, reservoir, and engineering integration and the design of pressure drive scheme are carried out for the target well group, which improves the reliability of the design results and provides a reference for the optimal design of pressure drive scheme of such reservoirs.

(3) Pressure flooding water injection has the characteristics of simple construction technology, rapid replenishment of formation energy, and considerable economic benefits. It has achieved remarkable implementation effect on site, and has a good popularization and application prospect in the same type of reservoirs.

Data Availability

The figures and tables used to support the findings of this study are included in the article.

Conflicts of Interest

The authors declare that they have no conflicts of interest.

Acknowledgments

The authors would like to acknowledge the techniques used in this research.

Hindawi
Journal of Chemistry
Volume 2023, Article ID 9807940, 1 page
https://doi.org/10.1155/2023/9807940

Retraction

Retracted: Design of Noise-Reducing Two-Stage Cage Control Valve and Its Fluid Characteristics and Cavitation Study

Journal of Chemistry

Received 28 November 2023; Accepted 28 November 2023; Published 29 November 2023

This article has been retracted by Hindawi, as publisher, following an investigation undertaken by the publisher [1]. This investigation has uncovered evidence of systematic manipulation of the publication and peer-review process. We cannot, therefore, vouch for the reliability or integrity of this article.

Please note that this notice is intended solely to alert readers that the peer-review process of this article has been compromised.

Wiley and Hindawi regret that the usual quality checks did not identify these issues before publication and have since put additional measures in place to safeguard research integrity.

We wish to credit our Research Integrity and Research Publishing teams and anonymous and named external researchers and research integrity experts for contributing to this investigation.

The corresponding author, as the representative of all authors, has been given the opportunity to register their agreement or disagreement to this retraction. We have kept a record of any response received.

References

[1] R. Yu and X. Lu, "Design of Noise-Reducing Two-Stage Cage Control Valve and Its Fluid Characteristics and Cavitation Study," *Journal of Chemistry*, vol. 2022, Article ID 7322655, 23 pages, 2022.

Hindawi
Journal of Chemistry
Volume 2022, Article ID 7322655, 23 pages
https://doi.org/10.1155/2022/7322655

Research Article

Design of Noise-Reducing Two-Stage Cage Control Valve and Its Fluid Characteristics and Cavitation Study

Ruiming Yu and Xi Lu

School of Mechanical Engineering, University of Shanghai for Science and Technology, Shanghai 200093, China

Correspondence should be addressed to Ruiming Yu; 211170097@st.usst.edu.cn

Received 21 July 2022; Revised 27 August 2022; Accepted 30 August 2022; Published 23 September 2022

Academic Editor: Rabia Rehman

For all kinds of media noise, noise reduction valve cage cannot meet the equal percentage flow characteristics, and for manufacturing and processing and other technical problems, research and design of new noise reduction two-stage cage control valve are necessary. The valve adopts noise reduction valve cage and curve valve cage with noise reduction, forming a two-stage noise reduction, with uniform flow, diffusion, and noise reduction effect, to meet the regulating valve equal percentage flow characteristics. The spool is evenly stressed and not easy to loosen and fall off, and the small opening is not easy to vibrate and shake. The flow characteristics of the noise-reducing two-stage cage control valve are studied, and the fluid flow coefficients, flow characteristic curves, the relationship of flow coefficients with nominal diameter at the same stroke, and the relationship of flow coefficients with different nominal diameters at different strokes are analyzed. The relationship between nominal diameter constant opening and cavitation coefficient with inlet velocity, the relationship between inlet velocity and cavitation coefficient with nominal diameter at half opening, and the relationship between inlet velocity and cavitation coefficient with nominal diameter at full opening were studied, and the cavitation generation and its effect on noise were analyzed. The noise and cavitation test showed that noise is very small and cavitation is difficult to produce, all meeting the noise reduction requirements.

1. Introduction

In petroleum, petrochemical, power plant, refining, chemical, and pharmaceutical industries, it is often necessary to regulate and control the flow, pressure, and temperature of steam, gas-liquid two-phase flow, gas, and other media [1, 2] to meet the needs of various chemical reactions or heating and cooling transduction [3, 4]. This has been studied by many scholars. By using high pressure as a processing tool, high-pressure technologies using subcritical and supercritical fluids offer the possibility to obtain new products with special characteristics or to design new processes that are environmentally friendly and sustainable [5]. Supercritical fluids have been used in several processes developed to commercial scale in the pharmaceutical, food, and textile industries. Bao et al. [6] utilized a unique microscale phenomenon of microfluidic systems to provide fast, accurate, and robust analysis, primarily for biomedical, oil, and gas applications. In addition to obtaining high temperatures and pressures, it has also driven extended applications in phase measurements associated with industrial carbon monoxide. Tan et al. [7] studied that as an important reactor form for catalytic reactions of gases, liquids, and solids, and the trickle-bed reactor (TBR) is widely used in the petroleum, biochemical, fine chemical, and pharmaceutical industries due to its flexibility, operational simplicity, and high throughput. Reactors are subject to high temperatures and pressures, fluid flow rates, and flow rates that need to be controlled during catalytic reactions. Ballesteros Martínez et al. [8] analyzed the low fluid load flows that often occur during the transport of gas products in various industries, such as oil and gas, food, and pharmaceutical industries. Modeling low liquid load flow rates in medium-sized (6–10 inches) pipelines analyzed how the presence of the liquid phase has a greater effect on process variables than its exact flow rate. Introducing the liquid phase into a single-phase

gas results in a threefold increase in pressure loss, but doubling the liquid velocity only increases the pressure loss by a further 30%.

Although the pressure before the valve or the pressure difference before and after the valve is only 0.4 MPa~2 MPa, the inherent noise characteristics of gas, liquid, and gas-liquid two-phase media can produce noise that affects the environment and human physiology when the opening degree changes [9–11]. Many papers [12–16] have analyzed and studied the valve noise with some results. For the cavitation and noise problems of hydraulic tapered valves, the variation laws of cavitation and noise are obtained based on the spool radial force analysis and considering the radial deviation of the spool [17]. The cavitation intensity changes slowly with the half cone angle of 45° and the noise level is minimized. Properly increasing the opening within a reasonable range can effectively suppress cavitation and reduce the noise level [18]. The effect of pressure and flow rate of conical throttle valve on cavitation noise is studied. The larger the pressure difference before and after the valve is, the more obvious cavitation is and the stronger the cavitation noise is, and the cavitation noise can be suppressed by reducing the pressure difference before and after the valve. Li et al. [19] proposed a numerical simulation method that integrates dipole and quadrupole sources to predict the aerodynamic noise during safety valve venting. The simulation method is used to calculate the exhaust noise of safety valve under six different working conditions and analyze the sound source characteristics of safety valve exhaust noise. Wei et al. [20] studied the characteristics of flow-induced noise in a high-pressure pressure reducing valve, based on computational fluid dynamics, using a numerical method to calculate the flow field and applying the Ffowcs Williams and Hawkings model to obtain the acoustic signal. Numerous scholars have studied the noise generation mechanism, influencing factors, and change patterns.

A frequently used noise reduction method is the installation of a noise reduction valve cage with holes drilled in the cage, which can only satisfy the linear flow characteristics due to the uniform distribution of the holes [21, 22]. Sotoodeh [23] investigated valve cages with many small holes drilled in the control valve to divide the flow into many small flows, using this design to reduce noise. Kang et al. [24] drilled many small holes in the valve cage according to the small outlet flow rate to meet the low noise requirement. Lah [25] analyzed that noise sounds more like a small explosion in a valve and the cage is either slotted or drilled to control the location in the valve where cavitation occurs and reduce the noise. If the equal percentage flow characteristics are to be satisfied, the holes must be drilled unevenly within 50% of the opening and the diameters of the holes must also be unevenly distributed, which will dramatically increase the manufacturing cost and processing difficulty by several times [26], and the use of the results is not satisfactory. Therefore, there is a need to research and design a regulating valve that can reduce noise, meet the equal percentage flow characteristics, and be easy to manufacture and process.

For all kinds of media noise, noise reduction valve cage cannot meet the equal percentage flow characteristics, and for manufacturing and processing and other technical problems, research and design of new noise reduction two-stage cage control valve are necessary. The cage type control valve can effectively reduce the harmful noise generated by gas, steam, and gas-liquid medium and can perfectly ensure the equal percentage flow characteristics of the control valve, making the process parameter (flow, pressure, temperature, etc.) adjustment quality excellent, widely used in steam, gas-liquid two-phase flow, gas, evacuation, and other noise overload conditions, for the regulation and control of process parameters.

2. Materials and Structure

2.1. Materials. Each component of the control valve is made of low-temperature carbon steel LCB, alloy steel casting WC6, pressure casting austenitic CF8M, stainless steel 304 and 316, martensitic stainless steel 420, etc. The material of each main component is shown in Table 1.

LCB is a kind of low-temperature carbon steel of American standard, which is a grade of cast steel, and 20# is a high-quality carbon structural steel of national standard. It is a low alloy steel with a temperature range of −46~343 and is generally used to manufacture valves. CF8M belongs to stainless steel. CF8M is an American stainless steel grade, which is equivalent to 316 stainless steel in our country. The maximum carbon content of this type of stainless steel is 0.08%, and it contains molybdenum elements. Its tensile strength is 485 MPa, and it has good corrosion resistance, good welding performance, and plasticity. It has the advantages of high strength and high temperature resistance and is used to make valve castings and chemical equipment. Among the components of stainless steel, 304 and 316 are the most used ones; they can be used as the inner liner of the thermos cup and can be made into various cookware and instruments. It is also a food-grade material, which is safe enough to be used in daily life. 304 stainless steel contains about 18% chromium and more than 8% nickel; on this basis, 316 stainless steel also adds 2% molybdenum, which has better corrosion resistance. There are also 201 series stainless steel and 430 series stainless steel. Compared with the above two, their quality and advantages are much weaker, so the usage rate is not high. Because 316 stainless steel contains molybdenum element, its anti-corrosion effect is better, and the performance of acid and alkali resistance is also improved. 304 stainless steel lacks molybdenum, so its corrosion resistance and acid and alkali resistance are not as good as 316. Although both are food-grade materials, they are used in different fields. For example, 316 stainless steel has good corrosion resistance, and many medical devices are made of 316.304 stainless steel is widely used in cookware, tableware, etc. and has a wide range of uses. Stainless steel countertops, cooking pots, and stainless steel tableware in our home all use 304.

2.2. Structure. Noise-reducing two-stage cage control valve structure includes valve body, valve seat, valve spool, noise-reducing cage, curved cage, valve stem, valve cover, packing,

Table 1: Each main component material.

Names	Valve seat	Valve body	Valve stem	Valve cover	Valve spool
Materials	316	LCB	420	WC6	CF8M

gland, disc spring, pressure plate, ball valve, clearance, long neck large window, short neck small window, and long neck area, and the structure is shown in Figure 1.

3. Design Method

The noise reduction double-stage cage adjustment valve includes valve body, valve seat, valve cover, valve stem, and valve spool. The packing is automatically compensated by the gland, disc spring, and pressure plate cooperatively pressed on the bonnet. The valve stem is connected to the valve spool, the valve seat is set in the valve body, the valve spool is sealed with the valve seat in contact, the valve body is provided with a noise reduction cage, the noise reduction cage is provided with noise reduction holes, the noise reduction cage is also provided with a curved valve cage, the curved valve cage is provided with a flow window, the valve spool is set in the curved valve cage axial movement, the valve spool and the curved valve cage cooperate to control the flow window opening size, and the noise reduction cage and the curved valve cage form a valve cage structure located above the valve seat through the valve spool in the curved valve cage to change the flow window opening size, so as to control the flow.

The noise reduction holes on the noise reduction valve cage are evenly distributed on the noise reduction valve cage and staggered up and down, and the noise reduction holes are set up with uniform flow rate and good diffusion effect, which can effectively reduce noise. The noise-reducing valve cage material adopts stainless steel nitriding treatment to improve the scouring resistance of the noise-reducing holes on the cage and the overall pressure-bearing strength of the cage. The diameter of the noise reduction hole is set from Φ1 mm to Φ6 mm, and the noise reduction valve cage adopts the internal and external double-layer valve cage structure, with a gap between the internal and external double-layer valve cage structure, and the noise reduction effect is better.

The flow window on the curve valve cage includes long-necked large window and short-necked small window, the long-necked large window and short-necked small window are the same and evenly distributed in a circle on the curve valve cage, making the number of flow windows on the curve valve cage increased and evenly distributed, the fluid beam distribution is more uniform, the flow window can not only control the flow volume but also achieve the purpose of noise reduction. It is similar to the noise reduction valve cage in forming a two-stage noise reduction function; with the increase of the number of flow windows on the curve cage, the rotating torque around the valve core is evenly distributed, eliminating the looseness and falling off problems caused by uneven force on the valve core. The number of flow windows on the curve cage is 8~16 and even, and they can be set symmetrically. The long neck area of the long neck window is biased towards the valve seat, as shown in Figure 2, the long neck area exceeds the short neck small window biased towards the valve seat, the long neck large window and the short neck small window cooperate to form a flow window with equal percentage flow characteristics, and the flow window is made according to the equal percentage flow characteristics; the flow window on the curve valve cage is used to achieve noise reduction and at the same time can meet the equal percentage flow characteristic adjustment. When the long-necked large window is in small opening, the spool only needs to open the long-necked area of the long-necked large window for small opening flow control, and in small opening, the area where the spool opens the flow window is concentrated in the long-necked area of the long-necked large window, in the case of uniform distribution of the long-necked large window and short-necked small window, avoiding the problems of small opening, and when the flow window size is too small, flow resistance is too large, flow rate is too fast, and flow rate instability causes valve vibration and oscillation.

Noise reduction valve cage and curve valve cage have a gap between them so that the media can be redistributed after passing through the upper cage and the media can flow evenly into the next cage, balancing media energy.

4. Fluid Properties

4.1. Fluid Flow Coefficient. By keeping the differential pressure flow coefficient between the inlet and outlet of the regulating valve at 105.5, the water flow rate of 40 ° C per hour can be obtained, which can measure the flow capacity of the regulating valve and facilitate the research on the opening and closing, regulation, noise reduction, and other performances of the regulating valve. A larger value of the flow coefficient (Cv) indicates a better flow capacity of the regulating valve. For incompressible fluids [27],

$$C_v = \frac{10U}{\sqrt{\Delta p/\varepsilon}}, \tag{1}$$

where C_v is the flow coefficient, U is the volume flow, Δp is the differential pressure before and after the control valve, and ε is the relative density of water which is 1.

For compressible media, such as gases, the compressible gas flow coefficient based on the expansion coefficient method is used. Control valve differential pressure ratio K is less than the product of the critical differential pressure ratio K_t and specific heat ratio coefficient λ ($K < K_t\lambda$), and the flow inside the valve cavity is non-blocking flow:

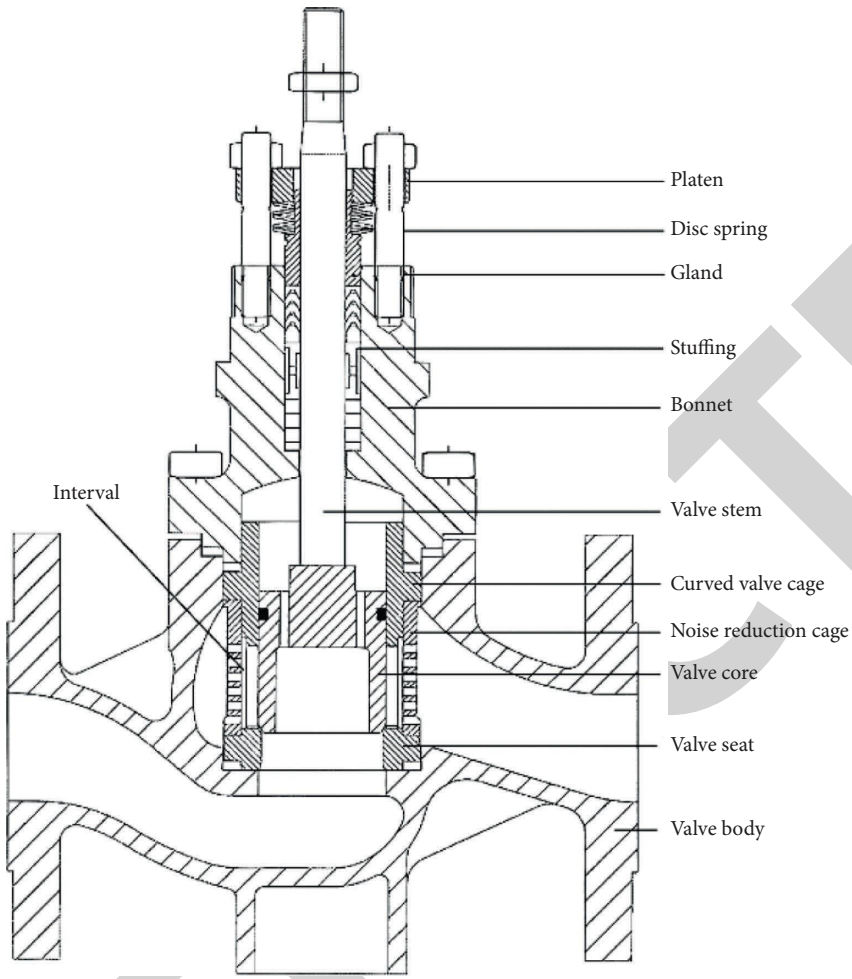

Figure 1: Noise-reducing two-stage cage control valve structure.

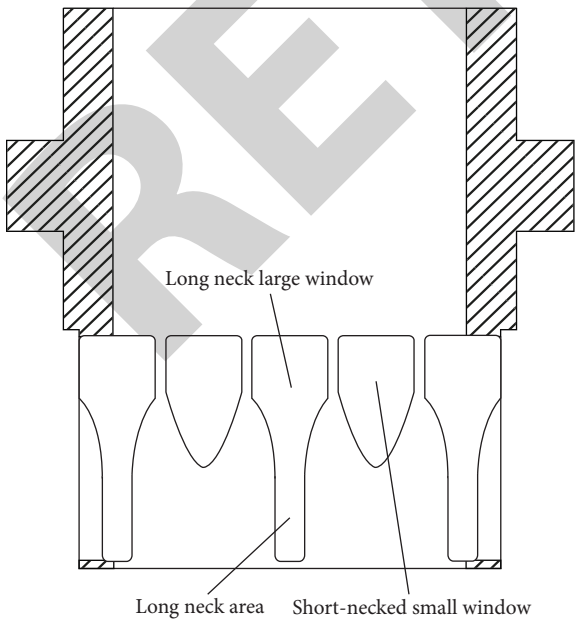

Figure 2: Curved valve cage structure.

$$C_v = \frac{U_0}{4.44 p_1 \eta}\sqrt{\frac{T\rho_1 Y}{K}},$$
$$\eta = 1 - \frac{K}{3\lambda K_t}, \quad (2)$$
$$K = \frac{\Delta p}{p_1},$$

where U_0 is the gas standard volume flow rate, p_1 is the prevalve pressure, η is the gas flow through the regulating valve density change expansion coefficient, T is the control valve inlet temperature, ρ_1 is the gas density at 273.15 K, 101300 Pa, Y is the compression factor, K is the compression ratio, K_t is the critical pressure difference ratio, and λ is the specific heat ratio coefficient.

Control valve differential pressure ratio$K$is greater than or equal to the product of the critical differential pressure ratio$K_t$and specific heat ratio coefficient λ ($K \geq K_t\lambda$), the internal flow of the valve cavity for blockage flow. The pressure before the valve$p_1$remains constant, and gradually reduce the pressure after the valve; the flow will not increase, at this time,

$$C_v = \frac{U_0}{2.48 p_1} \sqrt{\frac{T_0 \rho_1 Y}{\varsigma K_t}}, \quad (3)$$

where T_0 is the regulating valve inlet temperature during blockage flow and ζ is the gas isentropic index.

4.2. Flow Rate Characteristic Curve. Cv of each opening of the noise-reducing two-stage cage control valve is measured through the flow test. The characteristic test system of the control valve flow test system includes pressure pump, thermometer, throttle valve, temperature sensor, flow sensor, pressure sensor and flow meter, and so on. The schematic diagram of the control valve flow test system is shown in Figure 3.

The pipe before and after the control valve is a straight section, the length of the straight section needs to meet the test requirements to ensure that the fluid flow rate is uniform and continuous, and the nominal size of the test pipe and the location of the control valve are shown in Figure 4.

The pressure difference Δp, Cv, pressure recovery coefficient FL, flow resistance coefficient μ, and temperature t are measured for each degree of opening from 0% to 100% and from fully closed to fully open at 5% intervals, taking into account the flow status, piping material, and application conditions. The test medium is room temperature water at 21.6°C with a density of 1 g/cm^3. Fluid flow through the regulating valve produces flow resistance consumption and the pressure recovery coefficient FL:

$$\mathrm{FL} = \frac{U_{\max}}{0.1 C v \sqrt{(p_1 - 0.96 p_e)/p}}, \quad (4)$$

where FL is the pressure recovery factor, $U_{\max}$ is the maximum volume flow rate, p_e is the fluid saturated vapor pressure at the inlet temperature of the control valve, and ρ is the fluid density.

Fluid flow resistance coefficient [28]:

$$\mu = \frac{2\Delta p}{\rho v^2}, \quad (5)$$

where μ is the flow resistance coefficient and v is the flow rate.

Nominal diameter DN65, stroke of $L = 50$ mm, adjustable ratio of 50, rated Cv value of 85. differential pressure Δp, Cv, pressure recovery coefficient FL, flow resistance coefficient μ, and temperature t at each opening of the control valve are shown in Table 2.

The flow characteristic curve of the regulating valve is shown in Figure 5 by fitting the curve to the Cv value at each opening degree.

As seen in Figure 5, the flow characteristic curve of the noise-reducing two-stage cage control valve refers to equal percentage flow characteristic, indicating that the long-necked flow large window and short-necked flow small window on the curved valve cage ensure the equal percentage flow characteristic of the control valve. At 50% opening, the Cv value is 12.02, and at 100% opening, the Cv value is 85. At 0% to 50% opening, the Cv increases slowly and the flow is slow, and at 50% to 100% opening, the Cv increases dramatically and the flow capacity rises. The control valve regulates the flow smoothly and accurately and can meet the requirements of various media and working conditions.

The Cv curves for the nominal diameters DN65, DN80, and DN100 of the regulating valve with stroke $L = 50$ mm are shown in Figure 6.

For the same stroke $L = 50$ mm, the rated Cv is 85 for nominal diameter DN65, 110 for DN80, and 200 for DN100. From DN65 to DN80, the Cv increases by 25 for a 15 mm increase in nominal diameter and by 90 for a 20 mm increase in nominal diameter from DN80 to DN100. Under the same stroke, increasing the nominal diameter can improve the flow capacity of the regulating valve and nominal diameter with a small increase; the rated Cv will increase significantly, the flow capacity will also increase significantly, and the smaller the pressure loss of fluid through the regulating valve, the better the noise reduction of two-stage cage regulating valve flow regulation performance.

Itinerary $L = 50$ mm, nominal diameter DN80, stroke $L = 60$ mm, nominal diameter DN125, stroke $L = 75$ mm, nominal diameter DN200, stroke $L = 100$ mm, nominal diameter 300, stroke $L = 150$ mm, nominal diameter DN400, different strokes, different nominal diameters, and Cv curves are shown in Figure 7.

For different strokes and different nominal diameters, the rated Cv for stroke $L = 60$ mm, nominal diameter DN125 is 280, stroke $L = 75$ mm, nominal diameter DN200 is 690, stroke $L = 100$ mm, nominal diameter DN300 is 1300, stroke $L = 150$ mm, and nominal diameter DN400 has a rated Cv which is 1800; from DN80 to DN125, the nominal diameter increases by 45 mm, and the Cv increases by 170; from DN125 to DN200, the nominal diameter increases by 75 mm, and the Cv increases by 410; from DN200 to DN300, the nominal diameter increases by 100 mm, and the Cv increases by 610; from DN300 to DN400, the nominal diameter increases by 100 mm and the Cv increases by 500, indicating that the increase is stepwise; as the stroke increases, the nominal diameter also increases gradually, the rated Cv increases, and the curvature of the Cv curve increases rapidly, all of which are equal percentage characteristics. If the stroke increases, the nominal diameter increases; with the increase of opening, the Cv increases; if the same opening stroke and nominal diameter are large, the flow coefficient is also large, and the regulating valve flow capacity increases. For noise reduction double-stage cage adjustment for different strokes and different nominal diameters, the flow characteristics are equal percentage flow characteristics, and flow adjustment is gentle and sensitive.

4.3. Fluid Dynamics Simulation Analysis. Noise-reducing two-stage cage control valve with nominal diameter DN65 and rated stroke of $L = 50$ mm (Solidworks modeling) is shown in Figure 8.

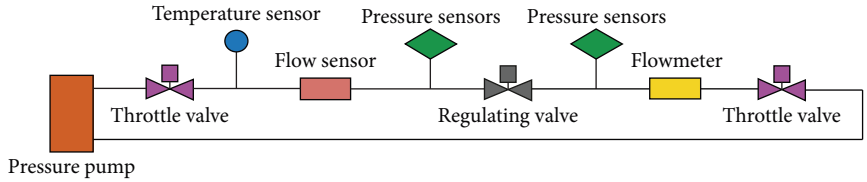

Figure 3: Schematic diagram of the control valve flow test system.

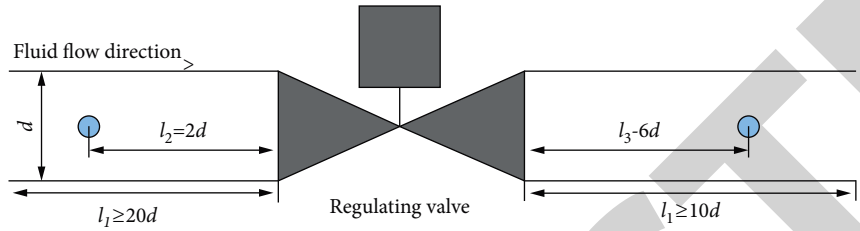

Figure 4: Nominal pipe size and adjustment position.

Table 2: Variation of opening and flow coefficient.

Openness (%0)	Δp (kPa)	μt/°	Cv	FL	
0	99.99	0.95	1.74	20.81	21.6
5	99.95	0.94	2.07	16.32	21.6
10	99.91	0.94	2.51	13.14	21.6
15	99.87	0.94	3.06	9.86	21.6
20	98.33	0.94	3.72	5.97	21.6
25	97.59	0.93	4.52	4.34	21.6
30	92.14	0.93	5.50	3.09	21.6
35	85.86	0.93	6.68	2.65	21.6
40	77.23	0.93	8.13	1.98	21.6
45	69.15	0.92	9.89	1.43	21.6
50	59.31	0.92	12.02	1.19	21.6
55	52.42	0.92	14.62	0.87	21.6
60	44.82	0.92	17.78	0.69	21.6
65	36.37	0.91	21.62	0.61	21.6
70	31.95	0.91	26.29	0.55	21.6
75	23.08	0.91	31.97	0.48	21.6
80	18.46	0.91	38.87	0.43	21.6
85	12.79	0.90	47.27	0.36	21.6
90	8.03	0.90	57.48	0.30	21.6
95	6.62	0.90	69.90	0.23	21.6
100	3.54	0.90	85.00	0.19	21.6

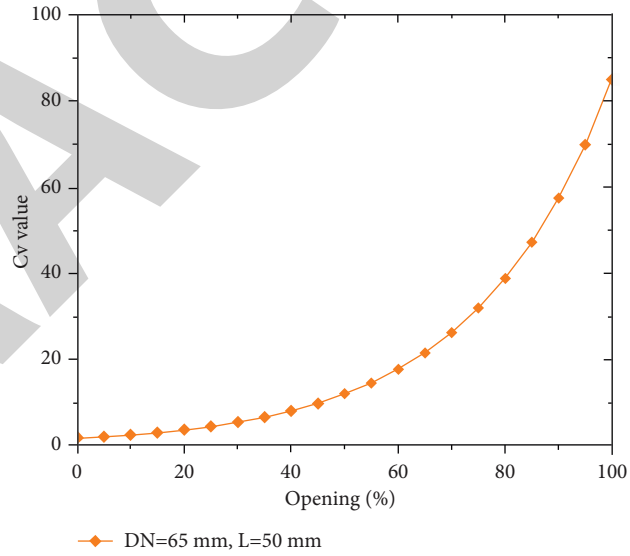

Figure 5: Control valve flow characteristic curve.

Solidworks Flow Simulation fluid dynamics simulation was performed to calculate and analyze parameters such as velocity, pressure, and vortex at 20% and 100% opening. The medium used is water vapor, having density of 0.6 kg/m^3, temperature of 20.05°C, and inlet velocity of 0.5 m/s, with static outlet pressure.

The pressure, velocity, flow traces, and vortex clouds are shown in Figures 9–12 for a 20% opening (small opening of the regulating valve).

From Figure 9, the maximum pressure of fluid in the valve cavity is 0.066 MPa, and the pressure decreases in steps through the curved cage and the noise reduction cage. It shows that the curved cage and the noise reduction cage not only reduce the noise by pressure change but also control the flow rate. The pressure around the inner side of the spool is evenly distributed, and the spool is evenly and firmly stressed. From Figures 10 and 11, the fluid from the valve cavity from bottom to top flows through the long neck area and noise reduction hole; when entering the long neck area of the long neck window, the circulation area decreases, and the maximum speed is 1.642 m/s; after flowing through the noise reduction hole, the speed drops to 0.076 m/s; after flowing through the curve valve cage and noise reduction valve cage, there is no significant change in speed compared with the flow. It shows that the flow velocity is uniform, the flow resistance is small, the control valve is stable, there is vibration damping, and the noise reduction effect is good. From Figure 12, the maximum value of vortex 278.161/s is located at the contact point between the small short neck window and the spool, and the vortex in the valve cavity and the inlet and outlet is low, indicating that the long and short neck windows and noise reduction holes reduce noise and play a role in noise reduction.

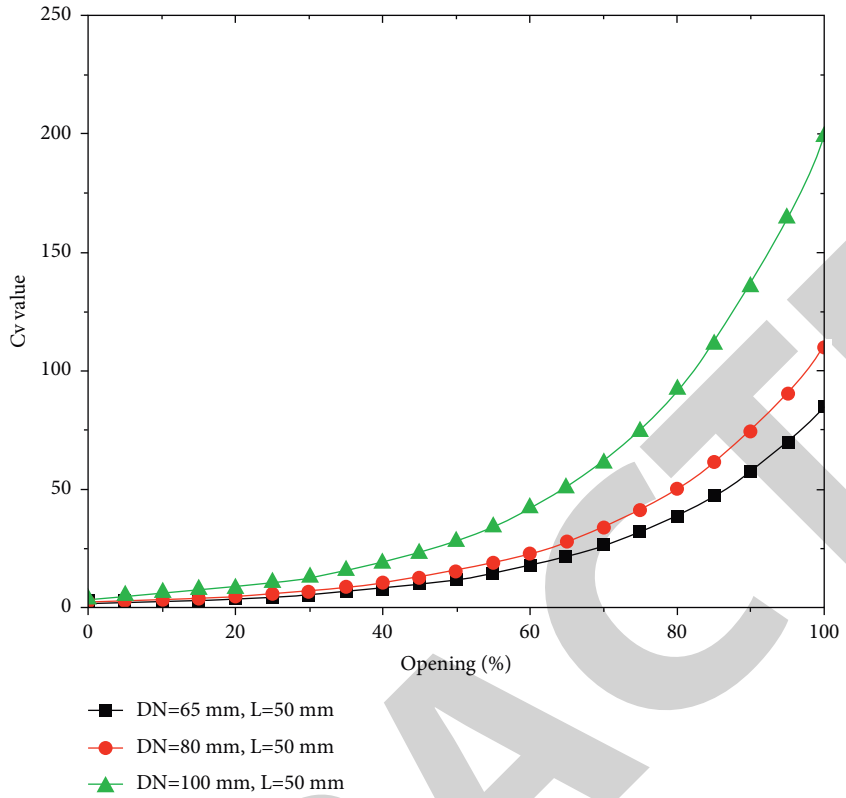

Figure 6: Variation of Cv with nominal diameter for the same stroke.

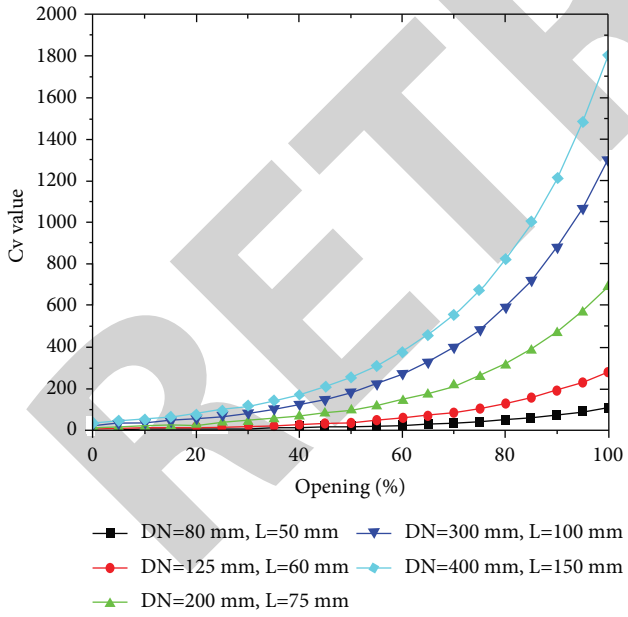

Figure 7: Variation of Cv for different strokes with different nominal diameters.

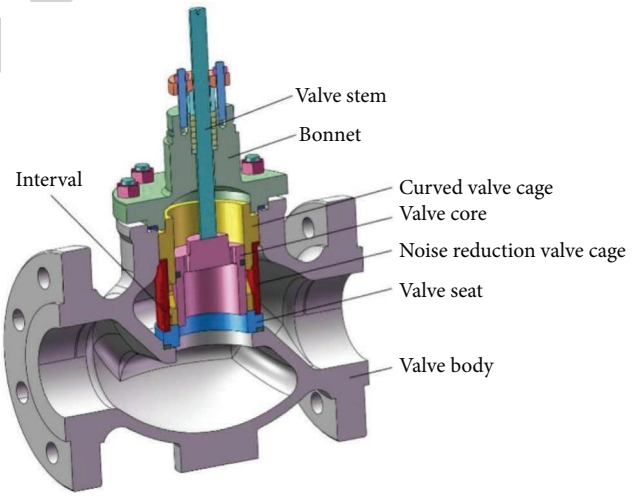

Figure 8: Ball valve model.

The pressure, velocity, flow traces, and vortex clouds are shown in Figures 13–16 for a 100% opening (fully open regulating valve).

Figure 13shows that the maximum pressure of the fluid in the valve chamber is 0.016 MPa. It can be seen that the fluid pressure of the long and short neck windows at the curve valve cage drops to 0.0004 MPa, and the fluid pressure between the right side of the noise reduction valve cage and the upper outlet of the valve chamber is also negative, which indicates that the fluid force is suction, the lower pressure is positive, and fluid flows out. The curved cage and the noise-reducing cage are shown to be effective in reducing noise through pressure changes while controlling flow. The pressure around the spool is evenly distributed and the force is evenly distributed, so there is no twisting force caused by uneven pressure. From Figures 14 and 15, the fluid from the valve cavity from bottom to top flows through the long and

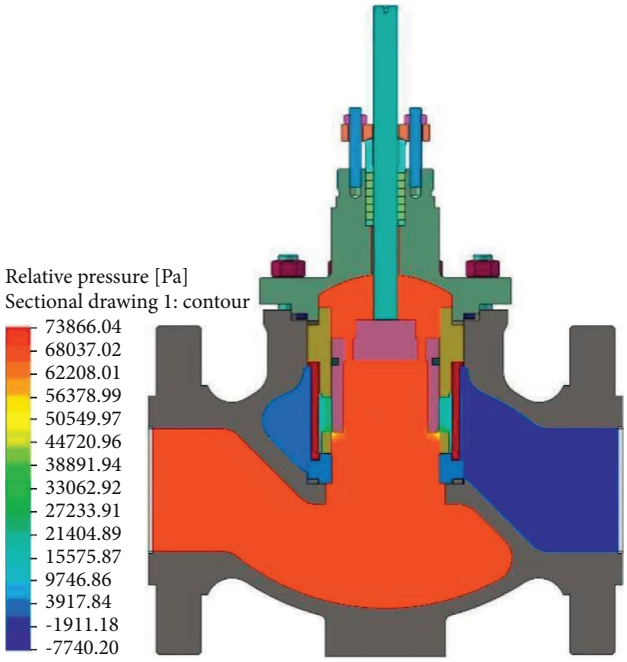

Figure 9: Pressure cloud chart for 20% opening.

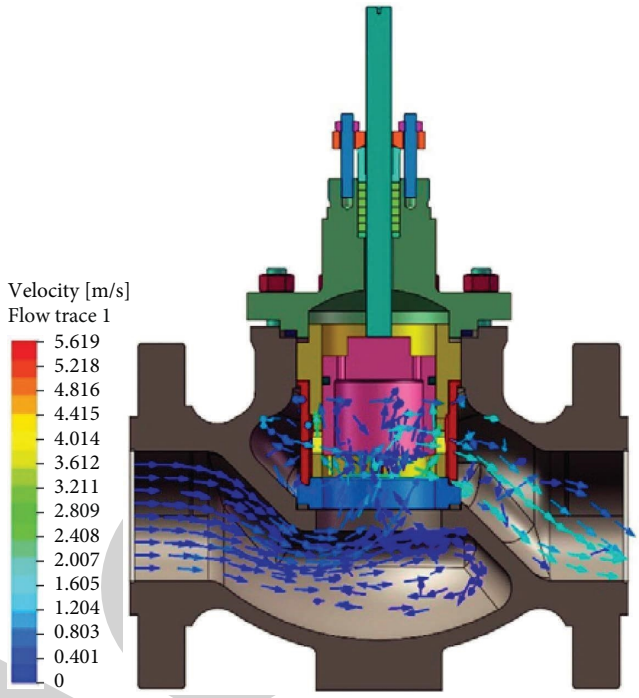

Figure 11: Flow trace diagram for 20% opening.

Figure 10: Speed cloud map for 20% opening.

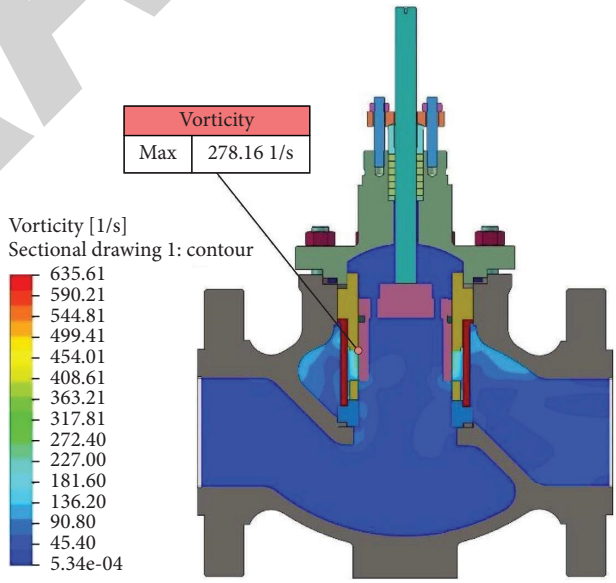

Figure 12: Vortex volume cloud map for 20% opening.

short neck area and noise reduction hole, and the maximum speed of fluid is 0.994 m/s, which is located in the middle area of the valve seat; after flowing through the noise reduction hole, the flow rate is 0.122 m/s, and the flow rate is significantly reduced. It shows that the long and short neck windows and noise reduction holes are evenly distributed, which makes the fluid beam distribution more uniform and the regulating valve smooth with effective noise reduction. From Figure 16, it can be seen that the maximum vortex flow is 125.131/s, and the vortex flow in the valve chamber, inlet, and outlet is lower than 801/s in the microgroove, which indicates that the whole valve chamber is low noise, and it can be concluded that the bending valve cage and noise reduction valve cage can significantly reduce the noise.

The inlet pressure-opening curve of the flow window on the left side of the control valve and the outlet pressure-opening curve of the noise-reducing orifice on the left side are shown in Figure 17.

Right flow window inlet pressure-opening curve and right noise reduction orifice outlet pressure-opening curve are shown in Figure 18.

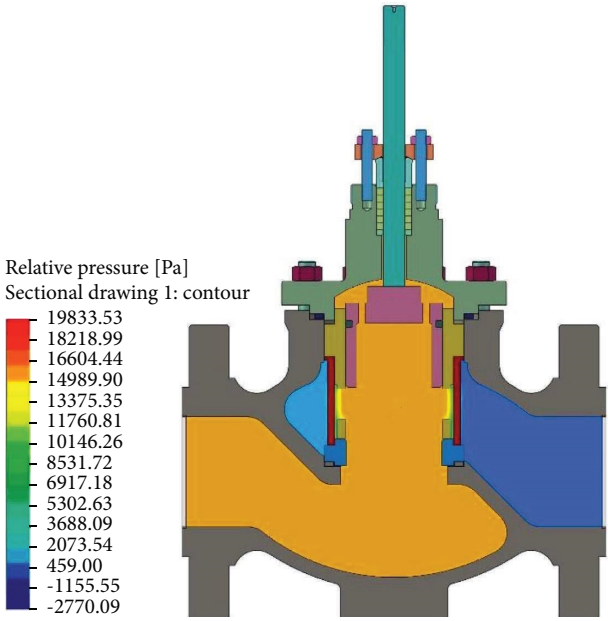

Figure 13: Pressure cloud map for 100% opening.

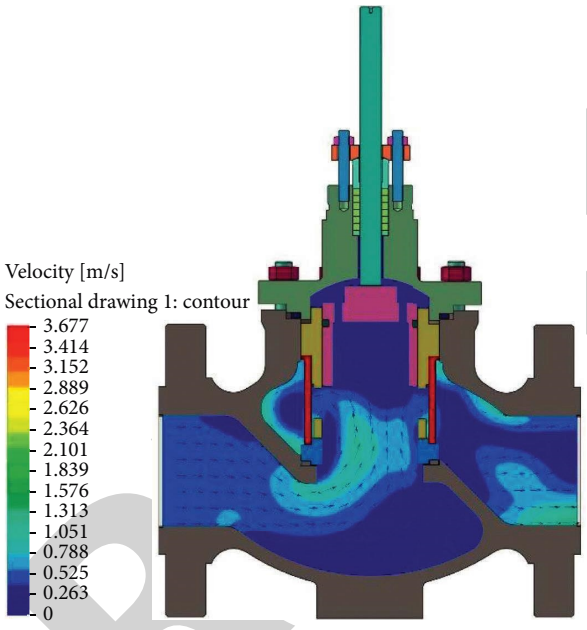

Figure 14: Speed cloud map for 100% opening.

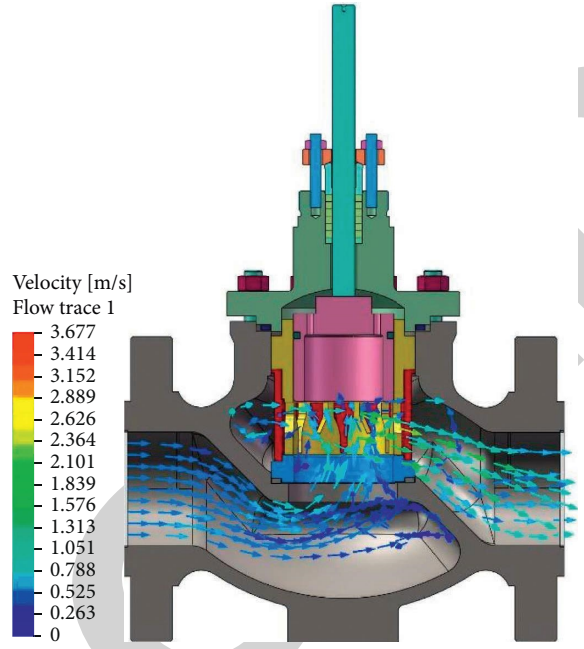

Figure 15: Flow trace diagram for 100% opening.

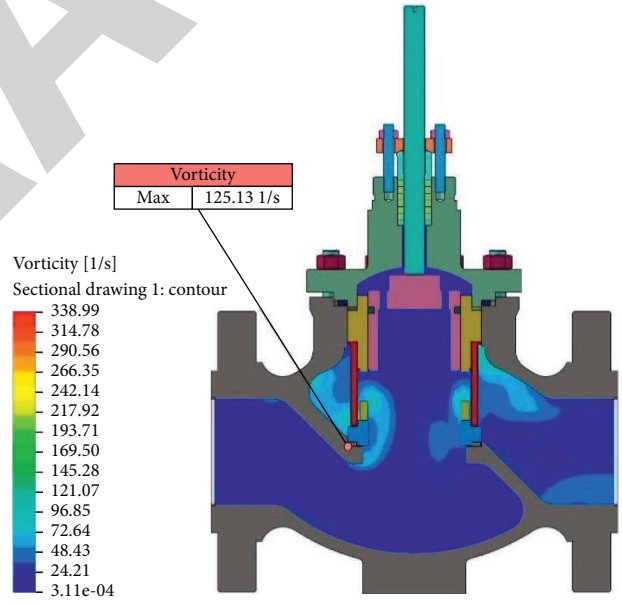

Figure 16: Vortex volume cloud map for 100% opening.

In the left and right sides of the flow window, noise reduction hole fluid inlet and outlet pressure increases first with the opening degree and then decreases; in the small opening degree of 5%~15%, pressure value reaches the maximum. The pressure before entering the flow window is less than the noise reduction orifice outlet pressure, and the right noise reduction orifice outlet pressure is less than the left noise reduction orifice outlet pressure, which is in line with the structural characteristics that the right side is the outlet and the pressure reduction is greater than the left side. The pressure before entering the flow window is less than the noise reduction orifice outlet pressure, and the right noise reduction orifice outlet pressure is less than the left noise reduction orifice outlet pressure, which is in line with the structural characteristics that the right side is the outlet and the pressure reduction is greater than the left side. It shows that the flow window and the noise reduction orifice make the pressure before and after the fluid change, and the pressure reduction makes the internal force of the fluid and the force of the fluid on the valve cavity reduce, the flow is regulated, and the noise is reduced.

The inlet velocity-opening curve of the left flow window and the outlet velocity-opening curve of the left noise reduction orifice are shown in Figure 19.

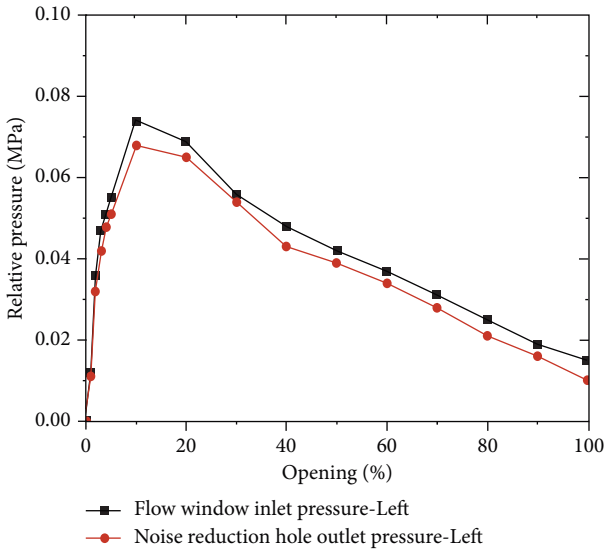

Figure 17: Pressure-opening curve at the inlet and outlet of the left flow window noise reduction orifice.

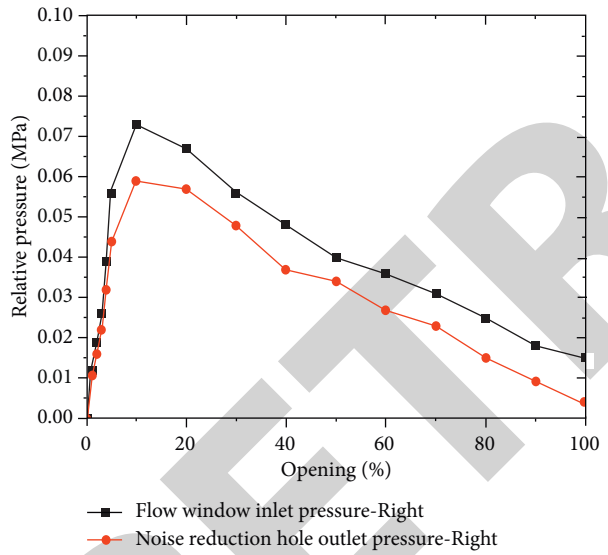

Figure 18: Right flow window noise reduction orifice inlet and outlet pressure-opening curve.

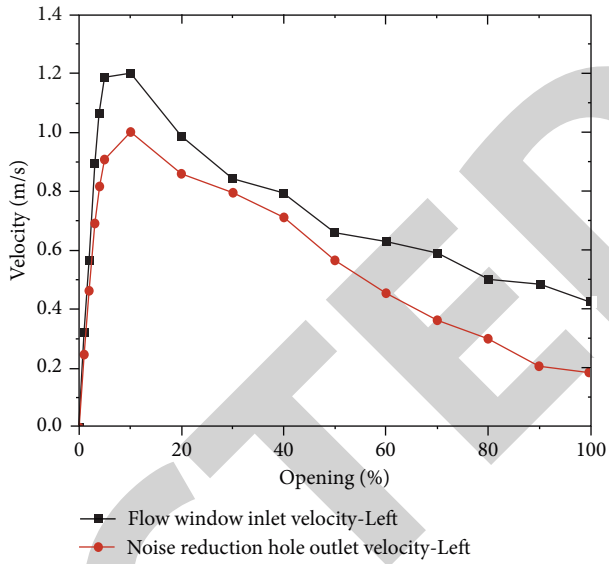

Figure 19: Left flow window noise reduction orifice inlet and outlet velocity-opening curve.

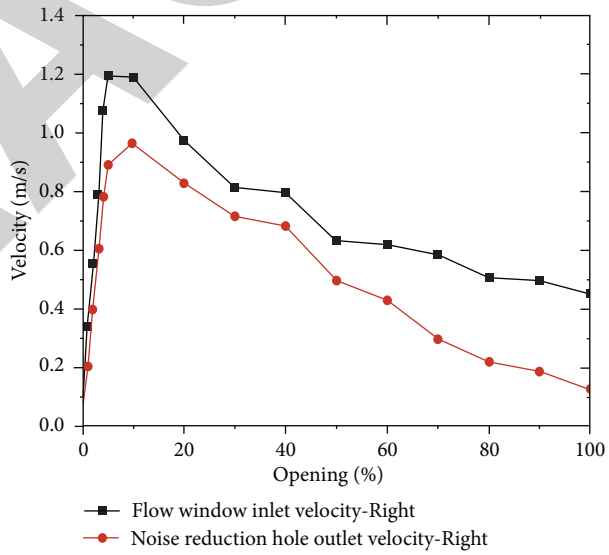

Figure 20: Right flow window noise reduction orifice inlet/outlet velocity-opening curve.

The inlet velocity-opening curve of the right flow window and the outlet velocity-opening curve of the right noise reduction orifice are shown in Figure 20.

The velocity of fluid in and out of the noise-reducing orifice on the left and right sides of the flow window also increases with the opening degree and then decreases, reaching the maximum velocity value at a small opening degree of 5% to 15%. The flow rate changes before and after the flow window and noise reduction orifice, the internal velocity of the fluid is reduced, and the reduced flow rate not only regulates the flow rate but also reduces the noise.

The vortex curve of the noise-reducing two-stage cage control valve is shown in Figure 21.

From Figure 21, the vortex volume increases and then decreases with the increase of the opening degree. The vortex volume is large at small opening of 5%~10% and decreases exponentially and rapidly at opening of 10%~25%; at opening of 25%~40%, the vortex volume continues to decrease; at opening of 40%~100%, the vortex volume changes very little and tends to be constant. At large opening, the flow rate is larger, but the vortex movement changes very little, and the regulating valve still operates stably.

The drag coefficient curve of the noise-reducing two-stage cage control valve is shown in Figure 22.

From Figure 22, the test and simulation results show the same trend, the drag coefficient decreases with the increase of opening degree. The resistance coefficient is large at small opening and decreases rapidly in exponential form at 0%–25% opening; at 25%–50% opening, the resistance coefficient

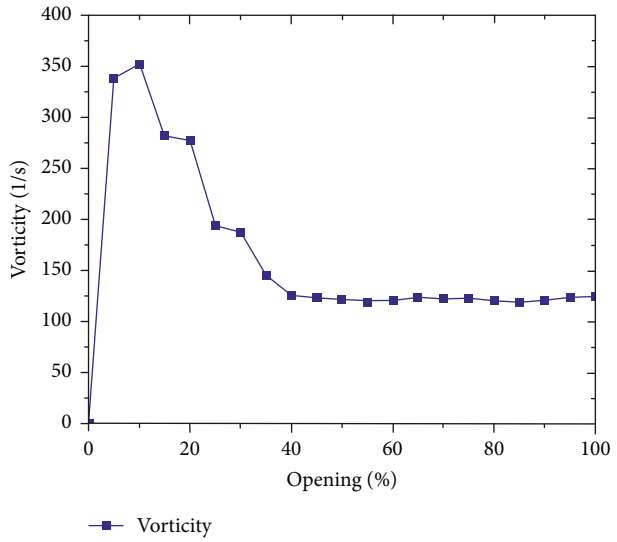

Figure 21: Vortex volume curve.

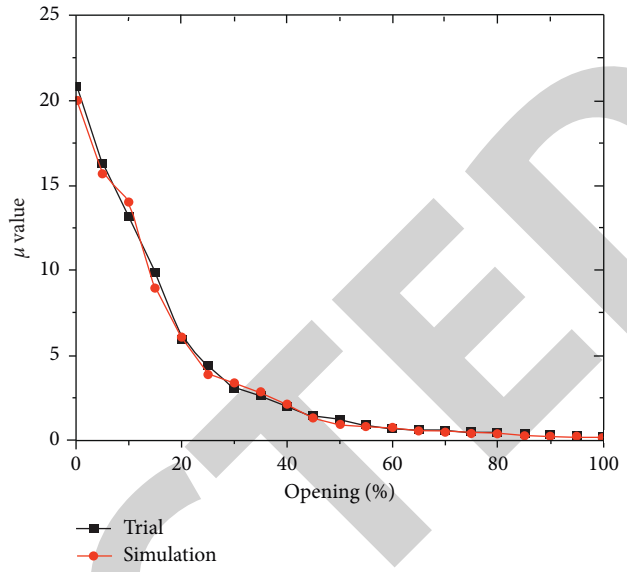

Figure 22: Resistance coefficient curve.

decreases continuously, but at a slower rate; at 50%–100% opening, the resistance coefficient changes very little and remains basically stable. The effect of curved valve cage and noise-reducing valve cage on the resistance coefficient of the regulating valve is larger at small openings, and the effect on the resistance coefficient of the regulating valve is relatively small at large openings. At small opening, the flow resistance is small, the flow rate is small, and the regulating valve operates stably.

4.4. Cavitation Properties of Air Cavities

4.4.1. Air Cavitation Analysis. Liquid flows through the regulating valve due to the throttling effect, and the flow rate and pressure at the throttle port will be a sharp change. When the pressure reaches or is lower than the fluid temperature, part of the liquid vaporizes into bubbles, and sublimation occurs. The fluid is in a gas-liquid two-phase state. When the fluid leaves the throttle valve, the pressure rises, which is greater than the saturated steam pressure, and the bubble breaks into liquid. Vapor forms cavitation, which is the main factor to generate flow noise and affects the stability and service life of the regulating valve.

The magnitude of cavitation generation is measured by the cavitation coefficient, σ_c:

$$\sigma_c = \frac{p_2 - p_v}{p_1 - p_2}, \tag{6}$$

where σ_c is the air cavity coefficient, p_2 is the pressure at the valve, and p_v is the fluid saturated vapor pressure at the throttle.

The magnitude of the cavitation effect is measured by the cavitation coefficient. Cavitation coefficient k_a [29]:

$$K_a = \frac{p_2 - p_v}{\sigma_c (p_1 - p_v)}, \tag{7}$$

where k_a is the cavitation factor.

In the flow of noise, there are liquid power noise and gas power noise, and noise affects the performance of the regulating valve, so noise estimation is important for noise reduction. When the liquid flows, $\Delta p \le p_r$, liquid flow sound pressure level:

$$\mathrm{SPL}_0 = 10\lg\left(1.17C_{v_0}\right) + 20\lg(0.01\Delta p) - 30\lg b + 70, \tag{8}$$

where SPL_0 is the fluid dynamic noise sound pressure level, C_{v_0} is the flow coefficient at a specific flow rate, b is the pipe wall thickness, and Δp_r is the regulating valve differential pressure at the start of cavitation.

When the liquid flows, $\Delta p_r < \Delta p < \Delta p_s$, the initial cavitation sound pressure level:

$$\mathrm{SPL}_1 = 10\lg\left(1.17C_{v_0}\right) + 20\lg(0.01\Delta p) + \frac{5[\Delta p - K_a(p_1 - p_v)]}{(p_1 - p_v)\left(\mathrm{FL}^2 - K_a\right)} \cdot \lg[0.145(p_2 - p_v)] - 30\lg\varepsilon + 70, \tag{9}$$

where SPL_1 is the initial cavitation fluid flow sound pressure level, K_a is the initial cavitation factor, and Δp_s is the regulating valve differential pressure at full cavitation.

When the liquid flows, $\Delta p > \Delta p_s$, $p_2 > p_v$, fully cavitated sound pressure level:

$$\mathrm{SPL}_2 = 10\lg\left(1.17C_{v_0}\right) + 20\lg(0.01\Delta p) + \frac{5[\Delta p - K_a(p_1 - p_v]}{\left(p_1 - p_v\left(\mathrm{FL}^2 - K_a\right)\right.} \cdot \lg[0.145(p_2 - p_v)] - 30\lg\varepsilon - 5\lg[0.01(\Delta p - \Delta p_r)] + 64, \tag{10}$$

where SPL_2 is the sound pressure level of fully cavitated fluid flow.

Water vapor sound pressure level when the gas is flowing:

$$\mathrm{SPL}_3 = 10\lg\left[6.8\times10^3 C_{v_0}\mathrm{FL}p_1p_2D^2\beta\frac{(1+0.00126T_1)^6}{\varepsilon}\right], \tag{11}$$

where SPL_3 is the water vapor flow sound pressure level, D is the diameter of pipe downstream of control valve, β is the audio efficiency, and T_1 is the steam superheat temperature.

Sound pressure level of gas other than water vapor when the gas is flowing:

$$\mathrm{SPL}_4 = 10\lg\left(30C_{v_0}\mathrm{FL}p_1p_2D^2\beta\frac{T_2}{\varepsilon^3}\right) + \mathrm{SL}_g, \tag{12}$$

where SPL_4 is the sound pressure level of gas flow other than water vapor, T_2 is the fluid temperature, and SL_g is the gas characteristic coefficient.

Translated withhttps://www.DeepL.com/Translator (free version):

$$M_{a1} = \frac{138W\left(1+0.00126T_1\right)}{p_2d^2}, \tag{13}$$

where M_{a1} is the Mach number of water steam outlet of control valve, W is the water vapor mass flow rate, and d is the control valve outlet diameter.

Control valve outlet diameter:

$$\mathrm{SPL}_5 = 10\lg\left[\frac{0.0208p_2^2d^2D^2M^8a_1\left(1+0.001267T_1^6\right)}{\varepsilon^3}\right], \tag{14}$$

where SP_5 is the control valve outlet water vapor sound pressure level.

Mach number of gases other than water vapor:

$$M_{a2} = \frac{6.2U_1\sqrt{\varepsilon T_2}}{p_2d^2}, \tag{15}$$

where M_{a2} is the Mach number of gas other than water vapor at the outlet of the control valve U_1 is the water vapor volume flow rate.

Sound pressure level of gases other than water vapor:

$$\mathrm{SPL}_6 = 10\lg\left(\frac{2.8p_2^2d^2D^2M^8a_2T_2}{10^4\varepsilon^3}\right) + SL_g, \tag{16}$$

where SPL_6 is the sound pressure level of gas other than water vapor at the outlet of control valve.

4.4.2. Cavitation Simulation Analysis. The cavitation phenomenon will generate vibration and noise, which affects the noise reduction of the regulating valve, so it is especially important to study the cavitation phenomenon. The model of the regulating valve is imported into Solidworks Simulation 2021, and the simulation model is shown in Figure 23.

Water at 90°C flows through the pipe at a speed of 4 m/s. The water flow is partially blocked in the middle by the spool, curved cage, and noise reduction cage, and the flow velocity and pressure drop are changed. The fluid density, Mach number, and acoustic pressure energy level clouds are shown in Figures 24–26 for 20% opening of the control valve.

The regulating valve opening (40%) fluid density cloud, Mach number cloud, and acoustic pressure energy level cloud are shown in Figures 27–29.

The 60% fluid density cloud, Mach number cloud, and acoustic pressure energy level cloud of the regulating valve opening are shown in Figures 30–32.

The regulating valve opening (80%) fluid density cloud, Mach number cloud, and acoustic pressure energy level cloud are shown in Figures 33–35.

With opening of 20%, 40%, 60%, and 80%, it is clear from Figures 24, 27, 30, and 33 that the fluid density in the pipe and ball valve is uniformly distributed and there are no areas of reduced density; therefore, no cavitation is generated in the pipe and ball valve by fluid flow. From Figures 25, 28, 31, and 34, we know that the maximum values of Mach number are 0.00632, 0.00561, 0.00546, and 0.00551, respectively, which are less than 1 and very small, indicating that the flow velocity is very low and the noise is very small. From Figures 26, 29, 30, and 35, the maximum values of acoustic energy level are 35.87 dB, 16.92 dB, 17.05 dB, and 16.73 dB, respectively, the acoustic energy level of 20% opening is below 40 dB, the acoustic energy levels of 40%, 60%, and 80% opening are below 20 dB, and the acoustic energy level of each opening is low, indicating that the noise is very small. The regulating valve is a quiet environment when working.

Opening of 20%, temperature variation, and inlet velocity vs. average fluid density curve are shown in Figure 36.

Opening of 20%, inlet velocity variation, and temperature vs. average fluid density curve are shown in Figure 37.

For the opening degree of 20%, in the case of constant opening degree, the temperature remains the same, and the average density increases with the inlet speed; at this time, the inlet speed should be increased to increase the average density of fluid to avoid cavitation. Noise reduction double-stage cage control valve small opening average density change is small, and cavitation is difficult to produce.

Opening of 100%, temperature variation, and inlet velocity vs. average fluid density curve are shown in Figure 38.

Opening of 100%, inlet velocity variation, and temperature vs. average fluid density curve are shown in Figure 39.

The opening degree is 100%; in the case of constant opening degree, the temperature remains unchanged, and the average density decreases with the increase of inlet speed; at this time, the inlet speed should be properly reduced to avoid the rapid decrease of the average density of the fluid, resulting in cavitation; the inlet speed remains unchanged, and the average density remains constant with the increase of temperature. Although the average density decreases with the increase of inlet velocity when the noise reduction double-stage cage control valve is opened at large degrees, the average density changes are small, and it is difficult to generate air pockets.

Constant inlet velocity, varying temperature, and opening vs. average fluid density curve are shown in Figure 40.

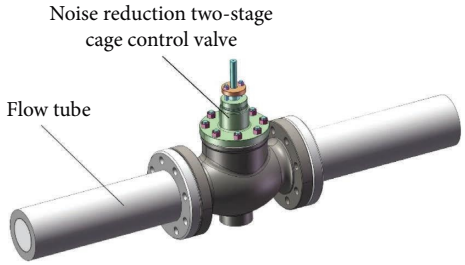

Figure 23: Calculation model of cavitation simulation.

Temperature vs. average fluid density curve with constant inlet velocity and varying opening is shown in Figure 41.

The inlet speed is constant, the temperature is constant, the average density increases with the opening degree, the opening degree increases, the flow capacity increases, and the flow rate increases; the opening degree is constant, and the average density changes very little with the increase in temperature and basically tends to remain the same. Noise reduction double-stage cage control valve inlet speed is constant, the average density change is small, and cavitation is difficult to produce.

With constant temperature and varying opening, the inlet velocity vs. average fluid density curve is shown in Figure 42.

With constant temperature and varying inlet velocity, the opening vs. average fluid density curve is shown in Figure 43.

The temperature remains unchanged, the opening degree is 20%, the inlet speed is 3.5 m/s~4.0 m/s, and the average density decreases with the increase of inlet speed; at this time, the inlet speed should be increased so that the inlet speed is greater than 4 m/s to improve the average density and avoid cavitation, the inlet speed is 4.0 m/s~6.0 m/s, and the average density increases with the increase of inlet speed; the opening degree is 40%, 60%, and 80%. The average density decreases as the inlet speed increases; at this time, the inlet speed should be reduced to avoid cavitation generation. The average density increases with the increase of opening degree and the increase gradually decreases, the average density remains unchanged with the increase of opening degree, the average density decreases with the increase of opening degree, the average density decreases with the increase of opening degree and the decrease gradually increases, and the opening degree should be reduced at this time to avoid cavitation; for the opening degree of 40%~80%, the average density increases with the increase of opening degree. Noise-reducing two-stage cage control valve temperature remains unchanged, the average density change is small, and cavitation is difficult to produce.

The size of the cavitation coefficient determines the size of the possibility of cavitation generation; the smaller the cavitation effect, the smaller the noise generated. With constant nominal diameter and varying inlet velocity, the cavitation coefficient varies with the opening curve, as shown in Figure 44.

For the inlet velocity of 3.5 m/s, 4.0 m/s, and 4.5 m/s, the cavitation coefficients are lower than 0.5, indicating that the inlet velocity is lower than 5 m/s; regardless of the opening degree, cavitation is not generated. At the inlet velocity of 5.0 m/s, the cavitation coefficient is greater than 0.5 for 20% and 40% opening and less than 0.5 for 60% and 80% opening, indicating that cavitation will be generated under small opening, which should increase the opening and reduce the cavitation coefficient, and cavitation will not be generated under large opening. The cavitation coefficient is higher than 0.5 when the inlet speed is 5.5 m/s and 6.0 m/s. The smaller the opening degree, the larger the cavitation coefficient, indicating higher possibility of cavitation, and the larger the opening degree, the smaller the cavitation coefficient, indicating smaller possibility of cavitation.

The variation curve of cavitation coefficient with inlet velocity for nominal diameter change and regulating valve half open is shown in Figure 45.

The cavitation coefficients of DN80, DN125, DN200, DN300, and DN400 nominal diameter control valves are lower than 0.5 when the inlet velocity is 3.5 m/s~5 m/s, indicating that the inlet velocity is lower than 0.5 m/s and no cavitation will occur for each nominal diameter control valve. The cavitation coefficients of DN80, DN125, and DN200 nominal diameter control valves increase with the inlet speed from 5 m/s to 6 m/s. The cavitation coefficients of DN300 and DN400 control valves also increase with the inlet speed, but the increase is smaller and the cavitation coefficients are less than 0.5, indicating that the smaller the nominal diameter is, the easier the cavitation occurs. The smaller the nominal diameter is, the easier the cavitation is generated; if the cavitation coefficient is greater than 0.5, it should increase the nominal diameter, reduce the cavitation coefficient, and reduce the possibility of cavitation.

The variation curve of cavitation coefficient with inlet velocity for nominal diameter change and full opening of regulating valve is shown in Figure 46.

The cavitation coefficients of DN80, DN125, DN200, DN300, and DN400 nominal diameter control valves are lower than 0.5 when the noise-reducing two-stage cage control valve is fully open and the inlet speed is 3.5 m/s~5 m/s, indicating that no cavitation occurs for each nominal diameter control valve. For the inlet speed of 5 m/s~6 m/s, the cavitation coefficient of nominal diameter DN80, DN125, DN200, DN300, and DN400 control valves increases with the increase of inlet speed; the smaller the nominal diameter, the greater the increase.

5. Test

In order to verify the effective noise reduction, flow control, equal percentage flow characteristic adjustment, and other functions of the noise reduction two-stage cage control valve, this chapter tests the control valve operation, valve small opening vibration, oscillation, valve element stress, and other factors.

5.1. Test Conditions. The test object is the control valve. Its specific parameters are diameter DN350, rated stroke 150 mm, rated flow coefficient 1600, nominal pressure PN20, pressure class 150, and leakage class IV. It is pneumatically

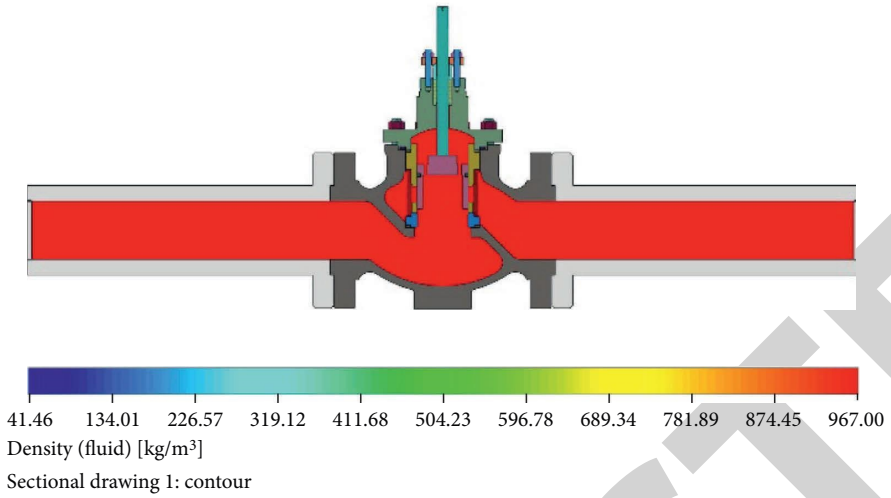

Figure 24: Fluid density cloud for 20% opening.

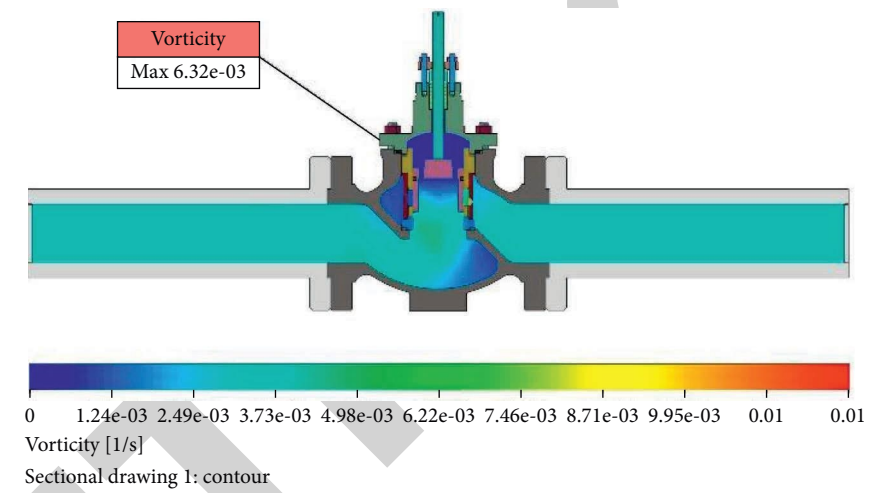

Figure 25: Mach number cloud map for 20% opening.

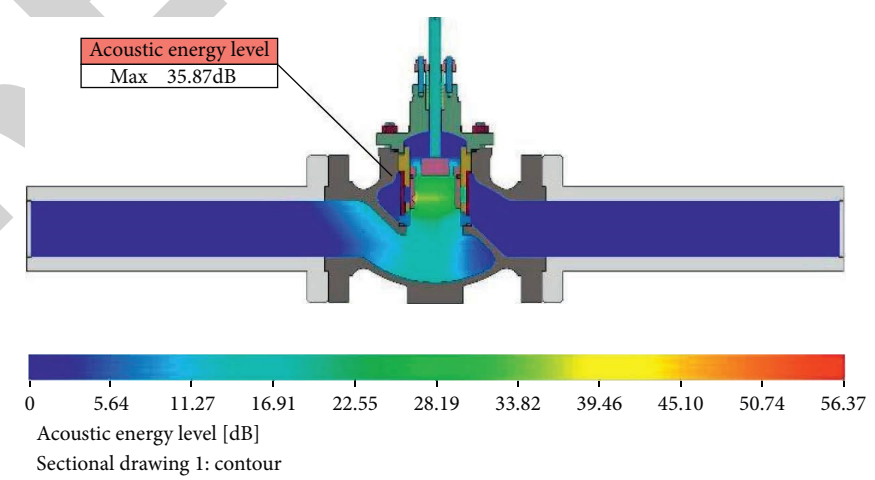

Figure 26: Acoustic energy level cloud map for 20% opening.

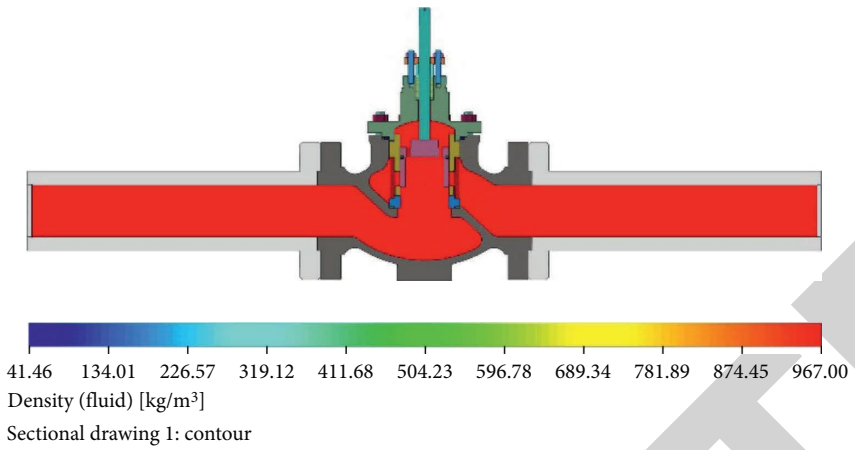

Figure 27: Fluid density cloud map for 40% opening.

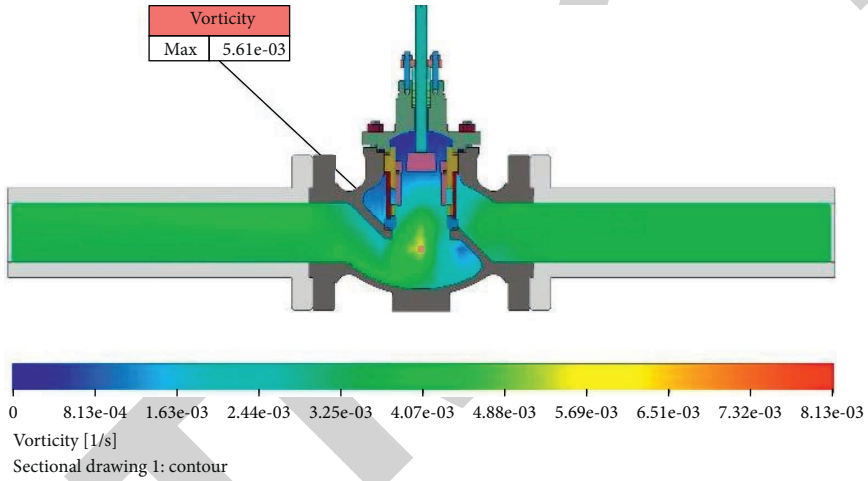

Figure 28: Mach number cloud map for 40% opening.

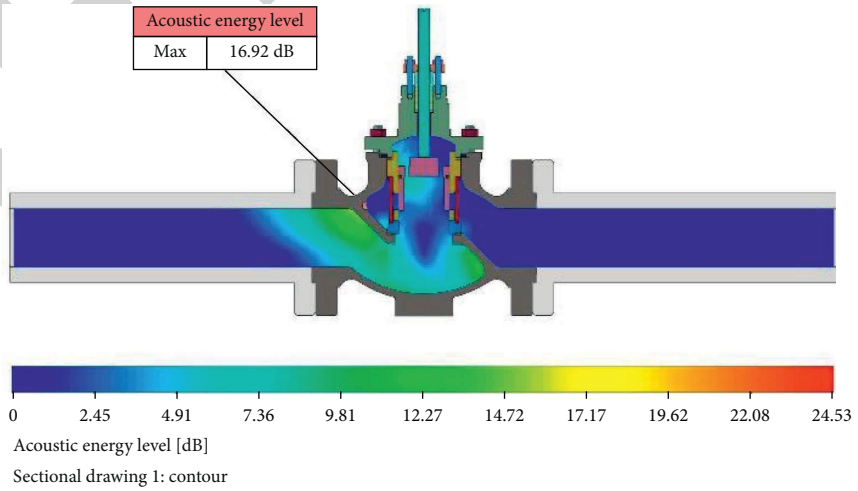

Figure 29: Acoustic energy level cloud map for 40% opening.

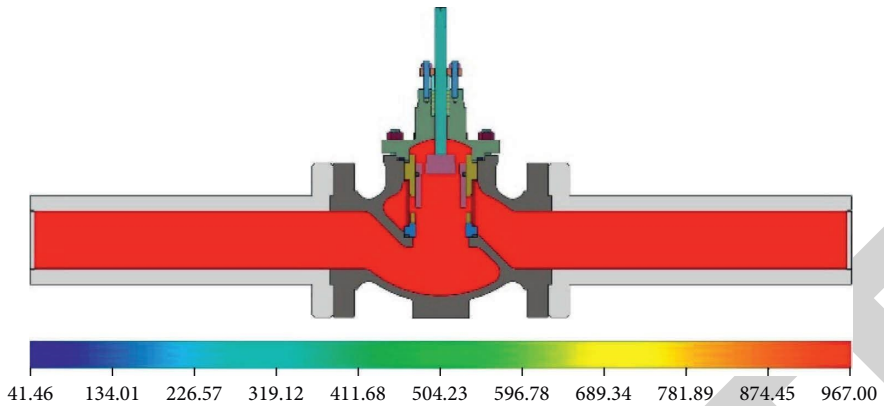

Figure 30: Fluid density cloud map for 60% opening.

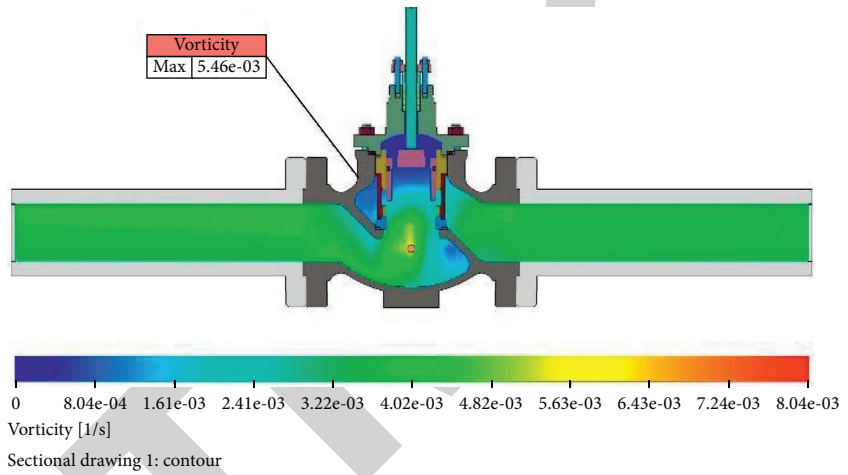

Figure 31: Mach number cloud map for 60% opening.

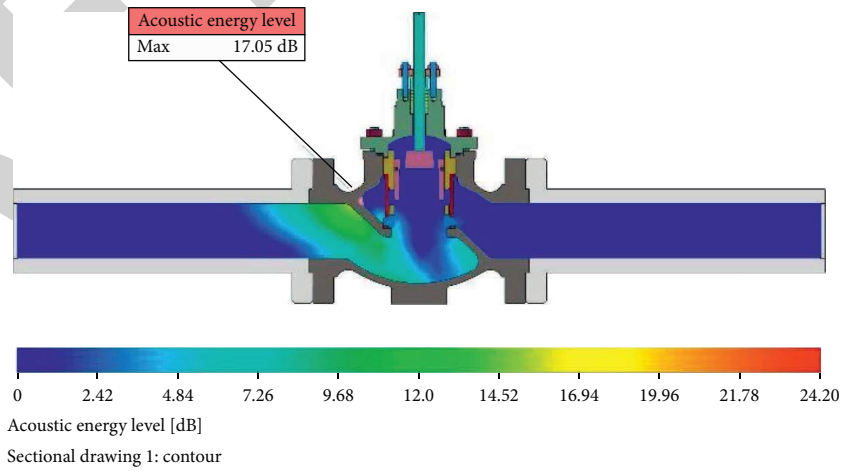

Figure 32: Acoustic energy level cloud map for 60% opening.

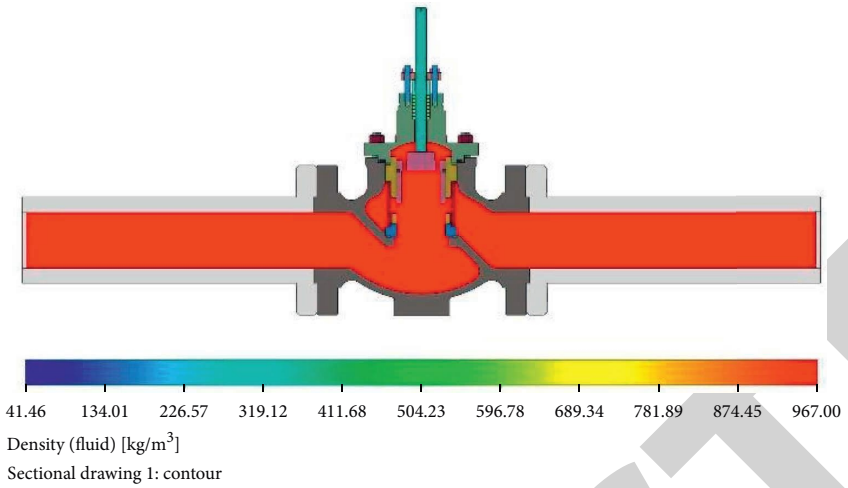

Figure 33: Fluid density cloud map for 80% opening.

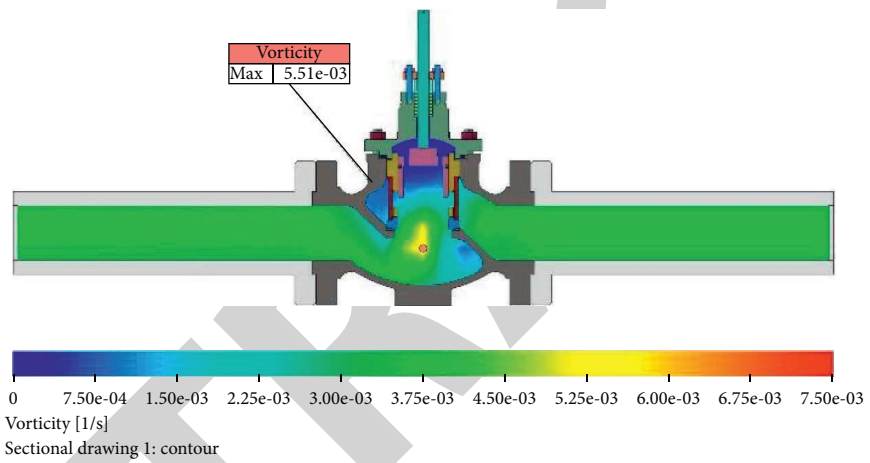

Figure 34: Mach number cloud map for 80% opening.

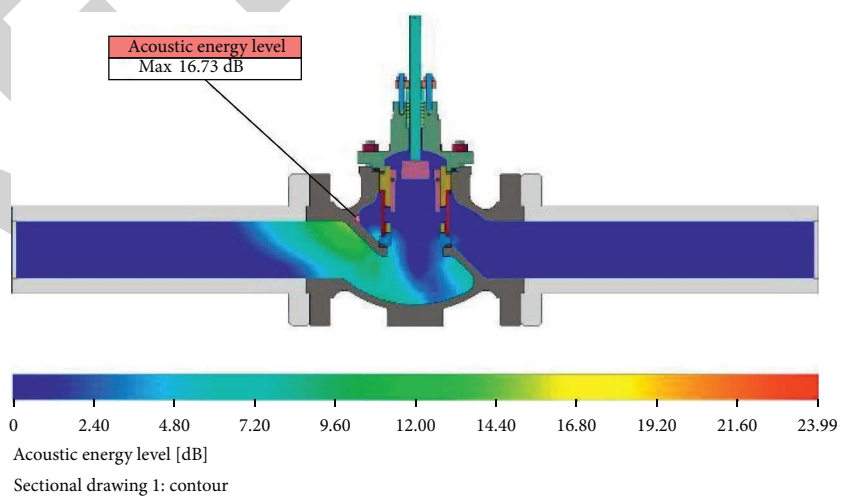

Figure 35: Acoustic energy level cloud map for 80% opening.

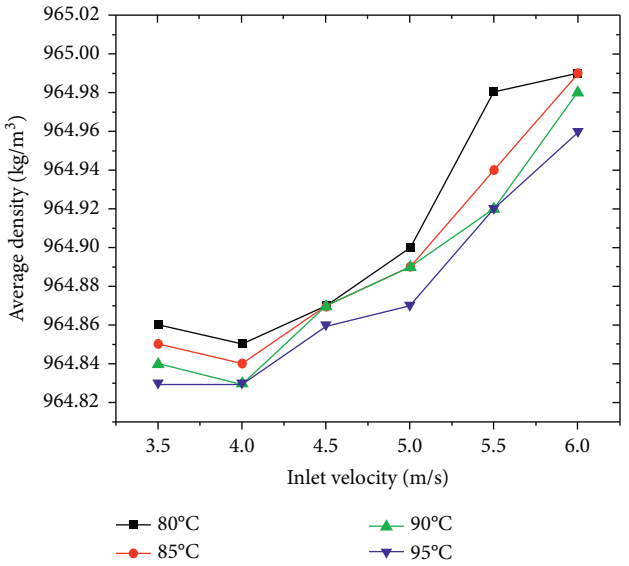

Figure 36: Inlet velocity and average density with temperature for 20% opening.

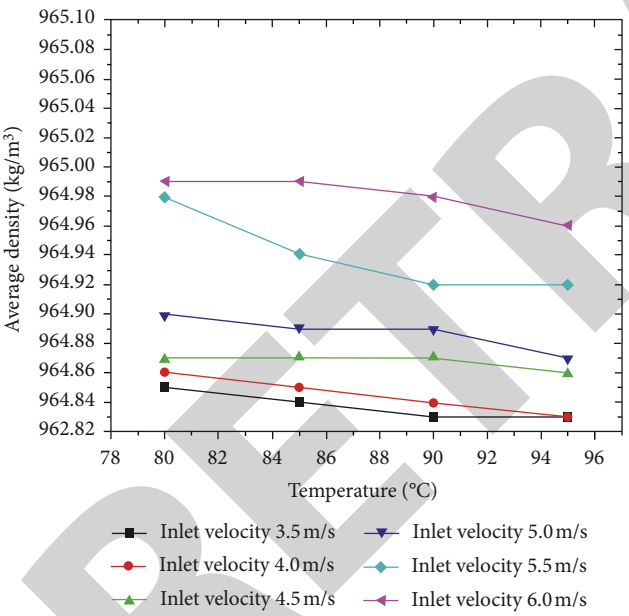

Figure 37: Temperature and average density with inlet velocity for 20% opening.

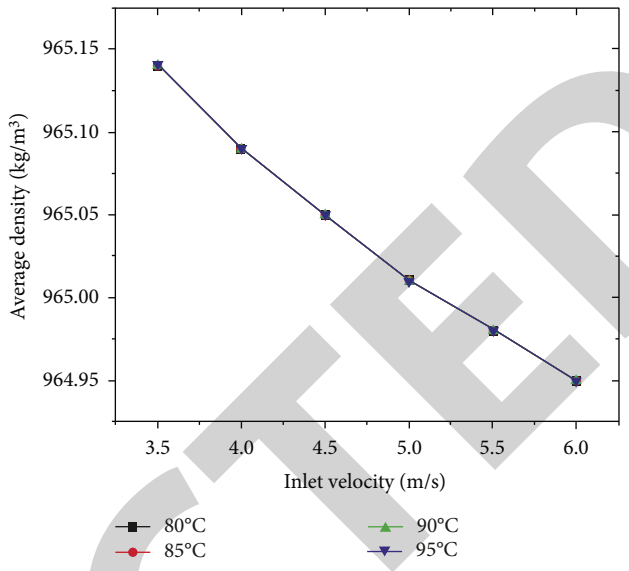

Figure 38: Inlet velocity and average density with temperature for 100% opening.

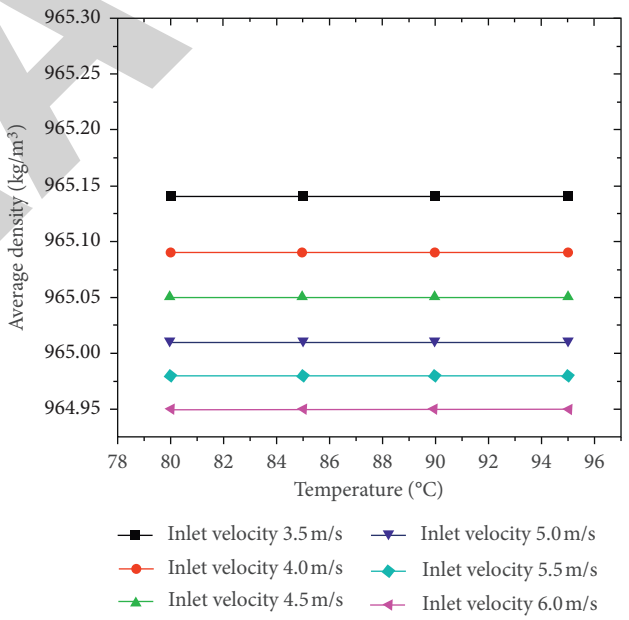

Figure 39: Inlet velocity and average density with temperature for 100% opening.

and manually driven. Test implementation standards are GB/T 4213, GB/T 13927, and ANSI FCI 70-2-2006.

The noise reduction two-stage cage control valve manufacturing prototype is shown in Figure 47.

5.2. Test Process. The control valve is installed on the test bench, the two ends of the inlet and outlet and pipeline connection fixed, the upper part is suspended by a hook fixed, the medium from the left end of the valve port flow in, the right end of the valve port out, change the medium pressurization pressure, and test the valve body pressure strength and valve cover sealing. The test is shown in Figure 48.

When testing the pressure resistance and sealing of the regulating valve, since the regulating valve can be used for both regulating and switching, a low-pressure sealing test and a high-pressure sealing test are performed on the regulating valve. The control valve noise and cavitation tests are shown in Figure 49. The control valve is installed in a piping system consisting of a throttle valve, sensor, control valve and piping, etc. The sound power level,

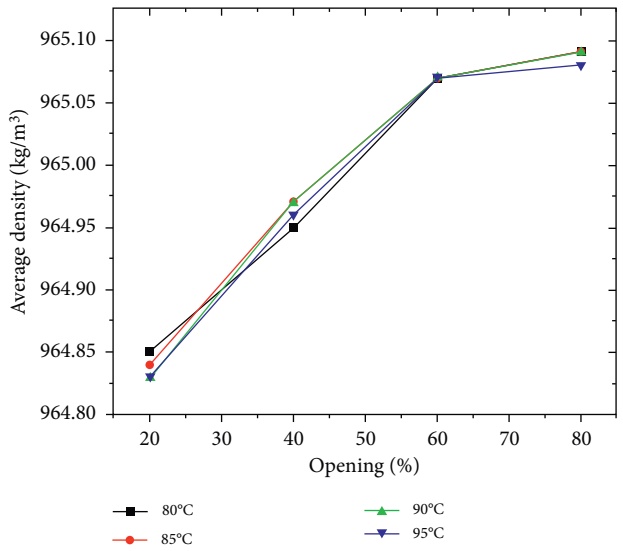

Figure 40: Variation of inlet velocity constant opening and average density with temperature.

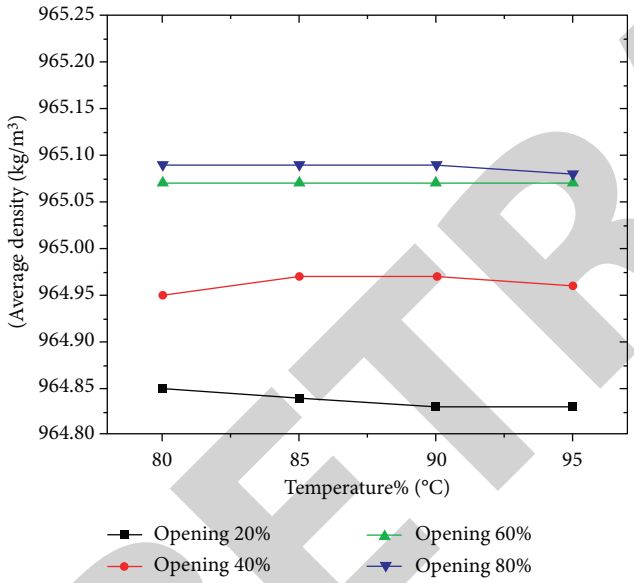

Figure 41: Variation of inlet velocity constant temperature and average density with openness.

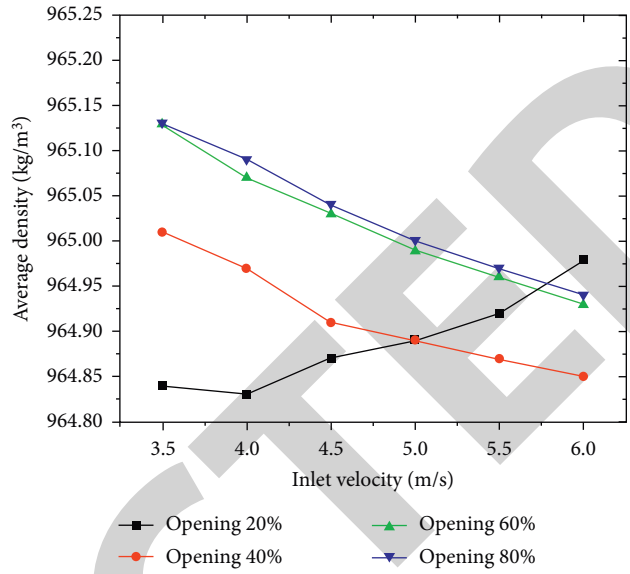

Figure 42: Variation of inlet velocity and average density with openness at constant temperature.

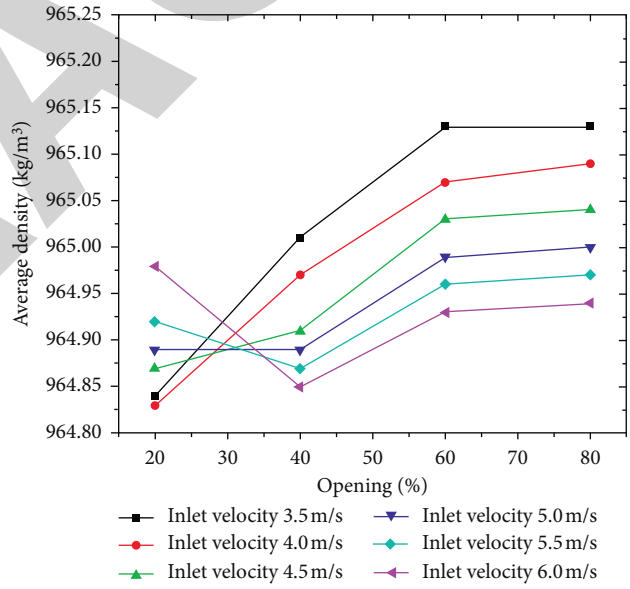

Figure 43: Variation of temperature-constant openness and average density with inlet velocity.

average density of liquid flow, and cavitation coefficient are tested.

5.3. Analysis of Test Results. The results of pressure test, low-pressure sealing test, and high-pressure sealing test of control valve are shown in Table 3.

Control valve noise and cavitation test results are shown in Table 4.

The maximum sound power level is 36.24 dB, 16.51 dB, 16.03 dB, 15.78 dB, 14.32 dB, 14.32 dB, and 13.91 dB, respectively, which are small and decrease with the increase of opening degree, indicating that the fluid flow noise is very small. It is a normal flow quiet environment. The average density of liquid flow is 966.11 kg/m^3, 965.51 kg/m^3, 965.52 kg/m^3, 965.48 kg/m^3, 965.63 kg/m^3, and 965.67 kg/m^3, respectively, and the average density changes very little with the increase of opening degree, so it is difficult to produce air pockets. The cavitation coefficients are 0.39, 0.36, 0.34, 0.31, 0.28, and 0.26, respectively, which are less than 0.5 and decrease gradually with the increase of the opening degree; therefore, no cavitation occurs.

The yield strength of each material is shown in Table 5.

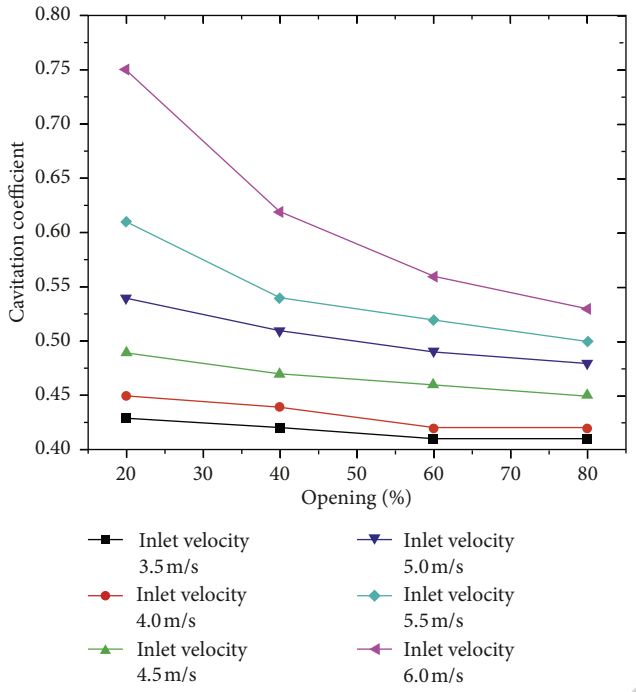

Figure 44: Nominal diameter constant opening and cavitation coefficient with inlet velocity.

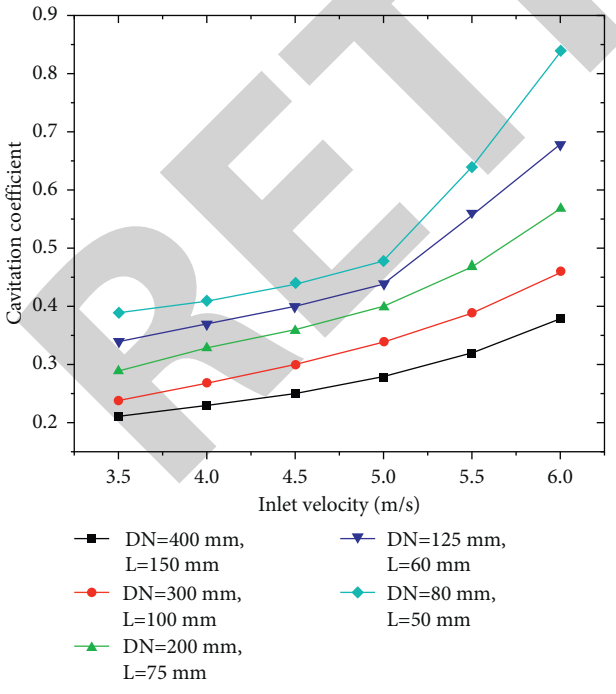

Figure 45: Variation of inlet velocity and cavitation coefficient with nominal diameter at half opening.

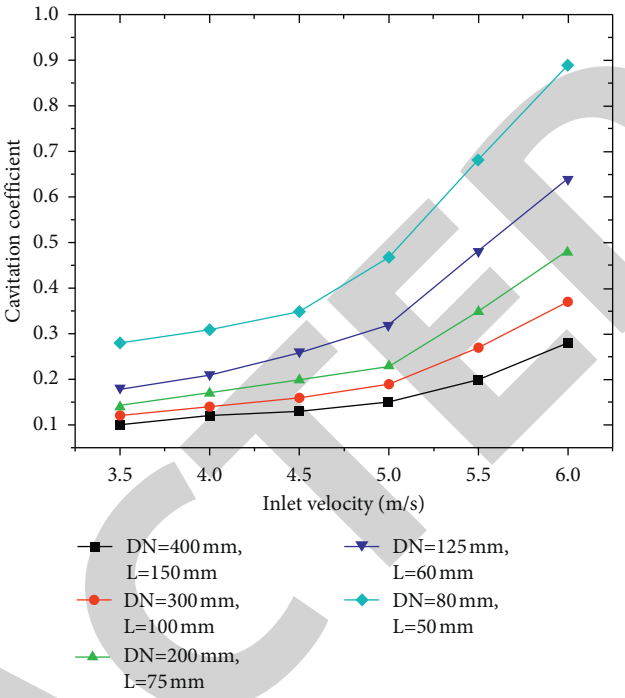

Figure 46: Variation of inlet velocity and cavitation coefficient with nominal diameter at full opening.

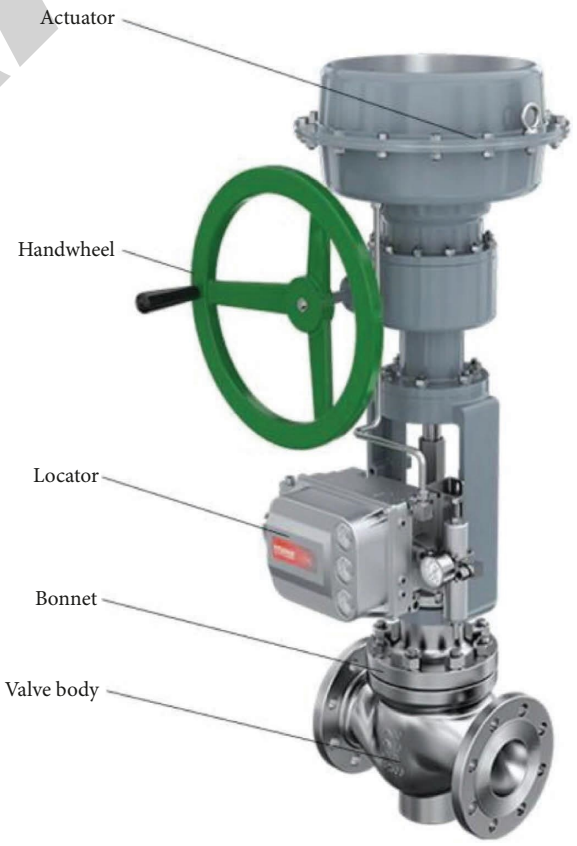

Figure 47: Noise-reducing double-stage cage control valve.

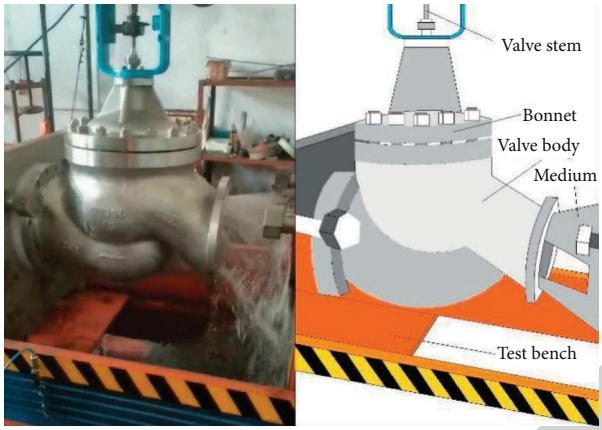

Figure 48: Noise-reducing two-stage cage control valve pressure resistance and sealing test.

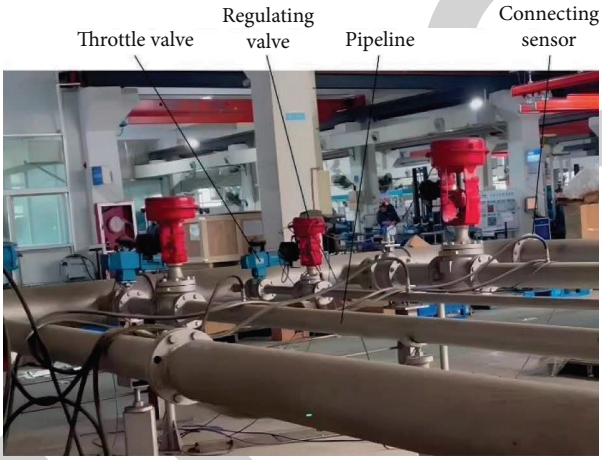

Figure 49: Control valve noise and cavitation test.

Table 3: Test results.

Test items	Valve body pressure resistance test	High-pressure sealing test	Low-pressure sealing test
Pressure setting value (MPa)	0.35	3.00	2.20
Holding time (s)	180	300	180
Leakage setting value (ml/min)	1.50	0.00	1.50
Measured leakage volume (ml/min)	0.42	0.00	0.67
Actual value of pressure (MPa)	0.36	3.02	2.20
Holding pressure drop value (MPa)	0.01	0.02	0.00

Table 4: Test results.

Openness (%)	Maximum sound power level (dB) flow (kg/m^3)	Cavitation factor	Average density of liquid
20	966.11	36.24	0.39
40	965.51	16.51	0.36
50	965.52	16.03	0.34
60	965.48	15.78	0.31
80	965.63	14.32	0.28
100	965.67	13.91	0.26

Table 5: Yield strength of each material.

Names	CF8M	LCB	420	WC6	316
Yield strength (MPa)	200	275.8	345	170	20

6. Conclusion

Noise reduction double-stage cage type control valve adopts noise reduction valve cage and curve valve cage for noise reduction, forming a two-stage noise reduction, with uniform flow rate, good diffusion effect, and good noise reduction effect, which can meet the equal percentage flow characteristics of the control valve, effectively reduce the noise generated by gas, steam, and gas-liquid medium, and can perfectly ensure the equal percentage flow characteristics of the control valve, making the process parameter (flow, pressure, temperature, etc.) regulation quality excellent. Therefore, this innovative technology has substantial features and progress compared with the prior art. The flow characteristics of the noise-reducing two-stage cage control valve are studied, and the fluid flow coefficient, the flow characteristic curve, the change of flow coefficient with nominal diameter under the same stroke, and the change of flow coefficient under different strokes with different nominal diameters are analyzed. The cavitation phenomenon of cavitation was studied, and the fluid density cloud, Mach number cloud, and acoustic pressure energy level cloud were calculated by simulation to analyze the effect of cavitation on noise. The relationship between inlet velocity and cavitation coefficient with nominal diameter at half open and the relationship between inlet velocity and cavitation coefficient with nominal diameter at full open were studied, and the cavitation generation and its effect on noise were analyzed.

In the future, we will use complete test equipment to simulate more severe test environments to test new steel body features.

Data Availability

The experimental data used to support the findings of this study are available from the corresponding author upon request.

Conflicts of Interest

The authors declare that they have no conflicts of interest.

Authors' Contributions

Yu Ruiming was responsible for conceptualization, data curation, formal analysis, software, validation, methodology, and original draft preparation. Lu Xi was responsible for supervision and project administration. All authors reviewed and approved the final manuscript.

Acknowledgments

This study was supported by the National Natural Science Foundation of China (Grant: 51975379) and the Shanghai Natural Science Foundation of China (grant no. 19ZR1435500).

References

[1] V. Hessel, P. Angeli, A. Gavriilidis, and H. Löwe, "Gas-liquid and gas-liquid-solid microstructured reactors: contacting principles and applications," *Industrial & Engineering Chemistry Research*, vol. 44, no. 25, pp. 9750–9769, 2005.

[2] A. Varvani Farahani and S. Abolfathi, "Sliding mode observer design for decentralized multi-phase flow estimation," *Heliyon*, vol. 8, no. 2, Article ID e08768, 2022.

[3] A. Tanimu, S. Jaenicke, and K. Alhooshani, "Heterogeneous catalysis in continuous flow microreactors: a review of methods and applications," *Chemical Engineering Journal*, vol. 327, no. 11, pp. 792–821, 2017.

[4] S. Keskin, D. Kayrak-Talay, U. Akman, and Ö Hortaçsu, "A review of ionic liquids towards supercritical fluid applications," *The Journal of Supercritical Fluids*, vol. 43, no. 1, pp. 150–180, 2007.

[5] Ž Knez, E. Markočič, M. Leitgeb, M. Primožič, M. Knez Hrnčič, and M. Škerget, "Industrial applications of supercritical fluids: a review," *Energy*, vol. 77, no. 11, pp. 235–243, 2014.

[6] X. Xie, X. Pan, F. Shao, W. Zhang, and J. An, "MCI-Net: multi-scale context integrated network for liver CT image segmentation," *Computers & Electrical Engineering*, vol. 101, Article ID 108085, 2022.

[7] J. Tan, Y. N. Ji, W. S. Deng, and Y. F. Su, "Process intensification in gas/liquid/solid reaction in trickle bed reactors: a review," *Petroleum Science*, vol. 18, no. 4, pp. 1203–1218, 2021.

[8] M. Ballesteros Martínez, E. Pereyra, and N. Ratkovich, "CFD study and experimental validation of low liquid-loading flow assurance in oil and gas transport: studying the effect of fluid properties and operating conditions on flow variables," *Heliyon*, vol. 6, no. 12, Article ID e05705, 2020.

[9] X. Nie, Y. Zhu, and L. Li, "The flow noise characteristics of a control valve," *The Open Mechanical Engineering Journal*, vol. 8, no. 1, pp. 960–966, 2014.

[10] J. Zhang, Q. Yang, R. Lv, B. Liu, and Y. Li, "Research on noise generation mechanism and noise reduction ball valve measures of ball valve," *IEEE Access*, vol. 8, no. 1, Article ID 15973, 2020.

[11] A. S. Prakash, K. S. Ram, and V. R. Kishore, "Aeroacoustics analysis of globe control valves," *International Journal of Automotive and Mechanical Engineering*, vol. 15, no. 3, pp. 5547–5561, 2018.

[12] L. F. Zeng, G. W. Liu, J. R. Mao et al., "Flow-induced vibration and noise in control valve," *Proceedings of the Institution of Mechanical Engineers-Part C: Journal of Mechanical Engineering Science*, vol. 229, no. 18, pp. 3368–3377, 2015.

[13] W. Xu, Q. Wang, D. Wu, and Q. Li, "Simulation and design improvement of a low noise control valve in autonomous underwater vehicles," *Applied Acoustics*, vol. 146, no. 3, pp. 23–30, 2019.

[14] J. Liu, T. Zhang, and Y. Zhang, "Numerical study on flow-inducednoise for a steam stop-valve using large eddy simulation," *Journal of Marine Science and Application*, vol. 12, no. 3, pp. 351–360, 2013.

[15] S. Sreekala and S. Thirumalini, "Investigation on aerodynamic noise evaluation and attenuation in a globe valve using CFD analysis," *The International Journal of Multiphysics*, vol. 10, no. 1, pp. 43–52, 2016.

Hindawi
Journal of Chemistry
Volume 2023, Article ID 9891764, 1 page
https://doi.org/10.1155/2023/9891764

Retraction

Retracted: Characteristics of Sedimentary Microfacies of Late Triassic Yanchang Formation in North-Central Ordos Basin

Journal of Chemistry

Received 28 November 2023; Accepted 28 November 2023; Published 29 November 2023

This article has been retracted by Hindawi, as publisher, following an investigation undertaken by the publisher [1]. This investigation has uncovered evidence of systematic manipulation of the publication and peer-review process. We cannot, therefore, vouch for the reliability or integrity of this article.

Please note that this notice is intended solely to alert readers that the peer-review process of this article has been compromised.

Wiley and Hindawi regret that the usual quality checks did not identify these issues before publication and have since put additional measures in place to safeguard research integrity.

We wish to credit our Research Integrity and Research Publishing teams and anonymous and named external researchers and research integrity experts for contributing to this investigation.

The corresponding author, as the representative of all authors, has been given the opportunity to register their agreement or disagreement to this retraction. We have kept a record of any response received.

References

[1] J. Wei, F. Li, S. Zhang, H. Cheng, Q. Qin, and D. Cadasse, "Characteristics of Sedimentary Microfacies of Late Triassic Yanchang Formation in North-Central Ordos Basin," *Journal of Chemistry*, vol. 2022, Article ID 1513503, 10 pages, 2022.

Hindawi
Journal of Chemistry
Volume 2022, Article ID 1513503, 10 pages
https://doi.org/10.1155/2022/1513503

Research Article

Characteristics of Sedimentary Microfacies of Late Triassic Yanchang Formation in North-Central Ordos Basin

Jiangwei Wei,[1] Fawang Li,[2] Shikuo Zhang,[2] Hanlie Cheng,[3] Qiang Qin,[3] and David Cadasse[4]

[1]*No. 5 Oil Production Plant of Changqing Oilfield Company, PetroChina, Yinchuan, Ningxia 750000, China*
[2]*No. 10 Oil Production Plant of Changqing Oilfield Company, PetroChina, Qingyang, Gansu 745000, China*
[3]*COSL-EXPRO Testing Services (Tianjin) Co. Ltd., Tianjin 300457, China*
[4]*The King's School, BP 1560, Bujumbura, Burundi*

Correspondence should be addressed to David Cadasse; davidcadasse@ksu.edu.bi

Received 6 August 2022; Accepted 8 September 2022; Published 22 September 2022

Academic Editor: Rabia Rehman

Sedimentary microfacies refer to the smallest unit with unique rock structure, structure, thickness, rhythm, and other sedimentary characteristics and certain plane configuration rules in the subfacies zone. Sedimentary microfacies research is the most basic sedimentary unit formed in the same or basically the same sedimentary background. Sedimentary microfacies marks are the key to the division of sedimentary microfacies. If we cannot find effective marks, we cannot correctly divide sedimentary microfacies. These marks are mainly obtained from detailed observation of cores. On the premise of fully understanding the regional tectonic background of the study area, the sedimentary facies and sedimentary subfacies types within the oilfield control range are determined. In this study, the single-well facies and profile facies are deeply analyzed by observing and describing the cores of Chang 2 reservoir group in Huangjialing, north-central Ordos Basin, and comprehensively utilizing the data of coring, logging, and core analysis and testing. The basic sedimentary characteristics, types of sedimentary facies and microfacies, and plane distribution of sedimentary facies in this area are systematically studied. The results show that there are mainly three microfacies: underwater distributary channel, natural dike, and distributary bay. Among them, the microfacies of the underwater natural dike are relatively undeveloped, mainly the microfacies of underwater distributary channel and underwater distributary bay. These studies have important practical significance for the later exploration of oil and gas in Ordos Basin.

1. Introduction

In the Late Triassic, Ordos Basin was an asymmetric depression basin with gentle in the east and steep in the west. The main oil and gas resources of Yanchang formation were distributed in the eastern gentle slope zone. The gentle slope zone has flat terrain, shallow water body, and wide distribution area. The density of river water carrying a large amount of sediment is greater than that of lake water. After entering the lake, it still maintains a high flow rate and flows forward along the flat lake bottom for a long time, thus forming a wide delta sedimentary front. Sedimentary microfacies are four-level facies that are divided into sedimentary facies based on the sedimentary environment, combined with hydrodynamic conditions and sedimentary characteristics [1]. Sedimentary microfacies can not only be used to characterize paleontological and petrological characteristics but also can be used as a marker to divide rock types. The study of sedimentary microfacies begins with the study of carbonate rocks. The discovery of large carbonate reservoirs has aroused a worldwide upsurge in the study of carbonate rocks by scholars [2, 3]. In terms of diagenetic model, depositional environment, depositional model, etc., it has gradually penetrated into the research field of terrigenous clastic rocks. Through comprehensive research on carbonate rock microfacies, it is found that both dolomite and limestone can be used as good reservoirs for oil and gas [4, 5]. This important theoretical significance and guiding

significance for exploration and development practice work have promoted the research on carbonate rock microfacies [6]. According to the characteristics of different layers of sedimentary bodies, Chinese scholars divide sedimentary facies into subfacies and further subdivide them into "sedimentary microfacies" and even "microfacies" on this basis. Different types of sedimentary microfacies show different frequencies and different distribution horizons on the stratigraphic section. Therefore, the study and analysis of sedimentary microfacies can be used to restore the paleogeographic environment during the depositional period and deduce the change process of the depositional environment [7–9].

The Danish geologist was the first person to introduce facies as a geology concept into the literature related to geology, emphasizing that facies refer to a certain geological period showing the general appearance of a certain part of the Earth's surface [10]. The Swiss geologist used the concept of sedimentary facies in sedimentary rocks in the mid-17th century, extending the meaning of facies to sedimentology. The performance of different aspects is different, and the change is the essence of sedimentary facies. Since then, the geoscience community has recognized and used this concept. The concept of phase has different meanings with the continuous development and evolution [11–13]. When it represents lithological feature units or biological assemblages, it refers to lithofacies or biological facies, such as shale facies and graptolite facies. When it represents the product of sedimentation, it is the interpretation of the cause of rock formation, such as platform facies. When it represents the product of tectonic movement, it refers to sedimentary formations, such as molasse facies. When it represents the performance of the depositional environment, it refers to sedimentary facies, such as delta facies [14–16]. Chinese sedimentologist proposed in the middle of the 20th century that sedimentary facies have stratigraphic and paleogeographic significance, because it is a combination of depositional environments and should be reflected in the corresponding time and space [17].

On the one hand, sedimentary microfacies are developing in depth, with a higher and higher degree of refinement and a stronger degree of comprehensiveness. Instead of only using logging and seismic data to analyze sedimentary facies and delineate facies zones in the past, researchers use various kinds of information for multi-angle prediction [18]. On the other hand, there is still a certain gap between China and the international level, which is mainly reflected in the quantitative aspect of research. China has taken a huge step from the uncertainty of the past to semiquantitative [19, 20]. Compared with the international advanced level, which is mainly based on quantitative research, there is still a lot of room for improvement in China. Technologies such as three-dimensional modeling led by computer technology and statistical quantification of mathematical methods are powerful means of quantitative research. In this study, through the observation and description of the core of the Huangjialing Chang 2 oil formation in the north-central Ordos Basin, the basic sedimentary characteristics, sedimentary facies and microfacies types, and the planar distribution of sedimentary facies were systematically studied [21].

2. Geological Background

Ordos Basin is one of the giant energy basins in China, which is rich in oil, natural gas, and coal resources. Today, the basin is surrounded by orogenic belts in different periods, forming a distribution pattern of "basin" and "mountain." It is connected to Yinshan Mountain in the north, Qinling Mountain in the south, Luliang Mountain in the East, and Helan Mountain in the west. The basin is adjacent to the Hetao Basin across the Wulanger bedrock uplift in the north, facing the Weihe River Basin in the south, the Jinxi flexure fold belt in the East, and the Luliang Uplift in the East, and facing Liupanshan and Yinchuan basins in the west through the overthrust structural belt. The outline is rectangular. It crosses the five provinces of Shaanxi, Gansu, Ningxia, Mongolia, and Shanxi and is located on the western edge of the North China Craton, with an area of $25 \times 10\%\ km^2$.

The Upper Triassic Yanchang Formation in the Ordos Basin is a set of fluvial-lake facies terrigenous clastic rock sedimentary systems accumulated during the continuous depression and stable subsidence of the basin. It is a set of major oil-bearing rock series in the basin. The evolution process of this large inland freshwater lake basin includes formation and development to extinction. During the depositional period of the Yanchang Formation, the Ordos Basin has the characteristics of large area, wide water area, shallow depth, flat terrain, and weak segmentation [22]. The Yimeng uplift, the western Jinxi flexural fold belt, the Weibei uplift, and the western margin thrust developed around the lake basin. Therefore, the provenance is abundant and the sedimentary thickness is large. The axial direction of the basin is northwest-southeast, and the sedimentary center of the lake basin is south of the 38° latitude line. The distribution of facies belts is slightly ring-shaped, in which the lake shoreline of the southwest margin is in the Shigouyi-Pingliang-Yongshou area, and near-source and near-shore subaqueous fan deposits are developed along the lake shoreline [23]. The northern lake shoreline may move southward continuously from the Wushenqi-Jingbian-Hengshan-Zizhou area (Figure 1), and a series of lake delta deposits developed along the lake shoreline strongly advancing toward the lake. The lake basin is asymmetric in shape, steep in the west, and gentle in the east.

Alluvial fan, fan delta, fluvial, braided river delta, meandering river delta, and lacustrine deposits are widely developed in Ordos Basin in Late Triassic. The alluvial fan and delta are related to the steep basin margin. Braided river delta is related to the steep gradient of basin margin. The meandering river delta is related to the gentle slope depression type boundary, which is characterized by river sedimentation and lake sedimentation.

3. Results and Discussion

3.1. Types of Sedimentary Microfacies. Sedimentary system analysis is one of the most important advances in modern

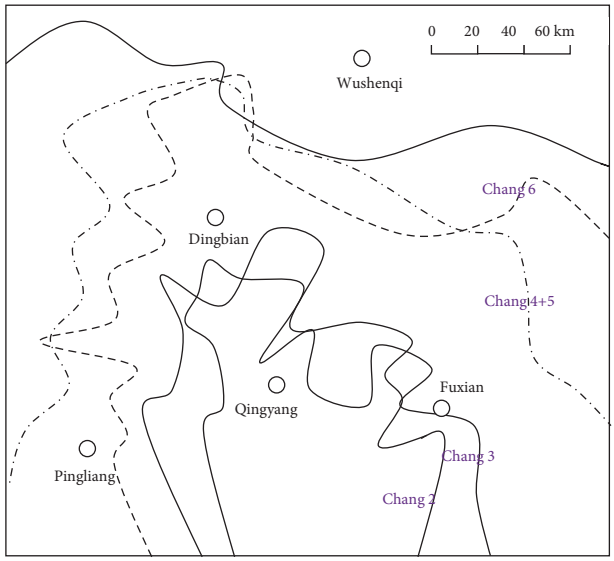

Figure 1: Schematic diagram of late Triassic Lake shoreline migration in the central and northern Ordos Basin.

sedimentology. Since the 1960s, sedimentologists have begun to apply the principles of sedimentary systems to analyze sedimentary basins. The so-called sedimentary system refers to the aggregation of sedimentary facies related to the action. We can also understand it as a three-dimensional stratigraphic unit composed of genetically related sedimentary facies in space. Its meaning includes three-dimensional combination of supply source, action process, and geographical environment.

The Huangjialing Chang 2 sand body is composed of light gray, light gray-green fine sandstone, silt sandstone, and sandstone with a large thickness of single layer due to sufficient provenance supply, fast deposition rate, and large superimposed thickness of sand layers. It is composed of gravel-coarse sandstone, mudstone, and argillaceous siltstone, reflecting the characteristics of underwater distributary channels with slow and stable channel migration, forming a relatively characteristic thick and massive bedding fine sandstone facies. There are four types of rhythm in the reservoir sand body: homogeneous, compound rhythm, positive rhythm, and inverse rhythm. The shape of SP curve is mainly box-shaped and box funnel-shaped (90.6%), and a few are bell-shaped.

The rock has low structural maturity and low compositional maturity, sandstone sorting is moderate, roundness is poor, the clastic particles are mostly subcircular-subangular, and the grain size is mainly fine-grained sandstone, followed by medium grains. The particle size probability curve is mainly composed of jumping and suspension (Figures 2 and 3), indicating that during the process of flowing water, the detrital particles are obviously transformed by the action of lake waves. This kind of transformation can form a wide range of particle size distribution, reflecting the delta sedimentary characteristics of the underwater distributary channel of the front.

The delta front is the main underwater part of the river entering the lake, the most active place of delta deposition, the development zone with concentrated sand layers in the delta, the most important skeleton part of the delta, the coastal shallow lake gentle slope zone below the estuary, and the river lake interaction zone.

The research results of regional sedimentary facies show that the sedimentary period of Chang 2 Member is the period of the gradual disappearance of lake basins. The sedimentary facies type of Chang 2 Member in Huangjialing area of Zhiluo oilfield is lacustrine-delta facies, and the sedimentary subfacies is dominated by delta front subfacies. The hydrodynamic conditions are moderate to weak, and it has a certain wave transformation effect and river effect.

On the basis of the previous regional sedimentary background analysis, comprehensive analysis was carried out according to various sedimentary facies markers such as reservoir coring well lithology, sedimentary structure, sequence characteristics, grain size characteristics, and electrical survey curve shape. The sedimentary microfacies of the small layer and single layer of the oil layer group are divided into three kinds of microfacies. There are mainly three types of microfacies developed: underwater distributary channel, natural levee, and interdistributary bay. Among them, the underwater natural levee microfacies is relatively undeveloped, and the underwater distributary channel and underwater interdistributary bay microfacies are mainly developed.

The underwater distributary channel is the underwater extension of the distributary channel in the delta plain. The sand body of underwater distributary channel has the characteristics of normal cycle of coarse at the bottom and fine at the top in the longitudinal section. There is a scouring surface at the bottom, and mudstone and gravel bearing sandstone are often developed. Upward, it is thick-bedded medium-fine sandstone, intercalated with thin layers of siltstone and argillaceous siltstone and silty mudstone in the distributary bay.

The subaqueous distributary bay is located between the subaqueous distributary channels and is dominated by fine-grained sediments. The lithology is thick gray black silty mudstone, argillaceous siltstone, siltstone, and mudstone with thin layer of gray and gray-green fine sandstone. Plant leaf fossils are developed in mudstone. Sand ripple cross-bedding is developed in siltstone, with carbon debris and vertical wormholes. The natural potential curve of the distributary bay is low and flat, the natural gamma curve is medium and high value, showing a tooth shape, and the resistivity curve is medium and low value.

3.2. Analysis of Sedimentary Microfacies Characteristics

3.2.1. Rock Types and Characteristics. Color is one of the important macroscopic characteristics of sedimentary rocks, which is closely related to its own composition and formation environment. There is a lack of coring data in the study area, but judging from the logging data and the core data in the adjacent area, the main medium and fine sandstones are mainly gray, gray-green, and light gray; the siltstones are mostly dark gray; and the mudstones are black.

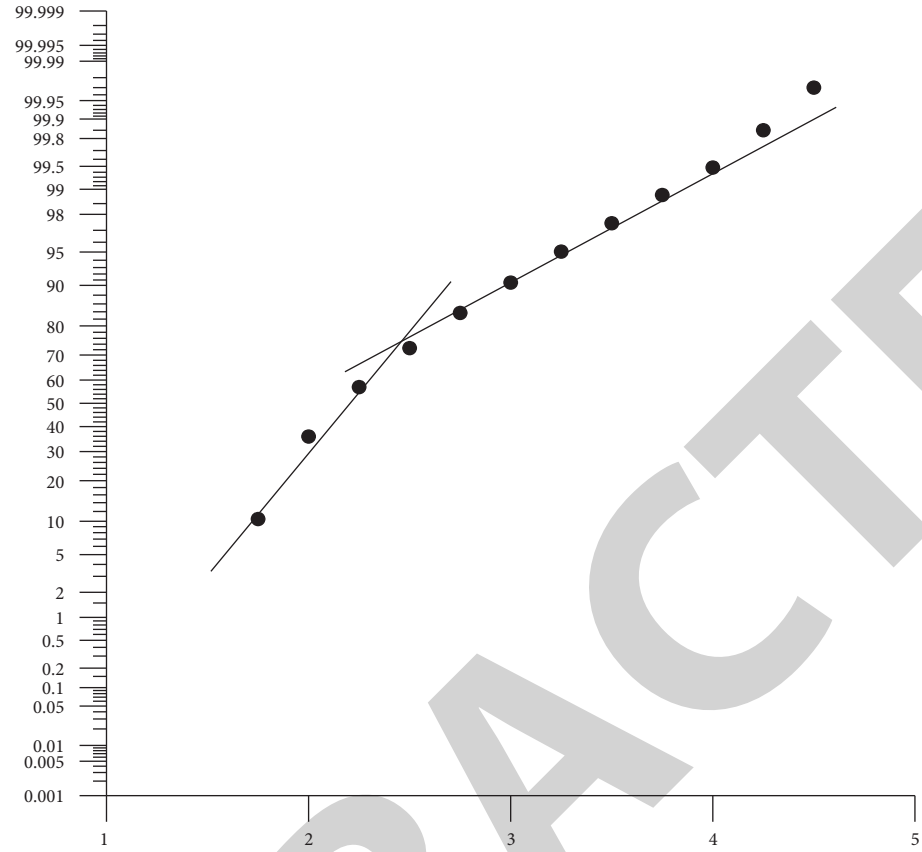

Figure 2: Probability curve of particle size distribution in Well Lu 203.

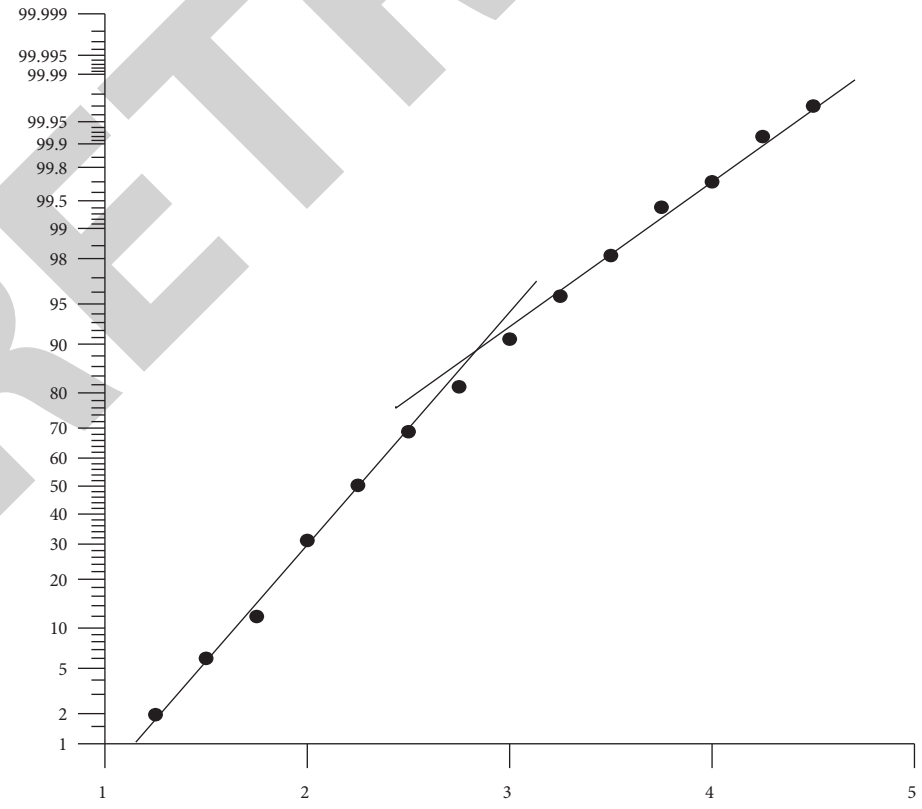

Figure 3: Probability curve of particle size distribution in Well Lu 29.

The main factors affecting the color of sandstone and mudstone are the content of ferrous iron, ferric iron, and organic matter, which are related to the relative stability of the water body and the environment of the redox medium. Generally speaking, the higher the content of organic matter in the rock (especially in the mudstone), the darker the color. The rocks are purple-red. The higher content of ferrous iron and organic matter generally indicates a reducing depositional environment, while the higher content of ferric iron indicates an oxidative depositional environment. The data of the study area and its adjacent areas show that the color of the Yanchang Formation indicates that the study area is a weak reduction-reduction environment. The characteristics of the rock components in the study area are generally high quartz content and high feldspar content. The content of interstitial material is between 8% and 16%, the components are mainly argillaceous and calcareous, and the cements are mainly chlorite, kaolinite, and calcite.

The early sedimentary stage of Yanchang formation is the formation stage of lakes, the fluvial sedimentation is developed, and the delta is in the construction stage of gradual development. Sandstone is the main rock type of terrigenous clasts, and its clastic material mainly comes from the products of mechanical crushing of parent rock, which is an important indicator of material source. The statistics of rock components in different areas show that the early sedimentary period of Yanchang formation is dominated by arkose.

3.2.2. Sedimentary Structural Markers. Sedimentary structure refers to the overall characteristics of the spatial distribution and arrangement of the components of sedimentary rocks, or the sum of the mutual arrangement of the particles of the rocks. The structures formed in the process of sediment formation and before sedimentation consolidation and diagenesis are called primary structures, such as bedding and bedding structures. The structures formed after consolidation diagenesis are secondary structures, such as sutures. The sedimentary structures in clastic rocks, especially the primary sedimentary structures of physical origin, can best reflect the hydrodynamic conditions in the process of sediment formation. The sedimentary structures preserved in the study area mainly include flow-derived structures, syngenetic deformation structures, and biogenic structures, which are the most important signs for analyzing and judging sedimentary facies.

(a) The Structure of Flow Genesis

① Horizontal bedding: in mudstone and silty mudstone, the thickness of the single layer is small, the laminae are parallel to each other and parallel to the layer, and the bedding sees fine plant debris and abundant mica flakes, often formed under the wave base or in the low-energy environment. In the low flow state and in the case of insufficient material supply, it is mainly formed by the slow vertical accumulation of suspended matter. This kind of sedimentary structure is mainly developed in the delta front and the interdistributary bay of the plain, underwater natural embankment, and prodelta shallow lakes (Figure 4).

② Parallel bedding: the lithology is dominated by medium- and fine-grained sandstone. The thickness of the laminae is generally 0.5 to 1.0 cm. It consists of straight continuous or intermittent textures that are parallel to each other and parallel to the layers. The texture can be plant debris, cuttings or dark minerals, and colors. The difference shows that it is often formed under the hydrodynamic conditions of shallow water and rapid flow, and is mainly found in the estuary sand bar or underwater distributary channel sediments with strong hydrodynamic force.

③ Plate cross-bedding: the lithology is composed of gray-light gray medium- and fine-grained sandstone. The main feature is that the large-scale stratum is composed of straight bedding at the upper and lower interfaces, which is plate-shaped. The stratum is 15–20 cm, and the thickness is relatively stable. On the left and right, the texture is continuous and intermittent. There are fine carbon chips and plant debris on the lamina layer. The lamina can converge to the bottom surface of the layer system, and the included angle is often less than 10°. It is formed by the migration of sand waves, and this area often occurs in the sedimentary environment of delta front estuarine sand bars and underwater distributary channels.

④ Trough-shaped cross-bedding: the lithology is fine sandstone and silty sandstone, and small trough-shaped cross-bedding is developed. Small charcoal debris, plant debris, and occasionally small scour surfaces, generally migrated from large asymmetric tongue-shaped or crescent-shaped sand slopes, mostly formed in underwater distributary channels and estuary sand bars in the delta front.

⑤ Sand grain cross-bedding: it is composed of a series of laminae obliquely crossing the interface of the layer system. The relationship between the laminae and the layer system can be combined by overlapping, interlacing, and cutting. Cross-bedding is caused by the flow of sedimentary media. When the flow velocity is constant, a series of sand waves can be generated in the sand bed. The downstream migration of sand waves forms an oblique layer system composed of a series of laminae on the side of the steep slope. The laminae trend indicates the direction of media flow. The layers are parallel to each other or cut each other to form cross-bedding of different shapes. It mainly occurs in siltstone and argillaceous siltstone. It is a small cross-bedding of multilayered series. The lower interface of the layered series is microwave, the laminar layer is irregular, discontinuous, or continuous, and the fine layer is inclined to one side. Fine plant debris, charcoal, and abundant mica flakes are seen on the bedding surface and often coexist with parallel bedding, plate

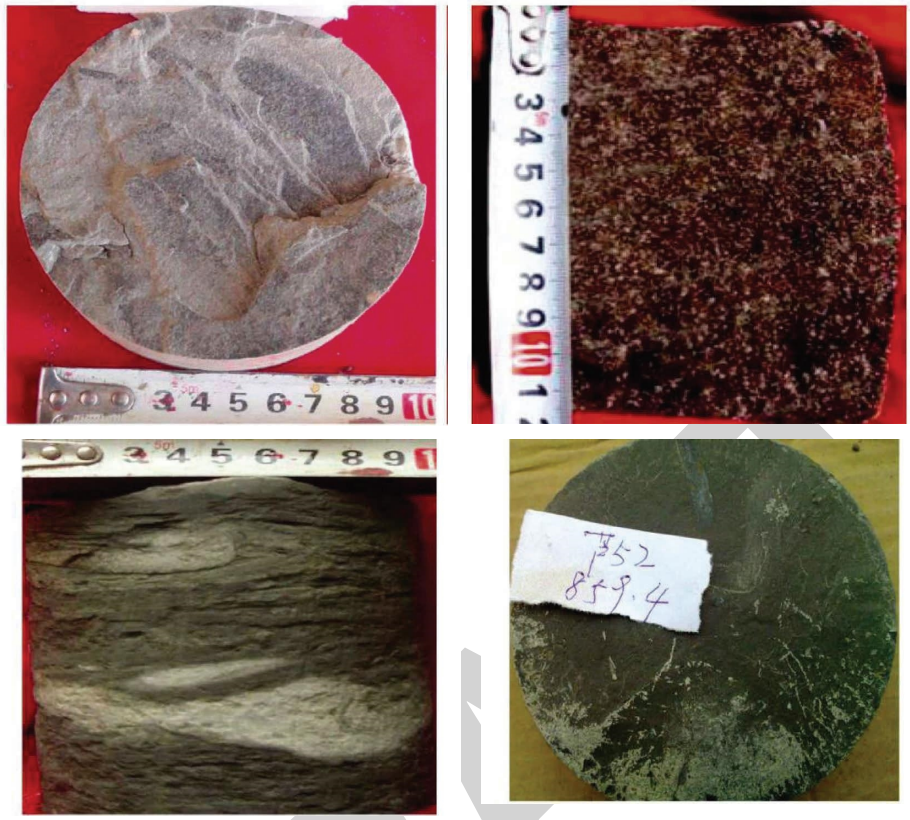

Figure 4: Main sedimentary structure of Chang 2 oil reservoir group. (a) Parallel-bedded fine sandstone. (b) Tabular cross-bedded fine sandstone. (c) Gray-black mudstone intercalated with fine sandstone lens. (d) Horizontal bedding mudstone, with carbonized plant fossils.

bedding, and small cross-bedding. It is formed by sand grain migration and is mainly formed in environments with weak hydrodynamic conditions, such as interdistributary bays in delta fronts, underwater natural dikes, far sand bars, and prodeltas.

⑥ Lenticular layering: the lens sand of lenticular bedding is of silt grade. It is formed when the hydrodynamic conditions are weak, the supply of sand is insufficient, and the supply, deposition, and preservation of mud are more favorable than those of sand.

⑦ Wave bedding: it is composed of many undulating fine layers overlapped together and formed under oscillating hydrodynamic conditions or wind force. The formation of wavy bedding generally requires a large amount of suspended matter deposition, and the deposition rate is greater than the erosion rate of flowing water so that continuous fine layers can be preserved. Commonly found in fine sandstone and siltstone, it is a small bedding; the laminae are discontinuous or continuous wave or microwave; and mainly continuous wave, fine charcoal, plant debris, and abundant mica are seen on the bedding surface. It is more common in sedimentary environments such as estuarine sand bars and far-estuarine sand bars.

⑧ Massive bedding: massive bedding developed in large-scale distributary channel deposits, representing a rapid, continuous, uniform, and stable depositional process. It is mainly medium-fine sandstone, the internal material is uniform, and there is no differentiation in composition and structure.

⑨ Scrub surface: it is a layered structure generated under high flow conditions. Due to the small volume of the core, only a gentle scouring surface can be seen on the core. The scouring surface mostly appears at the bottom of the underwater channel, where a large amount of redeposited mud is common.

(b) Syngenetic Deformation Structure

The syngenetic deformation structure is a kind of sedimentary structure in the sedimentary layer caused by the action of gravity and the action of sediment liquefaction flow during the time interval between the deposition of the sediment and the consolidation of the diagenesis. The area mainly occurs in the interbedded lithology of fine sandstone, siltstone, and silty mudstone, including slump deformation structure, wrapping bedding, and sand pillow sand ball structure. They occur in estuarine sand bars and the upper parts of underwater distributary channels.

① Wrapping bedding: it is a bedding crumpling phenomenon within a layer, which is composed of continuous open "synclines" and tight "anticlines,"

but the layers are continuous. It is generally limited to bedding deformation within a layer and does not involve the upper and lower layers. It is mainly caused by the distortion of the thin layer caused by the lateral flow in the liquefied layer within the sedimentary layer. Most of the enveloping bedding in this area occurs in the estuary sand bar and the upper part of the underwater distributary channel in the delta front.

② Slump deformation structure: most of the slump-deformed structures are formed by the continuous sliding of the encapsulated bedding. The laminae in the sedimentary layers appear discontinuous and disorderly accumulation, and even sediment fragments appear. Mud tearing debris is common in sandstones. The slump deformation structure is generally produced with rapid deposition. It is a good sign of underwater landslides and is mostly distributed in the delta fronts with slopes.

③ Ball pillow structure: this kind of structure often appears in sand and mud interbeds, and refers to the ellipsoid or pillow-shaped blocks formed by the sandstone layer breaking and sinking into the mudstone. Only a ball-pillow structure about ten centimeters in size can be seen in the core. It is found in predelta or interdistributary bay environments.

(b) Syngenetic Deformation Structure

The syngenetic deformation structure is a kind of sedimentary structure in the sedimentary layer caused by the action of gravity and the action of sediment liquefaction flow during the time interval between the deposition of the sediment and the consolidation of the diagenesis. The area mainly occurs in the interbedded lithology of fine sandstone, siltstone, and silty mudstone, including slump deformation structure, wrapping bedding, and sand pillow sand ball structure. They occur in estuarine sand bars and the upper parts of underwater distributary channels.

① Wrapping bedding: it is a bedding crumpling phenomenon within a layer, which is composed of continuous open "synclines" and tight "anticlines," but the layers are continuous. It is generally limited to bedding deformation within a layer and does not involve the upper and lower layers. It is mainly caused by the distortion of the thin layer caused by the lateral flow in the liquefied layer within the sedimentary layer. Most of the enveloping bedding in this area occurs in the estuary sand bar and the upper part of the underwater distributary channel in the delta front.

② Slump deformation structure: most of the slump-deformed structures are formed by the continuous sliding of the encapsulated bedding. The laminae in the sedimentary layers appear discontinuous and disorderly accumulation, and even sediment fragments appear. Mud tearing debris is common in sandstones. The slump deformation structure is generally produced with rapid deposition. It is a good sign of underwater landslides and is mostly distributed in the delta fronts with slopes.

③ Ball pillow structure: this kind of structure often appears in sand and mud interbeds, and refers to the ellipsoid or pillow-shaped blocks formed by the sandstone layer breaking and sinking into the mudstone. Only a ball-pillow structure about ten centimeters in size can be seen in the core. It is found in predelta or interdistributary bay environments.

① Wrapping bedding: it is a bedding crumpling phenomenon within a layer, which is composed of continuous open "synclines" and tight "anticlines," but the layers are continuous. It is generally limited to bedding deformation within a layer and does not involve the upper and lower layers. It is mainly caused by the distortion of the thin layer caused by the lateral flow in the liquefied layer within the sedimentary layer. Most of the enveloping bedding in this area occurs in the estuary sand bar and the upper part of the underwater distributary channel in the delta front.

② Slump deformation structure: most of the slump-deformed structures are formed by the continuous sliding of the encapsulated bedding. The laminae in the sedimentary layers appear discontinuous and disorderly accumulation, and even sediment fragments appear. Mud tearing debris is common in sandstones. The slump deformation structure is generally produced with rapid deposition. It is a good sign of underwater landslides and is mostly distributed in the delta fronts with slopes.

③ Ball pillow structure: this kind of structure often appears in sand and mud interbeds, and refers to the ellipsoid or pillow-shaped blocks formed by the sandstone layer breaking and sinking into the mudstone. Only a ball-pillow structure about ten centimeters in size can be seen in the core. It is found in predelta or interdistributary bay environments.

(c) Biogenic structure: it is mainly a wormhole structure, which is a tubular burrow dug by organisms in the coastal zone to feed on suspended organisms and avoid the impact of water waves. It is usually straight and tubular, indicating an underwater environment near a lake shoreline.

3.2.3. Logging Facies Signs. Different sedimentary microfacies have different logging response forms; in other words, different logging response forms are the embodiment of different sedimentary microfacies. The so-called logging facies refers to the sum of the logging responses that characterize the formation characteristics, and this logging response feature is different from other surrounding logging responses. Therefore, logging facies analysis is an indispensable aspect of sedimentary facies research, and sedimentary facies can be reshaped by logging facies analysis.

The elements that make up the log facies are all log responses, including not only qualitative aspects (characteristics of the curve) but also quantitative aspects (values of logging parameters). The content of logging facies analysis includes the selection of logging response sequence, the analysis of logging response curve characteristics, and the analysis of logging facies characteristics. According to the combination characteristics of formation lithology characteristics, sedimentary characteristics and logging response curve, and its resolution, it can be seen that the natural gamma curve is mainly selected in the study area. The log facies analysis is performed with the supplemented logging response sequence, and the effect is good. The characteristics of the logging response curve include abnormal amplitude, smoothness, convergence of tooth centerline, curve shape and top-bottom contact relationship, etc. They reflect the lithology, grain size, shale content, and vertical changes of the formation from different aspects.

① Amplitude: the amplitude of the logging curve (such as natural potential and natural gamma curve) can reflect the grain size and shale content of the sediment to a certain extent, so as to infer the hydrodynamic strength of the sedimentary medium. It is divided into three types: low, medium, and high. The Yanchang Formation in the study area is dominated by medium and low amplitudes, especially with low amplitudes accounting for the largest proportion, which is related to the finer sediment particle size. The sandstone in the study area is mainly composed of fine sand and medium-fine sand, with high content of silt and mud.

② Contact relationship: it refers to the top and bottom shape of the logging curve of a single-layer sand body, which can reflect the changes of hydrodynamic conditions and sediment supply conditions in the initial and final stages of sedimentary deposition to a certain extent.

The abrupt type shows the drastic changes in hydrodynamic conditions and sediment supply before and after the deposition of sedimentary bodies, and can be further divided into top abrupt type and bottom abrupt type. Mutant contacts are well developed in this region; in particular, bottom mutations are more common.

Corresponding to the sudden change, the gradual change indicates the gradual change of the hydrodynamic conditions and sediment supply conditions in the sand body deposition process, and can be further divided into top gradual change and bottom gradual change. The top gradual change indicates the gradual change of the hydrodynamic strength of the sedimentary medium. The bottom gradient type is caused by the gradual increase of hydrodynamic force and/or the gradual increase of relative coarse-grained sediment supply.

③ Smoothness of the curve: the smoothness of the logging curve can reflect the sediment sorting to a certain extent. It can be divided into three types: smooth, microtooth, and dentate. The latter two in the Huangjialing well area; in particular, the microtooth is more common, indicating that the sandstone has a moderate degree of sorting.

④ The shape of the curve: the shape of the logging curve (including single layer or combined shape) is one of the important contents of logging facies research, and it is often divided into bell-shaped, box-shaped, funnel-shaped, and some combined shapes. The box shape reflects the relatively stable deposition process of water energy, and there is a continuous and stable supply of sediment; the bell shape and the funnel shape indicate that the deposition process has water energy from strong to weak and from weak to strong, respectively. The common logging curve shapes in the study area are as follows:

(a) Bell-shaped. The amplitude is high in the middle and lower parts of the curve, and the amplitude in the upper part is low. From bottom to top, the amplitude of the curve decreases, showing a bell shape with a wide bottom and a narrow top, indicating that the supply of sediment is reduced and the hydrodynamic force of the sedimentary medium is weakened. This shape is relatively developed in the Chang 2 oil-bearing formation in the Huangjialing well area, and microdentate formation is common, with a gradual relationship upward and abrupt contact downward. Mud-gravel, muddy strips, and scour structures are sometimes seen at the bottom of the sandstone, and parallel bedding or plate-like cross-bedding are common inside, which is a reflection of the positive grain sequence characteristics of distributary river deposits.

(b) Bell-box combination. The bell-box combination is a relatively well-developed logging curve shape type for the Chang 2 oil layer group in the study area. It is a box-shaped combined curve, with abrupt contact at the bottom and a gradual relationship at the top.

(c) Box-shaped. The curve has a relatively high amplitude and a large width, and the top and bottom fluctuations are basically the same, indicating that the sediment particle size is relatively coarse, with continuous strong hydrodynamic conditions and relatively stable and sufficient provenance supply. The box-shaped curve of the sand bodies in this area is dominated by medium and low amplitudes, and the sedimentary grain size is relatively fine (fine sand), mainly channel sediments, smooth, and toothed, and the top and bottom are basically showing abrupt contact relationship.

(d) Funnel-shaped. The amplitude in the middle and upper parts of the curve is relatively high, and the amplitude in the downward direction gradually decreases. The funnel-shaped curve in this area is rare.

4. Conclusion

Through the observation and description of the cores of Chang2 oil formation in Huangjialing, central and northern Ordos Basin, the study comprehensively analyzed the single well facies and profile facies by using coring, logging, and core analysis and testing data, and systematically studied the basic sedimentary characteristics, sedimentary facies, and microfacies types and the planar distribution of sedimentary facies in this area. The results are as follows:

(1) According to the comprehensive analysis of various sedimentary facies markers such as reservoir coring well lithology, sedimentary structure, sequence characteristics, grain size characteristics, and electrical survey curve shape, it is considered that the sublayer and single layer of the Chang 2 oil layer group in this area are the most important. The sedimentary microfacies is divided into 3 kinds of microfacies. There are mainly three types of microfacies developed: underwater distributary channel, natural levee, and interdistributary bay. Among them, the underwater natural levee microfacies is relatively undeveloped, and the underwater distributary channel and underwater interdistributary bay microfacies are mainly developed.

(2) The color of the extension group indicates that the study area is a weak reduction-reduction environment. The characteristics of the rock components in the study area are generally high quartz content and high feldspar content. The sedimentary structures in clastic rocks, especially the primary sedimentary structures of physical origin, can best reflect the hydrodynamic conditions in the process of sediment formation. The sedimentary structures preserved in the study area mainly include flow-derived structures, contemporaneous deformation structures, and biogenic structures.

(3) According to the combination characteristics of formation lithology characteristics, sedimentary characteristics and logging response curve, and its resolution, it can be seen that the natural gamma curve is mainly selected in the study area, and combined with the natural potential curve, the resistivity and acoustic time difference curve, the log facies analysis is performed with the supplemented logging response sequence, and the effect is good.

Data Availability

The figures used to support the findings of this study are included within the article.

Conflicts of Interest

The authors declare that they have no conflicts of interest.

Acknowledgments

The authors would like to show sincere thanks to those technicians who have contributed to this research.

References

[1] C. T. Perry and A. Berkeley, "Intertidal substrate modification as a result of mangrove planting: impacts of introduced mangrove species on sediment microfacies characteristics," *Estuarine, Coastal and Shelf Science*, vol. 81, no. 2, pp. 225–237, 2009.

[2] X. Ma and S. Guo, "Comparative study on shale characteristics of different sedimentary microfacies of late permian longtan formation in southwestern Guizhou, China," *Minerals*, vol. 9, no. 1, p. 20, 2018.

[3] X. Wei, J. Liu, and J. Liu, "Study on sedimentary microfacies and impact on development of Chang 6 1 reservoir in Shijiapan area, Ordos Basin," *Northwestern Geology*, vol. 51, no. 4, pp. 255–262, 2018.

[4] C. T. Perry, A. Berkeley, and S. G. Smithers, "Microfacies characteristics of a tropical, mangrove-fringed shoreline, Cleveland Bay, Queensland, Australia: sedimentary and taphonomic controls on mangrove facies development," *Journal of Sedimentary Research*, vol. 78, no. 2, pp. 77–97, 2008.

[5] J. L. Wilson, "Microfacies and sedimentary structures in deeper-water lime mudstones," *AAPG Bulletin*, vol. 51, no. 3, pp. 485-486, 1967.

[6] Y. Wang, D. Dong, X. Li, J. Huang, S. Wang, and W. Wu, "Stratigraphic sequence and sedimentary characteristics of lower silurian longmaxi formation in sichuan basin and its peripheral areas," *Natural Gas Industry B*, vol. 2, no. 2-3, pp. 222–232, 2015.

[7] X. Lu, D. Sun, X. Xie et al., "Microfacies characteristics and reservoir potential of triassic Baikouquan Formation, northern Mahu sag, Junggar Basin, NW China," *Journal of Natural Gas Geoscience*, vol. 4, no. 1, pp. 47–62, 2019.

[8] A. Seyrafian, "Microfacies and depositional environments of the Asmari Formation, at Dehdez area (a correlation across central Zagros basin)," *Carbonates and Evaporites*, vol. 15, no. 2, pp. 121–129, 2000.

[9] M. H. Basyoni and M. A. Aref, "Sediment characteristics and microfacies analysis of Jizan supratidal sabkha, Red Sea coast, Saudi Arabia," *Arabian Journal of Geosciences*, vol. 8, no. 11, pp. 9973–9992, 2015.

[10] C. Sun, M. Hu, X. Luo, and D. Gao, "High-frequency sequence and sedimentary microfacies evolution characteristics of the 3rd member of the Ordovician Yingshan formation in the Gucheng area, Tarim Basin, NW China," *Arabian Journal of Geosciences*, vol. 14, no. 22, pp. 2433–2519, 2021.

[11] R. Zhang, J. Wang, Y. Ma, G. Chen, Q. Zeng, and C. Zhou, "Sedimentary microfacies and palaeogeomorphology as well as their controls on gas accumulation within the deep-buried Cretaceous in Kuqa depression, Tarim Basin, China," *Journal of Natural Gas Geoscience*, vol. 1, pp. 45–59, 2016.

[12] Y. Liu, X. Yu, S. Li, W. Du, M. Li, and S. Li, "Characteristics and evolution of sedimentary microfacies of Chang 6 – 4 + 5 layer in the northern area of western Mahuang mountain," *Earth Science Frontiers*, vol. 16, no. 4, pp. 277–286, 2009.

[13] H. Hüneke, F. J. Hernández-Molina, F. J. Rodríguez-Tovar et al., "Diagnostic criteria using microfacies for calcareous contourites, turbidites and pelagites in the Eocene-Miocene

Hindawi
Journal of Chemistry
Volume 2023, Article ID 9764037, 1 page
https://doi.org/10.1155/2023/9764037

Retraction

Retracted: Differential Scanning Calorimetry Material Studies: Benzil Melting Point Method for Eliminating the Thermal History of DSC

Journal of Chemistry

Received 28 November 2023; Accepted 28 November 2023; Published 29 November 2023

This article has been retracted by Hindawi, as publisher, following an investigation undertaken by the publisher [1]. This investigation has uncovered evidence of systematic manipulation of the publication and peer-review process. We cannot, therefore, vouch for the reliability or integrity of this article.

Please note that this notice is intended solely to alert readers that the peer-review process of this article has been compromised.

Wiley and Hindawi regret that the usual quality checks did not identify these issues before publication and have since put additional measures in place to safeguard research integrity.

We wish to credit our Research Integrity and Research Publishing teams and anonymous and named external researchers and research integrity experts for contributing to this investigation.

The corresponding author, as the representative of all authors, has been given the opportunity to register their agreement or disagreement to this retraction. We have kept a record of any response received.

References

[1] Z. Zhu, W. Li, Y. Yin, R. Cao, and Z. Li, "Differential Scanning Calorimetry Material Studies: Benzil Melting Point Method for Eliminating the Thermal History of DSC," *Journal of Chemistry*, vol. 2022, Article ID 3423429, 9 pages, 2022.

Hindawi
Journal of Chemistry
Volume 2022, Article ID 3423429, 9 pages
https://doi.org/10.1155/2022/3423429

Research Article

Differential Scanning Calorimetry Material Studies: Benzil Melting Point Method for Eliminating the Thermal History of DSC

Ziyang Zhu,[1,2] **Wei Li**,[1] **Yilin Yin**,[2] **Ruilin Cao**,[1] **and Zenghe Li**[2]

[1]*Calibration &Test Center, China Household Electric Appliance Research Institute, Beijing 100029, China*
[2]*Collage of Chemistry, Beijing University of Chemical Technology, Beijing 100029, China*

Correspondence should be addressed to Zenghe Li; lizh@mail.buct.edu.cn

Received 15 July 2022; Revised 12 August 2022; Accepted 16 August 2022; Published 19 September 2022

Academic Editor: Rabia Rehman

How to eliminate the thermal history present in differential scanning calorimetry, this question has been widely concerned. Benzil has a serious thermal history that is not well eliminated by conventional thermal history methods. Herein, using benzil as a target, we developed a freeze-gradient temperature rate heating up method to eliminate the thermal history of DSC. Compared with the conventional method, this method avoids the introduction of new thermal histories by new crystalline forms that may appear during the cooling crystallization process. The results show that the peak shape of the melting peak is sharper and the peak emergence position is closer to the theoretical melting point after the elimination of the thermal history by the freeze-gradient heating up method. Based on this method, we optimized other factors to establish a complete method for the determination of melting point by DSC, analyzed the uncertainty of the method, and obtained an extended uncertainty of 0.19°C for DSC in this method. The validation results show that the p-nitrotoluene of the melting point reference substance was 52.64°C, which is within its reference value of (52.53 ± 0.20) °C, showing that this method is reliable. This study provides a reference for other thermal analysis methods to eliminate thermal history.

1. Introduction

Differential scanning calorimetry (DSC), as a representative of modern thermal analysis methods, can accurately and quickly analyze the thermodynamic properties of samples, because of simple operations such as without the need to add internal or external standard substances. The DSC has been widely used in a diverse of different fields, such as environmental analysis [1, 2], drug purity determination [3], and rapid determination of melting point [4]. Among these applications, the accuracy of the melting point of samples is receiving growing attention from DSC. However, some samples show some malformed peaks during the determination process of DSC. The presence of malformed peaks interferes with the determination of melting point and purity. For example, Jalali et al. found malformed peaks caused by thermal history when studying the nucleation and crystallization of poly-lactic acid (PLA). Thermal history refers to the fact that during the production and processing of the sample, due to the difference in the molecular crystal form within the sample, some malformed peaks may appear in the DSC measurement curve, which affects the determination of the melting point. Because these malformed peaks may interfere with the selection of normal melt peaks, some studies suggest that the malformed peaks arise because of the presence of disordered crystalline patterns within the molecule [5]. It has been shown that some samples such as PLA exhibit two different crystalline phases, one is the ordered form and the other is the disordered form. Several studies confirm this conclusion, by means of FTIR and WAXD analysis [6]. The presence of a disordered form in the crystalline phase can induce thermal history occurrence. Due to the presence of these peaks, the uncertainty of DSC is not easily assessed systematically.

The uncertainty of the DSC is systematically evaluated by eliminating the thermal history of the DSC. For the elimination of thermal history, the heating and cooling method for the sample was used [5–9], and keeping the melting point

temperature at a constant temperature is usually adopted. Multiple heating eliminates thermal history by first heating the sample to a predetermined temperature and then cooling it at a constant rate. Several studies have shown that the results of eliminating thermal history differ for different cooling rates [5]. When cooling rates are low, thermal history was eliminated. Decreasing the cooling rate led to an increase in the nuclei density, and this operation can make the crystal phase arrangement more orderly [9]. Due to the slow cooling rate, the molecules have enough time to move and adjust during crystallization to form an ordered arrangement [10–12], thereby eliminating thermal history in the sample [13–16]. It is also formed by the movement of intramolecular crystals to form an orderly arrangement. However, there are some problems with these two methods. For example, the analysis takes a long time [17, 18], and the thermal history of the sample cannot be completely eliminated in many cases [19–22]. Therefore, the development of a new method for the elimination of thermal history is highly desirable.

Benzil is a commonly used and important intermediate in organic synthesis and can be used in the preparation of many valuable organic intermediates [23, 24]. The benzil is particularly important in organic synthesis. Also, it was shown that the benzil's enthalpy of fusion is important in the determination of gas-phase ion energetics [25]. For the determination of the purity of benzil, the commonly used methods are gas chromatography [26], liquid chromatography [27], and DSC [28]. During the use of benzil, the thermodynamic properties of benzil need to be characterized with the help of DSC. The melting point of benzil was used as a calibration for thermodynamic instruments [29]. Some studies have found that benzil has a serious thermal history phenomenon when using DSC to measure the thermodynamic parameters of benzil [26]. The reasons for the appearance of benzil's thermal history and the method of elimination are similar to PLA, because they all have the presence of disordered crystalline patterns within the molecules. But this method also does not eliminate benzil's thermal history very well.

In this study, we design a method of freeze-gradient heating up gradient heating to eliminate the thermal history of DSC, and we systematically analyzed the uncertainty of DSC. This study used the melting point reference substance p-nitrotoluene for comparison experiments to verify the accuracy of the method. An accurate determination method for measuring benzil melting point is established, which can provide a promising reference for improving the melting point determination level of organic high-purity substances.

2. Experiments

2.1. Materials and Instruments. Benzil was purchased from Acros Organics (USA). Indium and p-nitrotoluene were purchased from the National Institute of Metrology (Beijing, China).

A differential scanning calorimeter (DSC 8000, Perkin Elmer, USA) was used to determine the melting point of the sample. 20 μL crucible (Perkin Elmer, USA) was used to hold the sample. XP205 electronic balance (Mettler Toledo, Switzerland) was used to weigh the samples. KZY-1 tablet press (Shanghai Kaizheng Instrument Co., Ltd.) was used to seal aluminum pans. MERLIN compact field emission scanning electron microscope (Zeiss, Germany) was used for the characterization of sample surface morphology.

2.2. DSC Measurement. According to the relevant provisions of ISO 11357-3-2018, the DSC measurement method is set as follows: the benzil (5.0 mg) and indium (5.0 mg) were accurately weighed. The samples were put in a crucible and were used pressed. The furnace body of DSC was cleaned. The prepared samples were put into the DSC sample dish, and the same empty crucible was put into the DSC reference dish. The prepared indium sample was put into the DSC sample pan to be tested. The temperature was raised to 180°C at 10°C·min^{-1}. The melting curve of indium was measured, and the DSC completed the calibration. After completing the calibration and cooling to 25°C, the benzil samples were placed in DSC sample dishes. The furnace was purged with high-purity N_2 at a flow rate of 20 mL/min. The temperature was rapidly heated up to 20°C below the melting point and held for 2 min. Then, the temperature was heated at 1.0°C·min^{-1} to exceed the melting point. The melting point was automatically calibrated by Perkin Elmer's software.

2.3. Effects of Different Experimental Conditions

2.3.1. The Influence of Thermal History Elimination. Four benzil samples of different masses including 1.0 mg, 2.0 mg, 3.0 mg, and 4.0 mg were used.

(1) Elimination of Thermal History by Constant Temperature near Melting Point. The temperature was kept at a constant temperature near the melting point for 5 min, cooled down to 60°C at the same rate, and then ramped up to above the melting point at 1.0°C·min^{-1}. Other conditions are the same as the method mentioned in Section 2.2.

(2) Elimination of Thermal History by Repetitive Heating Up. The method in Section 2.2 was used. After heating above the melting point, the temperature was cooled to 25°C at the same rate. We repeated this process 3 times.

(3) Elimination of Thermal History by Freeze-Constant Temperature Rate Heating Up. The temperature was maintained at −40°C for 2 min, ramped up to above the melting point at 1.0°C·min^{-1}, and the other operations were the same as in the methods mentioned in Section 2.2.

(4) Elimination of Thermal History by Freeze-Gradient Temperature Rate Heating Up. The temperature was maintained at −40°C for 2 min, ramped up to 60°C at 2.0°C·min^{-1} and ramped up to above the melting point at 1.0°C·min^{-1}, and the other operations were the same as in the methods mentioned in Section 2.2.

2.3.2. The Influence of Sample Mass and Heating Rates. Four benzil samples of different masses including 1.0 mg, 2.0 mg, 5.0 mg, 7.5 mg, 10.0 mg, and 12.5 mg were used. The heating rates were set to 0.5°C·min^{-1}, 1.0°C·min^{-1}, 2.0°C·min^{-1}, 5.0°C·min^{-1}, 10.0°C·min^{-1}, and 20.0°C·min^{-1}, respectively. According to the optimized method in Section 2.3, the influences of different mass factors on the melting point were explored.

2.4. Experimental Method Verification. In this study, p-nitrotoluene was used to verify the experimental method on the optimized experimental method. The sample mass is 5.0 mg; other operations are similar to the methods in Section 2.2. According to the optimized experimental method, the method of eliminating the thermal history in Section 2.3.2 was used.

3. Results and Discussion

3.1. Thermal History Factor Optimization

3.1.1. Determination of Non-Eliminated Thermal History Samples. For most organic compounds, there was no processing before performing DSC experiments. The severe thermal history phenomenon was shown in the DSC curve. Figure 1 presents the DSC measurement curves of benzil without any treatment at four different masses. Figure 1 shows that the thermal history phenomenon occurred when the mass was 1.0 mg, 2.0 mg, 3.0 mg, and 4.0 mg, due to the presence of disordered crystalline patterns within the molecule when the mass was 1.0 mg, 2.0 mg, and 3.0 mg. The presence of disordered crystalline forms led to a thermal history during DSC testing of benzil. The DSC curve exhibited malformed peaks. The malformed peaks disappeared when the mass was 4.0 mg. Due to the fact that when the mass increases, the sample arrangement inside the pan becomes more compact, the proportion of disordered crystalline forms decreases, and the proportion of ordered crystalline forms increases. However, a peak occurred at 107°C. This may be due to the mixing of the two crystal phases, which caused a thermal history phenomenon. To eliminate the thermal history phenomenon, it is necessary to eliminate the disordered crystal phases in the molecule. Therefore, in order to accurately determine the melting point of benzil, it is important to eliminate the thermal history.

3.1.2. Elimination of Thermal History by Constant Temperature near Melting Point. We designed the method of constant temperature near the melting point to eliminate the thermal history. Figure 2(a) presents the method of constant temperature mode near melting point to the elimination of thermal history at 1.0 mg, 2.0 mg 3.0 mg, and 4.0 mg, respectively. The peak that appears at 95°C undergoes a significant distortion. This is due to the fact that it is the first temperature rise and the distorted peak exhibited by not eliminating the thermal history [30], and the peak appearing at 105°C is the melting peak formed after the method of

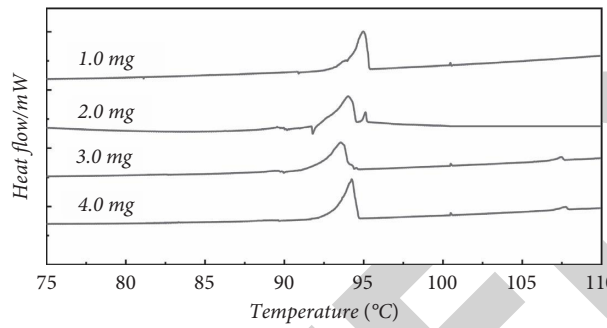

Figure 1: DSC curves of Benzil's samples without thermal history elimination.

eliminating the thermal history by using the melting point thermostat method. It can be seen that at this time, the peak shape is significantly optimized compared to the first time, but the melting range grows significantly. This is due to the fact that after the first temperature rises to reach the melting point, the melting undergoes a phase change, and the ordered and disordered crystalline shapes within the molecule disappear. Then, due to the presence of a cooling crystallization process, new crystalline forms are formed again during this process, which makes the melting range grow [31]. Therefore, this method is not suitable for thermal history elimination.

3.1.3. Elimination of Thermal History by Repetitive Heating Up. We designed another method of repetitive heating sample to eliminate the thermal history, because the abovementioned method not only did not eliminate the original thermal history but also introduced a new one. Figure 2(b) presents the method of repetitive heating to the elimination of thermal history at 1.0 mg, 2.0 mg 3.0 mg, and 4.0 mg, respectively. The malformed peaks occurred at 95°C at four masses. This is due to the fact that the repeated heating did not make the intramolecular crystalline arrangement neat, and there are still disordered crystalline shapes in the molecule, so the melting peak is preceded by a spurious peak. The appearance of the spurious peak at 105°C is probably due to the presence of a cooling crystallization process, new crystalline forms are formed again during this process [32]. The presence of the new crystalline form makes the DSC curve show the stray peak at 105°C. Therefore, repeated heating also does not eliminate the thermal history well.

3.1.4. Elimination of Thermal History by Freeze-Constant Temperature Rate Heating Up. The malformed peaks on the DSC curve are due to the disordered crystalline shapes. Therefore, to eliminate the thermal history, the disordered crystalline shape within the molecule has to be eliminated first. The key to the first two methods is to give the crystals within the molecule time to move and arrange themselves into a neat crystalline pattern. However, since there is a phase change, other crystalline patterns may appear when

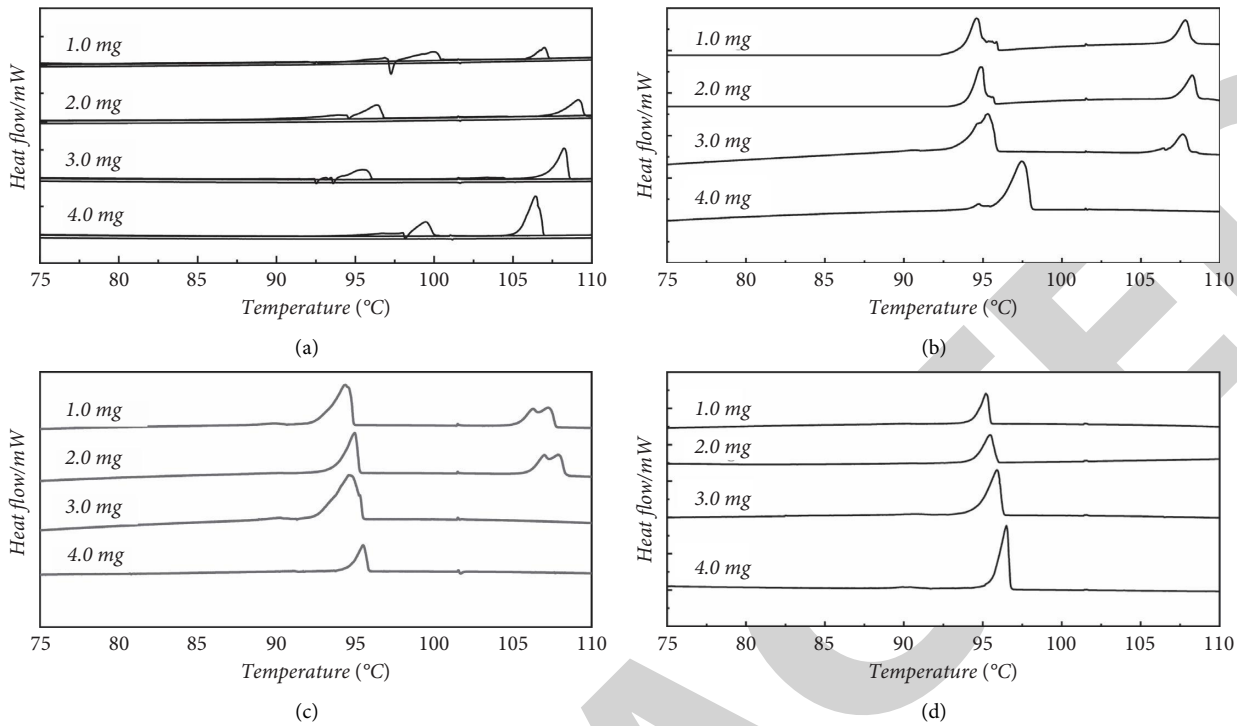

Figure 2: The DSC curves of four thermal history elimination methods. (a) The method of constant temperature near the melting point. (b) The method of repetitive heating. (c) The method of freeze-constant temperature heating. (d) The method of freeze-constant temperature heating.

crystallizing again [33]. In order to allow enough time for the crystals within the molecule to align and not crystallize again, we devised a method to extend the heating range.

(Figure 2(c) presents the method of freeze-constant heating up to the elimination of thermal history at 1.0 mg, 2.0 mg 3.0 mg, and 4.0 mg, respectively. Compared with the two previous methods, the peak shape of the melting peak is significantly improved. The peak shape becomes sharper and the position of the peak emerges closer to the theoretical melting point. This is due to the longer melting range, which gives enough time for the molecules to arrange into neat crystalline shapes internally. Also, due to the absence of a cooling crystallization process, no spurious peaks appeared around 105°C for masses of 3.0 mg and 4.0 mg. But, when the mass is 1.0 mg and 2.0 mg, there are heterogeneous peaks. This is due to the presence of an inhomogeneous thermal field in the crucible with large sample voids when the mass is less, which makes some of the samples' crystalline transformation slower. When the mass increases, the sample inside the crucible is packed compactly, which makes the heat transfer inside more uniform than that of 1.0 mg and 2.0 mg. Therefore, when the mass is increased, the crystalline shape is neatly arranged and the elimination of thermal history is better than in the first two. This method can better solve the elimination of thermal history when the mass is large. But, sometimes this method is problematic when the mass of the sample to be measured is small.

3.1.5. Elimination of Thermal History by Freeze-Gradient Temperature Rate Heating Up. Because the method of constant temperature heating does not solve the thermal history well when the masses are small, based on Section 3.1.4, we designed the method of freeze-gradient heating up gradient heating to eliminate the thermal history.

Figure 2(d) presents the method of freeze-gradient heating to eliminate thermal history at 1.0 mg, 2.0 mg 3.0 mg, and 4.0 mg, respectively. Figure 2(d) shows that using this method, the melting peak has a good peak shape and no spurious peaks appear, indicating that the thermal history is well eliminated. Because of the appropriately increased heating rate in the first section, the heat transfer inside the crucible is enhanced. When the mass is very small, there is a stronger thermal field making the intramolecular crystalline shape move. The thermal history of smaller masses at constant temperature can be well solved. Increasing the rate appropriately makes the test time decrease. To explain this approach, we performed scanning electron microscopy analysis on the samples. Figure 3(a) shows that untreated benzil samples were heated to 60°C. Figure 3(b) shows that benzil samples were heated to 60°C using a cooling gradient. The results clearly show that the untreated benzil sample heated to 60°C has a more chaotic arrangement inside the microperspective. This is because due to the high initial temperature, the molecule is not evenly aligned before they reach the melting temperature and start melting. In the beginning, due to the disorderly arrangement, this makes the temperature gradient still exist inside the crystal

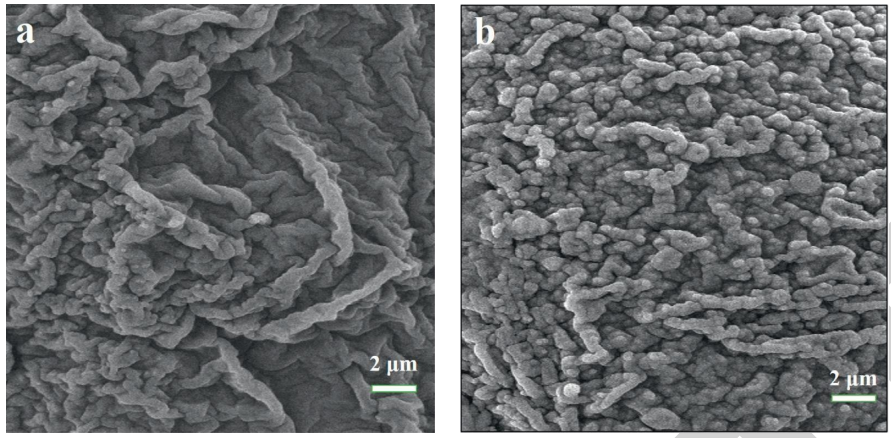

(a) (b)

Figure 3: The electron microscope scans under different methods. (a) The untreated sample was heated to 60°C. (b) The sample of cooling gradient was heated to 60°C.

when the temperature is continued to increase, the temperature field inside the crystal is still not uniform, and the starting temperature of the crystal is different when melting. When the melting point is reached, it still shows the presence of thermal history. On the contrary, in the cooling-warming mode, there is enough time for a uniform arrangement within the molecules due to the different heating rates. Due to the internal alignment pattern, the samples are in a uniform temperature field, so the samples start at different temperatures during melting. Then, the thermal history can be effectively eliminated during melting. Therefore, the freezing gradient temperature rise method is used to eliminate the thermal history.

3.2. Optimization of Quality Factor and Heating Rate Factor. When the DSC was used, the quality of the sample and the heating rate are important factors that affect the results of melting point determination [34]. In order to further optimize the condition of the heating rate to eliminate the thermal history, and to explore the influence of the mass and the heating rate factors on the melting point determination, we designed an orthogonal experiment on the basis of optimized historical conditions. The experimental results are shown in Table 1. Table 1 shows the results of melting point determination for different masses of benzil samples at different heating rates. In order to visualize the changing trend more, we added the data in Table 1 into Figure 4.

Figure 4(a) shows the results of melting point determination for different masses of samples at the same heating rate. At heating rates of 0.5°C·min^{-1}, 1.0°C·min^{-1}, 2.0°C·min^{-1}, and 5.0°C·min^{-1}, the shortest melting range is measured under the same heating rate and different weighing quantities. Some traditional theories believe that the smaller the mass, the shorter the melting range [12]. But, experiments have shown that when the masses were 1.0 mg and 2.0 mg, the melting range will increase instead. This is because when the sample amount is small, the sample is not uniformly distributed in the crucible. This starts the heat transfer process in an uneven temperature field, resulting in

Table 1: The initial melting point at different mass points at different heating rates.

Quality (mg)	Heating rates (°C·min^{-1})					
	0.5	1.0	2.0	5.0	10.0	20.0
1.0	95.04	95.43	95.89	96.13	96.77	96.93
2.0	95.43	95.55	96.17	96.32	96.58	97.51
5.0	94.44	94.57	95.31	95.79	96.26	98.55
7.5	95.53	95.72	95.84	95.94	96.07	98.55
10.0	95.26	95.51	96.55	97.90	98.18	100.27
12.5	96.12	96.27	97.03	97.41	98.28	101.52

increased heat loss. When the masses are 7.5 mg, 10.0 mg, and 12.5 mg, the melting range will increase instead. Due to the increase of the sample mass, more heat needs to be transferred, so the melting range will also increase. When the heating rate is increased to 10.0°C·min^{-1} and 20.0°C·min^{-1}, the melting range with a mass of 5.0 mg is not the shortest. This is because when the heating rate increases, the temperature rises too fast, and the temperature field inside the entire furnace body is not uniform, resulting in a longer melting range. Therefore, the most appropriate sample weight is about 5.0 mg.

On the basis of the optimized historical conditions by freeze-constant temperature rate heating up, the heating rate of the second segment was set to 0.5°C·min^{-1}, 1.0°C·min^{-1}, 2.0°C·min^{-1}, 5.0°C/min, 10.0°C·min^{-1}, and 20.0°C·min^{-1}. The heating rate is for exploring the factor of the heating rate and further optimizing the condition of the heating rate to eliminate the thermal history. Figure 4(b) shows the results of melting point determination for different heating rates of samples at the same mass. Comparing the different heating rates at each quality point, it is not difficult to find that when the heating rate increases, the measured melting range of p-nitrotoluene also extends. This is because when the temperature rise rate is too fast, the sample does not have enough time to melt [35]. It will make the melting range increase greatly. To measure the most accurate melting

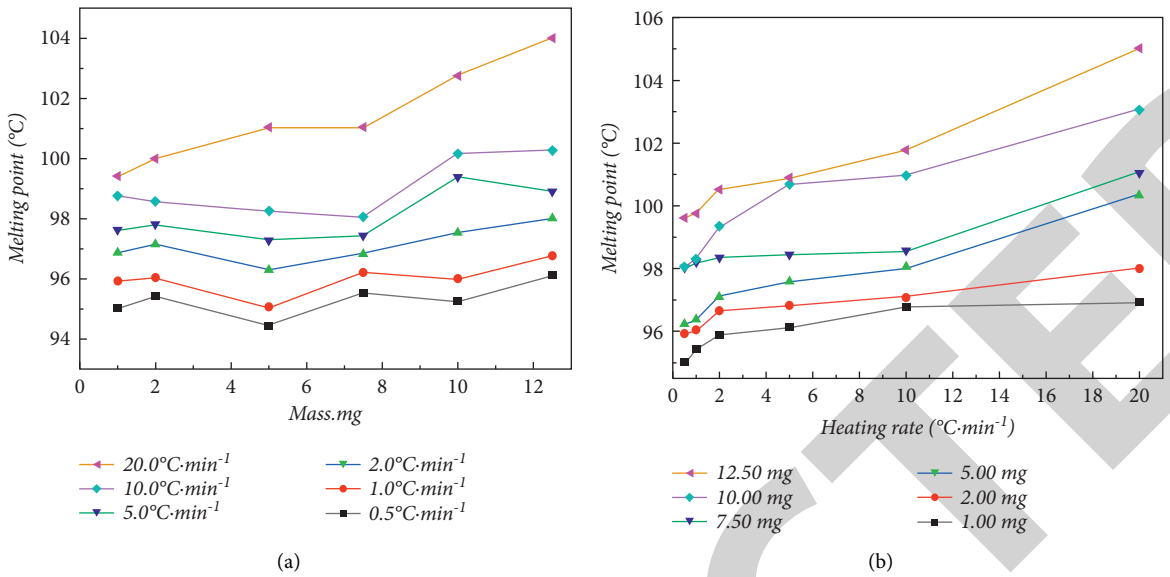

Figure 4: The initial melting point at different mass points at different heating rates. (a) The results of melting point determination for different masses of samples at the same heating rate. (b) The results of melting point determination for different heating rates of samples at the same mass.

Table 2: Evaluation results of the uncertainty of DSC method.

Category	Parameter	Meaning	Evaluation method	Standard uncertainty/u (°C)	Relative standard uncertainty/u_{rel}
Uncertainty introduced by the calibration process.	u_1	Uncertainty introduced by indium itself.	$u_1 = U/k$	0.13	8.30×10^{-4}
	u_2	Uncertainty introduced by repeated measurements of indium.	$u_2 =$ In RSD	0.0011	6.64×10^{-6}
	u_3	Uncertainty component introduced by instrument temperature error.	$u_3 = \triangle T_{max}/k$	0.0016	9.90×10^{-6}
Uncertainty introduced by the sample itself.	u_4	Uncertainty introduced by repeated measurements of samples.	$u_4 =$ Benzil's RSD	0.0027	4.45×10^{-5}
	u_5	Uncertainty component introduced by sample uniformity.	$u_5 = \sqrt{(s_1 - s_2)/n}$	0.045	2.47×10^{-4}
	u_6	Uncertainty component introduced by short-term stability.	$u_6 = s\ (\beta_1) \cdot t$	0.0028	2.53×10^{-5}
	u_7	Uncertainty component introduced by sample mass.	$u_7 = \triangle T_{max}/k$	0.029	3.05×10^{-4}
Uncertainty introduced by experimental conditions.	u_8	Uncertainty component introduced by heating rate.	$u_8 = {}^{\triangle}T_{max}/k$	0.029	3.05×10^{-4}
	u_9	Uncertainty component introduced by airflow rate.	$u_9 = \triangle T_{max}/k$	0.0016	1.21×10^{-4}
	u_{10}	Uncertainty component introduced by a thermal lag coefficient.	$u_{10} = \tau_0$'s RSD* dT/dt	0.0027	1.21×10^{-4}
Combination of uncertainties	$u_{DSC,rel}$	Relative standard uncertainty of DSC.			9.84×10^{-4}
	u_{DSC}	Combined standard uncertainty of DSC.			0.0932
	$U(k=2)$	Expanded uncertainty.			0.19

range, we should choose the lowest heating rate. However, when the heating rate is 0.5°C·min^{-1} and 1.0°C·min^{-1}, the measured melting range is similar, and the time required for the heating rate at 1.0°C·min^{-1} is shorter than the time required for 0.5°C·min^{-1}. Therefore, 1.0°C·min^{-1} is the most suitable heating rate.

3.3. Thermal Lag Factor Optimization. During the heating process of the differential scanning calorimeter, there is a heat loss phenomenon during the heat transfer between the furnace body and the aluminum crucible. At the same time, there is a heat loss phenomenon in the crucible due to the pores inside the sample molecules. These heat loss phenomena will cause the melting range to be extended, and the measured melting point peak will be delayed. If the heat loss is classified and discussed, the work is very tedious, so these factors that cause the melting range are classified as thermal hysteresis factors [36]. The melting range measured at different heating rates is corrected with the given melting point according to equation (1). Since the heating rate was 1°C·min^{-1}, combined with the relevant data in Table 1, the thermal hysteresis coefficient was 0.56 min and the RSD (relative standard deviation) of the thermal hysteresis coefficient was 2.97%.

$$T' = T + \tau_0 \cdot \frac{\mathrm{d}T}{\mathrm{d}t}, \tag{1}$$

where T' is the measured melting range, T is the theoretical melting point, τ_0 is the thermal hysteresis coefficient, and $\mathrm{d}T/\mathrm{d}t$ is the heating rate.

3.4. Uncertainty Evaluation. In order to improve the accuracy of the optimization method, we need to evaluate the uncertainty of this method. In the process of measuring melting points by DSC, the uncertainty mainly comes from three aspects: the calibration process, the sample itself, and the experimental method. The standard uncertainty of DSC is investigated according to (2). Table 2 shows the description and evaluation methods of all parameters. The extended uncertainty of this method was 0.19°C.

$$u_{\mathrm{DSC,rel}} = \sqrt{u_{1,\mathrm{rel}}^2 + u_{2,\mathrm{rel}}^2 + u_{3,\mathrm{rel}}^2 + u_{4,\mathrm{rel}}^2 + u_{5,\mathrm{rel}}^2 + u_{6,\mathrm{rel}}^2 + u_{7,\mathrm{rel}}^2 + u_{8,\mathrm{rel}}^2 + u_{9,\mathrm{rel}}^2}. \tag{2}$$

3.5. Validation of Experimental Methods. To verify the accuracy of the method, we used the melting point reference substance p-nitrotoluene for comparison experiments. We conducted 30 experiments for melting point determination. The experimental results showed that the average value of p-nitrotoluene's melting point was 52.64°C, which was within its reference value of (52.53 ± 0.20) °C. The RSD of the measured results was 0.11%. Therefore, the optimized method can be considered accurate.

4. Conclusions

In this study, we design a new method of freeze-gradient temperature rate heating up to eliminate the thermal history of DSC, using benzil as the study object. In the method of constant temperature near the melting point to eliminate the thermal history, after the first temperature rises to reach the melting point, a phase change occurs by melting and the ordered and disordered crystalline shapes within the molecule disappear. The new crystalline forms are formed in the process due to the presence of the cooling crystallization process. Another method of repeated heating of the sample to eliminate the thermal history has a false peak before the melting peak because the repeated heating did not result in a neat arrangement of crystallites within the molecule, and there are still disordered crystalline forms in the molecule. The artifactual peak at 105°C may be due to the presence of a cooling crystallization process in which a new crystalline form is formed again. This method avoids the introduction of a new thermal history by cooling the crystallization, and this method was able to eliminate the thermal history of benzil well, resulting in a sharper melt peak shape and no other spurious peaks appeared. Based on this method, we optimized other factors to establish a complete method for the determination of melting point by DSC and analyzed the uncertainty of the method. The result shows the extended uncertainty U ($k = 2$) of DSC at 0.19°C. The p-nitrotoluene was used to validate this method and the melting point value of p-nitrotoluene was within the reference range, indicating that this method is feasible. The method provides a reference for DSC to develop melting point standards for the accurate determination of the melting points of substances.

Data Availability

The datasets used and/or analyzed during the current study are available from the corresponding author upon reasonable request.

Conflicts of Interest

The authors declare that they have no conflicts of interest.

References

[1] I. De Las Heras, J. Dufour, and B. Coto, "A novel method to obtain solid–liquid equilibrium and eutectic points for hydrocarbon mixtures by using differential scanning calorimetry and numerical integration," *Fuel*, vol. 297, Article ID 120788, 2021.

[2] J. Kovinich, S. A. Hesp, and H. Ding, "Modulated differential scanning calorimetry study of wax-doped asphalt binders," *Thermochimica Acta*, vol. 699, Article ID 178894, 2021.

[3] W. Su, L. Gao, L. Wang, and H. Zhi, "Calibration of differential scanning calorimeter (DSC) for thermal properties analysis of phase change material," *Journal of Thermal Analysis and Calorimetry*, vol. 143, no. 4, pp. 2995–3002, 2021.

[4] D. Gaona, E. Urresta, J. Marinez, and G. Guerron, "Medium-temperature phase-change materials thermal characterization by the T-History method and differential scanning calorimetry," *Experimental Heat Transfer*, vol. 30, no. 5, pp. 463–474, 2017.

[5] A. Jalali, M. A. Huneault, and S. Elkoun, "Effect of thermal history on nucleation and crystallization of poly (lactic acid)," *Journal of Materials Science*, vol. 51, no. 16, pp. 7768–7779, 2016.

[6] P. Pan, B. Zhu, W. Kai, T. Dong, and Y. Inoue, "Effect of crystallization temperature on crystal modifications and crystallization kinetics of poly (L-lactide)," *Journal of Applied Polymer Science*, vol. 107, no. 1, pp. 54–62, 2008.

[7] F. Benali, M. Hamidouche, H. Belhouchet, N. Bouaouadja, and G. Fantozzi, "Thermo-mechanical characterization of a silica-alumina refractory concrete based on calcined algerian kaolin," *Ceramics International*, vol. 42, no. 8, pp. 9703–9711, 2016.

[8] J. Kang, J. He, Z. Chen et al., "Effects of β-nucleating agent and crystallization conditions on the crystallization behavior and polymorphic composition of isotactic polypropylene/multi-walled carbon nanotubes composites," *Polymers for Advanced Technologies*, vol. 26, no. 1, pp. 32–40, 2015.

[9] R. Androsch, C. Schick, and M. L. Di Lorenzo, *Kinetics of Nucleation and Growth of Crystals of Poly(L-lactic acid). In: Di Lorenzo, M., Androsch, R. (eds) Synthesis, Structure and Properties of Poly(lactic acid). Advances in Polymer Science*, Springer, vol 279. Springer, Cham, Switzerland, 2017.

[10] M. R. Kamal, R. El Otmani, A. Derdouri, and J. S. Chu, "Flow and thermal history effects on morphology and tensile behavior of poly (oxymethylene) micro injection molded parts," *International Polymer Processing*, vol. 32, no. 5, pp. 590–605, 2017.

[11] A. Hasan, S. McCormack, M. Huang, and B. Norton, "Characterization of phase change materials for thermal control of photovoltaics using Differential Scanning Calorimetry and Temperature History Method," *Energy Conversion and Management*, vol. 81, pp. 322–329, 2014.

[12] T. Truong, S. Prakash, and B. Bhandari, "Effects of crystallisation of native phytosterols and monoacylglycerols on foaming properties of whipped oleogels," *Food Chemistry*, vol. 285, pp. 86–93, 2019.

[13] E. Parodi, L. E. Govaert, and G. Peters, "Glass transition temperature versus structure of polyamide 6: a flash-DSC study," *Thermochimica Acta*, vol. 657, pp. 110–122, 2017.

[14] I. A. Van Wetten, A. van Herwaarden, R. Splinter, R. Boerrigter-Eenling, and S. van Ruth, "Detection of sunflower oil in extra virgin olive oil by fast differential scanning calorimetry," *Thermochimica Acta*, vol. 603, pp. 237–243, 2015.

[15] M. Safari, A. Martinez de Ilarduya, A. Mugica, M. Zubitur, S. Munoz-Guerra, and A. J. Muller, "Tuning the thermal properties and morphology of isodimorphic poly [(butylene succinate)-ran-(ε-caprolactone)] copolyesters by changing composition, molecular weight, and thermal history," *Macromolecules*, vol. 51, no. 23, pp. 9589–9601, 2018.

[16] P. Das and P. Tiwari, "Thermal degradation kinetics of plastics and model selection," *Thermochimica Acta*, vol. 654, pp. 191–202, 2017.

[17] J. Bai, B. Zhang, J. Song, G. Bi, P. Wang, and J. Wei, "The effect of processing conditions on the mechanical properties of polyethylene produced by selective laser sintering," *Polymer Testing*, vol. 52, pp. 89–93, 2016.

[18] F. De Santis, V. Volpe, and R. Pantani, "Effect of molding conditions on crystallization kinetics and mechanical properties of poly (lactic acid)," *Polymer Engineering & Science*, vol. 57, no. 3, pp. 306–311, 2017.

[19] L. Deng, K. Kosiba, R. Limbach, L. Wondraczek, U. Kuhn, and S. Pauly, "Plastic deformation of a Zr-based bulk metallic glass fabricated by selective laser melting," *Journal of Materials Science & Technology*, vol. 60, pp. 139–146, 2021.

[20] O. Yousefzade, F. Hemmati, H. Garmabi, and M. Mahdavi, "Thermal behavior and electrical conductivity of ethylene vinyl acetate copolymer/expanded graphite nanocomposites: effects of nanofiller size and loading," *Journal of Vinyl and Additive Technology*, vol. 22, no. 1, pp. 51–60, 2016.

[21] Y. Chen, X. Chen, D. Zhou, Q. D. Shen, and W. Hu, "Low-temperature crystallization of P (VDF-TrFE-CFE) studied by Flash DSC," *Polymer*, vol. 84, pp. 319–327, 2016.

[22] D. Vaes, M. Coppens, B. Goderis, W. Zoetelief, and P. Van Puyvelde, "Assessment of crystallinity development during fused filament fabrication through fast scanning chip calorimetry," *Applied Sciences*, vol. 9, no. 13, Article ID 2676, 2019.

[23] V. V. Baranov, T. N. Vol'khina, Y. V. Nelyubina, and A. N. Kravchenko, "New aspects of reactions of methyl (thio) ureas with benzil," *Mendeleev Communications*, vol. 31, no. 5, pp. 673–676, 2021.

[24] M. Mizusaki, S. Enomoto, and Y. Hara, "Novel fabrication method of polymer-sustained-alignment liquid crystal cell formed from the monomer containing benzil-group," *Liquid Crystals*, vol. 48, no. 2, pp. 263–272, 2021.

[25] A. Fattahi, S. R. Kass, J. F. Liebman, M. A. R. Matos, M. S. Miranda, and V. M. F. Morais, "The enthalpies of formation of o-m-and p-benzoquinone: gas-phase ion energetics, combustion calorimetry, and quantum chemical computations combined," *Journal of the American Chemical Society*, vol. 127, no. 16, pp. 6116–6122, 2005.

[26] M. Bekan, *Profil Hlapljivih Spojeva Meda Kestena*, University of Split. Faculty of Chemistry and Technology. Division of Chemistry, Split, Croatia, 2021.

[27] R. Kołodziejska, R. Studzinska, A. Tafelska-Kaczmarek, H. Pawluk, D. Mlicka, and A. Wozniak, "Microbial synthesis of (S)-and (R)-Benzoin in enantioselective desymmetrization and deracemization catalyzed by aureobasidium pullulans included in the blossom Protect™ agent," *Molecules*, vol. 26, no. 6, Article ID 1578, 2021.

[28] S. Kahwaji, M. B. Johnson, and M. A. White, "Thermal property determination for phase change ma terials," *The Journal of Chemical Thermodynamics*, vol. 160, Article ID 106439, 2021.

[29] G. Knothe and R. O. Dunn, "A comprehensive evaluation of the melting points of fatty acids and esters determined by differential scanning calorimetry," *Journal of the American Oil Chemists' Society*, vol. 86, no. 9, pp. 843–856, 2009.

[30] Y. Zhang, Y. Li, Y. Huang, S. Li, and W. Wang, "Characteristics of mass, heat and gaseous products during coal spontaneous combustion using TG/DSC–FTIR technology," *Journal of Thermal Analysis and Calorimetry*, vol. 131, no. 3, pp. 2963–2974, 2018.

[31] D. Spathara, D. Sergeev, D. Kobertz, M. Muller, D. Putman, and N. Warnken, "Thermodynamic study of single crystal, Ni-based superalloys in the $\gamma+\gamma'$ two-phase region using

Hindawi
Journal of Chemistry
Volume 2023, Article ID 9831807, 1 page
https://doi.org/10.1155/2023/9831807

Retraction

Retracted: Bioactivation of Polyaniline for Biomedical Applications and Metal Oxide Composites

Journal of Chemistry

Received 28 November 2023; Accepted 28 November 2023; Published 29 November 2023

This article has been retracted by Hindawi, as publisher, following an investigation undertaken by the publisher [1]. This investigation has uncovered evidence of systematic manipulation of the publication and peer-review process. We cannot, therefore, vouch for the reliability or integrity of this article.

Please note that this notice is intended solely to alert readers that the peer-review process of this article has been compromised.

Wiley and Hindawi regret that the usual quality checks did not identify these issues before publication and have since put additional measures in place to safeguard research integrity.

We wish to credit our Research Integrity and Research Publishing teams and anonymous and named external researchers and research integrity experts for contributing to this investigation.

The corresponding author, as the representative of all authors, has been given the opportunity to register their agreement or disagreement to this retraction. We have kept a record of any response received.

References

[1] K. A. Omran, "Bioactivation of Polyaniline for Biomedical Applications and Metal Oxide Composites," *Journal of Chemistry*, vol. 2022, Article ID 9328512, 9 pages, 2022.

Hindawi
Journal of Chemistry
Volume 2022, Article ID 9328512, 9 pages
https://doi.org/10.1155/2022/9328512

Research Article

Bioactivation of Polyaniline for Biomedical Applications and Metal Oxide Composites

Khalida Abbas Omran

Ibn Khaldoun University College, Baghdad, Iraq

Correspondence should be addressed to Khalida Abbas Omran; khalida.abass@ik.edu.iq

Received 18 July 2022; Revised 24 July 2022; Accepted 28 July 2022; Published 23 August 2022

Academic Editor: Rabia Rehman

In this work, the oxidative chemical synthesis of polyaniline (PANI) in the presence of glutamic acid (GA) is presented, using ammonium persulfate (APS) as the oxidizing agent. Syntheses were performed by varying the molar ratio of aniline:amino acid: oxidant. The products of the different reactions were characterized by SEM, TEM, and FTIR techniques. It was observed that the molar ratio of aniline:amino acid:oxidant used in the synthesis determines the composition and conformation of the resulting polymer and its morphological and electrochemical properties. Composite hydrogels were prepared by incorporating the drug-loaded PANI nanofibers in situ through polymerization and cross-linking of acrylamide. TEM images of the cross-section of the hydrogel revealed the formation of a three-dimensional system of the polyaniline nanofibers maintained by the insulating matrix of the polyacrylamide hydrogel. The *in vitro* release of the drug from the hydrogels composed of polyacrylamide/polyaniline against buffer solutions at different pH and temperature was studied, using orbital agitation. Finally, considering the potential of hydrogels composed of polyacrylamide/polyaniline for the controlled release of drugs, a study was conducted to evaluate their cytotoxicity against normal mouse subcutaneous tissue cells.

1. Introduction

Polyaniline has received much attention among conductive polymers, and extensive research has been done on it in both its native and functionalized forms. This is due to the ease with which polyaniline and its composites can be made. Polyaniline is traditionally synthesized by oxidative polymerization [1] from an aniline monomer or an anilinium salt using chemical synthesis and electrochemical synthesis [2]. Polyaniline is one of the most researched polymers due to its wide range of applications. The biocompatibility, biodegradability, and antiproliferative power of the polyaniline against pathogenic bacteria, as well as its conjugation capacity with biologically active molecules, have led to its use in enzymatic biosensors for triglyceride detection, support for enzyme immobilization, controlled drug release systems, tissue engineering, artificial muscles, and nerve growth and regeneration [3–5]. The reversible volumetric changes that polyaniline undergoes under controlled electrical pulses, on the other hand, have been used in the fabrication of actuators, as well as other biomedical applications [3–6]. A gel is a three-dimensional network of flexible chains made up of segments that are connected in a specific pattern and swollen by a liquid. If the solvating liquid is organic, it is called an organogel; if the solvating liquid is water, it is called a hydrogel. Hydrogels are made up of natural or synthetic polymers that intertwine to form a network that swells to form soft and elastic materials when exposed to water or biological fluids [7]. These systems increase their volume significantly while maintaining their shape until they reach physical-chemical equilibrium. Hydrogels that are sensitive to an electric field are gaining popularity due to their numerous applications. These materials have been used in the pharmaceutical industry for the controlled release of drugs. Sheng Tsai et al. [8] made electroconductive hydrogels out of polyvinyl alcohol cross-linked with diethyl acetamidomalonate and polyaniline as the conductive component. Electrical control was used to evaluate the hybrid system for

cumulative ON-OFF indomethacin release. The efficiency of these devices was around 70% [8]. Hydrogels' properties have allowed them to be used in biomedical applications such as biosensors, drug delivery systems, contact lenses, catheters, and wound dressings [9]. One of the most popular applications is matrices for immobilizing and stabilizing enzymes [8, 9]. Because of this, conductometric, amperometric, and optical transduction have been used in biorecognition systems. We can use it as a microbioreactor to capture and stabilize biological molecules and high control of biological reactions because of its high water content and structural distribution. Hydrogels have been used as bioactive films to hold various types of antibodies and to make DNA biochips in this way [9, 10]. Their ability to change volume and shape in response to solvent composition, temperature, pH, and electric field has led to their use in MEMS and artificial muscles. Its application in genetic engineering has been enabled by its high water content, elastic modules that are very similar to human tissues, and biocompatibility properties *in vitro* and *in vivo* [11].

Generally, electroactive films or polymeric membranes are used to release, exchange, or move specific molecules, usually ions. When a concentration gradient is maintained on each side of the membrane, cyclically increasing the concentration within the membrane, continuous electrical pumping is possible. When an electric field is established on opposite sides of the membrane, the oxidation states of the polymer are altered, resulting in release activation. Zhou et al. were the first to show that the oxidation state of anions influences their transport through polypyrrole films [12]. Tong-Sheng Tsai et al. [8] developed electroconductive hydrogels based on polyvinyl alcohol and polyaniline as an electroconductive polymer in 2011 for the controlled release of indomethacin via electrical stimulation. The current work examines the technique of incorporating glutamic acid into polyaniline structures manufactured by chemical means and the polymeric system's capacity for regulated drug release.

2. Materials and Methods

2.1. Materials. Aniline L-glutamic acid (GA) (98%), the pH, and temperature of the release medium can be used to control the release of amoxicillin from hydrogels made of polyacrylamide and polyaniline.Other chemicals used in the current study were purchased from Sigma-Aldrich with AR grade 98-99% purity, and the reaction was continuously stirred. After 24 hours, the reaction mixture was filtered with deionized water until the filtrate's pH reached 6. And we can conclude that hydrogels composed of polyacrylamide polyaniline can be considered potential candidates for applications in electrically controlled release devices, such as iontophoretic patches, based on the ability to control drug release.

2.2. Methods

2.2.1. Chemical Synthesis of Polyaniline in the Presence of L-Glutamic Acid. To carry out the aniline polymerization, 2 g of L-glutamic acid (GA) were weighed and dissolved in 132 mL of deionized water, using magnetic stirring and a temperature of 60°C [13]. The GA solution was placed in a 3-necked flask and 5 mL of previously distilled aniline was added to it. Separately, 12.52 g of ammonium persulfate were dissolved with 70 mL of deionized water. The APS solution was placed in an addition funnel. The reaction system was closed, and a nitrogen flow was allowed to pass for 10 to 15 minutes. After the air was evacuated, the reaction system was sealed and the APS solution was dropped dropwise. Importantly, before and after adding the oxidant solution, the reaction flask was kept in an ice bath. The reaction was left under continuous stirring for 24 hours. Once 24 hours had elapsed, the reaction mixture was washed by filtration with deionized water until the filtrate reached a pH of 6. The product of this stage consisted of an aqueous suspension with a concentration of structures PANI fibrillar cells coated with GA. In Table 1, the syntheses performed according to molar ratios are listed.

FTIR spectra were obtained on GX Perkin-Elmer Spectrum equipment. The remaining suspension was used to carry out the characterizations by scanning electron microscopy (SEM) JEOL 5410LV model, transmission electron microscopy (TEM) JEOL JEM-2,100 F model, and UV-visible absorption spectra were acquired using a Perkin Elmer Lambda 20 spectrophotometer (USA), as well as for drug loading/release studies.

2.2.2. Study of the Aniline-Glutamic Acid Interaction. To evaluate the existence of interactions between the monomer and the amino acid before the aniline oxidation process, a titration curve of aniline with GA was obtained using UV-Vis absorption spectroscopy. An acetate buffer solution (0.2 M) was used to control the pH at 5, resembling the initial conditions of the chemical environment before the polymerization process. Aliquots of a GA solution (0.2738 M) were gradually added to 2.99 mL of the aniline solution in a buffer until a molar ratio of 1:0.25 was obtained.

2.2.3. Amoxicillin Loaded on Polyaniline Structures. The incorporation of the antibiotic was carried out by mixing 20 mL of the polyaniline suspension (0.0148 g/mL) with 10 mL of an aqueous solution of the drug (200 mg/L) for 24 hours, the optimal time from which does not increase the absorption of amoxicillin. The resulting mixture was transferred to dialysis tubes, which were placed in a beaker containing 500 mL of deionized water, to remove the drug not adsorbed on the polymer particles. Drug concentration was determined from the absorbance of the dialysis solution at 273 nm, using a calibration curve constructed by UV-Vis absorption spectroscopy from solutions of known concentration.

2.2.4. Release of Adsorbed Amoxicillin in Buffer Solutions. The dialysis tubes containing the polyaniline particles loaded with the antibiotic were immersed in 450 mL of buffer solutions of pH 5 (acetate (0.1 M)), 7 (phosphate (0.1 M)), and 9 (borate chloride (0.1 M)). The antibiotic release process was carried out in a Barnstead/Lab-Line/E-Class MAX 4000

Table 1: The polyaniline synthesis in molar ratios using the monomer amino acid oxidizing agent.

Synthesis	Molar ratio aniline:GA:APS
1	1:0.13:1.0
2	1:0.25:1.0
3	1:0.38:1.0
4	1:0.50:1.0
5	1:0.25:0.6
6	1:0.25:1.4

(USA) model incubator at a controlled temperature of 37°C and orbital agitation of 80 rpm. Amoxicillin concentration in the release medium was monitored by taking 2 mL aliquots every 2 hours for 4 days. A similar buffer volume was added to the release medium to maintain immersion conditions.

2.2.5. Preparation of Hydrogels Composed of Polyacrylamide and Polyaniline Loaded with Amoxicillin for Release Studies in Buffer Solutions. The polyaniline/amoxicillin system was incorporated into a polyacrylamide hydrogel by adding a portion of the polyaniline colloidal suspension loaded with the antibiotic during the process of cross-linking and hydrogel formation. Aqueous solutions of acrylamide (AAm, monomer) and bisacrylamide (BisAAm, cross-linking monomer) were prepared at different weight-volume concentrations, as shown in Table 2. Fifteen milliliters of the AAm/BisAAm solution were taken and mixed with 10 ml of the polyaniline/amoxicillin suspension, by means of constant magnetic stirring at a temperature of 5°C. Once the previous mixture had been homogenized, 1 mL of an APS solution (initiator) with a concentration of 10% weight/volume was added, and stirring was continued, keeping the temperature at 5°C. After 3 minutes, 0.2 mL of a 99% solution of TEMED (catalyst) was added, and stirring was continued. After 2 minutes, the mixture was removed from the ice bath and kept at room temperature until the end of the polymerization process and gel formation. The hydrogels were identified as shown in Table 2. Under conditions identical to those described in the previous paragraph, a polyacrylamide hydrogel without incorporation of the polyaniline particles was prepared. This hydrogel was loaded with a dose of drug similar to that present in hydrogels containing the electroconductive polymer.

2.2.6. Cytotoxicity Study of Hydrogels Composed of Polyacrylamide and Polyaniline. For the toxicity studies of the composite hydrogels, the normal cell line L-929 (normal mouse subcutaneous tissue) was used, provided by the immunology laboratory of the University of Sonora. Cultures were maintained in DMEM supplemented with 5% fetal bovine serum and in a Fischer Scientific (USA) Isoterm incubator at 37°C, 5% CO_2, and 80–90% relative humidity. In order to determine how the hydrogels affected the cells, a cell viability assay was performed. This test involved using the MTT method to incubate polyacrylamide or polyacrylamide/polyaniline hydrogels in a cell culture medium. The results of this experiment were then analyzed. At 37°C, three hydrogel cylinders of each composition, measuring 7 mm in diameter and 3 mm in thickness, were immersed in 10.2 mL of cell culture. After 24 hours, the hydrogels were removed, and the medium that contained the soluble compounds of the hydrogel was used for the viability assay. This medium is referred to as a "conditioned medium." A cell suspension of 200,000 cells/mL was obtained starting with a culture in a logarithmic growth phase. Fifty microliters of the cell suspension were placed in a 96-well flat-bottom plate and incubated for 24 h for adherence. After this period, using the conditioned medium, a volume of 100 μL was completed in each well, reaching concentrations of the conditioned medium of 50, 25, 12.5, and 6,250% (v/v). In the case of the control experiment, the 100 μL was completed only with a standard culture medium. The plate was incubated for a period of 48 h. During this period, the effect of the stimulus on cell morphology was observed using an inverted Nikon Eclipse microscope. Once the incubation time had elapsed, 10 μL of MTT were added to each well and incubated for a period of 4 h. Subsequently, 100 μL of acidic isopropanol were added and allowed to stand for 10 minutes. Finally, the absorbance of the solution was read at 570 nm and 655 nm in an ELISA reader (BIO-RAD).

The statistical treatment of the experimental data was carried out through an ANOVA analysis of variance, using the Microsoft Excel XLSTAT complement and establishing a confidence interval of 95%. The existence of statistically significant differences ($p < 0.05$) between the mean determined for each type of sample against the value obtained in the control test using Dunnett's test was verified.

3. Results and Discussion

3.1. Chemical Synthesis of Polyaniline in the Presence of L-Glutamic Acid. This section shows the results obtained from the different chemical-oxidative syntheses of polyaniline. Six types of synthesis were performed varying the aniline:amino acid and aniline:oxidizing agent molar ratios This study was carried out to establish the optimal reaction conditions that would favor obtaining polyaniline in its ES state, the incorporation of the amino acid into the polymeric system, and the formation of structures with a morphology with a high aspect ratio (quotient of the maximum dimension to the minimum of the particle).

3.2. Characterization Studies

3.2.1. Scanning Electron Microscopy (SEM). Figure 1 shows the SEM microscopy images of the reaction products of the different syntheses. It is observed on a micrometric scale that the oxidation product of aniline in the presence of GA has a cylindrical morphology with a high aspect ratio (length-diameter ratio). It is also appreciated that there are agglomerated particles, observing material where the individual structures are not distinguished. The diameter of the cylinders found for the different molar ratios ranges from 360 nm. It is observed that the morphology and the amount of agglomerated material of the structures have a strong dependence on the concentration of FA and APS.

The TEM microscopy images shown in Figure 2, for the different molar ratios, preferentially produce primary

Table 2: Concentrations and volumes for amoxicillin composite hydrogels used in release versus buffer solutions.

Hidrogel	AAm/BisAAm solution/ concentration (g/mL)			Polyaniline/ amoxicillin suspension	Amoxicillin solution	APS solution		TEMED solution	
	AAm	BisAAm	Volume (mL)	Volume (mL)	Volume (mL)	Concentration (%)	Volume (mL)	Concentration (%)	Volume (mL)
A	0.58	**0.01**	15	10	0	10	1	99	0.2
B	0.58	**0.02**	15	10	0	10	1	99	0.2
C	0.58	**0.03**	15	10	0	10	1	99	0.2
D ∗	0.58	**0.02**	15	0	10	10	1	99	0.2

∗AAm: acrylamide monomer and BisAAm: bisacrylamide (cross-linking monomer).

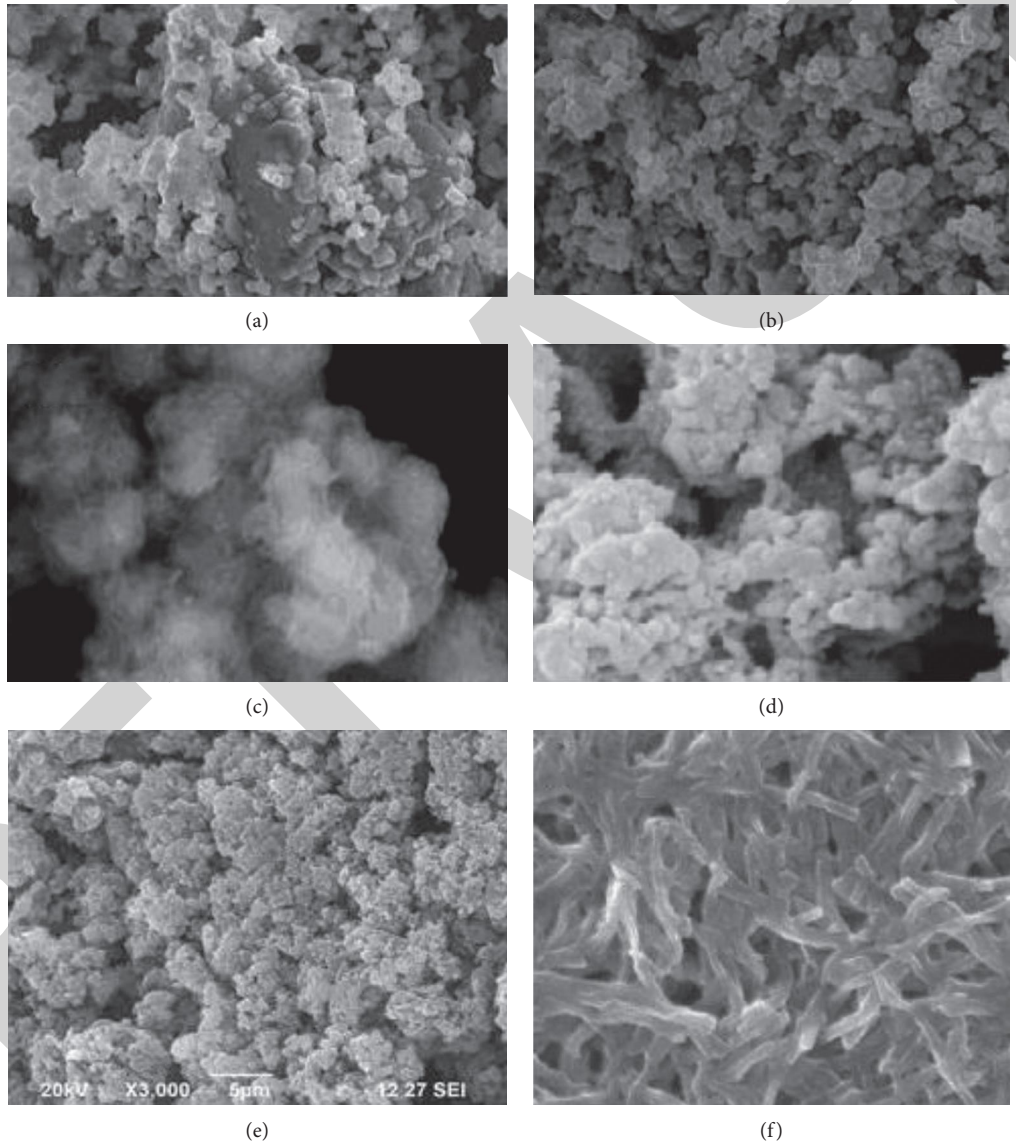

Figure 1: SEM images of polyaniline synthesized at aniline:GA:APS molar ratios of six samples.

structures with a cylindrical morphology, as had been observed by SEM microscopy at larger scales. It is important to highlight that for obtaining the TEM images, the diluted polyaniline suspensions were previously subjected to sonication to improve the visualization of the primary structures. It was observed that the individual cylindrical structures present a diameter from a nanometric scale (<100 nm) to micrometric scales (between 100 nm and 1 μm) and that the morphology of the submicron/nanostructures varies strongly with the concentration of FA and APS; that is, the shape of the

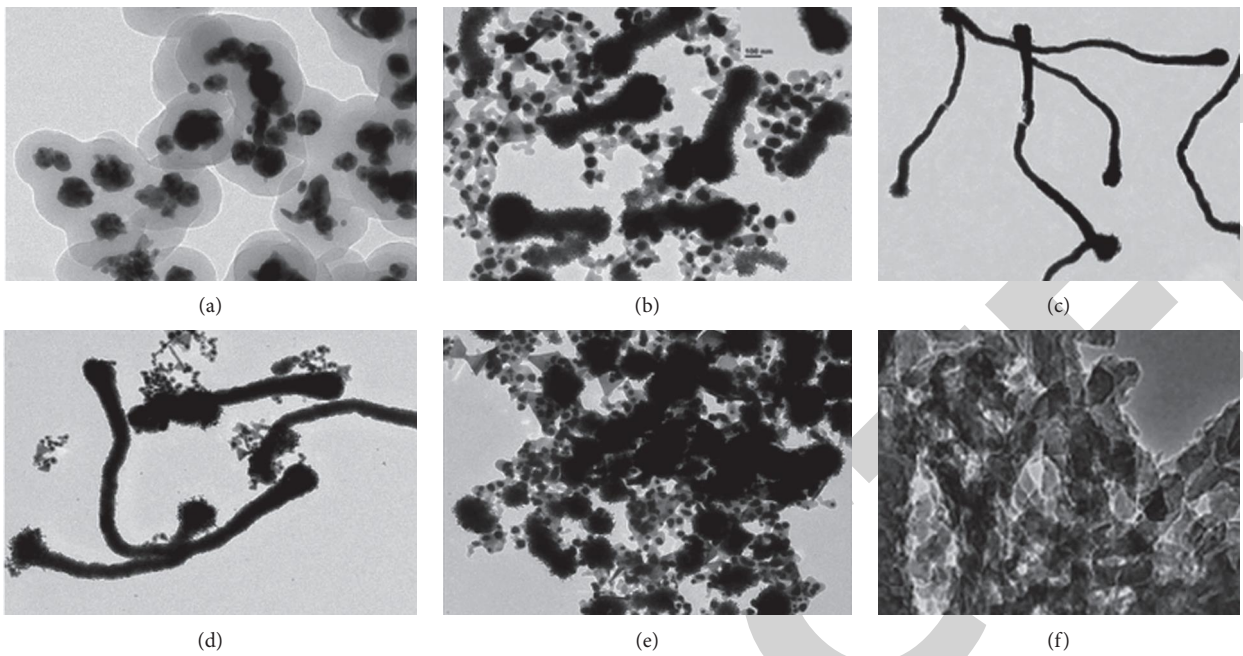

Figure 2: Transmission electron microscopic images of polyaniline samples at different concentrations (refer to Table 1).

structures can be controlled by changing the aniline:GA:APS molar ratio. For example, the primary structures of samples 1: 0.13:1 and 1:0.25:1 showed a fibrillar morphology with a higher length-to-diameter ratio than those of other samples.

3.2.2. Infrared Spectroscopy (FTIR). FTIR spectra corresponding to polyaniline synthesized at different molar ratios are shown in Figures 3(a) and 3(b). The samples show very similar spectra regardless of the aniline:GA and aniline:APS molar ratios used in the synthesis. In the spectrum region between 1,800 and 700 cm^{-1}, main bands are observed with transmittance minima at 1,580 and 1,506 cm^{-1} that are attributed to the C–C stretching of the ring, in quinoid diimines benzenoid diamines, respectively [14]. Likewise, a peak at 1,288 cm^{-1} is detected, which is assigned to the vibration by stretching the C–N bonds between the quinoid and benzenoid units. Around 1,402 and 1,442 cm^{-1}, there are two bands associated with the imine C–N bond strain and the intermediate order C–N bond strain between amine N and imine N. The bands with minima around 1,142 and 820 cm^{-1} are associated with the electronic absorption of the conjugate structure that forms the quinoid ring and the neighboring nitrogens and with the bending of the C–H bonds of the 1,4-disubstituted ring of polyaniline., respectively [15]. The appearance of these last signals indicates that the synthesized polymer predominantly presents a linear conformation, without structural defects, which is closely related to optimal values of electrical conductivity.

3.2.3. UV-Visible Absorption Spectroscopy. The characteristic bands of the ES state of polyaniline are identified in the UV-Vis absorption spectra. The spectra of the varied synthesis routes are very similar in general. Without taking into account the 1:0.25:1 sample, absorptions were attributed to π–$\pi*$ (λ_{max} ~348 nm), $-\pi*$ (λ_{max} ~430 nm), and π -polaron (λ_{max} between 800 and 860 nm) transitions with well-localized bands in the remaining samples. These findings are in line with the conductive properties observed in all synthesized samples as well as those previously reported for other ES samples, such as polyaniline doped with camphor sulfonic acid [16]. The presence of an absorption maximum in the visible-near IR boundary region also suggests that the product of these syntheses presents its chains in a compact conformation. The fact that the polarons of each tetrameric unit are isolated from each other causes torsional defects between the aromatic rings, resulting in this type of conformation. As a result, the polaronic band appears to be well localized and has little energy dispersion. The localized band of the - polaron transition seen in the other samples is replaced by an elongated tail of free carriers in the near IR region in the 1: 0.25:1 sample. This is typical of an extended chain conformation, in which torsion defects between aromatic rings are removed, favoring interaction between isolated adjacent polarons, resulting in increased polaronic band energy dispersion and delocalization.

3.3. Study of the Aniline-Glutamic Acid Interaction. Aniline was initially softened in an aqueous medium of GA prior to the oxidation process, and the pH of the solution that was produced by this step was approximately 5. An equimolar mixture of neutral aniline molecules, which are easily oxidized, and anilinium cations, which oxidize much more slowly, was present in this pH region. The pH of the medium drops rapidly to a range between 0.9 and 1.5 after the addition of APS and/or hydrogen sulfate salts [8]. GA exists primarily as a monovalent cation in this pH range,

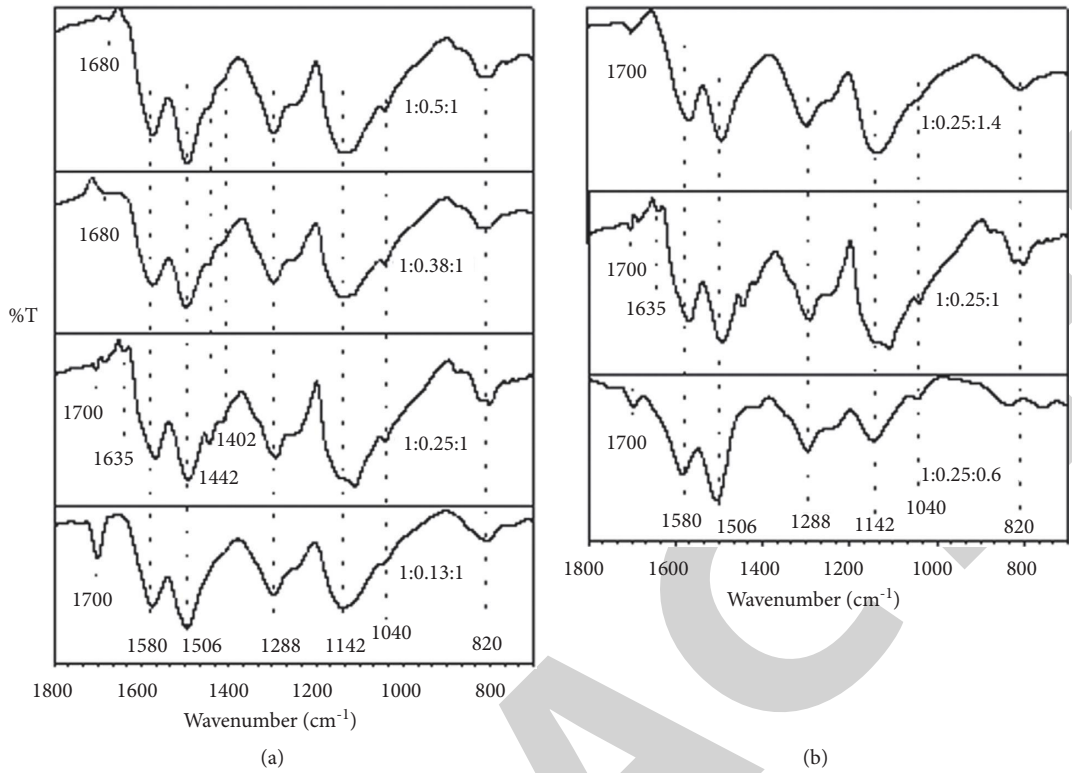

Figure 3: Analyses of polyaniline synthesized at different molar ratios of aniline:GA and APS were performed using FTIR. For the sake of comparison, the spectrum from the 1:1.25:1 sample is repeated.

and it cannot form part of the polymer chain as a dopant ion in this state. It can, however, form supramolecular interactions with the polymer chain, while sulfate and hydrogen sulfate ions derived from APS reduction stabilize the charged polymer chain and act as dopant ions. After completion of the reaction and purification of the polymer, the pH of the resulting polyaniline suspension was around 5. In this condition, the GA takes the form of a monovalent anion, which allows it to stabilize the charge of the polyaniline chain as the counterion. This conclusion is based on the results of electrical conductivity FTIR, where the presence of the amino acid and sulfur-containing species was demonstrated, once the polymerization process had finished.

3.4. Release of Adsorbed Drug versus Buffer Solutions. At 25 and 37°C with continual mechanical stirring, amoxicillin release profiles from the polyaniline/amoxicillin systems encapsulated in cellophane membranes were compared to buffer solutions. At 37°C, the cumulative drug release quantities at pH 5, 7, and 9 were 0.667 g (82.9%), 0.615 g (75.9%), and 0.791 g (98.0%), respectively, after 48 h of exposure to these pH values. It is hypothesized that an ion exchange process between the buffer ionic species and the counterions of the polyaniline salt system is responsible for the drug's release in both neutral and acidic environments (pH = 7 and 5). Amoxicillin is a zwitterion in this pH range; hence, it cannot interact with the polymeric structure electrostatically.

3.5. Hydrogels Composed of Polyacrylamide and Drug-Loaded Polyaniline. Composite polyacrylamide/polyaniline/amoxicillin hydrogels were prepared using the drug-loaded 1:0.25:1 polyaniline sample. Qualitatively, at the macroscopic level, the hydrogels presented a soft consistency, maintaining their geometry once extracted from the mold, which allowed their easy handling in drug characterization and release studies.

3.5.1. Morphological Characterization. Figure 4 presents micrographs obtained from the cross-section of hydrogel B. The images reveal the presence of polyaniline submicro/nanostructures, as observed after its synthesis by SEM (Figure 1(b)) and TEM (Figure 2(b)) within the hydrogel matrix. It is observed that the structures maintain their fibrillar morphology after the drug loading process and its incorporation into the hydrogel, conserving a high length-diameter aspect ratio and being distributed homogeneously, in random directions, and without significant agglomeration. A few SEM and TEM images in the literature show irregular granules of the electroconductive polymer filling the micrometric voids of the hydrogel, which is worth pointing out [17]. A three-dimensional network of polyaniline nanofibers supported by an insulating hydrogel matrix can be formed using the method described in this study.

3.5.2. In Vitro Release of Amoxicillin from Drug-Loaded Polyacrylamide-Polyaniline Composite Hydrogel Using Orbital Shaking. The release kinetics of amoxicillin adsorbed

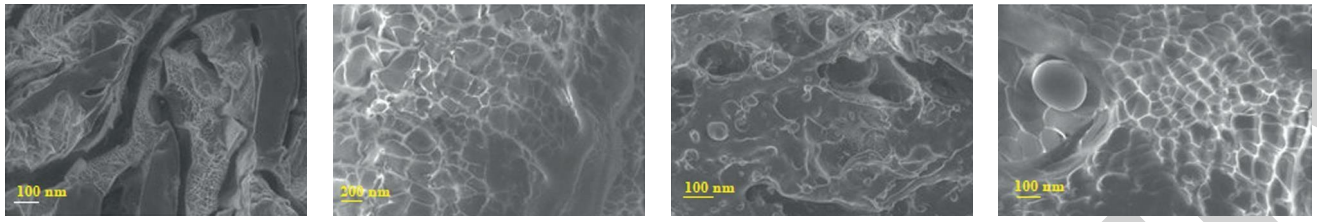

(a) (b) (c) (d)

Figure 4: TEM pictures of the hydrogel (hydrogel (a, b, c, and d)) made of polyacrylamide, polyaniline, and amoxicillin.

on polyaniline structures from polyacrylamide/polyaniline/amoxicillin composite hydrogels was studied as a function of the degree of cross-linking of the hydrogel (AAm:BisAAm mass ratio), the pH of the release medium, and the temperature for which the three formulations described. Additionally, the effect on the release kinetics of the form of incorporation of the drug into the hydrogel was analyzed, for which the formulation of the polyacrylamide gel without particles was used of polyaniline, loaded only with the antibiotic.

Results observed that the amount of antibiotic released varies with respect to the pH of the release medium, regardless of the degree of cross-linking of the hydrogel. At a higher pH value, the release kinetics is faster, and the % release is higher at equilibrium. This behavior is explained by taking into account the nature of the electroconductive polymer. The more significant release in the basic medium is mainly attributed to the undoping of polyaniline, which releases FA molecules surrounding the polyaniline structures and functions as counterions [17]. Consequently, the release of FAs is induced by amoxicillin molecules. The drug release in neutral and acid medium is explained by an ionic exchange process between the polyaniline doping species and the buffer anions, a process that according to the experimental results is less favored in acid medium. Hydrogel A, which contains a lower concentration of BisAAm, showed a different behavior than expected. By having a less cross-linking agent, it was expected that the polymeric network would be less compact than the rest of the concentrations, and therefore, the release would be favored, in agreement with the swelling results for this type of hydrogel. However, the experimental result showed that at this ratio, the release kinetics is slower and the % release at equilibrium is lower than for hydrogel B, a result that was corroborated by repeating the experimental procedure. The influence of temperature on the antibiotic release kinetics was analyzed in hydrogel B, since the highest equilibrium % release was achieved in this formulation. It is concluded that the adsorption of the drug on the polyaniline structures and its subsequent incorporation into the hydrogel favors its application in a prolonged drug release system; however, a more exhaustive analysis should be carried out on the kinetics that controls the release of bioactive molecules in a temperature-controlled environment. The "ON/OFF" type release pattern of the drug from the electroconductive system due to the effect of the electrical stimulus can be associated with the movement of the charged drug molecules by the impulse of the electric field. In the polyaniline/amoxicillin system, the first effect was ruled out because amoxicillin at neutral pH has no net charge. Therefore, drug release was attributed to the electrochemical reduction of polyaniline, which causes changes in the charge density of the polymer and contraction of its volume, which synergistically leads to the release of amoxicillin noncovalently bound submicron/polyaniline nanostructures.

3.5.3. Cellular Cytotoxicity Study. The recent results have indicated that polymer purification substantially improves biocompatibility, eliminating residues or by-products responsible for cytotoxicity [18]. Considering the potentiality shown by hydrogels composed of polyacrylamide/polyaniline for the controlled release of drugs, a study was carried out to evaluate the cytotoxicity of the polyacrylamide and polyacrylamide/polyaniline systems, analyzing their effect on cell proliferation using a cell viability assay. Figure 5 demonstrates the feasibility of normal mouse subcutaneous culture cells visible to different concentrations of the medium in contact with the hydrogels (conditioned medium).

In both systems, viability greater than 85% is observed for all cases, with a statistically significant reduction in cell viability being observed only for the highest concentration of conditioned medium (50%) compared to the control sample (cells exposed to medium) standard crop. However, cell viability remains above 80% even in this case.

In particular, for polyacrylamide/polyaniline hydrogels, viability declines with increasing concentration of the conditioned medium; however, no significant difference is observed at the same concentration between both gels. This fact suggests a minimal toxic effect of polyaniline nanostructures on cells. The decrease in viability observed when 50% of the medium is conditioned can be attributed to unpolymerized acrylamide residues, a monomer whose toxicity has been widely documented [18].

In general, viability of 80% or higher is indicative of the absence of cytotoxicity in accordance with the ISO 10993–5 standard. The results found by this assay show high cell viability when the cells have been exposed to culture media conditioned with polyacrylamide or polyacrylamide/polyaniline hydrogels, which is indicative of minimal cytotoxicity of these systems. These *in vitro* cytotoxicity results also suggest that a washing step for the hydrogels may be desirable before being exposed to continuous contact with cells to minimize acrylamide residues. Cell viability was 100%

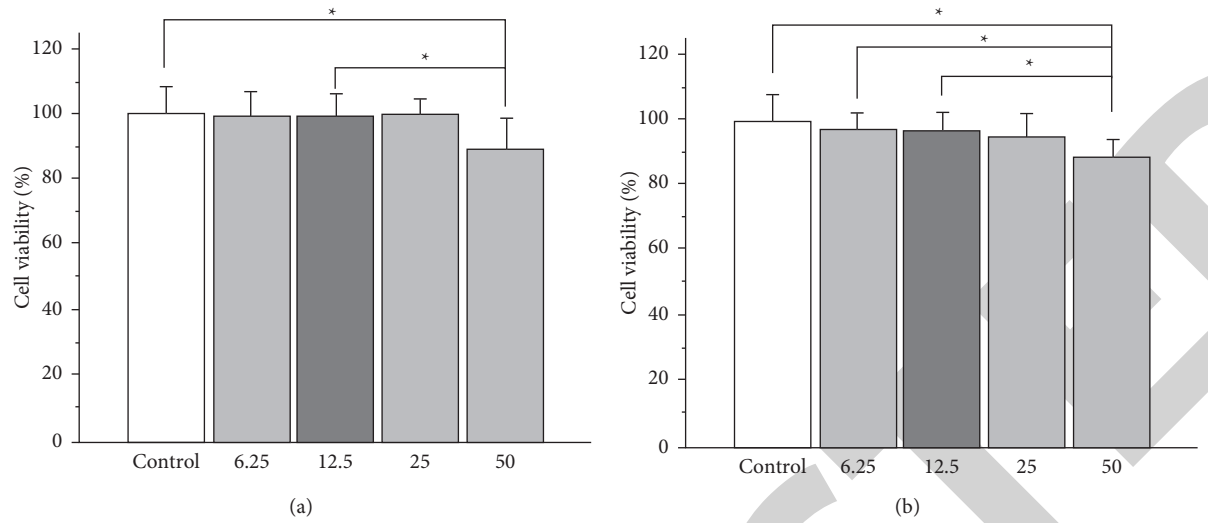

Figure 5: Percentage of cell viability of hydrogels of (a) polyacrylamide and (b) PAAm/polyaniline on the normal cell line L–929 (normal mouse subcutaneous tissue). The error bar represents the standard deviation ($n \geq 3$).

when cells were exposed to a conventional culture medium (the control) as well as polyacrylamide/polyaniline gel-conditioned conditions. Conditions medium with polyacrylamide and polyacrylamide/polyaniline hydrogels (50% concentration) exposed cells display a similar shape to control cells, with no signs of cell injury. These findings are in line with those in Figure 5, which depicts the vitality of cells.

4. Conclusions

Ammonium persulfate can be employed as an oxidant to create one-dimensional nanostructured polyaniline systems with high length/diameter ratios. Glutamic acid is used as a dopant in polyaniline structures, along with sulfur-containing anions produced by ammonium persulfate reduction. The resultant products' composition, electrical, morphological, and optical properties vary depending on the molar ratio of aniline:amino acid:oxidant used in the synthesis. The release of amoxicillin from polyaniline-based fibrillar structures may be modulated as the pH of the release medium varies, allowing for accurate dosage. By integrating amoxicillin-loaded polyaniline particles in situ during acrylamide polymerization and cross-linking, amoxicillin-loaded polyaniline particles can be efficiently encased in a polyacrylamide hydrogel. When amoxicillin is just in the bulk of the hydrogel, it is more strongly held on the polyaniline particles. When compared to a hydrogel without polyaniline fibers, the composite hydrogel has a slower drug release kinetics, allowing it to be used in prolonged-release systems. The pH and temperature of the release medium can be used to control the release of amoxicillin from hydrogels made of polyacrylamide and polyaniline. We can conclude that hydrogels composed of polyacrylamide/polyaniline can be considered potential candidates for applications in electrically controlled release devices, such as iontophoretic patches, based on the ability to control drug release using low-intensity voltages and the lack of cytotoxicity found for this material in *in vitro* cell viability studies. While conventional iontophoretic devices are based on the electromigration of ionized pharmaceuticals, the release from the polyacrylamide/polyaniline system is regulated by the redox characteristics of the electroconductive polymer, which broadens the spectrum of possibilities to molecules in a neutral state.

Data Availability

The data underlying the results presented in the study are available within the manuscript.

Conflicts of Interest

The author declares that there are no conflicts of interest regarding the publication of this paper.

References

[1] I. Sapurina and M. Shishov, *Oxidative Polymerization of Aniline: Molecular Synthesis of Polyaniline and the Formation of Supramolecular Structures*, InTechOpen, London, UK, 2012.

[2] J. Kinyanjui, J. Hanks, D. Hatchett, A. Smith, and M. Josowicz, "Chemical and electrochemical synthesis of polyaniline/gold composites," *Journal of the Electrochemical Society*, vol. 151, pp. D113–D120, 2004.

[3] Q. N. Al-Haidary, A. M. Al-Mokaram, F. M. Hussein, and A. H. Ismail, "Development of polyaniline for sensor applications: a review," *Journal of Physics: Conference Series*, vol. 1853, no. 1, Article ID 012062, 2021.

[4] Z. A. Boeva and V. G. Sergeyev, "Polyaniline: synthesis, properties, and application," *Polymer Science—Series A C*, vol. 56, no. 1, pp. 144–153, 2014.

[5] U. Riaz, N. Singh, F. Rashnas Srambikal, and S. Fatima, "A review on synthesis and applications of polyaniline and polypyrrole hydrogels," *Polymer Bulletin*, vol. 275, 2022.

[6] N. R. Tanguy, M. Thompson, and N. Yan, "A review on advances in application of polyaniline for ammonia